The University Of Sheffield.

University of Sheffield

DOCTORAL THESIS

Characterisation of GaAsBi based semiconductors

Author:
Yuchen Liu

First Supervisor:
Prof. John David
Second Supervisor:
Dr. Robert Richards

A thesis submitted in partial fulfilment of the requirements for the degree of Doctor of Philosophy

in the

Semiconductor Material and Devices Group
Department of Electronic and Electrical Engineering

December 5th, 2020

Declaration of Authorship

I, Yuchen Liu, declare that this thesis titled, "Characterisation of GaAsBi based semiconductors" and the work presented in it are my own. I confirm that:

- This work was done wholly or mainly while in candidature for a research degree at this University.
- Where any part of this thesis has previously been submitted for a degree or any other qualification at this University or any other institution, this has been clearly stated.
- Where I have consulted the published work of others, this is always clearly attributed.
- Where I have quoted from the work of others, the source is always given. With the exception of such quotations, this thesis is entirely my own work.
- I have acknowledged all main sources of help.
- Where the thesis is based on work done by myself jointly with others, I have made clear exactly what was done by others and what I have contributed myself.

Signed: Yuchen Liu

Date: 05/12/2020

Abstract

GaAsBi alloys have recently attracted much attention due to its large bandgap reduction, temperature insensitivity behaviour and giant spin-orbit splitting properties. These special characteristics enable enormous potential for GaAsBi in applications such as shortwave infrared optoelectronics, thermoelectricity and photovoltaics.

Two conditions have restricted high-quality GaAsBi growth. First, a low growth temperature at ~400°C while maintaining the As/Ga atomic flux ratio close to stoichiometry is required. Second, the lattice mismatch with the substrate will inevitably lead to strain relaxation in thick structures. Therefore, there are very few reports of GaAsBi device with >400nm thick intrinsic region from the literature.

In this work, four systematic series of bulk GaAsBi p-i-n and n-i-p samples with varying i-region thickness and bismuth content were grown using molecular beam epitaxy. The optical and electrical properties of those samples were characterised by various techniques. From the optical characterisations, the devices grown with thick structures show higher strain relaxation, which was confirmed by cross-hatch patterns observed by Nomarski microscopy and X-ray diffraction. The bismuth content of each wafer obtained from valence band anti-crossing model and XRD simulations match well. Current-voltage measurements show good diode behaviour with a clear relationship between the dark current and bismuth content.

Comprehensive multiplication measurements were performed in those four sets of GaAsBi diodes at room temperature. A large disparity between the electron and hole ionisation coefficients has been found. Further analysis on the onset of multiplication of 400nm thick p-i-n and n-i-p with different bismuth content showed that adding Bi into GaAs significantly reduces the hole ionisation coefficient while the electron ionisation coefficient remains virtually unchanged. This is the first time such a peculiar discovery was observed in a dilute III-V alloy system and is attributed to the effect bismuth has on the spin-orbit splitting energy. This new and significant find will provide a new route to enhance the α/β ratio, making GaAsBi a promising material for low noise avalanche photodiodes.

List of publications

Journal papers

1. **Y. Liu,** X. Yi, N. J. Bailey, Z. Zhou, T. B. O. Rockett, L. W. Lim, C. H. Tan, R. D. Richards and J. P. R. David, *Valence Band Engineering of GaAsBi for Low Noise Avalanche Photodiodes*, Nature Communications 12, 4784, (2021)
2. R. D. Richards, F. Harun, M. R. M. Nawawi, **Y. Liu**, T. B. O. Rockett and J. P. R. David, *Temperature and bandgap dependence of GaAsBi p-i-n diode current-voltage behaviour*, Journal of Physics D: Applied Physics 54, 195102 (2021)
3. T. B. O. Rockett, R. D. Richards, Y. Gu, F. Harun, **Y. Liu**, Z. Zhou, J. P. R. David, *Influence of growth conditions on the structural and opto-electronic quality of GaAsBi*, Journal of Crystal Growth 477, 139-143 (2017)
4. N. Baladés, D. L. Sales, M. Herrera, C. H. Tan, **Y. Liu**, R. D. Richards and S. I. Molina, *Analysis of Bi Distribution in Epitaxial GaAsBi by Aberration-Corrected HAADF-STEM,* Nanoscale Research Letters (2018) 13:125

Oral and poster presentations

1. R. D. Richards, T. B. O. Rockett, Z. Zhou, **Y. Liu**, J. P. R. David, *GaAsBi work at the University of Sheffield,* UK MBE User Group Meeting, Cambridge, UK, 18th March 2016
2. Z. Zhou, R. D. Richards, Y. Gu, T. B. O. Rockett, F. Harun, **Y. Liu**, J. S. Cheong, A. Baharuddin, J. P. R. David, *Investigation of photo-multiplication in GaAsBi diodes,* 7th International Workshop on Bismuth Containing Semiconductors, Shanghai, China, 25th July 2016
3. T. B. O. Rockett, R. D. Richards, Y. Gu, F. Harun, **Y. Liu**, Z. Zhou, J. P. R. David, *Opto-electronic measurements of GaAsBi PIN diodes,* Semiconductors and Integrated Opto-Electronics, Cardiff, UK, 18th April 2017
4. R. D. Richards, T. B. O. Rockett, **Y. Liu**, J. P. R. David, *Bismides in the basement update,* UK MBE User Group Meeting, Edinburgh, UK, 21st April 2017
5. R. D. Richards, T. B. O. Rockett, **Y. Liu**, F. Harun, J. S. Roberts, J. P. R. David, *Making progress in photovoltaics: Can dilute bismides fill the 1 eV band gap*?, Wroclaw University of Science and Technology, Wroclaw, Poland, 11th May 2017
6. R. D. Richards, T. B. O. Rockett, **Y. Liu**, F. Harun, J. P. R. David, *Hole trapping in GaAsBi/GaAsMQWs: Lessons from dilute nitrides*, UK Semiconductors, Sheffield, UK, 12th July 2017
7. T. B.O. Rockett, R. D. Richards, Y. Gu, F. Harun, **Y. Liu**, Z. Zhou, J. P. R. David, *Electroluminescence and current-voltage measurements of GaAsBi PIN diodes*, 8th International Workshop on Bismuth Containing Semiconductors, Marburg, Germany, 25th July 2017
8. Z. Zhou, R. D. Richards, **Y. Liu**, T. B. O. Rockett, F. Harun, J. P. R. David, *The investigation of photomultiplication in GaAsBi diodes*, 8th International

Workshop on Bismuth Containing Semiconductors, Marburg, Germany, 25th July 2017

9. **Y. Liu**, R. D. Richards, N. Bailey, T. B. O. Rockett, M. R. Nawawi, J. P. R. David, *Update on Sheffield bismides activity*, UK MBE User Group Meeting, Nottingham, UK, 13th April 2018
10. Xin Yi, **Y. Liu**, Z. Zhou, F. Harun, R. D. Richards, C.H. Tan and J. P. R. David, *Investigation of photo-multiplication in GaAsBi diodes,* Semiconductors and Integrated Opto-Electronics, Cardiff, UK, 18th April 2018
11. **Y. Liu**, R. D. Richards, T. B. O. Rockett, F. Harun, Y. Gu, J. P. R. David, *Electroluminescence study of GaAsBi devices of different growth conditions*, UK Semiconductors, Sheffield, UK, 4th July 2018
12. T. B. O. Rockett, R. D. Richards, **Y. Liu**, F. Harun, Z. Zhou, Y. Gu, J. P. R. David, *GaAsBi/GaAs multiple quantum wells with up to 120 periods*, 9th International Workshop on Bismuth Containing Semiconductors, Kyoto, Japan, 18th July 2018
13. **Y. Liu**, R. D. Richards, T. B. O. Rockett, Y.Gu, J.P. R. David. Oral Presentation: How Growth Conditions Affect GaAsBi Device Electroluminescence. The 20th International Conference on Molecular Beam Epitaxy, Shanghai, China, 2-7th September 2018

Acknowledgements

First and foremost, I would like to thank my supervisor Prof. David for his invaluable guidance and supervision throughout the project. During my PhD studying, he spent countless time with me to discuss my research topic. Besides, he has been very supportive in my life and also provides lots of suggestions for my career development. I also would like to express my deep gratitude to Dr Robert Richards, who has provided most of the instructive advice for my research.

I am grateful to Dr Thomas Rockett for all his help on my work. During the research, he taught me the fundamental MBE growth technique and shared his experiences. I would like to thank our Bismide team, especially Nick, Zhizhe, Nada, Riduwan, Faezah for their friendship and discussions.

I would like to thank member for Impact Ionisation Group who have helped me with measurements, particularly Leh Woon Lim for his help on the device fabrication and showed me how to use the Janis probe setup. My appreciation is also extended to Xiaojin, Yuting, Aina, Cheong, Simon for their help and discussions.

Special thanks go to my friend Xin Yi. He helps me a lot with electrical measurements and modelling. He always encouraged me, making me feel not frustrating as I was meeting the difficulties. I will always cherish our friendship.

Last but wholehearted thanks go to my wife and my parents for their unreserved and constant love and support.

Contents

List of Figures

List of Tables

Chapter 1: Introduction

The introduction section includes two main topics. First, starting with an overview of III-V materials, the main characteristics of GaAsBi will be described to help us understand why people have become interested in this unusual material in recent years. Second, it reviews the current application and the prospect of GaAsBi. At the end of this section, the motivation and a brief summary of this thesis will be given.

1.1 III-V elements

Alloys of elements from group III and group V of the periodic table are known as III-V materials, which are shown in Figure 1.1. One of the most commonly known materials is GaAs.

In general, III-V materials are mainly used as optoelectronic devices such as detectors and light emitting diodes. This is because the materials have direct bandgap and excellent thermal stability. Moreover, the bandgap of the III-V compounds offers a wide coverage of the electromagnetic spectrum from deep ultraviolet to far-infrared. Over the past two decades, researchers have experimented the incorporation of elements such as nitrogen (N) and bismuth (Bi) into III-V compounds due to unusual properties exhibited. One important discovery is that these N-/Bi-incorporated materials induces a significant reduction in the bandgap[1], [2].

III	IV	V
B	C	N
Al	Si	P
Ga	*Ge*	*As*
In	*Sn*	*Sb*
Tl	*Pb*	*Bi*

Table 1.1 Group III, IV and V materials in the periodic table, the element commonly used in III-V alloy which are highlights to red.

1.2 Ternary III-V alloys and Vegard's law

The binary III-V semiconductors only satisfy a limited demand for devices. However, different combinations of binary materials to form ternary III-V alloys can offer a broader range of choice, as shown in Figure 1.1. The bandgap and lattice constant of

the ternary alloys are in between the two binary constituents. In order to make lattice-matched devices, the epilayers must have the same lattice constant as the substrate. It is well known that Vegard's law is a universal equation [3] to describe the lattice constant for most of ternary alloys, the general formula of a conventional ternary III-V can be expressed as

$$a(A_{1-x}B_xC) = xa(BC) + (1-x)a(AC) \qquad (1.1)$$

where a is the lattice constant for each material, x is the fraction of group III atoms. The bandgap of most III-V ternary alloys also can be modelled in the same method, with an additional bowing parameter that is material dependent.

$$E_g(A_{1-x}B_xC) = xE_g(BC) + (1-x)E_g(AC) + bx(1-x) \qquad (1.2)$$

where E_g is the bandgap for each material, b is the bowing parameter. In general, the value of the bowing parameter is typically less than 1eV for most of the semiconductor alloys [4]. However, it has been found that both dilute GaAsN and GaAsBi alloys have a large bowing parameter [4], [5]. For these particular cases, Vegard's law cannot be used to predict the value of bandgap accurately. In order to predict the band gap, an alternative model was developed. The model is named the Band Anticrossing Model.

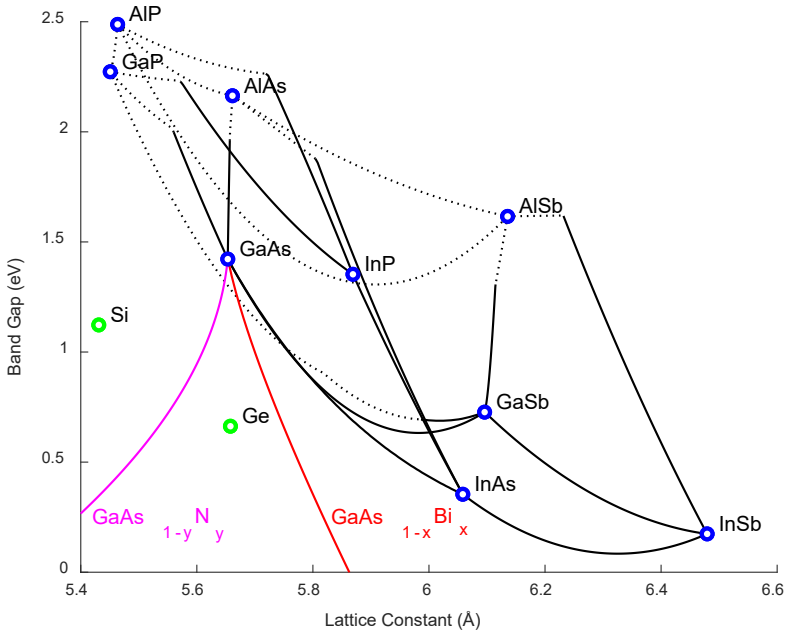

Figure 1.1 Lattice constant diagram versus bandgap for common III-V semiconductors(blue). The IV element Silicon and germanium are labelled in green. The solid line represents the ternary alloys with a direct band gap material and the dash line represents the ternary alloys with an indirect band gap material. The pink and red solid line represents GaAsN and GaAsBi respectively in theoretical prediction.

1.3 To calculate bandgap of GaAsBi using valence band anti-crossing model

Due to the distinctly different ionic radius of N and As, incorporating N into GaAs will lead to a highly mismatched alloy (HMA). In order to explain how the electronic structure of bandgap changes with dilute nitride, the band anti-crossing model was proposed by Shan *et al.* [6]. A similar phenomenon is also observed in $GaAs_{1-x}Bi_x$, in which the atomic radius of Bi is much larger than that of As. Besides that, it is also found that incorporating Bi into GaAs will have the most effect on the valence band rather than the conduction band. Therefore, an extended model used to explain the bandgap change affected by Bi was proposed by Alberi *et al.* [7], named the valence band anti-crossing (VBAC) model.

Incorporating Bi into GaAs will introduce defect states of Bi that are below the valence band maximum (VBM). The interaction between the resonant state of Bi and valence band results in a split on the heavy-hole (HH) and light-hole (LH) valence band, then making them from the original two sub-bands into four sub-bands, which are defined as HH E^+ , LH E^+, HH E^- and LH E^-. By increasing the Bi content, the splitting leads to an upward motion of HH E^+ and LH E^+ that results in a large bandgap reduction. It is also found that a big shift in split orbit splitting band occurs due to the anti-crossing interaction.

As described by A.R. Mohmad [8], the energy of sub-band E^+ and E^- is given by:

$$E_{\pm}(GaAsBi) = \frac{E_v(GaAs) + E_{Bi} \pm \sqrt{(E_v(GaAs) - E_{Bi})^2 + 4xC_{Bi}^2}}{2} \quad (1.3)$$

where E_{Bi} is the defect state of bismuth, $E_v(GaAs)$ is the energy of the valence band maximum of GaAs, x is the composition of bismuth and C_{Bi} is the matrix element that describes the coupling between Bi-states and the extended conduction-band states. According to A.R Mohmad, when the defect state of bismuth is 0.4 eV below the VBM of GaAs, the value of C_{Bi} is 1.6eV [8].

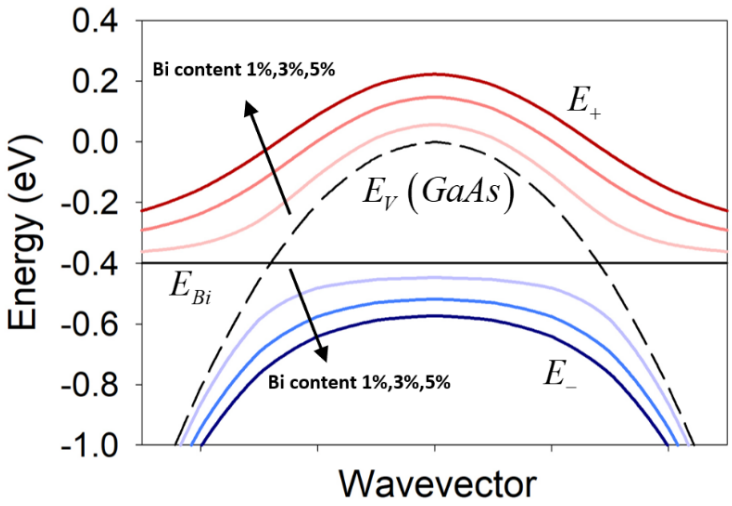

Figure 1.2 The calculated valence band structure of GaAsBi using the VBAC model for different Bi content.

The conduction band is also affected by the perturbation between bismuth and host GaAs, which can be explained by using virtual crystal approximation (VCA), given by equation 1.4 [8].

$$E_{CB-VCA} = E_g - \Delta E_{CBM} x \quad (1.4)$$

where E_g is the conduction band minima of GaAs, and ΔE_{CBM} =2.3eV is a constant parameter that is attributed by the conduction band offset between GaAs and GaBi. Therefore, the bandgap of GaAsBi is then described by

$$E_g(GaAsBi) = E_g(GaAs) - \Delta E_{CBM} x - E_+ \quad (1.5)$$

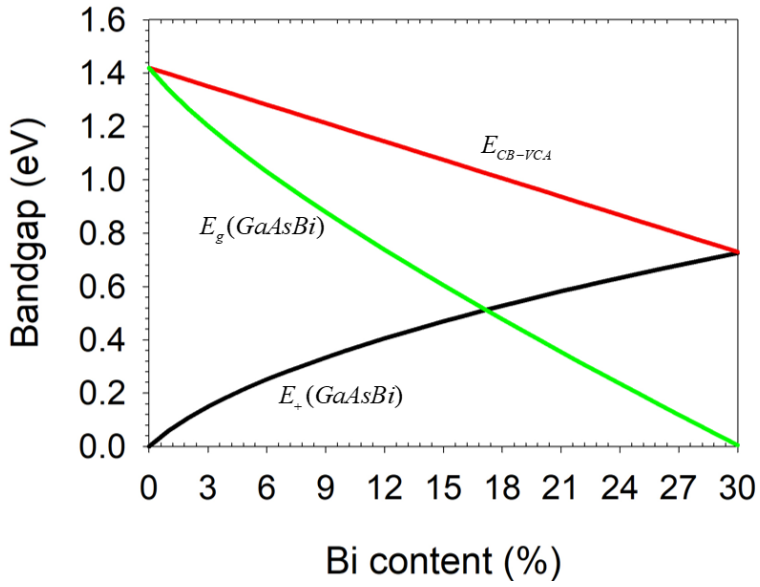

Figure 1.3 Bandgap of GaAsBi related to band offset between the conduction band minima of GaAs and $E_+(GaAsBi)$.

From Figure 1.3, it is evident that by increasing Bi content, a considerable bandgap reduction in GaAsBi can be obtained. The model predicts that when the Bi content is over 30%, a negative bandgap can be achieved. Using this model, the predicted bandgap of GaBi is -2.34eV, which contradicts with theoretical modelling suggesting a value of -1.45eV [9]. However, a good fitting with experimental data still holds true for bismuth contents less than 12%.

The bandgap of other III-V GaAs based materials with different alloy composition are shown in Figure 1.4, in which the reduction of the bandgap is significant using nitrogen and bismuth rather than indium or antimony. For GaAsSb and InGaAs, the rate of bandgap reduction is linear. In terms of GaAsN and GaAsBi, the rate of bandgap reduction is not following a linear relationship. The bandgap reduces dramatically at the initial few compositions of N and Bi and then maintains at the gentle rate of decline. The more considerable change in bandgap for GaAsN and GaAsBi is due to the distinct difference in size and electronegativity between N/Bi and As atoms.

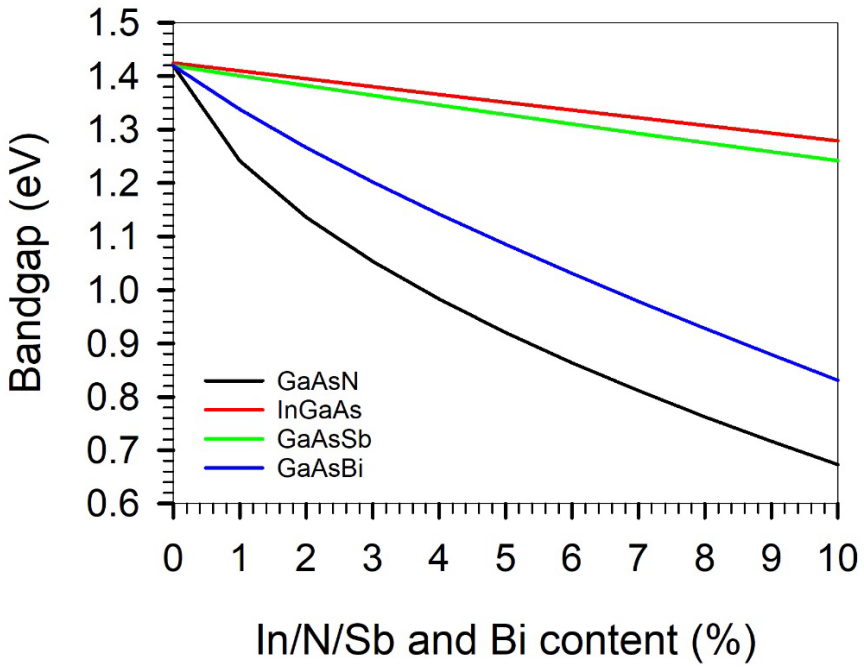

Figure 1.4 The bandgap of GaAs based ternary III-V alloys, the bandgap of InGaAs was calculated by equation taken from [10] , the BAC model was performed to calculate the bandgap of GaAsSb [11]and GaAsN [6]. The VBAC model was applied to calculate the bandgap of GaAsBi [7].

1.4 Lattice mismatch and strain

When Si epitaxial layers are grown on a silicon substrate, high-quality crystal layers can be obtained because there is no lattice mismatch. Heteroepitaxy growth refers to the epitaxial growth of a different material on the substrate. High-quality crystal layers can be grown when the lattice constant and lattice structure are the same for these two materials. For example, GaAs and AlAs both have zincblende crystal lattices and the lattice constants are similar, at 5.6533Å and 5.6611Å, respectively [12]. Therefore, the ternary alloy AlGaAs can be grown on GaAs substrate with only a slight mismatch [13].

As shown in Figure 1.1, in order to grow the lattice-matched structure, the value of compositions in a ternary compound is varied. For example, the ternary compound $In_xGa_{1-x}As$, where x takes a value between 0 to 1, InGaAs can be grown lattice-matched to an InP substrate when x is equal to 0.53. However, in reality the compatibility between the epitaxial layer and the substrate cannot fit perfectly, which will result in mismatch strain. The lattice misfit is expressed in equation 1.6 [14].

$$F_s = \frac{a_s - a_e}{a_e} \qquad (1.6)$$

a_s is the lattice constant of the substrate, and a_e is the relaxed lattice constant of the epilayer. The two types of strain, compressive and tensile, depends on the value of lattice mismatch. If F_s is larger than 0, it is defined as tensile strain. Whereas compressive strain is defined when F_s is less than 0. For a thin layer with mismatch of less than one percent, strain can be tolerated to allow epilayer growth onto the substrate. Such layer is known as pseudomorphic layer as shown in Figure 1.5(a). The lattice of the epilayer is tetragonally distorted. Therefore, the lattice parameter of the epitaxial layer perpendicular to the surface, *t*, is larger than the relaxed lattice constant, a_s, of the epilayer due to strain.

Based on Matthews and Blakeslee theory [15], any given strain on a heteroepitaxial growth will have a critical thickness, t_c. If the thickness of epitaxial layer is kept thin enough to maintain the energy that below the energy of dislocation formation, at this point it is the thermodynamically stable state, also called pseudomorphic limit. Figure 1.5 (a) gives the example. As the epilayer of pseudomophic layer grows thicker, the thickness of the epilayer will eventually exceed the critical thickness. The accumulated strain then leads to the formation of misfit dislocation, as shown in Figure 1.5(b). Although the effect of these dislocations can reduce the elastic strain caused by lattice mismatch, it is a detrimental effect that can degrade the optical properties of the material.

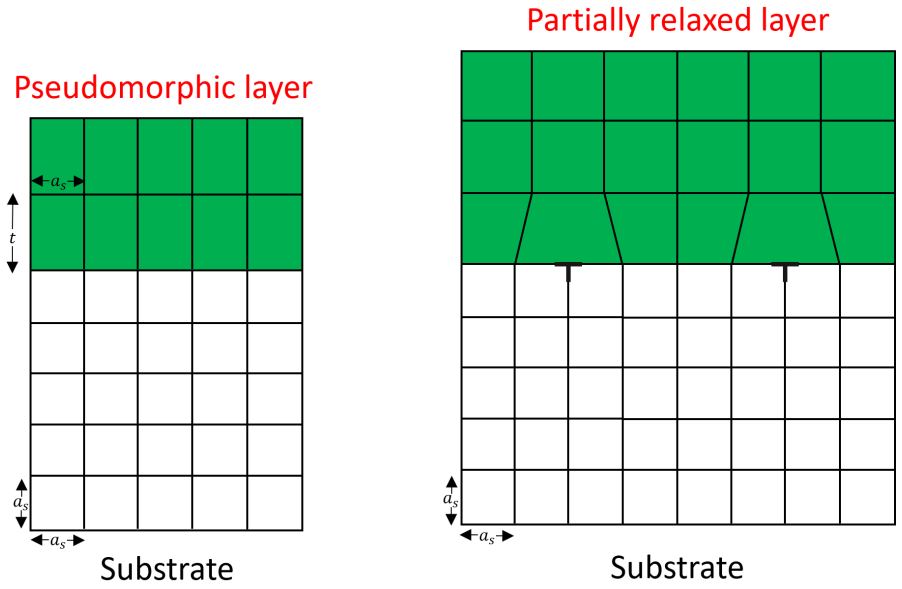

Figure 1.5 Heteroeptaxy and misfit dislocations. (a) When the layer thickness is less than the critical thickness, pseudomorphic growth occurs. (b) However, when $t>t_c$, misfit dislocations are formed at the interface of epilayer and substrate.

1.5 The lattice balanced GaAsNBi

Although the GaAsBi alloy has unique properties that simultaneously modify both the lattice constant and the bandgap, to grow high-quality GaAsBi alloy on GaAs substrates is difficult due to the large difference in atomic size between Bi and As. As a result, the lattice mismatch will result in strained or relaxed layers when growing GaAsBi on GaAs substrates, impacting negatively on the optical properties of the material. In order to overcome this problem, the potential alloy, GaAsNBi, has been proposed to compensate for lattice mismatch [16], since the disparate atomic size between Bi and N can balance each other. The lattice constant of $GaAs_{1-x-y}N_xBi_y$ can be calculated based on the Vegard's law [3], which is given by:

$$a(x,y) = (1-x-y)a_{GaAs} + xa_{GaN} + ya_{GaBi} \qquad (1.7)$$

Where a_{GaAs}, a_{GaN} and a_{GaBi} are the lattice constant of GaAs, GaN and GaBi which are calculated in [9] as 5.653Å, 4.448Å and 6.324Å, respectively. When $y = 1.7x$, this alloy can be made lattice-matched to GaAs substrate. By tailoring the composition of N and Bi, the GaAsNBi lattice matched to GaAs substrate can be achieved to realise 1.3 μm solid-state lasers or high-efficiency solar cells [17].

For GaAsN and GaAsBi, incorporating 4.5% N or 6.5% Bi can also reach the goal band gap of 1eV [9]. However, high lattice mismatch will seriously affect the working performance of the material. GaAsNBi has an obvious advantage compared with N or Bi the GaAs based alloy, which only needs a small amount of N and Bi , 2.7% and 4.5%, to achieve the 1eV band gap, and to a certain extent, reducing N composition can greatly improve the optical and transport performance of the alloy [18], [19].

1.6 Other benefits of bismuth for optoelectronic devices

In addition to the large bandgap reduction, GaAsBi has other advantages, such as temperature insensitivity [1], [20], large spin-orbit splitting energy [5], [21], and Bi is also an excellent surfactant [22], [23]. Because of these advantages, Bi has great potential in optoelectronic devices.

- **Temperature insensitive bandgap**

The temperature-insensitive bandgap of GaAsBi offers significant advantages in reducing the cost of wavelength-division-multiplexing (WDM) optical fibre communication networks. In conventional WDM system where GaInAsP

semiconductor lasers are used, one of the major problems is that the laser output wavelength fluctuates as the ambient temperature varies. This is due to the temperature dependent band gap of GaInAsP.

Thereby, an additional Peltier element cooling system used to control the laser temperature must be equipped, which makes the system more cumbersome and expensive. Research has shown that the bandgap of GaAsBi is relatively insensitive to changes in the temperature [1], [24]. The author of [1] noted that the temperature coefficient of GaAsBi is as small as 0.1 meV/K from temperature-dependent PL measurement. This is five times less than that compared with GaAs. The temperature-insensitive bandgap is related to the alloy composition of a semiconductor that consists of a semiconductor (GaAs) and a semimetal (GaBi), which have band gaps that have the opposite dependence on temperature. A similar effect also has been observed in HgCdTe [24] and InAsBi alloy [25]. Such temperature-insensitive property will make GaAsBi an alternate choice instead of InGaAsP for use in WDM laser systems without cooling packages.

- **Large spin-orbit splitting energy**

The large increase in the spin-orbit splitting energy shown by GaAsBi makes it potentially suitable for spintronic applications. Furthermore, studies have shown that Bi containing alloys also offer the possibility to suppress Auger recombination [26]. The details of Auger recombination are expanded in Section 4.32. As shown in Figure 1.6(a), both bandgap and spin-orbit-splitting can be changed dramatically by increasing Bi content. When the incorporation of Bi composition is over 10% the magnitude of spin-orbit-splitting exceeds the bandgap of the material ($\Delta So > E_g$). Therefore, one of the major auger recombination pathways cannot occur because there is no available state based on the conservation of energy.

Figure 1.6(b) shows how Bi affects the spin-orbit-splitting, and consequently results in suppressing the Auger recombination.

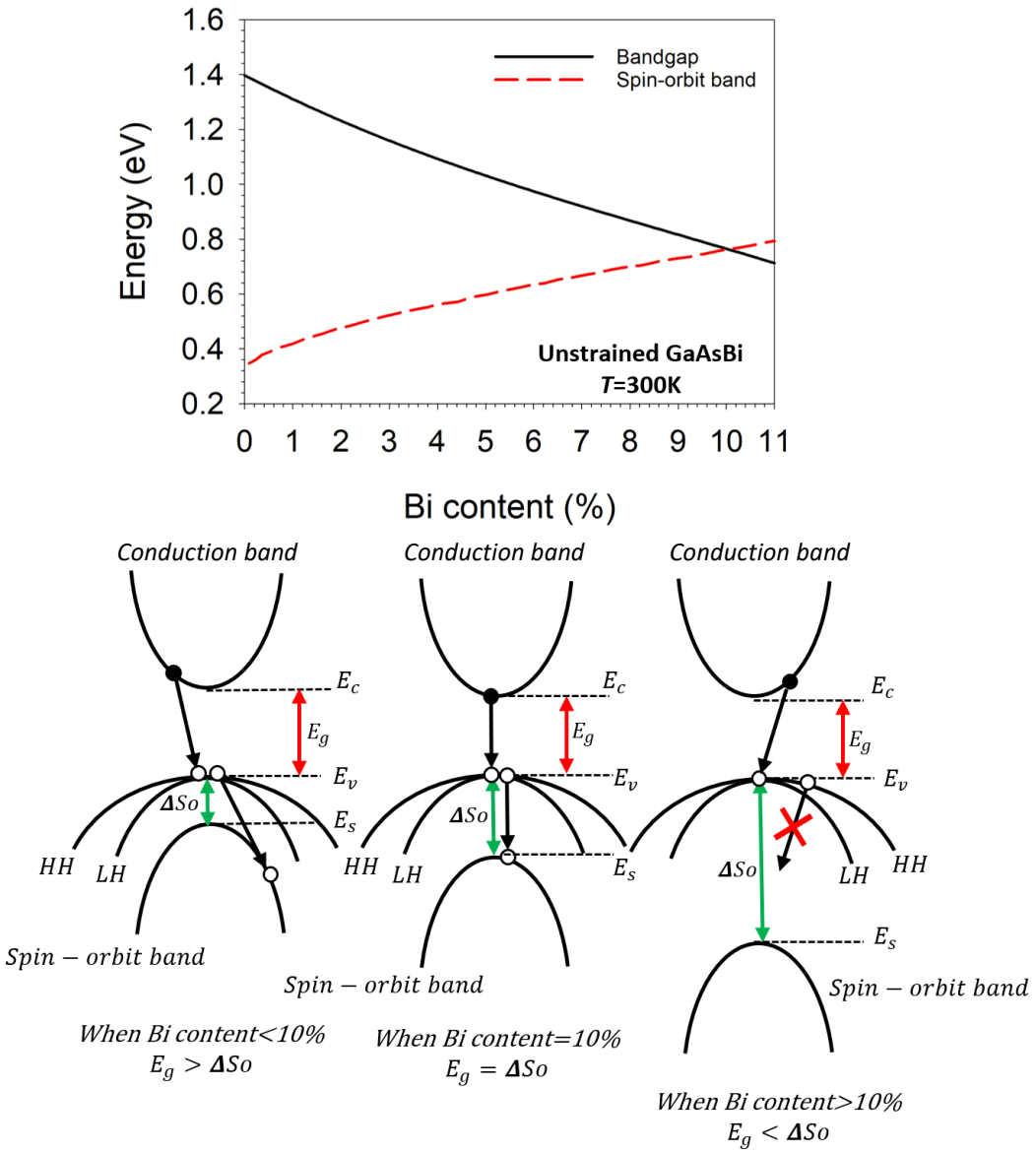

Figure 1.6 a) Room temperature band gap and spin-orbit-splitting as a function of Bi content. The strained effect is not considered in here (Adapted from [3]) b) Illustration of the suppression of Auger recombination with increasing Bi content. The Green arrow represents the spin-orbit splitting energy and the red arrow is the bandgap of material. The red cross represents the suppressed Auger recombination.

- **Bismuth as a surfactant**

It is known from prior studies that incorporating bismuth into III-V semiconductor is difficult under normal growth condition [1], [27], [28]. Instead, bismuth atoms are more likely to remain on the growth surface. Among the group III-V elements, bismuth has

one of the smallest segregation coefficients and the solid solubilities, 10^{-4} and $10^{-17}cm^{-3}$ respectively. Such properties make bismuth a good surfactant.

Early studies used bismuth as a surfactant during the growth of Ge/Si heterojunctions [22], [29]. After that, bismuth has been used as a surfactant for growth of InGaAs [23], InGaAsN[30] and GaAsN [30], [31] based on GaAs substrates to reduce the surface roughness. The author of [22] claimed that bismuth has a low self-incorporation rate compared with other surfactants.

Meanwhile, it could also effectively suppress surface roughening and Ge segregation. Besides, the bismuth surfactant layer is easy to thermally desorb at the temperature of 575°C, and such low temperature can ensure an abrupt silicon/germanium interface is preserved. From the results in [30], the author found that bismuth not only decreases surface roughness but also aids nitrogen incorporation in GaAsN. In addition to that, the peak photoluminescence intensity of the sample with bismuth flux improves a factor of two compared with the surfactant-free sample.

1.7 Current application of GaAsBi

Based on the characteristic of large bandgap reduction and a large spin-orbit splitting in GaAsBi, the wavelength of the photons that emits and absorbs by GaAsBi material can be increased to greater than 1μm. Thereby, the working region of the current GaAsBi application is between the near-infrared and the short-wave infrared. Based on its properties, the band engineering of GaAsBi has great potential for LEDs, lasers, photodetectors, solar cells, THz sources, etc.

1.7.1 LED and MIR Laser

A GaAsBi LED that emits light at 987nm with 1.8% Bi was first demonstrated by Lewis *et al.* in 2009 [27]. The authors found two distinct results from temperature-dependent PL and EL measurement. The peak wavelength of GaAsBi from EL measurements shows temperature-independent characteristics from 100-300K, while PL measurement on the same structure shows the opposite results. For temperature insensitivity of the GaAsBi EL peak, the author explained it occurred due to the compensation between the variation of bandgap and the emission from lower energy states [27].

Another bulk structure GaAsBi LED grown on the GaAs substrate with 6% Bi was reported by Richards [32]. The emission wavelength is around 1.2μm from room-temperature (RT) EL measurements. The temperature dependence of the integrated

emitted luminescence (IEL) results fitted well with the Varshni equation but also showed a S-shaped temperature dependence. This indicated that the Bi-induced localised states exist in the bandgap.

The first photo-pumped GaAs/GaAsBi/GaAs heterojunction Fabry-Perot (FP) laser grown on GaAs substrate was demonstrated proposed by Yoshimoto group in 2010 [33]. The active region of the laser was a 390nm GaAsBi layer with Bi content of 2.5%, which was grown at a temperature of 350 °C by MBE. The laser operated at both RT and 240K and showed a narrow laser spectrum at 982.8nm and 986.2nm, respectively. From 160 to 240K, the laser emission energy showed a constant decrease rate of 0.18meV/K. This is around 40% of the temperature coefficient of GaAs in the same temperature range. The threshold pumping densities of the laser showed a linear relationship with increasing temperature. However, it has a dramatic increase above 240K, at which point the emission energy of laser shifts to a shorter wavelength. The author explained this might be due to the structure of the material's bandgap, in which there is a large band offset of the valence band and a relatively flat band offset of the conduction band.

In 2013, the Yoshimoto group improved their GaAsBi laser diode design [34]. Prior to the growth of GaAsBi active layer, an AlGaAs electron-blocking layer was grown instead of a GaAs layer in the previous design. The Bi content in this laser design was 5.8%, over a factor of two higher than the previous design, with the emission wavelength of 1204nm at RT. The laser output was measured over the temperature range 20 to 80 °C, and the laser wavelength temperature coefficient was roughly 40% of that of a 1.3μm GaInAsP FP laser.

An electrically pumped GaAsBi single quantum well laser was first reported by Ludewig *et al.* in 2013 [35]. The active layer was 6.4nm of GaAsBi with 2.2% Bi, which was embedded between two 150nm $Al_{0.2}Ga_{0.8}As$ barriers and further sandwiched between two 1.4μm $Al_{0.4}GaAs$ n-doped and p-doped layers. The purpose of using $Al_{0.2}Ga_{0.8}As$ was to increase the electron confinement in the conduction band as Bi mainly affects the valence band. The threshold current density was around 1.56 kA/cm^2 with an emission peak wavelength of 947nm at RT.

In 2014, Yoshimoto et al. reported a similar structure for electrically pumped GaAsBi laser diodes grown by MBE [36]. The different laser diodes include 3% and 4% Bi

content, with maximum emission peak wavelength up to 1045nm at RT. From the laser wavelength temperature dependence testing, the temperature coefficient of the $GaAs_{0.97}Bi_{0.03}$ laser diode was reduced to 0.17nm/K. The result is consistent with the $GaAsBi_{0.025}$ optically-pumped laser they previously reported.

Sweeney *et al.* also reported an electrically pumped GaAsBi laser grown by MOVPE with up to 4.4% Bi [37]. They investigated the electrical and optical confinement in different laser structures, with varying Al composition in the AlGaAs barriers and with different numbers of quantum wells. Besides, they also found the threshold current of laser is mostly due to the non-radiative recombination which accounts for over 80% of the total current. The maximum peak emission wavelength of their laser structure was 1038nm working at 180 K.

1.7.2 Terahertz applications

The research of terahertz applications has been limited by the mature development of its adjacent band applications. Since 2000, the rapid growth of materials technology has increased the demand for terahertz applications, gradually thrusting them from obscurity into the limelight.

For conventional semiconductors, the carrier recombination times are relatively long (in the nanosecond range) impeding their performance as ultrafast optoelectronic devices. In order to overcome the long carrier recombination times, the low-temperature growth technique (LTG) has been developed. As the most common and high resistivity material, the LTG-GaAs has been extensively studied. It was found that LTG can significantly reduce electron lifetime to as short as sub-100-fs, making the LTG-GaAs an appropriate candidate for high-speed emitters and detectors [38]. However, the cut-off wavelength of GaAs (873nm) limits its applications at the mid-infrared region (1-1.5μm). Although InGaAs can successfully cover this spectral region, the shortest carrier lifetimes are only 2ps after growing at low temperature [39]. Besides that, it has a low resistivity by its nature.

Incorporating dilute amounts of Bi into GaAs can reduce the bandgap significantly, which results in extended wavelength detection. Furthermore, due to the large atomic size of Bi, successful growth requires a low temperature (less than 400 °C). The unique features of Bi have great potential for terahertz devices.

In 2006, K. Bertulis *et al.* reported GaAsBi could be used as photoconductive terahertz emitters and detectors [40]. Two GaAsBi samples were grown by MBE at the temperature of 330 and 280 °C, respectively. The results from the optically pumped-terahertz probe technique showed that the growth temperature plays an important role. The induced terahertz absorption decays much faster when growth temperature was lower. The electron lifetimes were estimated to reduce from 20ps to around 1ps when the layer was grown at 280 °C. LTG GaAsBi layer with short carrier lifetimes were fabricated as photoconductive antennas, which was used to generate THz pulses. The measured terahertz transient and its Fourier spectrum were measured when the emitter was biased at 10V. The spectrum of transient shows the frequency was over 3THz, with an amplitude comparable to that of terahertz transients measured by LTG GaAs using the same bias voltage.

In 2009, the same group reported further terahertz emitters and detectors, containing a GaAsBi layer [41]. Three extra GaAsBi samples were grown at temperature region within 240-265 °C. From RT Hall effect measurements, the resistivity of the layer was exceeding 2000 Ω cm, which is much larger than previous results they reported in 2006 (60 Ω cm). Compared with their previous GaAsBi terahertz application, the electron lifetimes show a similar magnitude (0.8ps to 0.9ps). Besides, the frequency of THz pulse spectrum had a noticeable improvement, extended to 4.5 THz with a high optical-to-THz conversion efficiency.

1.8 Future perspective of GaAsBi

Since the 20th century, the public environmental awareness has increased significantly as well as the need for energy. Inevitably, the search for clean and renewable sources of energy has become a major concern. There have been numerous breakthroughs in research on converting solar energy. After several generations of technological innovation, the current highest solar efficiency for multi-junction solar cell reported by National Renewable Energy Laboratory (NREL) is around 47.1%. [42], [43] .

The tandem solar cell consists of multi-junctions which are made of different semiconductor materials [44]. In order to achieve the maximum efficiency, the proper materials must be obtained with the required bandgaps covering the solar spectrum sequentially. Besides that, it needs to be lattice-matched to currently available substrates. The potential triple-junction solar cell GaInP/GaAs/Ge with bandgaps of

1.9/1.42/0.66eV lattice-matched on Ge substrate can successfully overcome these problems.

Recently, a new approach of adding an extra fourth junction with 1 eV bandgap into the current triple-junction solar cell can further improve the efficiency [45]. From [46], it reported $GaAs_{0.94}Bi_{0.06}$ has a direct bandgap of 1 eV with only 0.7% lattice-mismatched to GaAs substrate. The large bandgap reduction and low lattice mismatch make GaAsBi a good candidate for the fourth junction material used in the tandem solar cell.

1.9 Motivation of thesis

Avalanche photodiodes are key optical components that amplify weak optical signals via the impact ionisation process. However, the stochastic nature of this process adds 'excess' noise, and this sets the limit to the useful signal to noise ratio (or sensitivity) that is practically achievable. The excess noise term is related to the ratio of the electron to hole ionisation coefficients (α/β or $1/k$) and these are in turn dependent on the band structure of the semiconductor. Most III-V semiconductor materials, including GaAs, have α/β ratios of ~1 compared to silicon which possesses a large α/β ratio of >10. It is known from multiple works on Bi-containing III-V semiconductors, that the valence band is altered via the incorporation of Bi atoms. In particular, the energy level of the heavy hole band and spin-orbit split-off band can be manipulated by the Bi incorporation. As such, it is hypothesised that the hole ionisation properties can be altered when incorporating Bi into GaAs.

Currently, no work on the impact ionisation behaviour of GaAsBi has been reported in the literature. Therefore, this project aims to characterise and understand the impact ionisation properties of $GaAs_{1-x}Bi_x$ with varying Bi content in a wide range of electric field.

1.10 Thesis organisation

Chapter 1 summarised the basic characteristics of GaAsBi based on research from different groups around the world. From the literature, the current GaAsBi applications are described, which shows the main research directions of GaAsBi application. Additionally, it outlines the prospect of GaAsBi and the motivation of this project.

Chapter 2 presents the background theory of some crucial features of APD, such as absorption of light, impact ionisation mechanism and excess noise characteristics. As

unintentional doping is low in most of the samples, only the local theory of impact ionisation and excess noise will be presented.

Chapter 3 describes the growth techniques used in this work. The essential components in MBE and its in-situ monitoring system (RHEED) are illustrated in detail. Besides, the growth method for GaAs and GaAsBi will be demonstrated.

Chapter 4 details the optical and electronic techniques used to characterise the wafers and devices studied in this work. The related physics concepts also will be explained. Furthermore, the calibration of measurements and the analysis of data will be mentioned.

Chapter 5 presents a detailed study of the optical and electrical properties of $GaAs_{1-x}Bi_x$ ($0<x<5.5\%$) with nominally 0.1-1.6μm i-region thickness.

Chapter 6 gives a detailed investigation of the impact ionisation of $GaAs_{1-x}Bi_x$ samples described in Chapter 5. The ionisation coefficients of different Bi composition were extracted from the pure injection multiplication measurements. The predicted breakdown voltage of ~4% Bi sample with 1μm thick i-region compared with a universal breakdown voltage model is presented. The reason to explain the large α/β of GaAsBi correlated with spin-orbit splitting energy will be given in the end of chapter.

Chapter 7 gives a summary of the whole thesis and proposes a future work plan for this project.

1.11 Reference

[1] K. Oe and H. Okamoto, 'New Semiconductor Alloy GaAs1-xBix Grown by Metal Organic Vapor Phase Epitaxy', *Jpn. J. Appl. Phys.*, vol. 37, no. Part 2, No. 11A, pp. L1283–L1285, Nov. 1998, doi: 10.1143/JJAP.37.L1283.

[2] M. Weyers, M. Sato, and H. Ando, 'Red Shift of Photoluminescence and Absorption in Dilute GaAsN Alloy Layers', *Jpn. J. Appl. Phys.*, vol. 31, no. Part 2, No. 7A, pp. L853–L855, Jul. 1992, doi: 10.1143/JJAP.31.L853.

[3] L. Vegard, 'Die Konstitution der Mischkristalle und die Raumfüllung der Atome', *Z. Für Phys.*, vol. 5, no. 1, pp. 17–26, Jan. 1921, doi: 10.1007/BF01349680.

[4] I. Vurgaftman, J. R. Meyer, and L. R. Ram-Mohan, 'Band parameters for III–V compound semiconductors and their alloys', *J. Appl. Phys.*, vol. 89, no. 11, pp. 5815–5875, Jun. 2001, doi: 10.1063/1.1368156.

[5] B. Fluegel, S. Francoeur, A. Mascarenhas, S. Tixier, E. C. Young, and T. Tiedje, 'Giant Spin-Orbit Bowing in GaAs 1 − x Bi x', *Phys. Rev. Lett.*, vol. 97, no. 6, p. 067205, Aug. 2006, doi: 10.1103/PhysRevLett.97.067205.

[6] W. Shan *et al.*, 'Band Anticrossing in III–N–V Alloys', *Phys. Status Solidi B*, vol. 223, no. 1, pp. 75–85, 2001, doi: 10.1002/1521-3951(200101)223:1<75::AID-PSSB75>3.0.CO;2-1.

[7] K. Alberi *et al.*, 'Valence-band anticrossing in mismatched III-V semiconductor alloys', *Phys. Rev. B*, vol. 75, no. 4, p. 045203, Jan. 2007, doi: 10.1103/PhysRevB.75.045203.

[8] A. R. Mohmad *et al.*, 'Localization effects and band gap of GaAsBi alloys', *Phys. Status Solidi B*, vol. 251, no. 6, pp. 1276–1281, 2014, doi: 10.1002/pssb.201350311.

[9] A. Janotti, S.-H. Wei, and S. B. Zhang, 'Theoretical study of the effects of isovalent coalloying of Bi and N in GaAs', *Phys. Rev. B*, vol. 65, no. 11, p. 115203, Feb. 2002, doi: 10.1103/PhysRevB.65.115203.

[10] R. E. Nahory, M. A. Pollack, W. D. Johnston, and R. L. Barns, 'Band gap versus composition and demonstration of Vegard's law for $In_{1-x}Ga_xAs_yP_{1-y}$ lattice matched to InP', *Appl. Phys. Lett.*, vol. 33, no. 7, pp. 659–661, Oct. 1978, doi: 10.1063/1.90455.

[11] J. Wu, W. Shan, and W. Walukiewicz, 'Band anticrossing in highly mismatched III V semiconductor alloys', *Semicond. Sci. Technol.*, vol. 17, no. 8, pp. 860–869, Aug. 2002, doi: 10.1088/0268-1242/17/8/315.

[12] S. Adachi, 'GaAs, AlAs, and $Al_xGa_{1-x}As$: Material parameters for use in research and device applications', *J. Appl. Phys.*, vol. 58, no. 3, pp. R1–R29, Aug. 1985, doi: 10.1063/1.336070.

[13] B. G. Streetman and S. Banerjee, *Solid State Electronic Devices*. Prentice Hall, 2000.

[14] J. E. Ayers, *Heteroepitaxy of Semiconductors : Theory, Growth, and Characterization*. CRC Press, 2018.

[15] J. Matthews, 'Defects in epitaxial multilayers I. Misfit dislocations', *J. Cryst. Growth*, vol. 27, pp. 118–125, Dec. 1974, doi: 10.1016/0022-0248(74)90424-2.

[16] A. Mascarenhas, Y. Zhang, J. Verley, and M. J. Seong, 'Overcoming limitations in semiconductor alloy design', *Superlattices Microstruct.*, vol. 29, no. 6, pp. 395–404, Jun. 2001, doi: 10.1006/spmi.2001.0984.

[17] W. Huang, M. Yoshimoto, Y. Takehara, J. Saraie, and K. Oe, '$GaN_yAs_{1-x-y}Bi_x$ Alloy Lattice Matched to GaAs with 1.3 μm Photoluminescence Emission', *Jpn. J. Appl. Phys.*, vol. 43, no. No. 10B, pp. L1350–L1352, Sep. 2004, doi: 10.1143/JJAP.43.L1350.

[18] S. Dhar, A. Mondal, and T. D. Das, ‘Hall mobility and electron trap density in GaAsN grown by liquid phase epitaxy’, *Semicond. Sci. Technol.*, vol. 23, no. 1, p. 015007, Jan. 2008, doi: 10.1088/0268-1242/23/1/015007.

[19] M. Inagaki, S. Kimura, K. Ikeda, N. Kojima, Y. Ohshita, and M. Yamaguchi, ‘Effect of N-induced scattering centers on electron mobility in CBE grown GaAsN films’, in *2011 37th IEEE Photovoltaic Specialists Conference*, Seattle, WA, USA, Jun. 2011, pp. 000493–000495, doi: 10.1109/PVSC.2011.6186001.

[20] N. Hossain *et al.*, ‘Recombination mechanisms and band alignment of GaAs $_{1-x}$ Bi $_x$ /GaAs light emitting diodes’, *Appl. Phys. Lett.*, vol. 100, no. 5, p. 051105, Jan. 2012, doi: 10.1063/1.3681139.

[21] B. Pursley, M. Luengo-Kovac, G. Vardar, R. S. Goldman, and V. Sih, ‘Spin lifetime measurements in GaAsBi thin films’, *Appl. Phys. Lett.*, vol. 102, no. 2, p. 022420, Jan. 2013, doi: 10.1063/1.4781415.

[22] K. Sakamoto, K. Kyoya, K. Miki, H. Matsuhata, and T. Sakamoto, ‘Which Surfactant Shall We Choose for the Heteroepitaxy of Ge/Si(001)? -Bi as a Surfactant with Small Self-Incorporation-’, *Jpn. J. Appl. Phys.*, vol. 32, no. Part 2, No. 2A, pp. L204–L206, Feb. 1993, doi: 10.1143/JJAP.32.L204.

[23] M. R. Pillai, S.-S. Kim, S. T. Ho, and S. A. Barnett, ‘Growth of InxGa1-xAs/GaAs heterostructures using Bi as a surfactant’, vol. 18, no. 1232, p. 6, 2000, doi: 10.1116/1.591367.

[24] H. Asahi, ‘Temperature-Insensitive Band-Gap III-V Semiconductors: Tl-III-V and III-V-Bi’, in *Springer Handbook of Electronic and Photonic Materials*, S. Kasap and P. Capper, Eds. Cham: Springer International Publishing, 2017, pp. 1–1.

[25] O. Hiroshi and K. Oe, ‘Growth of Metastable Alloy InAsBi by Low-Pressure MOVPE’, *Jpn. J. Appl. Phys.*, vol. 37, pp. 1608–1613, Mar. 1998.

[26] S. J. Sweeney and S. R. Jin, ‘Bismide-nitride alloys: Promising for efficient light emitting devices in the near- and mid-infrared’, *J. Appl. Phys.*, vol. 113, no. 4, p. 043110, Jan. 2013, doi: 10.1063/1.4789624.

[27] R. B. Lewis, D. A. Beaton, Xianfeng. Lu, and T. Tiedje, ‘light emitting diodes’, *J. Cryst. Growth*, vol. 311, no. 7, pp. 1872–1875, Mar. 2009, doi: 10.1016/j.jcrysgro.2008.11.093.

[28] V. Pačebutas, K. Bertulis, G. Aleksejenko, R. Adomavičius, G. Molis, and A. Krotkus, ‘Growth and characterization of GaBiAs epilayers’, *Opt. Mater.*, vol. 30, no. 5, pp. 756–758, Jan. 2008, doi: 10.1016/j.optmat.2007.02.029.

[29] S. Kunihiro, M. Hirofumi, K. Keníchi, and M. Kazushi, ‘Abrupt Si/Ge/Si(001) Interfaces Fabricated with Bi as a Surfactant’, *Jpn. J. Appl. Phys.*, vol. 33, pp. 2307–2310, Nov. 1993.

[30] S. Tixier, M. Adamcyk, E. C. Young, J. H. Schmid, and T. Tiedje, ‘Surfactant enhanced growth of GaNAs and InGaNAs using bismuth’, *J. Cryst. Growth*, vol. 251, no. 1–4, pp. 449–454, Apr. 2003, doi: 10.1016/S0022-0248(02)02217-0.

[31] E. C. Young, S. Tixier, and T. Tiedje, ‘Bismuth surfactant growth of the dilute nitride GaNxAs1−x’, *J. Cryst. Growth*, vol. 279, no. 3–4, pp. 316–320, Jun. 2005, doi: 10.1016/j.jcrysgro.2005.02.045.

[32] R. D. Richards, A. R. Mohmad, J. P. R. David, C. J. Hunter, and F. Bastiman, ‘Telecommunication wavelength GaAsBi light emitting diodes’, *IET Optoelectron.*, vol. 10, no. 2, pp. 34–38, Apr. 2016, doi: 10.1049/iet-opt.2015.0051.

[33] Y. Tominaga, K. Oe, and M. Yoshimoto, ‘Low Temperature Dependence of Oscillation Wavelength in GaAs $_{1-x}$ Bi $_x$ Laser by Photo-Pumping’, *Appl. Phys. Express*, vol. 3, no. 6, p. 062201, Jun. 2010, doi: 10.1143/APEX.3.062201.

[34] T. Fuyuki, R. Yoshioka, K. Yoshida, and M. Yoshimoto, 'Long-wavelength emission in photo-pumped GaAs $_{1-x}$ Bi $_{x}$ laser with low temperature dependence of lasing wavelength', *Appl. Phys. Lett.*, vol. 103, no. 20, p. 202105, Nov. 2013, doi: 10.1063/1.4830273.

[35] P. Ludewig *et al.*, 'Electrical injection Ga(AsBi)/(AlGa)As single quantum well laser', *Appl. Phys. Lett.*, vol. 102, no. 24, p. 242115, Jun. 2013, doi: 10.1063/1.4811736.

[36] T. Fuyuki, K. Yoshida, R. Yoshioka, and M. Yoshimoto, 'Electrically pumped room-temperature operation of GaAs $_{1-x}$ Bi $_{x}$ laser diodes with low-temperature dependence of oscillation wavelength', *Appl. Phys. Express*, vol. 7, no. 8, p. 082101, Aug. 2014, doi: 10.7567/APEX.7.082101.

[37] I. P. Marko *et al.*, 'Physical properties and optimization of GaBiAs/(Al)GaAs based near-infrared laser diodes grown by MOVPE with up to 4.4% Bi', *J. Phys. Appl. Phys.*, vol. 47, no. 34, p. 345103, Aug. 2014, doi: 10.1088/0022-3727/47/34/345103.

[38] A. Krotkus, 'Semiconductors for terahertz photonics applications', *J. Phys. Appl. Phys.*, vol. 43, no. 27, p. 273001, Jul. 2010, doi: 10.1088/0022-3727/43/27/273001.

[39] M. Martin and E. R. Brown, 'Critical comparison of GaAs and InGaAs THz photoconductors', San Francisco, California, USA, Feb. 2012, p. 826102, doi: 10.1117/12.914028.

[40] K. Bertulis *et al.*, 'GaBiAs: A material for optoelectronic terahertz devices', *Appl. Phys. Lett.*, vol. 88, no. 20, p. 201112, May 2006, doi: 10.1063/1.2205180.

[41] V. Pačebutas, K. Bertulis, A. Bičiūnas, and A. Krotkus, 'Low-temperature MBE-grown GaBiAs layers for terahertz optoelectronic applications', *Phys. Status Solidi C*, vol. 6, no. 12, pp. 2649–2651, 2009, doi: 10.1002/pssc.200982538.

[42] F. Dimroth *et al.*, 'Wafer bonded four-junction GaInP/GaAs//GaInAsP/GaInAs concentrator solar cells with 44.7% efficiency', *Prog. Photovolt. Res. Appl.*, vol. 22, no. 3, pp. 277–282, 2014, doi: 10.1002/pip.2475.

[43] 'News Release: NREL Six-Junction Solar Cell Sets Two World Records for Efficiency', *NREL Transforming Energy*, Apr. 2020.

[44] H. Cotal *et al.*, 'III–V multijunction solar cells for concentrating photovoltaics', *Energy Env. Sci*, vol. 2, no. 2, pp. 174–192, 2009, doi: 10.1039/B809257E.

[45] X. Wang and Z. Wang, 'High-Efficiency Solar Cells: Physics, Materials, and Devices', 2014, doi: 10.1007/978-3-319-01988-8.

[46] T. Thomas *et al.*, 'Requirements for a GaAsBi 1 eV sub-cell in a GaAs-based multi-junction solar cell', *Semicond. Sci. Technol.*, vol. 30, no. 9, p. 094010, Sep. 2015, doi: 10.1088/0268-1242/30/9/094010.

Chapter 2: Background Theory

2.1 Absorption of light

It is well known that the carriers in the semiconductor will all be in the valence band at absolute zero. As the temperature increase, some carriers will hop from valence band to conduction band due to the thermal excitation. Carriers can also be excited into the conduction band when an incident photon that has energy higher than the bandgap of the semiconductor is absorbed. The relationship between photon energy, E, and the wavelength of light, λ, is expressed by

$$\lambda(\mu m) = \frac{hc}{E} = \frac{hc}{E_g} \approx \frac{1.24}{E_g} \qquad (2.1)$$

where h is Planck's constant, c is the speed of light. For a semiconductor detector, λ can be redefined as cut-off wavelength that is the longest detectable wavelength of the detector and E_g can be regarded as bandgap of the material.

Assuming a light source with a certain photon flux shines on a semiconductor, the photon flux represents that the number of photons per square centimetre in one second. The number of absorbed photons is proportional to the intensity of the light. Therefore, after travelling through a distance Δx into the semiconductor, the number of photons can be described as

$$\frac{d\Phi(x)}{d(x)}\Delta x = -\gamma\Phi(x)\Delta x \qquad (2.2)$$

The minus sign indicates that the intensity of light reduces with increasing distance. Put the boundary condition $\Phi(x) = \Phi_0$ when $x = 0$ into equation 2.2 yields

$$\Phi(x) = \Phi_0 \exp^{-\gamma x} \qquad (2.3)$$

Where $\Phi(x)$ is the light intensity after travelling through a material with distance x, Φ_0 is the initial light intensity of incoming light. The absorption coefficient, γ, based on semiconductor material, determines the ability of absorption of light in photodetectors. A small γ value indicates the light can penetrate deeper into the material. A large γ value means the light is easily absorbed closer to the surface of a material.

The carrier transitions from the valence band to the conduction band are controlled by the conservation laws, which means that both energy and momentum need to be conserved. The relationship between energy and momentum can be described as

$$\left\{ p = mv = \hbar k \,, E = \frac{1}{2} mv^2 = \frac{p^2}{2m} \right\} \Rightarrow E = \frac{\hbar^2 k^2}{2m} \qquad (2.4)$$

where p is momentum, m is mass, v is the velocity, $\hbar$ is reduced plank's constant, and k is wave vector that is equal to $2\pi/\lambda$.

By solving the second derivative of Equation 2.4, the curvature of *E*-*k* diagram can then be plotted. Figure 2.1 gives an example of *E*-*k* diagram of a direct and indirect semiconductor. In fact, the band structure is more complicated than this. In most case, the periodicity of the crystal lattice and momentum is determined by the crystal orientation, except *k*=0 point at which the momentum and effective mass of carrier are independent of crystal orientation.

In order to satisfy the *k*-conservation, the initial and final electron must have the same k value after the transition. For a direct bandgap material such as in Figure 2.1(a), the minimum of the conduction band and the maximum of the valence band has the same k value at *k*=0. The difference in energy level at *k*=0 is the bandgap of the material. While in the indirect material in Figure 2.1(b), the electron has to change its momentum to be transferred to the bottom of the conduction band; it needs phonon assistance to achieve *k*-conservation during the process. Therefore, both the generation and recombination process are much more efficient for the direct material than for the indirect material.

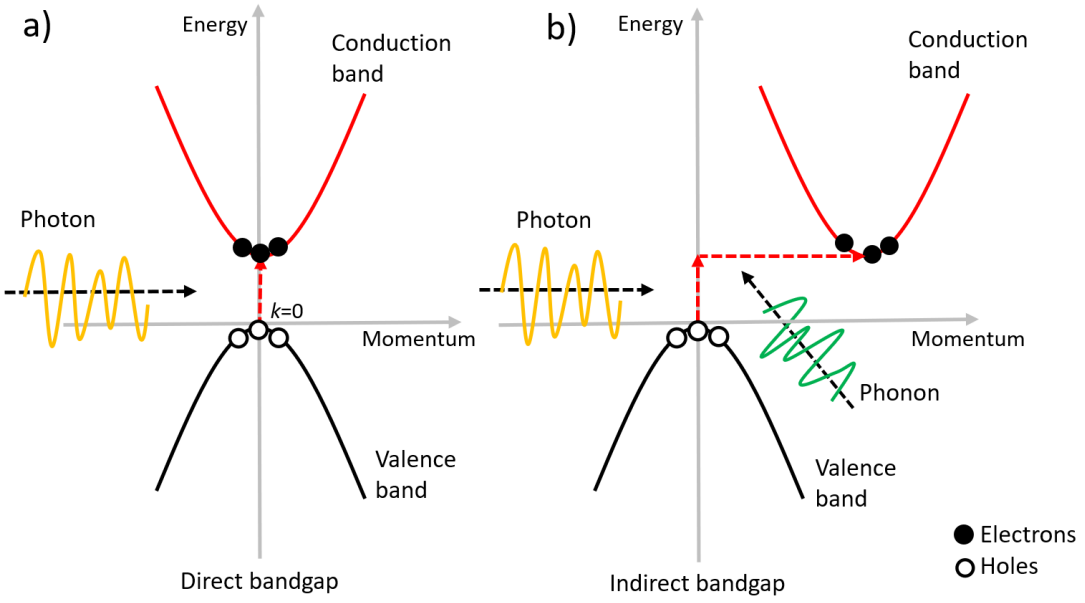

Figure 2.1 E-k diagram of (a) a direct bandgap material and (b)an indirect bandgap material

Equation 2.5 and 2.6. give the frequency dependence of the absorption coefficient for direct bandgap and indirect bandgap material, respectively [1], [2].

$$\begin{aligned} \gamma &\propto \left(\hbar\omega - E_g\right)^{\frac{1}{2}} \quad , \hbar\omega \geq E_g \\ \gamma &= 0 \qquad\qquad \hbar\omega < E_g \end{aligned} \tag{2.5}$$

$$\begin{aligned} \gamma &\propto \left(\hbar\omega - E_g \pm \hbar\omega_q\right)^2 \quad , \hbar\omega \geq E_g \\ \gamma &= 0 \qquad\qquad \hbar\omega < E_g \end{aligned} \tag{2.6}$$

Where ω is frequency of the photon, ω_q is frequency of the phonon. $\pm\hbar\omega_q$ is phonon absorption and emission. By plotting $\gamma^{1/2}$ and γ^2 versus E_g for direct and indirect material respectively, the bandgap of the material can be estimated from the x-intercept point. Figure 2.2 shows the absorption coefficient of some direct and indirect band semiconductors. The cut-off wavelength varies with different material. Compared with the direct bandgap material, the absorption coefficient of indirect bandgap material is much weaker near the cut-off wavelength.

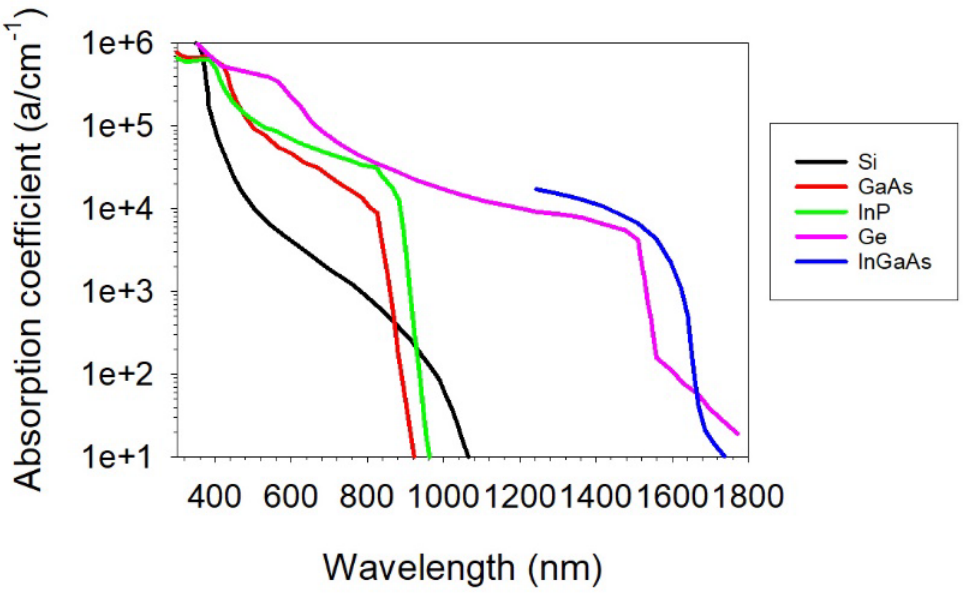

Figure 2.2 Absorption coefficient for Silicon [3], Ge [4], [5], GaAs [6], InP [4], [7] and In0.53Ga0.47As [8] semiconductor materials.

In the presence of an electric field, the band structure of the semiconductor will tilt compared with the equilibrium state. Due to the wave-particle duality of light, both the photon and electron can be described using wave functions [9]. Without photon absorption, as shown in figure 2.4(a), a valence band electron must tunnel through a triangular barrier to reach the conduction band. With the help of photon absorption, the barrier thickness reduces to [2]

$$t(\hbar\omega) = \frac{E_g - \hbar\omega}{q|E|} \qquad (2.7)$$

Where $t(\hbar\omega)$ is barrier thickness, q is electron charge and $|E|$ is the magnitude of electric field, as shown in figure 2.3 (b). Therefore, from the equation 2.7, it is obvious that the photon absorption enhances the tunnelling probability.

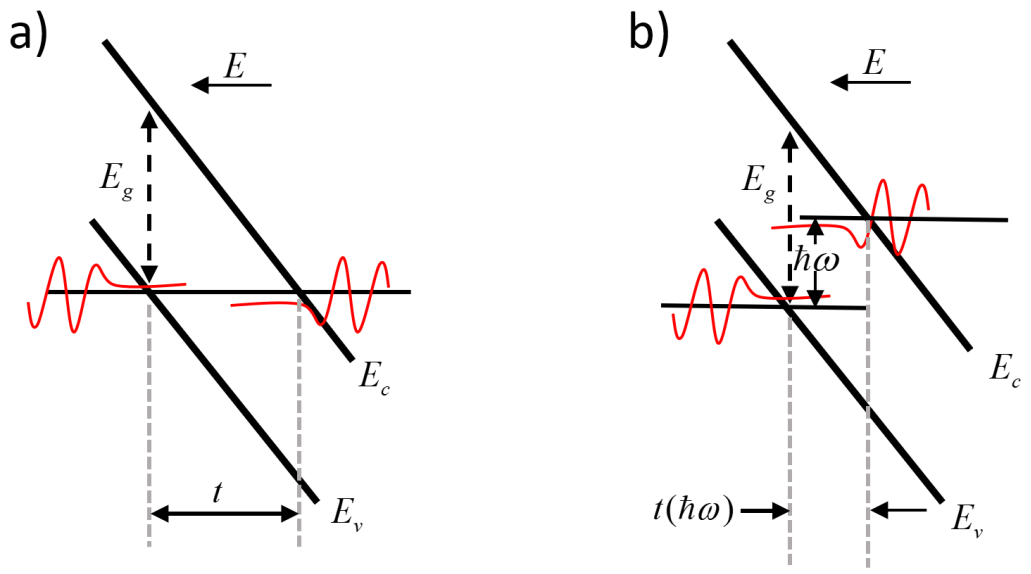

Figure 2.3 Energy band diagram in an electric field (a) without photon absorption (b) with photon absorption in which the energy of photon is ħω.

The higher the electric field is, the thinner the barrier is. At this point, it is found that the energy promotes an electron from the conduction band to the valence band below the energy of bandgap. This phenomenon was first studied by Franz [10] and Keldysh [11] in 1958, and is more commonly found in direct bandgap materials than in indirect bandgap materials.

In the presence of a uniform electron field, the absorption coefficient of a semiconducting crystal in terms of the Airey function was given by Tharmalingam [12] and Callaway [13].

$$\gamma = 1\times10^{4}\left(\frac{1+(m_h/m_e)^{-1}}{n}\right)\left(\frac{2\mu}{m_e}\right)^{\frac{4}{3}}\zeta^{\frac{1}{3}}\int_{\beta}^{x}\left|Ai(z)\right|^2 dz \qquad (2.8)$$

where m_e and m_h are the electrons and holes effective mass in the conduction and valence bands, respectively. n is refractive index, μ is reduced mass that is defined by $\frac{1}{\mu}=\frac{1}{m_e}+\frac{1}{m_h}$ and ζ is electric field strength (in V cm^{-1}). The last integral of Airey function in equation 2.8 can be expressed as

$$\int_{\beta}^{x}\left|Ai(z)\right|^2 dz = \left(\left|\frac{dAi(z)}{dz}\right|_{\beta}\right)^2 - \chi\left|Ai(z)\right|^2 \quad (2.9)$$

where χ is given by

$$\chi = 1.1\times10^{5}(E_g - \hbar\omega)\left(\frac{2\mu}{m}\right)^{\frac{1}{3}} E^{-\frac{2}{3}} \quad (2.10)$$

The simulated result of Franz-Keldsh (*F-K*) effect for the absorption coefficient of GaAs under the different electric field from 0.1kV/cm to 1000kV/cm as shown in figure 2.4. E_g=1.42eV was used in here. The *F-K* effects can extend the spectral response of GaAs to 1μm.

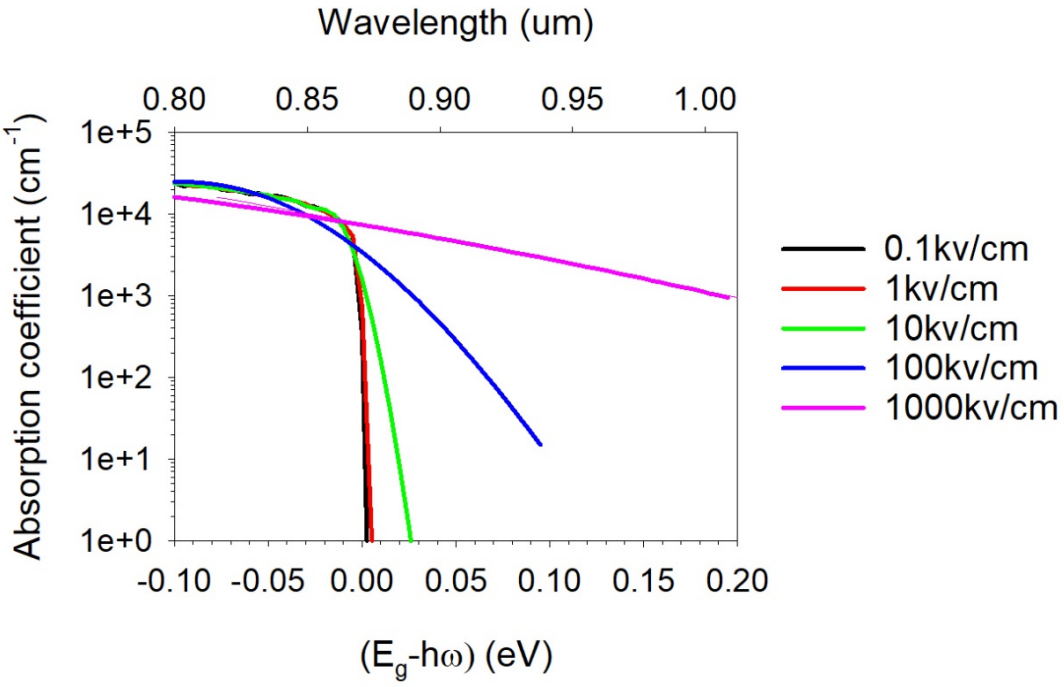

Figure 2.4 Electric field and photon energy dependence of the band to band absorption for GaAs.

2.2 Impact ionisation in semiconductors

Impact ionisation is the key characteristic of the avalanche photodiode. It is a process typically observed in the high electric fields. The free carriers, electron and hole, will keep accelerating and gaining energy in the presence of an electric field, and consequently initiate impact ionisation. During the process, in addition to the impact ionisation, the phonon scattering also needs to be considered. It is an important non-ionisation collision process that significantly affects impact ionisation rates. The collision between free carriers and phonons can be explained in three processes. The three processes are where the carriers will gain energy (phonon absorption), lose energy

(phonon emission) or exchange momentum (elastic). The average number of phonons in the crystal is defined as:

$$N_{ph} = \frac{1}{\exp\left(\frac{\hbar\omega}{k_B T}\right) - 1} \quad (2.11)$$

where k_B is Boltzmann's constant and T is the temperature. The phonon absorption scattering rate is proportional to N_{ph} and the phonon emission rate is proportional to $N_{ph} + 1$. Therefore, the carrier will lose energy after the phonon scattering. This then results in difficulty to achieve enough energy for impact ionisation, especially in a low electric field. At a sufficiently high electric field, the effect of phonon scattering is negligible. Some of the free carriers will gain enough energy to promote an electron from the valence band into the conduction band and leave a hole in the valence band.

After generating an electron-hole pair process, the initial carrier will lose the energy and move to a lower energy state. However, both the initial carrier and the newly formed carrier are still under the effect of the electric field and will continue to gain energy to create further electron and hole pairs. The nature of the impact ionisation processes is stochastic, and the hole impact ionisation process is the opposite of the electron. Figure 2.5 illustrates *E-K* diagrams for electron and hole-initiated impact ionisation process in a direct bandgap material.

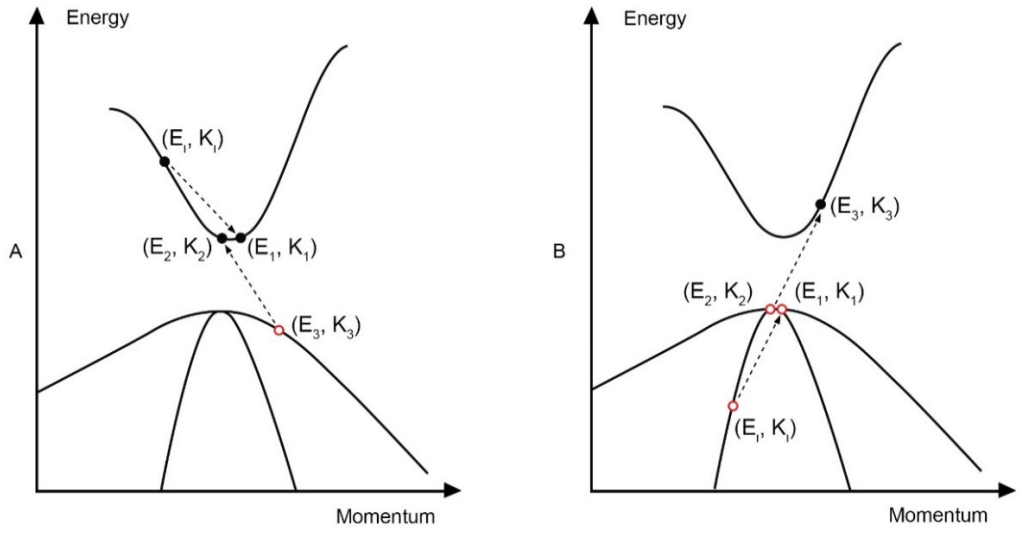

Figure 2.5 Schematic diagram of an (A) electron initiated and (B) hole-initiated impact ionisation processes. Black dot represents the electron and red dot represents the hole. E_i is the initial state of primary carrier, while the final states are defined as E_1, E_2 and E_3.

Threshold energy is the minimum energy needed for an impact ionisation event to occur. The threshold energy varies with material and typically depends on the band structure of the semiconductor [14]. Generally, the threshold energy needs to be greater than the bandgap of the material. In the past, researchers have investigated the threshold energy for various materials with the use of different hypotheses of the band structure. Wolff *et al.* [15] proposed an easy calculation by assuming the effective mass of electron and hole are the same for simple parabolic energy band. This provides us with a value of $3/2\,E_g$ for the threshold energy.

With the development of experimental and theoretical work, researchers found that the real energy bands are more complicated. Anderson and Crowell subsequently developed a new algorithm [16] to calculate the threshold energy of most III-V material using realistic band structures. The multiplicity of the field-dependent threshold for impact ionisation was found for materials such as GaAs, Ge, Si, GaP and InSb. Furthermore, an alternative and more accurate method was developed by Ballinger *et al.* [17]. As a result, the threshold energy is usually treated as an adjustable fitting parameter in experiment work.

2.3 Avalanche multiplication and breakdown

The current gain or multiplication of an avalanche photodiode can be described by the ionisation coefficients α and β for electrons and holes, respectively. The ionisation coefficient is defined as the reciprocal of the average distance a carrier moves before creating an electron-hole pair in a uniform electric field. In general, the ionisation coefficient will not be constant and strongly depends on the electric field. The standard equation [18] for α and β is given as

$$\alpha(\beta) = A\exp\left[-\left(\frac{B}{E}\right)^{C}\right] \qquad (2.12)$$

where E is the electric field, A, B and C are the fitting parameters that are dependent on the material. The current gain of a device can be triggered by a series of impact ionisation events, as illustrated in Figure 2.6. Figure 2.6 (a) and (b) shows two different cases where $\alpha = \beta$ and $\alpha >> \beta$ respectively. An electric field is provided in both cases and its direction is opposite to the electron. Therefore, a photogenerated electron will travel along the avalanche region from $x = 0$ towards $x = w$ initially.

In terms of $\alpha = \beta$ case, both electron and hole participate in the impact ionisation. This causes more fluctuation compared with $\alpha >> \beta$ case in which only the electron will be introduced in impact ionisation. The new generated hole will be rapidly swept out of the avalanche region by the electric field and will not experience any multiplication. In other words, the reduced fluctuation represents the low noise. Therefore, in order to build low noise photodetector, the material with a very dissimilar alpha and beta is required.

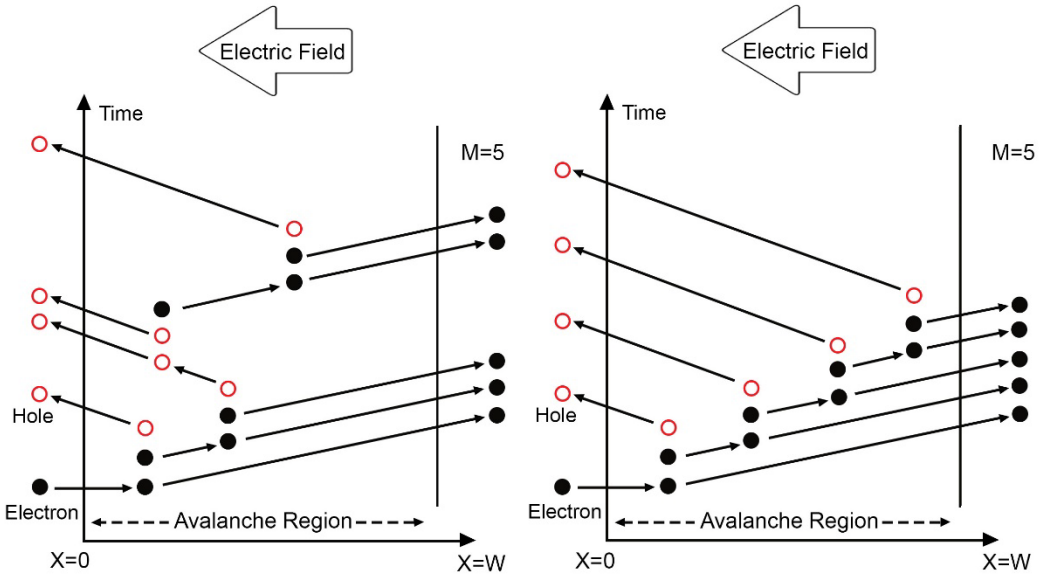

Figure 2.6 a) Avalanche gain process for α=β , both electron and hole participate impact ionisation event, in this case the multiplication gain initiated by electron is 5 b) Avalanche gain process for a»β , in this case the multiplication gain initiated by electron is 5.

In addition to the above cases shown in the Figure 2.6, the primary carriers also can be injected within the avalanche region rather than injected from the edge. Figure 2.7 shows the case that one electron-hole pair has been generated in the position *x* in the avalanche region, where an electric field will be applied. The electron will be swept in the opposite the direction to the electric field and hole will be swept in the same direction to the electric field.

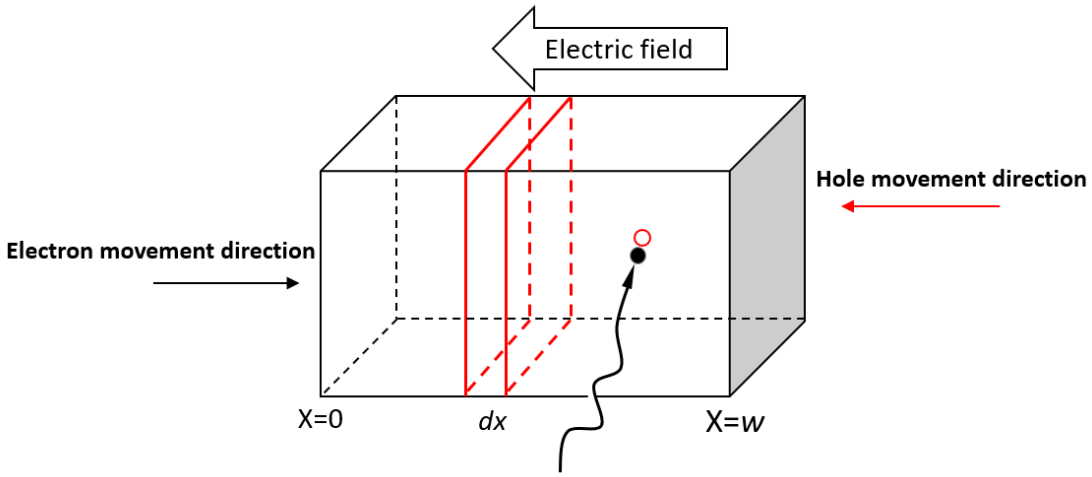

Figure 2.7 Injection of one electron-hole pair into the avalanche region, black dot represents the electron and red dot represents the hole (adapted from [19]).

The average number of ionisation collisions for the electron is αdx after passing a distance *dx*. Similarly, the hole will initiate βdx number of impact ionisation events as it passes through a distance *dx*. Therefore, the average total number of electron-hole pairs created will be described as [20] ,

$$M(x) = 1 + \int_0^x \alpha M(x')dx' + \int_x^w \beta M(x')dx' \qquad (2.13)$$

Solving Equation 2.13, when an electron and hole pair is generated within the avalanche region, at position *x* the mean multiplication can be expressed as

$$M(x) = \frac{\exp\left[-\int_0^x \alpha(x') - \beta(x')dx'\right]}{1 - \int_0^w \alpha(x') \exp\left[-\int_0^x \alpha(x'') - \beta(x'')dx''\right]dx'} \qquad (2.14)$$

When electron is injected at *x*=0, the multiplication for pure electron injection, M_e, can be expressed as

$$M_e = M(0) = \frac{1}{1 - \int_0^w \alpha(x') \exp\left[-\int_0^x \alpha(x'') - \beta(x'')dx''\right]dx'} \qquad (2.15)$$

Similarly, when hole is injected at *x*=w, the multiplication for pure hole injection, M_h , can be expressed as

$$M_h = M(w) = \frac{1}{1 - \int_0^w \beta(x') \exp\left[-\int_x^w \alpha(x'') - \beta(x'')dx''\right]dx'} \qquad (2.16)$$

In a perfect p-i-n and n-i-p structure, a uniform electric field is applied within the avalanche region. In this situation, the value of alpha and beta no longer depends on the position. Therefore, equation 2.15 and 2.16 can be simplified and expressed as

$$M_e = \frac{1}{1 - \frac{\alpha}{\alpha - \beta}\{\exp[(\beta - \alpha)w] - 1\}} \qquad (2.17)$$

$$M_h = \frac{1}{1 - \frac{\beta}{\alpha - \beta}\{\exp[(\alpha - \beta)w] - 1\}} \qquad (2.18)$$

The multiplication process causes an abrupt rise of free electrons and holes in the depletion region. As a result, a huge reverse current that is near infinite will flow through the PN junction, this type of breakdown is also called avalanche breakdown. At the avalanche breakdown voltage, the gain of the device can be considered close to infinite. In this case, the denominator of equation 2.17 and 2.18 become zero. It therefore proves that the breakdown voltage is independent of the type of carrier injection.

Two extreme cases regarding multiplication as shown in Figure 2.6 (a) and (b) will be discussed. For $\alpha = \beta$, equation 2.17 can be simplified to

$$Me = Mh = \frac{1}{1-\alpha w} \qquad (2.19)$$

The true breakdown voltage is obtained when $\alpha\omega$ =1. As mentioned before, long build-up time and high fluctuation in current are the main disadvantages in this case. Therefore, a material with such properties is not a suitable candidate for high speed and low noise APDs.

For another case $\alpha >> \beta$ with a uniform electric field, the multiplication is given by Equation 2.18, which is simplified to

$$M_h = \exp(\alpha w) \qquad (2.20)$$

Under this condition, the avalanche breakdown does not exist, for example InAs material [21]. M_h increases exponentially with the increasing value of $\alpha\omega$. The benefit of this case is only one carrier undergoes impact ionisation and there is no carrier feedback. Consequently, this results in only small fluctuations and a shorter build-up time in the avalanche region. Therefore, this is the ideal case for the highest performance APDs.

Local ionisation coefficient for α and β can be extracted by measuring electron and hole multiplication in a $p^+ - i - n^+$ or $n^+ - i - p^+$ structure with a constant electric field. Rearranging the equation 2.17 and 2.18 gives the expression

$$\alpha = \frac{1}{w}\left(\frac{M_e - 1}{M_e - M_h}\right)\ln\left(\frac{M_e}{M_h}\right) \qquad (2.21)$$

$$\beta = \frac{1}{w}\left(\frac{M_h - 1}{M_e - M_h}\right)\ln\left(\frac{M_e}{M_h}\right) \qquad (2.22)$$

2.4 Avalanche excess noise

The inherently random nature of impact ionisation will lead to a fluctuation in the multiplication. The multiplication described here represents the mean value of multiplication. The randomness of impact ionisation can be explained due to the uncertainty of position from where the primary carrier triggers an impact ionisation event and the specific quantity of secondary carrier produced. This fluctuation of multiplication introduces excess avalanche noise around the mean value of multiplication [22], which can be quantified by the excess noise factor, F, defined as

$$F = \frac{\left\langle M^2_{mean} \right\rangle}{\left\langle M_{mean} \right\rangle^2} \qquad (2.23)$$

For a normal semiconductor diode, the shot-noise fluctuations can be expressed as a mean-square shot-noise current,

$$< i_s >= 2qIB \quad (2.24)$$

where q is the electronic charge, B is the measurement bandwidth, and I is the current that flows through the diode. In a real APD, both multiplication and excess noise needs to be considered. The mean-square shot-noise current is expressed as

$$< i >= 2qI_{pr}FM^2B \qquad (2.25)$$

Avalanche noise statistics were initially studied by Tager [23], who pointed out that the positive feedback characteristic had been found if both alpha and beta are finite. From his prediction, he assumed that when $\alpha = \beta$, the shot noise current would be M times greater than that of an ideal case, when $\beta = 0$, and it can be expressed as

$$< i >= 2qI_{pr}M^3B \qquad (2.26)$$

McIntyre developed this analysis to the arbitrary value of ionisation coefficients [20]. Based on the local electric field, he pointed out that the excess noise factor could be described as the function of the ratio of the ionisation coefficients and the multiplication factor. In this case, it has a constant ratio between α and β. The excess noise factor for electrons is described as

$$F = kM_e + (2 - \frac{1}{M_e})(1-k) \quad (2.27)$$

where k is the ratio of ionisation coefficient, in this case $k = \beta/\alpha$, and M_e is the multiplication of electron. For hole excess noise, the foregoing equation still valid, it only needs to replace the multiplication of hole instead of electron and $k = \alpha/\beta$.

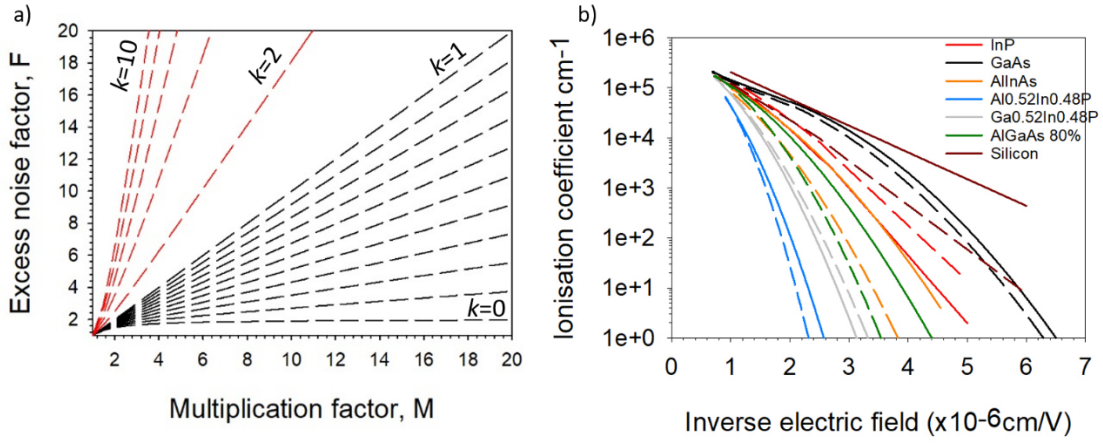

Figure 2.8 a) Excess noise factors calculated from equation 2.27 for k=0 to 1 in steps of 0.1 and k=2 to 10 in steps of 2 b) Measured ionisation coefficients in several semiconductors as a function of electric field (α and β shown as solid and dashed lines respectively)

It is obvious from figure 2.8 (a) that a low excess noise factor can be achieved by choosing a material with a large α/β ratio. Besides that, the structure of the device must be designed properly. The use of the wrong ionising carrier type will make the excess noise factor of the device worse than that of a device with an identical ionisation coefficient. In recent years, there has been a continuing interest in avalanche photodiodes, extensive experiments and analyses [24]–[35] have been done to investigate the ionisation coefficient and the performance of excess noise in different semiconductors.

Figure 2.8 (b) shows the ionisation coefficients for some popular materials. For most wider bandgap III-V materials, there is no significant difference in terms of the ratio of ionisation coefficients, especially at high electric fields. Despite an enhanced α/β ratio at low electric fields for some materials, there is still a longer response time of devices due to the thick design of the multiplication region. In order to fulfil the high-speed requirement, the design may utilise a thin multiplication layer with a higher electric field. However, this is contrary to McIntyre's local noise theory, which claims a low α/β ratio results in a high excess noise. In fact, the local noise model principle no longer

holds true when the multiplication region is very thin, and low excess noise can still be achieved due to the dead space effect [34], [36], [37]. The dead space can be defined as the minimum distance that a carrier has to travel to reach the threshold energy before initiating an impact ionisation. As the multiplication region becomes thinner, the dead space occupies a larger proportion to the total distance travelled by the carriers before ionisation. In the presence of a uniform electric field, the dead space of electrons and holes can be expressed as:

$$d_e = \frac{E_{the}}{qE} \quad \text{and} \quad d_h = \frac{E_{thh}}{qE} \qquad (2.28)$$

where q is the electronic charge, E is the electric field, E_{the} and E_{thh} are the threshold energies of electrons and holes, respectively.

The multiplication and excess noise of the local model is only valid when the dead space is very small compared to the total distance and the mean ionisation path length. Therefore, a non-local model with consideration of dead space will be investigated for thin structures.

2.5 Reference

[1] L. H. Hall, J. Bardeen, and F. J. Blatt, 'Infrared Absorption Spectrum of Germanium', *Phys. Rev.*, vol. 95, no. 2, pp. 559–560, Jul. 1954, doi: 10.1103/PhysRev.95.559.

[2] M. S. Dresselhaus, 'SOLID STATE PHYSICS PART II', p. 198.

[3] G. G. Macfarlane and V. Roberts, 'Infrared Absorption of Silicon Near the Lattice Edge', *Phys. Rev.*, vol. 98, no. 6, pp. 1865–1866, Jun. 1955, doi: 10.1103/PhysRev.98.1865.

[4] D. E. Aspnes and A. A. Studna, 'Dielectric functions and optical parameters of Si, Ge, GaP, GaAs, GaSb, InP, InAs, and InSb from 1.5 to 6.0 eV', *Phys. Rev. B*, vol. 27, no. 2, pp. 985–1009, Jan. 1983, doi: 10.1103/PhysRevB.27.985.

[5] G. G. Macfarlane and V. Roberts, 'Infrared Absorption of Germanium near the Lattice Edge', *Phys. Rev.*, vol. 97, no. 6, pp. 1714–1716, Mar. 1955, doi: 10.1103/PhysRev.97.1714.2.

[6] H. C. Casey, D. D. Sell, and K. W. Wecht, 'Concentration dependence of the absorption coefficient for $n-$ and $p-$type GaAs between 1.3 and 1.6 eV', *J. Appl. Phys.*, vol. 46, no. 1, pp. 250–257, Jan. 1975, doi: 10.1063/1.321330.

[7] H. Burkhard, H. W. Dinges, and E. Kuphal, 'Optical properties of $In_{1-x}Ga_xP_{1-y}As_y$, InP, GaAs, and GaP determined by ellipsometry', *J. Appl. Phys.*, vol. 53, no. 1, pp. 655–662, Jan. 1982, doi: 10.1063/1.329973.

[8] 'Optical Properties', in *Physical Properties of III-V Semiconductor Compounds*, John Wiley & Sons, Ltd, 2005, pp. 135–192.

[9] S. A. Rashkovskiy, 'Quantum mechanics without quanta: the nature of the wave–particle duality of light', *Quantum Stud. Math. Found.*, vol. 3, no. 2, pp. 147–160, Jun. 2016, doi: 10.1007/s40509-015-0063-5.

[10] W. F. Z. Naturforsch, 'Influence of an electric field on an optical absorption edge', *J. Exp. Theor. Phys.*, vol. 13a, p. 484, 1958.

[11] L. V. Keldysh, 'Behaviour of Non-Metallic Crystals in Strong Electric Fields', *J. Exp. Theor. Phys.*, vol. 33, 1957.

[12] K. Tharmalingam, 'Optical Absorption in the Presence of a Uniform Field', *Phys. Rev.*, vol. 130, no. 6, pp. 2204–2206, Jun. 1963, doi: 10.1103/PhysRev.130.2204.

[13] J. Callaway, 'Optical Absorption in an Electric Field', *Phys. Rev.*, vol. 134, no. 4A, pp. A998–A1000, May 1964, doi: 10.1103/PhysRev.134.A998.

[14] J. R. Hauser, 'Threshold Energy for Avalanche Multiplication in Semiconductors', *J. Appl. Phys.*, vol. 37, no. 2, pp. 507–509, Feb. 1966, doi: 10.1063/1.1708204.

[15] P. A. Wolff, 'Theory of Electron Multiplication in Silicon and Germanium', *Phys. Rev.*, vol. 95, no. 6, pp. 1415–1420, Sep. 1954, doi: 10.1103/PhysRev.95.1415.

[16] C. L. Anderson and C. R. Crowell, 'Threshold Energies for Electron-Hole Pair Production by Impact Ionization in Semiconductors', *Phys. Rev. B*, vol. 5, no. 6, pp. 2267–2272, Mar. 1972, doi: 10.1103/PhysRevB.5.2267.

[17] R. A. Ballinger, K. G. Major, and J. R. Mallinson, 'Impact ionization thresholds in semiconductors', *J. Phys. C Solid State Phys.*, vol. 6, no. 16, pp. 2573–2585, Aug. 1973, doi: 10.1088/0022-3719/6/16/011.

[18] M. A. Saleh *et al.*, 'Impact-ionization and noise characteristics of thin III-V avalanche photodiodes', *IEEE Trans. Electron Devices*, vol. 48, no. 12, pp. 2722–2731, Dec. 2001, doi: 10.1109/16.974696.

[19] M. H. Woods, W. C. Johnson, and M. A. Lampert, ‘Use of a Schottky barrier to measure impact ionization coefficients in semiconductors’, *Solid-State Electron.*, vol. 16, no. 3, pp. 381–394, Mar. 1973, doi: 10.1016/0038-1101(73)90013-0.
[20] R. J. McIntyre, ‘Multiplication noise in uniform avalanche diodes’, *IEEE Trans. Electron Devices*, vol. ED-13, no. 1, pp. 164–168, Jan. 1966, doi: 10.1109/T-ED.1966.15651.
[21] A. R. J. Marshall, *The InAs Electron Avalanche Photodiode and the Influence of Thin Avalanche Photodiodes on Receiver Sensitivity*. University of Sheffield, Department of Electronic and Electrical Engineering, 2010.
[22] F. Kocak, A. Kilic, and I. Tapan, ‘Investigation of Shot Noise in Avalanche Photodiodes’, *Acta Phys. Pol. A*, vol. 129, no. 4, pp. 721–723, Apr. 2016, doi: 10.12693/APhysPolA.129.721.
[23] A. S. Tager, ‘DIODE AND ITS USE IN MICROWAVES’, *Sov. Phys. Solid State*, vol. 9, p. 22, 1966.
[24] B. K. Ng *et al.*, ‘Avalanche multiplication characteristics of Al/sub 0.8/Ga/sub 0.2/As diodes’, *IEEE Trans. Electron Devices*, vol. 48, no. 10, pp. 2198–2204, Oct. 2001, doi: 10.1109/16.954454.
[25] S. A. Plimmer, J. P. R. David, G. J. Rees, and P. N. Robson, ‘Ionization coefficients in Al $_x$ Ga $_{1-x}$ As (x = 0 - 0.60)’, *Semicond. Sci. Technol.*, vol. 15, no. 7, pp. 692–699, Jul. 2000, doi: 10.1088/0268-1242/15/7/307.
[26] L. W. Cook, G. E. Bulman, and G. E. Stillman, ‘Electron and hole impact ionization coefficients in InP determined by photomultiplication measurements’, *Appl. Phys. Lett.*, vol. 40, no. 7, pp. 589–591, Apr. 1982, doi: 10.1063/1.93190.
[27] J. S. L. Ong, J. S. Ng, A. B. Krysa, and J. P. R. David, ‘Impact Ionization Coefficients in Al0.52In0.48P’, *IEEE Electron Device Lett.*, vol. 32, no. 11, pp. 1528–1530, Nov. 2011, doi: 10.1109/LED.2011.2165520.
[28] Y. L. Goh *et al.*, ‘Avalanche Multiplication in InAlAs’, *IEEE Trans. Electron Devices*, vol. 54, no. 1, pp. 11–16, Jan. 2007, doi: 10.1109/TED.2006.887229.
[29] R. Ghin *et al.*, ‘Avalanche Multiplication and Breakdown in Ga In P Diodes’, *IEEE Trans. ELECTRON DEVICES*, vol. 45, no. 10, p. 6, 1998.
[30] D. Scansen and S. O. Kasap, ‘Excess noise, gain, and dark current in Ge avalanche photodiode’, *Can. J. Physcis*, vol. 70, pp. 10–11, Oct. 1992.
[31] L. J. J. Tan, J. S. Ng, C. H. Tan, and J. P. R. David, ‘Avalanche Noise Characteristics in Submicron InP Diodes’, *IEEE J. Quantum Electron.*, vol. 44, no. 4, pp. 378–382, Apr. 2008, doi: 10.1109/JQE.2007.914771.
[32] C. H. Tan *et al.*, ‘Avalanche noise measurement in thin Si p+-i-n+ diodes’, *Appl. Phys. Lett.*, vol. 76, no. 26, pp. 3926–3928, Jun. 2000, doi: 10.1063/1.126823.
[33] A. R. J. Marshall, C. H. Tan, M. J. Steer, and J. P. R. David, ‘Extremely Low Excess Noise in InAs Electron Avalanche Photodiodes’, *IEEE Photonics Technol. Lett.*, vol. 21, no. 13, pp. 866–868, Jul. 2009, doi: 10.1109/LPT.2009.2019625.
[34] K. F. Li *et al.*, ‘Avalanche multiplication noise characteristics in thin GaAs p/sup +/-i-n/sup +/ diodes’, *IEEE Trans. Electron Devices*, vol. 45, no. 10, pp. 2102–2107, Oct. 1998, doi: 10.1109/16.725242.
[35] X. Yi *et al.*, ‘Extremely low excess noise and high sensitivity AlAs 0.56 Sb 0.44 avalanche photodiodes’, *Nat. Photonics*, vol. 13, no. 10, Art. no. 10, Oct. 2019, doi: 10.1038/s41566-019-0477-4.
[36] Chee Hing Tan, J. P. R. David, S. A. Plimmer, G. J. Rees, R. C. Tozer, and R. Grey, ‘Low multiplication noise thin Al/sub 0.6/Ga/sub 0.4/As avalanche photodiodes’, *IEEE Trans. Electron Devices*, vol. 48, no. 7, pp. 1310–1317, Jul. 2001, doi: 10.1109/16.930644.

[37] L. J. J. Tan, J. S. Ng, C. H. Tan, M. Hopkinson, and J. P. R. David, ‘Effect of Dead Space on Low-Field Avalanche Multiplication in InP’, *IEEE Trans. Electron Devices*, vol. 54, no. 8, pp. 2051–2054, Aug. 2007, doi: 10.1109/TED.2007.900010.

Chapter 3. Molecular beam epitaxy

3.1 Introduction

Since the end of the 1960s, material science, optoelectronics, and microelectronics have been greatly developed [1]. As an important part of the research, the epitaxial technologies of semiconductor were also actively developed. Several epitaxial growth technologies, such as liquid-phase epitaxy (LPE), vapour-phase epitaxy (VPE), metal-organic vapour-phase epitaxy (MOVPE), and molecular beam epitaxy (MBE), have been studied since. In this chapter, one of the epitaxial techniques, MBE, will be introduced in detail.

The MBE machine used in this work is an MBE-STM (scanning tunnelling microscope) reactor, which was manufactured by Omicron. The machine consists of seven material source effusion cells, in which aluminium, gallium, indium, arsenic and bismuth are used for growing III-V semiconductor alloys. Silicon and beryllium are used as dopants. The substrate size used is 11.4×11.8 mm, which is cleaved from 2-inch commercial wafers.

The STM section is held in an adjacent vacuum chamber connected to the main MBE chamber via a transfer tube. In order to study surface reconstruction after growth, the sample can be directly loaded from MBE to STM through a manipulator arm. In this case, the sample can avoid atmospheric exposure, which helps to minimise the atmospheric contamination and oxidation of the surface. However, the STM was not used in this work. Therefore, there will be no further discussion in the later chapters.

3.2 The structure of MBE system

In a typical MBE system, the operating principles can be simplified based on two steps. At the first stage, one or more molecular beams are generated through thermal evaporation from various types of effusion cells in an ultrahigh vacuum (UHV) system. A heated crystalline substrate is fixed in the pathway of the molecular beams. The rate of molecules accumulates or desorb on the substrate is related to sticking coefficient of the atom. At the second stage, the temperature of each effusion cell and growth rates of the overall sample structure needs precise control to obtain the desired composition and the expected layer thickness of the sample. During this stage, the reflection high energy electron diffraction (RHEED) system is used to analyse the surface morphology and evaluate the growth conditions.

It is an essential requirement to have ultraclean growth environment and high sample throughout for high quality epilayers. In order to satisfy this, a typical MBE system usually comprises multiple UHV chambers separated by gate valves. The deposition chamber is always kept at UHV condition. Another chamber called the preparation chamber is used to load and store substrates with a less rigorous vacuum condition. Besides that, the substrate outgassing can be performed in the preparation chamber. Unfortunately, the MBE system used in this project did not have a preparation chamber. In addition to that, there is also nowhere to store samples under vacuum inside the machine. Therefore, only one sample will participate during each growth run.

During the start of growth, the sample is directly loaded through a fast entry lock (FEL). This is the only entrance connecting to the atmosphere. In order to ensure that as little air as possible has been introduced before loading the sample from the entry lock chamber to the deposition chamber, a vacuum is established using a turbo-molecular pump backed with a scroll pump. The entry lock chamber has a much smaller volume compared with the deposition chamber. Preparation time of thirty minutes is required to pump down from the atmosphere to a middle vacuum level of 1×10^{-7} mbar. Then a manipulator arm is used to transfer the sample into the deposition chamber. Figure 3.1 shows the schematic diagram of our MBE system.

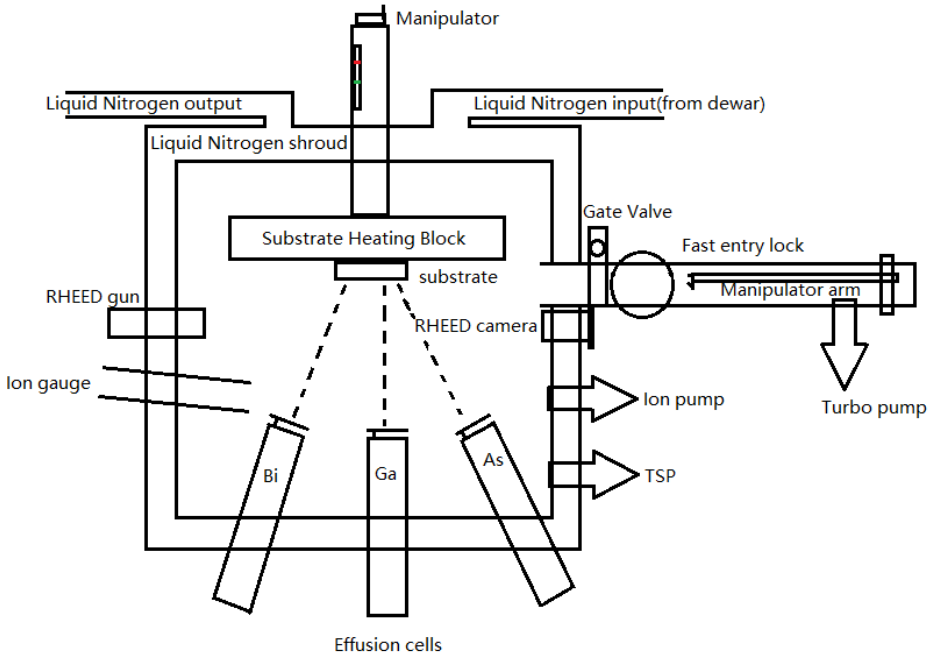

Figure 3.1 Schematic plot of Omicron MBE system

3.2.1 Ultra-high vacuum system

Normally, the vacuum condition needs roughly 10^{-11} mbar pressure for a good MBE system. On one hand, the ultra-high vacuum condition can minimise the incorporation rate of impurities, which will affect the sample growth quality. On the other hand, low pressure can increase the mean free path length of the molecular beams, which ensure they reach the substrate without colliding with other molecules in the chamber.

In order to effectively pump down the system into an ultra-high vacuum, the system must have no major leaks. The ConFlat flange, the most popular design, has been used in typical ultrahigh vacuum components and consists of a knife-edge, which is below the flange's flat surface. As two flanges are tightened, a soft metal gasket is placed between them, suffering from the force of both sides. The extruded metal will fill the matching marks and surface defects in the flange, effectively improving the seal. The metal gasket must withstand high temperature and is made of oxygen-free material. Copper gaskets are usually used. Silver gasket can be used when corrosion resistance is required. However, metal gaskets are single use as they are deformed by knife-edge on the flange. Therefore, this adds to the operating cost. Due to the frequent opening of the FEL for sample loading, using a rubber gasket is an alternative way to reduce costs.

The vacuum pump is the most important component to maintain a MBE system at ultrahigh vacuum. There are different types of pump used in commercial MBE systems. In our system, four types of pump can be divided into two main categories, the primary pumps are mainly used to ensure that the deposition chamber can be pumped down to ultra-high vacuum (10^{-10} mbar), which includes a turbo-molecular pump and an ion pump. The secondary pumps are used to further reduce the residual gas level (5×10^{-10} mbar), consisting of a liquid-nitrogen cryo-panel and a titanium sublimation pump (TSP).

3.2.1.1 Turbomolecular pump

The basic principle of turbomolecular pump is exploiting the interaction between gas molecular and high-speed surface. The multiple stages design has been used in most turbomolecular pumps. The turbomolecular pump consists of a rapidly rotating turbine blade and a stationary stator blade. These two types of blades are slanting, and have a similar size. The stationary stator blades are fixed on the wall of the cylindrical pump housing, with a 1mm gap between the high-speed turbine rotor blades and stationary stator blade. The schematic diagram of turbomolecular pumps is shown in Figure 3.2.

When the pumps operate, the gas molecules will transfer from the main chamber into the pump. The stator blade intercepts the molecules on their downward-facing side and moves them in an x-axial direction. In the meantime, the molecules continuously gain velocity from the rebounding of the rotor. The stator blade duplicates this process until the molecules move out through the outlet. As the major primary pumps in our MBE system, the turbomolecular pumps can maintain the pressure of deposition chamber around 10^{-6} to 10^{-7} mbar.

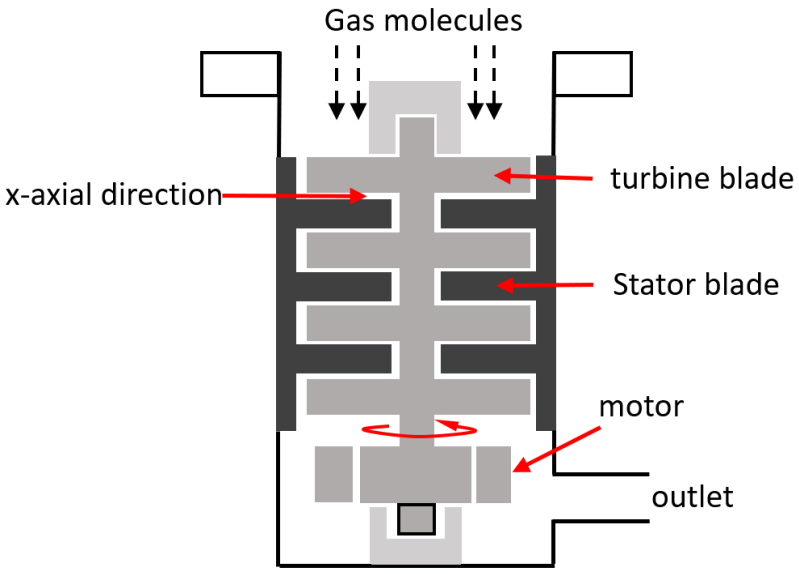

Figure 3.2 Schematic diagram of the turbomolecular pump. (Adapted from [2])

3.2.1.2 Sputter-ion pump

The most important component in a modern ion pump is the Penning cell. It consists of a pair of titanium cathodes that are parallel to each other[2], [3]. There is a cylindrical anode made of stainless steel between the pair of titanium cathodes. The strong magnetic fields are provided by permanent magnets located outside the pump. The direction of the magnetic field is parallel to the cylinder axis. A high voltage (typically 3kV to 7kV) is applied on the anode, whereas the cathodes are earthed. Due to the effect of the electric and magnetic field, the large number of free electrons follow spiral trajectories back and forth between the cathodes. The schematic of penning cell is shown in Figure 3.3 (a).

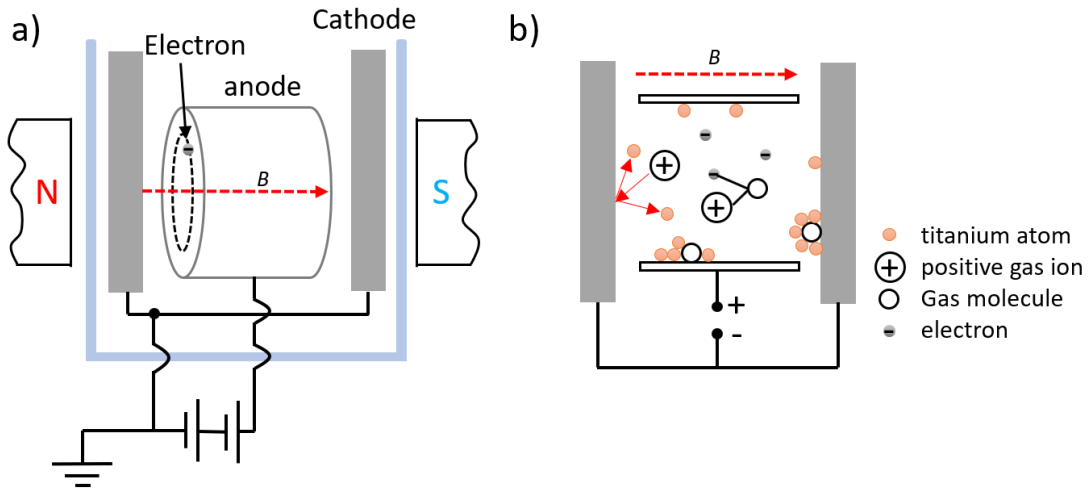

Figure 3.3 a) Penning cell for sputter-ion pump. b) Working mechanisms in sputter-ion pump. Adapted from [2]

When the ion pump operates, the gas molecules enter from the deposition chamber. Then the molecules are ionised by electrons and produce positive ions and another free electron. The newly created electron will join the existing electrons and continue ionising the gas molecules. In contrast to the electrons, the positive gas ion has a larger relative mass, and is less affected by the magnetic field. This results in the electric field accelerating the gas ion to strike the cathode. The collision between the gas ion and the cathode will result in the gas ion being buried within the cathode, or titanium materials will be sputtered onto the interior wall of the anode cylinder. The deposited titanium surface can be regarded as a getter of gas which will further improve the pressure of the chamber [2]. The Figure 3.3 (b) shows the pumping mechanisms in sputter-ion pump.

3.2.1.3 Titanium sublimation pump (TSP)

As a part of the secondary pumping system, the basic working principle of titanium sublimation pump (TSP) is capturing molecules by strongly bound chemisorbed material. This type of capture process is named ‘gettering’. The core element of TSP is a filament that is made of an alloy of Titanium and Molybdenum. The alloying design has high mechanical stability at high temperature and is suitable for cyclic use. When the pump works, a high current around 40 ampere passes through the filament. The filament then heats up and the titanium is thermally sublimated and deposited on the chamber walls, forming a surface of the titanium film. The titanium is highly reactive and can getter most gases except some chemically inert species, such as Helium, Neon and Argon [4].

3.2.1.4 Liquid nitrogen shroud

In general, the traditional MBE system is surrounded by a liquid nitrogen cooling shroud. The purpose of this design is by using the low-temperature characteristics of liquid nitrogen (LN_2) to further minimise gaseous impurities in the chamber. When a gaseous impurity molecule enters the growth environment and collides with the shroud, the low temperature of the cooling shroud will make the molecule lose its thermal momentum then stick to the shroud. However, the pumping ability of the cooling shroud depends on the freezing and boiling point of gaseous impurity. For our MBE system, the LN_2 is transferred from a dewar into the cryo-shroud. In order to maintain the maximum efficiency of the cryo-shroud, refilling of the LN_2 needs to be carried out every week.

3.2.2 Substrate holder and wafer heating

The wafer surface temperature is a crucial factor which directly affects the quality of thin films growth. In order to get a uniform and reproducible layer, the requirement of temperature across a substrate holder needs to be within ±5 °C. In general, the substrate holder is made of a refractory metal block (usually molybdenum). During the growth, the wafer is held in a parallel position to a heater block which connects with a pyrolytic graphite filament. A current is passed through the filament, causing it to heat up creating thermal heater on heater block. The distance between wafer and heater block is around 5mm, therefore the radiated heat can easily transfer through this small gap. A thermocouple is used to give temperature feedback. For most commercial MBE system, the substrate stage can be rotated during the growth to ensure a more uniform flux at all position on the wafer [5]. However, this feature is not available in our MBE system. The uniformity of the source fluxes can be ignored because of the small size of our growth sample.

3.2.3 Beam Generators, controllers and monitors

The most important property of a beam generator is to provide stable fluxes of molecular beams with a uniform and appropriate intensity during the sample growth.

3.2.3.1 Knudsen Effusion Cells

Knudsen effusion cells is the core element of beam generation. The usual technique to generate molecular beam is by thermally heating the source material to the point where it evaporates from the surface. Under the ideal case, the beam flux can be accurately expressed by equation 3.1 [6], [7].

$$J = 1.118 \times 10^{22} \frac{pA}{l^2 (MT)^{1/2}} molecules \cdot cm^{-2} \cdot s^{-1} \quad (3.1)$$

Where J is the flux rate, the number of molecules striking the substrate per unit area per second, A is the area of the aperture of the cell, p is the source pressure in the cell in Torr, l is the distance from the orifice of a cell to the substrate, M is the molecular weight of the source material and T is the absolute temperature of the cell.

Currently, it has different types of effusion cells used in the MBE system. The cells operate at different temperatures based on the vapour pressure of the source materials. In the MBE-STM machine, most cells are knudsen cells except the arsenic cell, which is a dissociation cell. The standard Knudsen effusion cell consists of a crucible, heater filaments, water cooling system, heat shields and an orifice shutter. During the growth process, the inner crucible is heated radiatively by the heater filament. The temperature of which can reach to over 1500 °C. Therefore, two design considerations need to be satisfied for the crucible material. Firstly, the materials being used must withstand high-temperature changes, and secondly, it cannot have any reaction with the source material. For commercial MBE system, the cells are usually in a semi-horizontal mounted design [7]. Unfortunately, there is insufficient space to adopt this design in our system. Therefore, the effusion cells have to mount below the substrate vertically. The disadvantage of this configuration is that there is a possibility that contamination will fall into the cells from the flakes of condensed matter, affecting the purity of the source material.

3.2.3.2 Crucible design

The pyrolytic boron nitride (PBN) material is one of the best choices for the crucible material. The material does not only have the impurity level less than 10 ppm, but also haven't a deleterious effect on the grown layer even at 1400 ˚C when nitrogen produced due to dissociation of this material [7]. There are still some advantages compared with other materials, the PBN can endure much higher temperatures than quartz, which is restricted to temperatures below 500 ˚C. Although ultrapure graphite is suitable for use at high temperature, it is difficult to completely outgas due to the material having a porous surface. Therefore, gas adsorption occurs easily when the material is exposed to the atmosphere. In addition to that, Al reacts with graphite at its evaporation temperature over 1100 ˚C.

3.2.3.3 Dissociation Cells

The group V material such as arsenic, phosphorus, and antimony are stored in a dissociation cell. We only use arsenic in our laboratory. The difference between dissociation cell and Knudsen cell is that there is an additional heating zone between the source material and the cell orifice known as a 'cracker' to break the tetramers into dimers. The efficient cracking temperature of the beams is calibrated by the mass spectroscopy experiments in [7] (See figure 3.4). Typically, the temperature ranges between 800-1000°C for 100% cracking. The cracking temperature varies depending on the different lab machine condition. Unfortunately, due to the lack of mass spectroscopy in this MBE machine similar experimental work cannot be done. In our lab, we therefore assume that a temperature of 1000°C will give very largely As_2 species and a temperature of 650°C will give As_4 species.

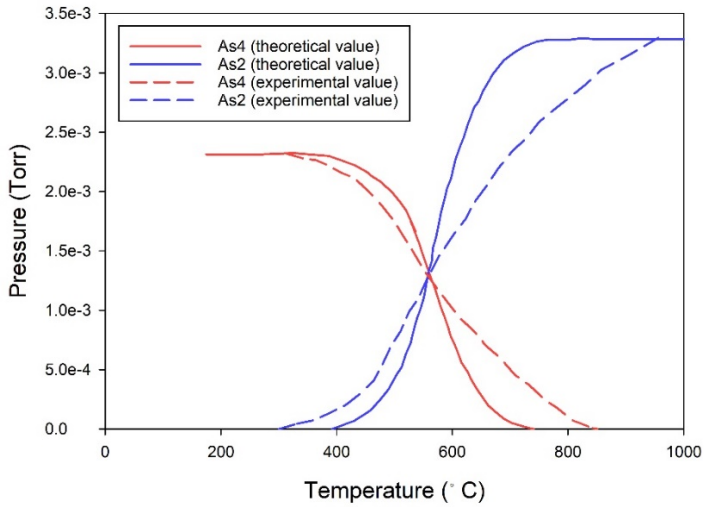

Figure 3.4 Theoretical pressure and experimental pressure of As4 and As2 shown a function a cracker zone temperature, adapted from [7]

3.2.3.4 Shutter transients

In order to precisely control the thickness and composition of the epitaxial layer, a shutter mechanism with an opening/closing time of less than 0.1s will effectively open/stop the molecular beam reaching the substrate. At the shutter closing condition, the blade reflects a portion of the thermal radiation into the cell. The cell will therefore need to provide less power to reach the desired temperature. When the shutter is opened, the reflected thermal radiation disappears, thus the temperature of the surface of the source cools slightly resulting in a small reduction of flux. This phenomenon is known

as shutter transient. This can be rectified by the increasing power supplied to the cell. The shutter transient can be neglected during the thick bulk sample growth; however, it needs to be carefully considered when growing quantum well structures.

3.2.3.5 Movable ion gauge (MIG)

Due to the MBE evaporation source stored in non-ideal Knudsen cells, it is hard to accurately measure the relationship between temperature and atomic flux arriving at the substrate. The simplest way is by measuring the thickness of the deposited layer of the group III atoms. The overall growth rate can then be estimated as the growth rate is directly dependent on the arrival rate of the group III atoms [8], [9]. Alternative ways such as capacitance-voltage profiling, electron microscopy etc., will give a combined growth rate. Specifically, secondary ion mass spectrometry (SIMS) can be used to provide precise results for dopant arrival rates, however, it is a destructive testing method that sample cannot be used after processing.

Nowadays, the most widely used method is by using a movable ion gauge (MIG) between the substrate and the beam path to determine beam fluxes [10], [11]. The structure of the MIG consists of a thin collector surrounded by a cylindrical shaped grid and three filaments place outside the grid. The geometry of this design is to minimise the X-ray limit problem by reducing the cross-section of the collector for collecting X-rays.

During the pressure measurement, electrons are thermionically emitted by these heated filaments and accelerate toward the positively charged grid. When the gas atoms are passing through the grid, they will collide with the electrons and be ionised. The positive gas ions are attracted to the collector with negative potential and generate a current that is directly proportional to the beam equivalent pressure of the gas atoms. The ion gauge has different detection efficiency for measuring different molecules. Therefore, the ion gauge is often used to measure one molecular flux at a time to minimise the experimental uncertainty.

3.2.4 Reflection High Energy Electron Diffraction (RHEED)

As a very sensitive and simple diagnostic tool, this technique can provide information of wafer surface reconstruction during the growth process based on the indication of "streakiness" in the RHEED pattern [12]. Surface reconstruction varies with the change

of flux rates and growth temperature. Understanding the surface variations from the RHEED pattern can help to evaluate the quality of the deposited layer.

The basic RHEED system consists of an electron gun and phosphorescent screen. During the operation, a collimated beam of electrons is generated by an electron gun with a high operating voltage 10-30 kV [13]. The electron beam strikes the wafer surface at a glancing angle less than 3°. The electron beam can only penetrate a few monolayers below the wafer surface and creates a diffraction pattern. The diffraction pattern is then observed on the phosphorescent screen.

The formation of a diffraction pattern in RHEED needs to satisfy two conditions. The first consideration is how the diffraction occurs. From Bragg's law, constructive interference occurs when $2d\sin\theta=n\lambda$ (details will be mentioned in chapter 4, X-rays section). Since the incident angle of the electron beam is small, only the top few monolayers contribute to diffraction. In this case, the lattice point of the top few monolayers converts to lattice rods in reciprocal space due to "shape effect".

The second consideration is the conservation of momentum. In RHEED, the electron is diffracted elastically. In other words, the scattered electrons have the same energy as the incident electrons. If considering all the possible incident and scattered electron in the form of wave-vector, it will form a sphere with the radius $2\pi/\lambda$, which was first proposed by Ewald [14].

The diffraction occurs at the intersect point between Ewald's sphere and the reciprocal lattice rods. As shown in figure 3.5, we will see the diffraction spots appear as a shape of the arc due to the cut-off degree between Ewald's sphere and reciprocal lattice rods. In reality, there are several semicircles diffraction patterns, which correspond to different Laue zones.

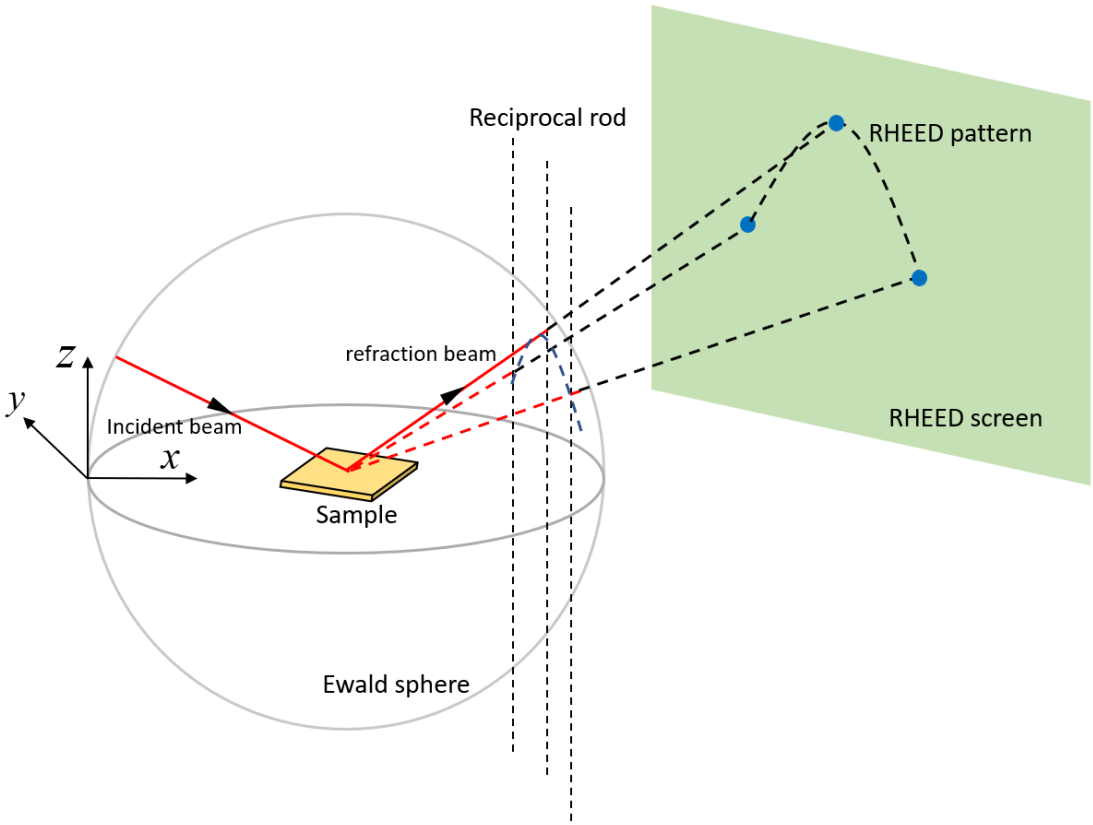

Figure 3.5 The schematic diagram of RHEED

3.2.5 RHEED as a calibration tool

RHEED can provide useful information to better control the growth conditions throughout our work, including the substrate temperature, growth rate, and cell flux. The procedure of each calibration will be described in this section.

3.2.5.1 Substrate temperature calibration

In our MBE-STM work, heating the wafer by thermal radiation relies on a sample heater stage above the wafer. A thermocouple is attached to the sample heater stage, which is used to measure the temperature of the wafer. However, there is a gap between the wafer and heater thus it causes measurement error between the real temperature and the temperature measured by the thermocouple. In our lab, the sample temperature is estimated from the current passing through the heater. Three calibration points due to temperature dependent RHEED transitions will be analysed.

The three-temperature dependent RHEED transitions for GaAs wafers are:

- As Cap removal temperature is around 295 °C [15], [16].

- The c (4 × 4) to (2 × 4) transition at 400-425 °C, there is no As flux in this process [16], [17].
- The oxide removal temperature is between 580 and 600 °C [18] .

When transferring a sample which was grown in one machine to another, the deposition of an As cap is a useful protection method to prevent the sample oxidising. In the lab, the temperature of As cap removal is also taken as a calibration point. In the process, a GaAs (100) substrate is used after removing the oxidised layer. As_2 tends to easily provide a better As cap than As_4, therefore As_2 is used. The As cap is easy to achieve on the substrate by fully opening the As valve at the substrate temperature 0°C for 1 hour in order to rapidly deposit an As cap of sufficient thickness. Once the cap is finished, the RHEED pattern changes from the original (2×4) to a hazy pattern because the amorphous As layer becomes thick enough to prevent the RHEED beam reaching the GaAs surface. After that, the As valve is closed and the substrate heater current is increased in increments every 15 minutes until the surface reconstruction is again observed on the RHEED screen.

Surface reconstruction c (4×4) will occur when the substrate temperature gradually increases to 350-400 °C. During this process, the valve of As is still closed. The surface becomes less As-rich as the As starts to evaporate at a temperature over 300°C dramatically. The c (4×4) to (2×4) transition will occur when a higher temperature applied with the absence of an As flux. The patterns for both patterns are shown in Figure 3.6 and 3.7.

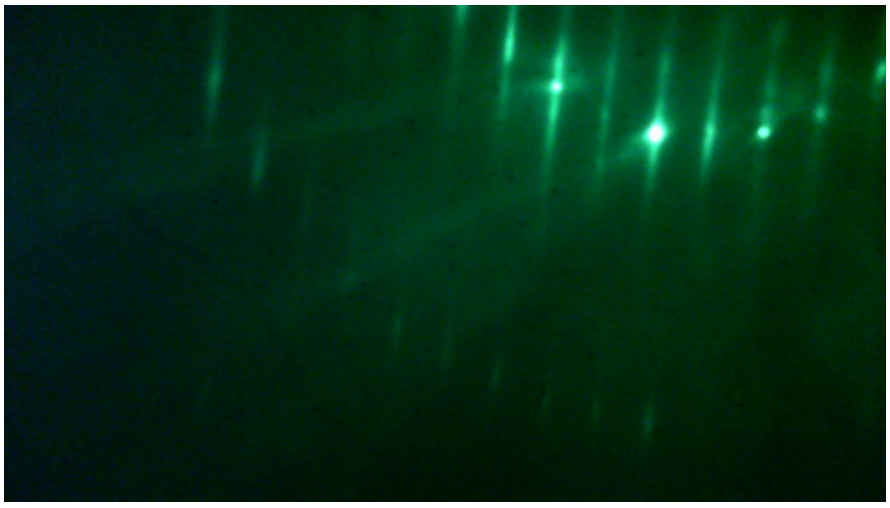

Figure 3.6 The surface reconstruction of RHEED pattern of GaAs c (4×4). Kikuchi line are visible in this figure.

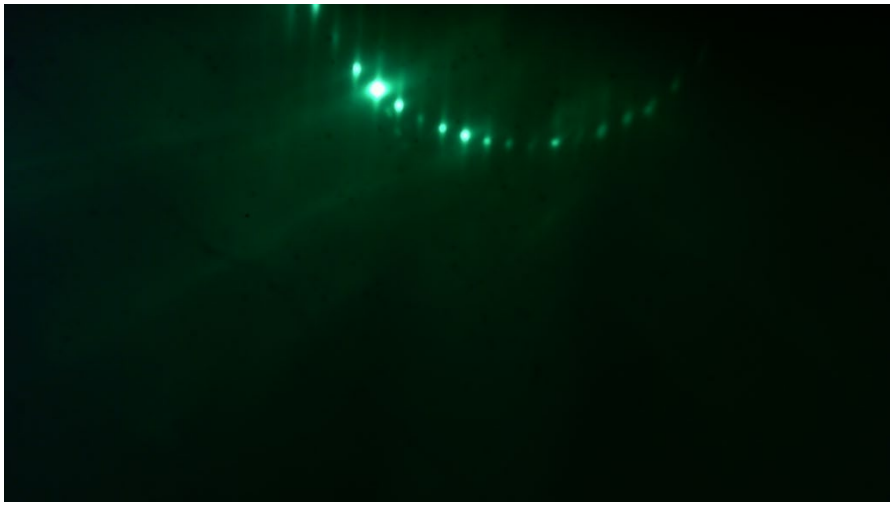

Figure 3.7 The surface reconstruction of RHEED pattern of GaAs (2×4). Only the 4× part is shown in the pattern.

The oxide removal temperature is another vital point of substrate temperature calibration. Due to exposure to air condition, the surface of commercial wafers has a thin amorphous oxide layer. To remove this oxide, the wafer is typically heated with an excess As flux for around half an hour. Figure 3.8 and 3.9 shows the RHEED pattern before and after the removal of surface oxide. It is obvious that the intensity of diffraction pattern is much brighter after removal of oxide.

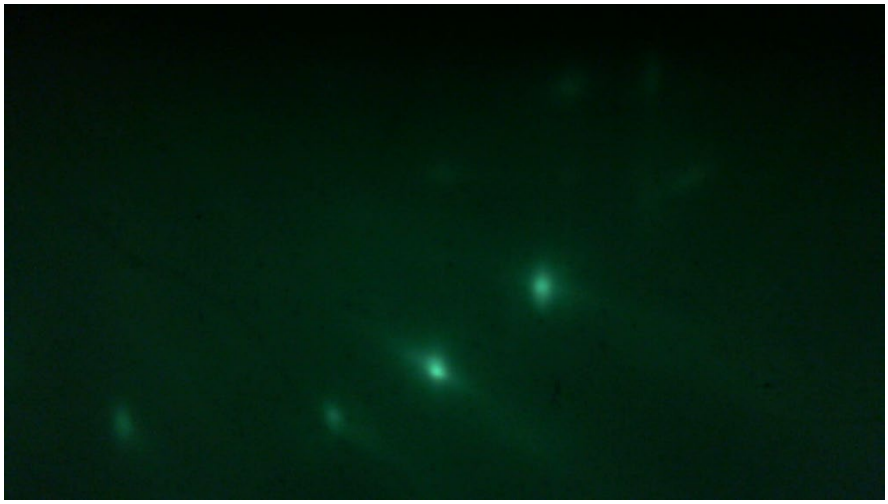

Figure 3.8 RHEED pattern of GaAs (001) before oxide removal process

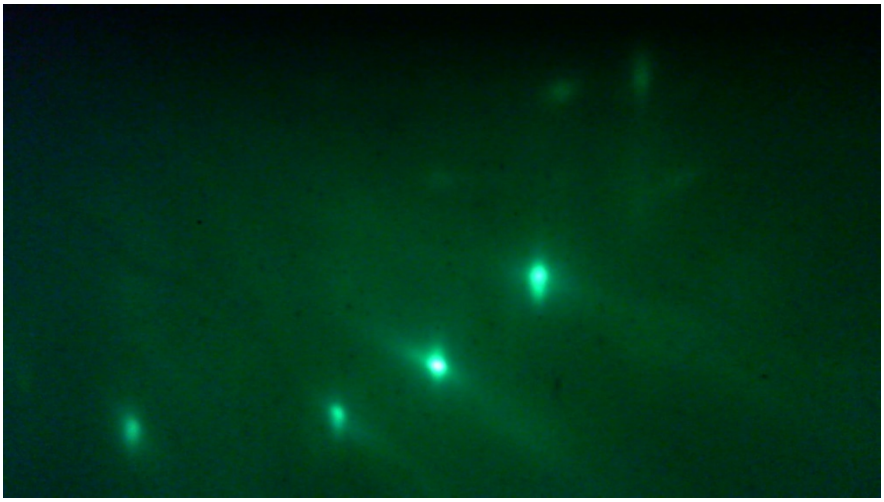

Figure 3.9 RHEED pattern of GaAs (001) after oxide removal process

The relationship between heater current and surface temperature can be depicted in Figure 3.10. A polynomial algorithm is used to fit these three calibration points. Besides, it also shows that the temperature calibration varies with substrate type. Undoped substrates need a larger current than doped substrates to reach a given temperature. This is because the doped substrates include additional absorption levels within the bandgap.

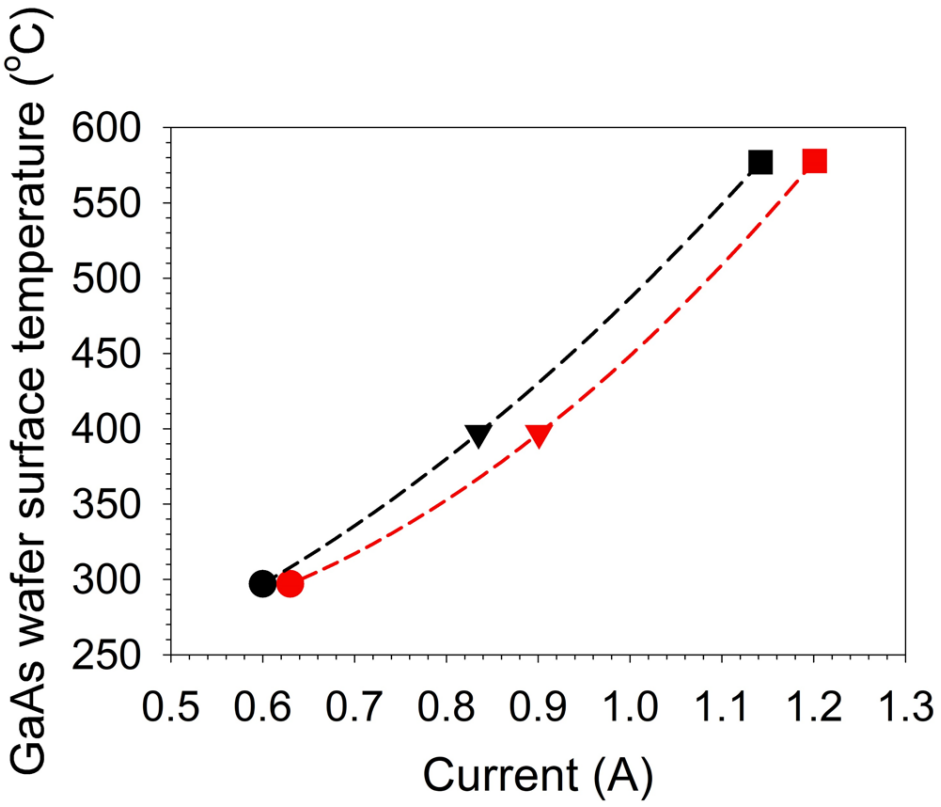

Figure 3.10 Graph of undoped (red) and n-type (black) GaAs sample temperature plotted against heater element current. The dash lines are the polynomial fit to the data.

3.2.5.2 Growth rate calibration

RHEED oscillations can provide an accurate and quick measurement of the growth rate [19]–[21]. The oscillation in specular intensity can be explained with respect to layer-by-layer growth, as shown in Figure 3.11. At the initial stage, a flat substrate surface is given with surface coverage (θ=0) means there are no atoms bound onto the surface, which gives a high diffraction intensity. When the atoms land on the surface, they will migrate around the surface and then form into islands in order to minimise the surface free energy, the intensity starts to decrease due to the surface roughness. The surface coverage (θ=0.5) means that half of a monolayer covers the surface. In this case, the intensity of RHEED signal will be the lowest. Finally, when a monolayer is completed, the intensity returns to the maximum and surface becomes flat (θ=1).

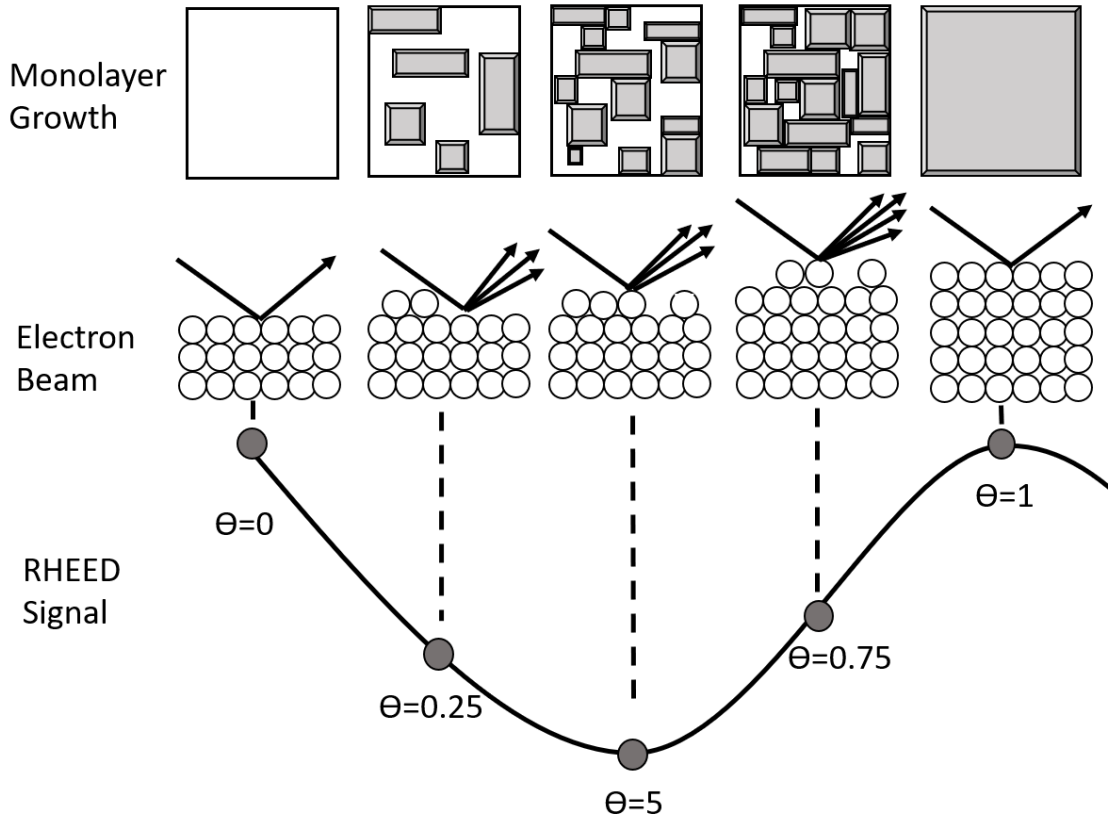

Figure 3.11 RHEED intensity oscillation during a monolayer growth

Figure 3.12 gives an example of RHEED oscillations during the growth of GaAs. The growth rate of this sample can be calculated by the number of RHEED oscillation in a certain time. There are 13 monolayers that are formed in 27 seconds. Therefore, in this case, the growth rate is 0.48 monolayers/s. The oscillation amplitude gradually decreases because the second monolayer starts to form before the first monolayer is

complete, increasing the surface roughness. Therefore, the intensity never reaches its full specular intensity. The region 27-60s shows the diffraction intensity after closing the Ga cell shutter. The intensity regains to its full specular intensity because the adsorbed atoms have time to migrate on the surface until they find an appropriate lattice position to minimise the surface free energy. Then the flat surface of GaAs has been recovered.

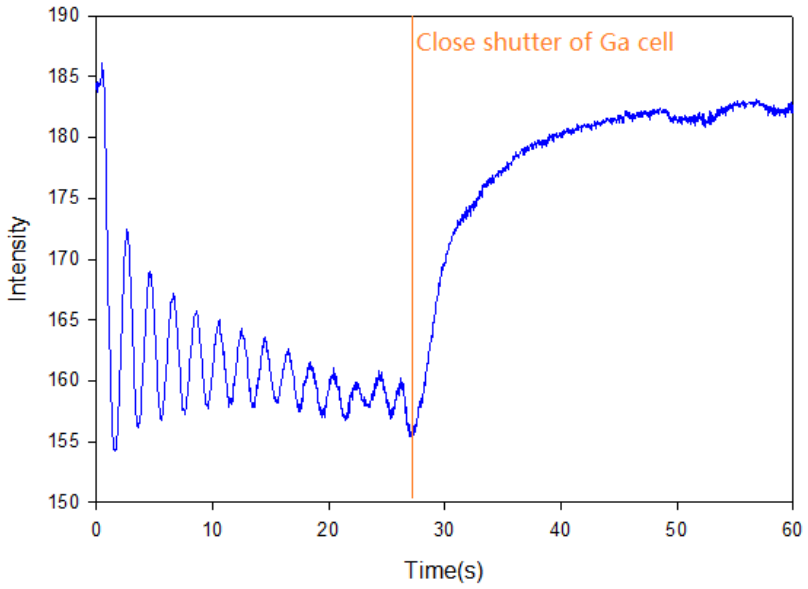

Figure 3.12 RHEED intensity oscillation during MBE growth of GaAs

3.2.5.3 Flux calibration

- **Ga Flux measurement**

Once the growth rate of Ga is known, the flux from the Ga cell can be calculated. A monolayer on any zinc blende (100) plane is half the lattice constant. In a GaAs unit cell, it consists of two monolayers, each of which includes two As atoms and two Ga atoms. Therefore, the flux of Ga atom can be described in Equation 3.2.

$$F_{Ga} = \frac{2 \times GR}{a_{GaAs}^2} \qquad (3.2)$$

Where F_{Ga} is the flux of Ga in the unit of atoms.nm^{-2}s^{-1}, a_{GaAs} is the lattice constant of GaAs that is 0.5633Å [22]. GR is the growth rate in the unit of monolayer per seconds.

- **As Flux measurement**

The method used to measure the Ga flux cannot be used for As because the sticking coefficient of As is not unity [10]. During the GaAs growth, the As will be in an oversupplied condition in order to compensate for the evaporation of As. At this point, the surface reconstruction will be As-rich (2x4). If the As is under-pressured, the surface reconstruction will change to Ga-rich (4x2). The As-rich (2x4)/Ga-rich (4x2) is a very useful calibration point [23], at which point the flux ratio of As to Ga is 1:1 and the As flux will be the same as Ga flux.

- **Bi Flux measurement**

The Bi flux cannot be measured using the same method as As flux since GaBi has not yet been synthesised. Instead, the method for measuring the Bi flux is to grow a thick Bi cap layer on a GaAs substrate setting at 0°C, because the sticking coefficient is unity at 0°C. Next, using scanning electron microscopy to measure the thickness of the cap layer. Because the atomic weight of Bi and density of Bi is known, therefore, the Bi flux can be easily calculated.

3.3 Substrate preparation

Substrate preparation is an important essential work before any 'real' growth can commence. Three processes will be adopted in our lab namely chemical treatment, layer outgas and oxide removal.

- **Chemical treatment**

Having a clean substrate is the first step for successful MBE growth. Normally, there are three solvents used in cleaning process, namely acetone, N-butyl acetate and isopropyl alcohol (IPA).

In our lab, we buy pre-treated doped and un-doped GaAs (001) substrate and cleave to 11.8mm × 11.4mm rectangular substrate to fit our substrate holder. A nitrogen gas gun is used to blow off crystal dust from the surface of the sample after cleaving. After that, three solvents are used to further clean the surface. Finally, the substrate needs to be placed under an optical microscope for surface inspection. The cleaning process may be repeated if there is still dust on the surface.

- **Outgas surface layer**

After chemical treatment, the prepared substrate can be loaded into the MBE system via FEL. The outgas process and removal of the surface oxide must be achieved before the growth of epitaxy layer can commence. The outgas process is a baking process which involves setting the substrate temperature to ~ 400 ˚C for 15-20 min. The purpose of outgassing of sample is to evaporate the water and volatile contamination on the substrate surface.

- **Oxide removal process**

The oxide removal process is different based on material, in the case of silicon, ion sputtering was used to bombard the surface and then annealed out at 850 ˚C for 5-10 min in early days. There is a new method developed recently, allowing silicon substrate to be cleaned by heating in vacuum at temperature around 850 ˚C [7]. To remove oxide of GaAs is much easier compared with silicon. The method is to heat the substrate between 580 and 600 ˚C for at least 20 mins, during which the surface will get rough since arsenic evaporates over 300 ˚C, therefore an excess arsenic flux needs to be provided to stabilise the surface. By comparing the intensity of the RHEED diffraction pattern, it can predict whether the oxide removal process is completed.

3.4 GaAs growth

Growing a high-quality GaAs buffer layer is prerequisite of growing GaAsBi. Therefore, to investigate the GaAs growth can provide us with a deeper understanding of MBE growth. Studies have shown that high-quality GaAs must be grown at a substrate temperature range between 600-640 °C [24], [25]. If the substrate temperature is above 650 °C, it will result in a reduction of the GaAs growth rate due to the evaporation of Ga from the surface [26]. Therefore, the critical temperature point of 650 °C, is also known as the congruent evaporation temperature for GaAs. Above this temperature, it is noted that both group III and V element are unstable. For an ideal growth, the growth temperature should always be set below the congruent evaporation temperature. In our laboratory, the heater current controls the temperature of the substrate; therefore a slight deviation from the actual temperature is unavoidable. In practice, it shows that the temperature above 600 °C cannot provide a satisfactory quality of GaAs in our machine, the temperature around 580 °C is used to ensure a better quality of growth.

There are two arsenic species, As_2 and As_4, that can be used for the growth of GaAs via MBE. The most important difference is that the reaction between As_2 and Ga atom is one of dissociative chemisorption involving one single Ga atom. While in the case of As_4, pairs of As_4 will react on adjacent Ga atoms [27]. Further studies have shown that the As_2 will induce lower electron trap concentration compared with As_4 at 537°C. And even at lower growth temperature, the growing sample shows better performance such as brighter PL and better interfaces by using As_2 rather than As_4. Therefore, during the growth process of GaAs, As_2 is used in our lab.

In order to avoid nonstoichiometric growth, the group V elements must be oversupplied during the growth process of III-V alloy. As a highly volatile element, arsenic will readily evaporate over 300 °C. With increasing temperature, the surface of the sample will become rough in the absence of an external As flux. The total required arsenic flux can be described in Equation 3.3.

$$As_{total} = As_{As} + As_{Ga} \quad (3.3)$$

The equation is easy to understand, the total As flux can be divided into two parts. As_{Ga} is the As flux used to compensate for the Ga flux, in order to satisfy the stoichiometric condition, the ratio between As and Ga needs to be 1:1. In addition, arsenic continually evaporates during the process. Therefore, it needs excess As to compensate As loss, which is defined as As_{As}. The minimum As overpressure is related to the substrate temperature. When the extra As flux is close to the minimum, it has obvious merits not only that the surface is readily annealed and flatten but also that it can reduce the waste of As. As a result, the ratio of As to Ga is 1.6:1 [28] with respect to the growth of GaAs in our lab.

3.5 GaAsBi growth

3.5.1 Review of GaAsBi growth investigation

Since the first GaAsBi sample was grown by MOVPE in 1998 [29], the growth conditions and material characteristics of GaAsBi have been investigated by many groups in the past 20 years. Understanding these research results can not only enable us to understand the growth and development history of Bi but also give us enlightenment on how to grow high-quality Bi samples.

- **Growth of GaAsBi needs low temperature and stoichiometric arsenic to gallium flux condition**

One of the early papers described molecular beam epitaxy growth of GaAsBi was reported by Tixier *et al.* [30]. They found that Bi has negligible incorporation into GaAs when the substrate temperature is higher than 450°C with a high arsenic to gallium flux ratio. Besides, they also found that an arsenic to gallium flux ratio close to the stoichiometric value is a beneficial condition for Bi incorporation**.**

Young *et al.* reported that Bi has a strong tendency to surface segregate using the usual GaAs growth conditions. Therefore, both low growth temperature and near stochiometric arsenic to gallium ratio are required during the growth. They grew GaAsBi at the growth temperature range between 320°C and 390°C. Besides, in-situ light scattering was used as a useful tool to define growth conditions [31].

- **Which arsenic species shall we choose for GaAsBi growth? -As2 or As4**

Under different As_2 and As_4 condition, Richards *et al.* grew a series of GaAsBi layers using a range of temperature to investigate the impact of As species to the growth of GaAsBi. The authors claimed that the incorporation of bismuth into GaAs is independent on the As species. Also, the authors conclude that no matter which arsenic species being used, there is no noticeable impact on the PL intensity of the samples. The authors suggested that As_4 is more suitable than As_2 during the growth of GaAsBi. Because of a wider range of As_4:Ga ratio, the optimal growth condition is more easily achieved compared with As_2 [32].

- **How growth rate impact on bismuth incorporation**

Ptak *et al.* proposed a concept of kinetic-limited growth regime for GaAsBi growth in 2012 [33]. The author grew a series of samples at a low growth temperature (315 ±5°C was used in this paper) with different growth rates and Bi flux. The RMS surface roughness is analysed using atomic force microscope (AFM) measurements. The authors found that bismuth incorporation is proportional to the Bi flux in the kinetic-limited region. Within this region, the Bi atoms do not possess enough energy to segregate on the surface, and therefore most of the Bi atoms are incorporated into the layer. The author also noted that the growth rate is a critical factor that impacts on the Bi incorporation. When the high growth rate and low bismuth flux are applied during the growth, the surface becomes rough due to insufficient surfactant effects. However, the layer with the same bismuth flux at the low growth rate shows a smooth surface. On the contrary, the sample shows significant roughness when high Bi flux is applied

at the low growth rate. This high RMS roughness can be interpreted by the formation of Bi droplets due to the high Bi flux which introduces more Bi atoms onto the surface, forming a Bi-metallic layer rather than incorporating into the layers. From the results, it provides a useful guide for the growth window for smooth, droplet-free GaAsBi growth.

- **How growth temperature limit to the dark current of GaAsBi diode**

Rockett *et al.* investigated the influence of growth conditions on the structural and optoelectronic quality of GaAsBi [34]. They grew a series of GaAsBi diodes using different growth temperatures and Bi fluxes. The temperature range of growth they used from 355 to 405 °C. The authors noted that the sample grown at high-temperature shows higher RT-PL intensity but non-uniform structural characteristics as determined by X-ray, which is consistent with the result in [35]. In addition, the current-voltage characteristic is significantly affected by the growth temperature. The dark current is inversely proportional to the growth temperature. Therefore, the authors suggested that growing at a high temperature is the essential factor to provide better performance on the electronic characteristics of GaAsBi devices.

3.5.2 Summary of GaAsBi growth condition

Through reviews of GaAsBi growth studies, the growth of GaAsBi should meet the following requirements. Firstly, the growth temperature should be below 450 °C with stoichiometric arsenic to gallium flux condition. Secondly, As_4 is used as the arsenic species for the growth process. Since the Bi content of our growth is generally below 5%, the low growth rate is more conducive to ensuring the quality of the sample. The purpose of this choice is to avoid the roughness of the surface due to the lack of surfactant. To sum up, the above methods may not be applicable to all samples, and an extra calibration is necessary for specific samples to achieve the best growth condition.

3.6 System maintenance (Bake out process)

Regular maintenance and inspection play a vital role in the stability of the MBE machine and to maintain a high sample growth quality. The bake-out process is an essential procedure to be performed for MBE systems. This is especially important after routine system maintenance such as filling cell materials or fixing of the substrate heater stage, which exposes the machine to the atmosphere. After the baking process, the

material sources will also require thorough outgassing to ensure that the sources are kept in a clean condition.

From the literature, the bake-out procedure is different from laboratory to laboratory [36]–[38]. After the machine is exposed to the atmosphere, contaminants and moisture in the air will be adsorbed onto the inner wall of the chamber. At room temperature, it needs a longer time to evaporate and pump down. Therefore, a fast-tracked way is to cover the machine in a thermally insulated stainless steel box which is then heated to over 100°C for 48 hours, which is shown in Figure 3.13. In this case, to withstand such a high temperature, all system components must be manufactured with refractory materials. It is important to remove parts that are unable to withstand high temperatures for extended durations such as water-cooling tubes, the motor of each cell, rubber gaskets and thermally sensitive connections before baking. In our lab, the bake-out temperature is set to 125°C for 2~3 days, the lowest achievable background pressure is below 5×10^{-10} mBar.

Figure 3.13 MBE Bake-out process

3.7 Reference

[1] C. B. Duke, 'The birth and evolution of surface science: Child of the union of science and technology', *Proc. Natl. Acad. Sci.*, vol. 100, no. 7, pp. 3858–3864, Apr. 2003, doi: 10.1073/pnas.0730358100.

[2] A. Chambers, *Modern vacuum physics*. Boca Raton: Chapman & Hall/CRC, 2005.

[3] M. Audi and M. de Simon, 'Ion pumps', *Vacuum*, vol. 37, no. 8, pp. 629–636, Jan. 1987, doi: 10.1016/0042-207X(87)90048-0.

[4] A. Gupta and J. Leck, 'An evaluation of the titanium sublimation pump', *Vacuum*, vol. 25, no. 8, pp. 362–372, Aug. 1975.

[5] A. Y. Cho and K. Y. Cheng, 'Growth of extremely uniform layers by rotating substrate holder with molecular beam epitaxy for applications to electro-optic and microwave devices', *Appl. Phys. Lett.*, vol. 38, no. 5, pp. 360–362, Mar. 1981, doi: 10.1063/1.92377.

[6] A. Y. Cho, 'Growth of III–V semiconductors by molecular beam epitaxy and their properties', *Thin Solid Films*, vol. 100, pp. 291–317, 1983.

[7] E. H. C. Parker, Ed., *The Technology and Physics of Molecular Beam Epitaxy*. Springer US, 1985.

[8] A. Y. Cho, J. R. Arthur, B. Laboratories, and M. Hill, 'MOLECULAR BEAM EPITAXY', *Prog. Solid-State Chem.*, vol. 10, pp. 157–191, 1975.

[9] B. A. Joyce and C. T. Foxon, 'KINETIC STUDIES OF THE GROWTH OF III–V COMPOUNDS USING MODULATED MOLECULAR BEAM TECHNIQUES', in *Vapour Growth and Epitaxy*, G. W. Cullen, E. Kaldis, R. L. Parker, and C. J. M. Rooymans, Eds. Elsevier, 1975, pp. 122–129.

[10] C. T. Foxon and B. A. Joyce, 'Interaction kinetics of As2 and Ga on {100} GaAs surfaces', *Surf. Sci.*, vol. 64, no. 1, pp. 293–304, Apr. 1977, doi: 10.1016/0039-6028(77)90273-4.

[11] C. E. C. Wood and B. A. Joyce, 'Tin-doping effects in GaAs films grown by molecular beam epitaxy', *J. Appl. Phys.*, vol. 49, no. 9, pp. 4854–4861, Sep. 1978, doi: 10.1063/1.325517.

[12] A. Ichimiya and P. I. Cohen, *Reflection High-Energy Electron Diffraction*. Cambridge: Cambridge University Press, 2004.

[13] J. A. Stroscio, D. T. Pierce, and R. A. Dragoset, 'Homoepitaxial growth of iron and a real space view of reflection-high-energy-electron diffraction', *Phys. Rev. Lett.*, vol. 70, no. 23, pp. 3615–3618, Jun. 1993, doi: 10.1103/PhysRevLett.70.3615.

[14] P. P. Ewald, 'Introduction to the dynamical theory of X-ray diffraction', *Acta Crystallogr. A*, vol. 25, no. 1, Art. no. 1, Jan. 1969, doi: 10.1107/S0567739469000155.

[15] M. C. Gallagher, R. H. Prince, and R. F. Willis, 'On the atomic structure and electronic properties of decapped GaAs(001)(2 x 4) surfaces', p. 10.

[16] F. Bastiman, 'In Situ Surface Studies of III-V Semiconductor Compounds', phd, University of Sheffield, 2010.

[17] K. Reginski, J. Muszalski, V. V. Preobrazhenskii, and D. I. Lubyshev, 'Static phase diagrams of reconstructions for MBE-grown GaAs(100) and AlAs(001) surfaces', *Thin Solid Films*, vol. 267, pp. 54–57, 1995.

[18] J. H. Neave and B. A. Joyce, 'Structure and stoichiometry of {100} GaAs surfaces during molecular beam epitaxy', *J. Cryst. Growth*, vol. 44, pp. 387–397, 1979.

[19] J. H. Neave, B. A. Joyce, P. J. Dobson, and N. Norton, ‘Dynamics of film growth of GaAs by MBE from Rheed observations’, *Appl. Phys. Solids Surf.*, vol. 31, no. 1, pp. 1–8, May 1983, doi: 10.1007/BF00617180.
[20] C. E. C. Wood, ‘RED INTENSITY OSCILLATIONS DURING MBE OF GaAs’, *Surf. Sci. Lett.*, vol. 108, pp. L441–L443, 1981.
[21] J. J. Harris and B. A. Joyce, ‘OSCILLATIONS IN THE SURFACE STRUCTURE OF &DOPED GaAs DURING GROWTH BY MBE’, *Surf. Sci. Lett.*, vol. 103, pp. L90–L96, 1981.
[22] J. S. Blakemore, ‘Semiconducting and other major properties of gallium arsenide’, *J. Appl. Phys.*, vol. 53, no. 10, pp. R123–R181, Oct. 1982, doi: 10.1063/1.331665.
[23] Á. Nemcsics, ‘Investigation of the Hysteretic Phenomena in RHEED Intensity Change in the Study of Surface Reconstruction’, *Acta Polytech. Hung.*, vol. 7, no. 5, p. 21, 2010.
[24] R. Fischer *et al.*, ‘Incorporation rates of gallium and aluminum on GaAs during molecular beam epitaxy at high substrate temperatures’, *J. Appl. Phys.*, vol. 54, no. 5, pp. 2508–2510, May 1983, doi: 10.1063/1.332317.
[25] H. Morkoç and A. Y. Cho, ‘High-purity GaAs and Cr-doped GaAs epitaxial layers by MBE’, *J. Appl. Phys.*, vol. 50, no. 10, pp. 6413–6416, Oct. 1979, doi: 10.1063/1.325732.
[26] B. A. Joyce, ‘Molecular beam epitaxy’, *Rep. Prog. Phys.*, vol. 48, pp. 1637–1697, 1985.
[27] C. T. Foxon and B. A. Joyce, ‘INTERACTION KINETICS OF As4 AND Ga ON {100) GaAs SURFACES USlNG A MODULATED MOLECULAR BEAM TECHNIQUE’, *Surf. Sci.*, pp. 434–450, Mar. 1975.
[28] M. Masnadi-Shirazi, D. A. Beaton, R. B. Lewis, X. Lu, and T. Tiedje, ‘Surface reconstructions during growth of GaAs1−xBix alloys by molecular beam epitaxy’, *J. Cryst. Growth*, vol. 338, no. 1, pp. 80–84, Jan. 2012, doi: 10.1016/j.jcrysgro.2011.09.055.
[29] K. Oe and H. Okamoto, ‘New Semiconductor Alloy GaAs1-xBix Grown by Metal Organic Vapor Phase Epitaxy’, *Jpn. J. Appl. Phys.*, vol. 37, no. Part 2, No. 11A, pp. L1283–L1285, Nov. 1998, doi: 10.1143/JJAP.37.L1283.
[30] S. Tixier *et al.*, ‘Molecular beam epitaxy growth of GaAs1−xBix’, *Appl. Phys. Lett.*, vol. 82, no. 14, pp. 2245–2247, Apr. 2003, doi: 10.1063/1.1565499.
[31] E. C. Young, M. B. Whitwick, T. Tiedje, and D. A. Beaton, ‘Bismuth incorporation in GaAs1–xBix grown by molecular beam epitaxy with in-situ light scattering’, *Phys. Status Solidi C*, vol. 4, no. 5, pp. 1707–1710, 2007, doi: 10.1002/pssc.200674291.
[32] R. D. Richards *et al.*, ‘Molecular beam epitaxy growth of GaAsBi using As2 and As4’, *J. Cryst. Growth*, vol. 390, pp. 120–124, Mar. 2014, doi: 10.1016/j.jcrysgro.2013.12.008.
[33] A. J. Ptak *et al.*, ‘Kinetically limited growth of GaAsBi by molecular-beam epitaxy’, *J. Cryst. Growth*, vol. 338, no. 1, pp. 107–110, Jan. 2012, doi: 10.1016/j.jcrysgro.2011.10.040.
[34] T. B. O. Rockett *et al.*, ‘Influence of growth conditions on the structural and opto-electronic quality of GaAsBi’, *J. Cryst. Growth*, vol. 477, pp. 139–143, Nov. 2017, doi: 10.1016/j.jcrysgro.2017.02.004.
[35] T.-H. Kim, K. Forghani, K. Collar, T. F. Kuech, and A. S. Brown, ‘Growth of GaAs1−xBix by molecular beam epitaxy: Trade-offs in optical and structural

characteristics', *J. Appl. Phys.*, vol. 116, no. 4, p. 043524, Jul. 2014, doi: 10.1063/1.4891874.
[36] J. C. M. Hwang, H. Temkin, T. M. Brennan, and R. E. Frahm, 'Growth of high-purity GaAs layers by molecular beam epitaxy', *Appl. Phys. Lett.*, vol. 42, no. 1, pp. 66–68, Jan. 1983, doi: 10.1063/1.93727.
[37] M. Heiblum, E. E. Mendez, and L. Osterling, 'Growth by molecular beam epitaxy and characterization of high purity GaAs and AlGaAs', *J. Appl. Phys.*, vol. 54, no. 12, pp. 6982–6988, Dec. 1983, doi: 10.1063/1.332015.
[38] E. C. Larkins, E. S. Hellman, D. G. Schlom, J. S. Harris, M. H. Kim, and G. E. Stillman, 'Reduction of the acceptor impurity background in GaAs grown by molecular beam epitaxy', *Appl. Phys. Lett.*, vol. 49, no. 7, pp. 391–393, Aug. 1986, doi: 10.1063/1.97597.

Chapter 4. Characterisation techniques

In this chapter, various characterisation methods will be introduced in detail for material and device analysis. These methods are categorised into structural, optical and electrical measurements.

4.1 X-ray diffraction (XRD)

As a powerful non-destructive structural characterisation technique, X-ray diffraction finds widespread use in the study of crystalline structures. The properties of crystals such as epilayer thickness, strain and relaxation, and lattice constant can be obtained through analysis of the X-ray diffraction pattern. X-rays can be regarded as high-energy electromagnetic radiation, and the typical wavelength range is between 0.07-0.2nm [1].

4.1.1 Bragg's law

It is well known that when visible light passes through a double slit, the light diffraction pattern can be detected on a screen. This is only possible when the width of the slit has a similar magnitude of the wavelength of visible light (around 10^{-6}m).

However, if the slit width is much larger than the wavelength of light, diffraction does not occur. In 1912, Max von Laue proposed a concept that a crystal lattice composed of atoms might be suitable for using x-rays to create a diffraction pattern. This is because the interatomic spacing has the same order of magnitude as the wavelength of the X-rays [2]. His hypothesis was proven by William Lawrence Bragg and William Henry Bragg in 1913 [3]. Bragg's law can be described with the following equation:

$$2d\sin\theta = n\lambda \tag{4.1}$$

Where d is the distance between two adjacent layers, or it should be half of the lattice constant, since each unit cell contains 2 monolayers, θ is the angle of the incident beam, n is an integer value and λ is the wavelength of the incoming beam.

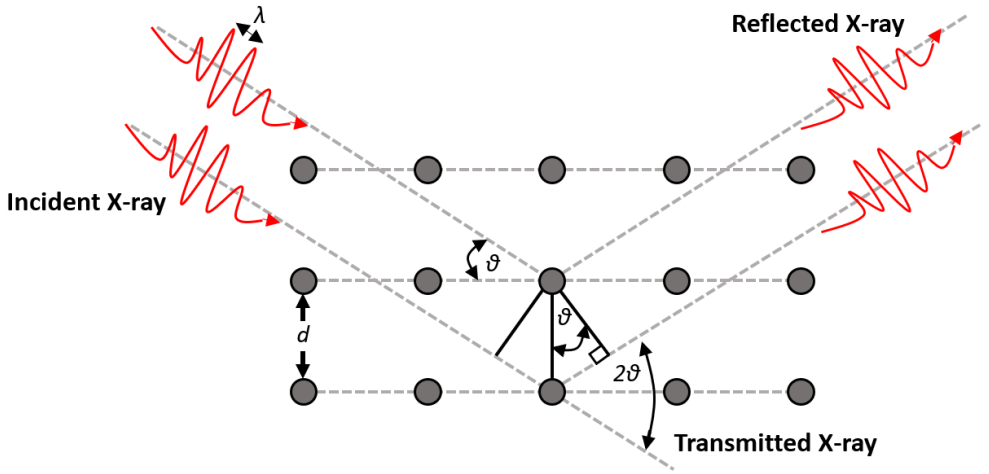

Figure 4.1 Bragg's law in x-rays diffraction

Figure 4.1 shows the crystalline structure acting as a grating in X-ray diffraction. Bragg's law states that constructive interference occurs when the path difference of the two parallel beams are equal to an integer number of wavelengths, otherwise, no signal can be detected due to the destructive interference.

4.1.2 X-ray production

An X-ray tube is used as a source for emitting X-rays. The tube contains two basic elements, a cathode, used as a source to provide electrons, and an anode that acts as the target for electron bombardment that subsequently releases X-rays. Both cathode and anode are sealed in a vacuum envelope, typically either made of ceramic or glass. In crystallography, copper is most common material used as anode it has a high proton number.

During the X-ray production, there are two types of radiation that constitute a full x-ray spectrum. A high voltage power supply provides power to accelerate electrons, which will strike the anode. Penetrating the target, some bombarding electrons will be attracted by the positively charged nucleus. With the subsequent electric field, the electrons will be deflected and then lose a portion of their kinetic energy. The lost energy is converted into radiation (X-ray photons) based on the law of conservation of energy. This process is called Bremsstrahlung (translation: braking radiation). The Bremsstrahlung process generates a continuous broad spectrum of X-rays, which is not desired for XRD measurement.

Characteristic x-rays are produced by collisions between a high-energy electron and inner shell electron (K-shell or L-shell). The inner shell electron will be ejected and this

leaves a vacancy in the shell. After that, an outer shell electron with higher energy will fill the vacancy. Subsequently, a characteristic X-ray will be created with energy equivalent to the difference of that between outer and inner shell electron. The characteristic x-rays are represented by narrow spectral lines compared with the continuous spectrum of bremsstrahlung radiation. The transition from the outer shell to the K-shell and L-shell are called K-lines and L-lines, respectively (see figure 4.2 (a)). In the case of the copper target, the K_{α} transition, an electron in the 2p shell to the 1s shell, and K_{β} transition, an electron in the 3p shell to the 1s shell, need to be considered. K_{α} usually has a much higher intensity than K_{β} , it is, therefore, the desired x-ray wavelength for XRD measurements. Although the characteristic X-rays are ideal for XRD measurements, they don't exist in isolation and are always superimposed on the continuous spectrum of X-rays. In order to make a monochromatic X-ray beam and retain only the K_{α} transition, a filter can be adopted by using a metal having one proton less than the anode material. The figure 4.2 (b) shows an example of a typical X-ray spectrum.

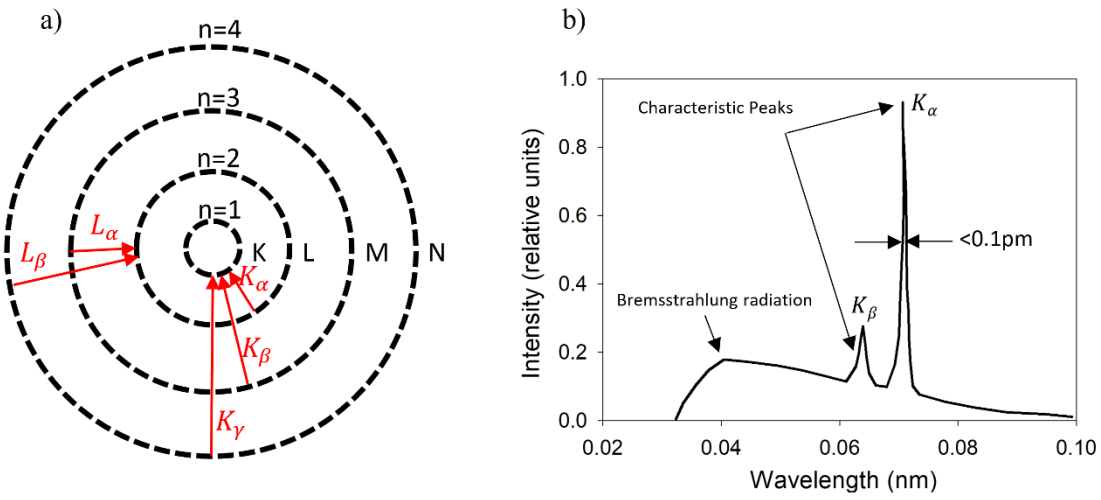

Figure 4.2 X-ray transition inside atom shell, the red arrow labels show the characteristic x-ray transition from the literature. b) An example of a molybdenum target x-ray spectrum, including both bremsstrahlung and characteristic radiation [4].

4.1.3 Design of diffractometer

In this work, a Bruker D8 Discover X-ray diffractometer was used, belonging to a triple-axis XRD system type. Compared with the double-axis model, the triple-axis XRD system has an extra analyser. The analyser constrains the detector so that only a 2-Theta angle is allowed to pass through it, furthering increase the resolution at the cost of a reduction in intensity.

The schematic diagram is shown in figure 4.3. The X-ray beam is generated by an X-ray tube where the electron is accelerated by a high voltage (typically 30kV in this work) towards the copper target. The slit is used to collimate the X-ray beam and so the X-ray intensity is determined by the slit size. With a higher intensity of X-ray hitting the sample, this comes at the expense of a decrease in angular resolution.

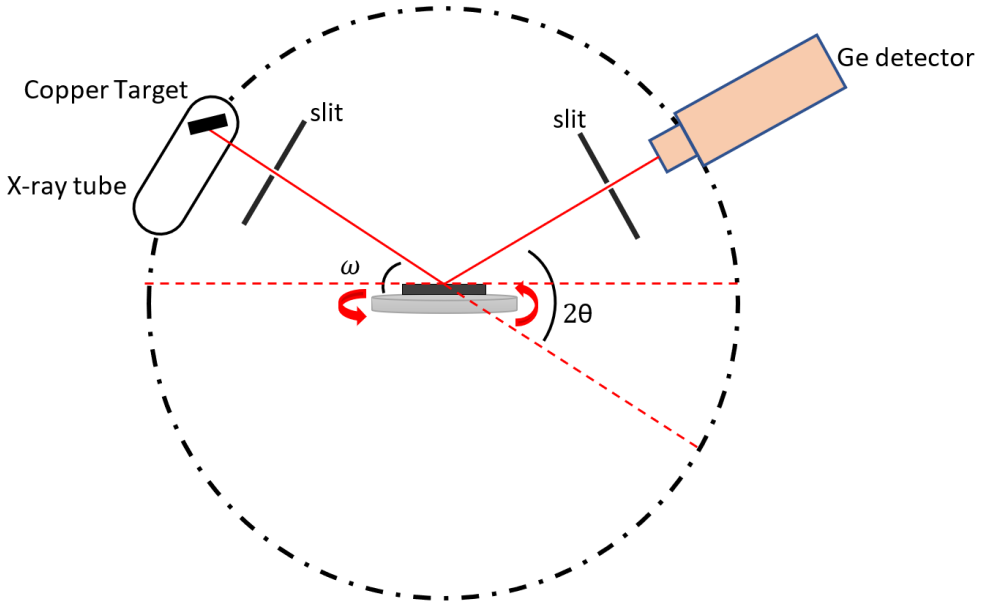

Figure 4.3 Schematic diagram of XRD measurement. The monochromator and analyser are not shown in this diagram for clarity.

The wafer is mounted on a porous ceramic vacuum chuck to secure the wafer when the stage tilts into a vertical direction during the test. Stepper motors are used to control the position of the stage, which not only moves in three-axis, but also can rotate in the angle of azimuth and altitude. The multidirectional range of motion allows users to optimise the wafer's position to obtain the highest X-ray intensity.

After diffraction by the wafer, the X-rays is collected by a germanium detector. The Bragg angle is not identical for different materials. Therefore, it is necessary to know the required Bragg angle of the material before measurement and set the parameters accordingly.

4.2 Nomarski microscopy

In the 1950s, George Nomarski first introduced the differential interference contrast (DIC) technology in microscopy [5]. As a rapid and useful optical imaging technique, the Nomarski microscope can be used to inspect the wafer surface after growth. A

schematic diagram including the basic components in a Normaski microscope is shown in figure 4.4.

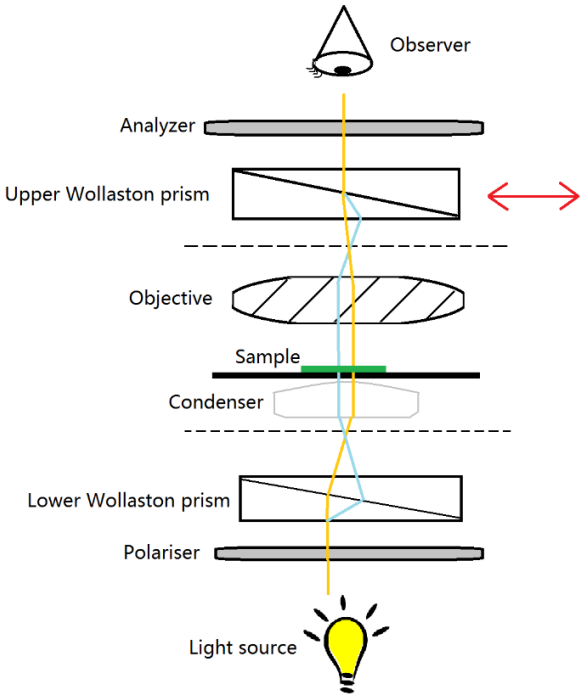

Figure 4.4 Basic components in a Nomarski microscope

The light is emitted from a hot-filament bulb then it will first be polarised at 45° after passing a polarising filter. The lower Wollaston prism split this individual light into two rays which polarised at 90° to each other. Therefore, these two rays won't interfere with each other. To prevent the appearance of double images, the distance between these two rays needs to separate by a very small distance, which is known as the "shear" distance (typically around 0.2μm). These two rays are focused by a condenser then pass through the sample at a slightly different position. If the position on the wafer is not ideal, the refractive index and thickness will be different compared with a smooth surface. This will result in a difference between the optical path length of the two rays. Subsequently, the two rays are focused again by an objective lens and then recombined by upper Wollaston prism. These two rays undergo constructive or destructive interference according to the optical path difference. Thus, the contrast of the image is enhanced.

As a preliminary inspection of the sample epilayer quality, Nomarski microscopy not only provides useful information about the surface condition of the epilayer such as

droplets and defects but also qualitatively verifies strain relaxation in the epilayer by the presence of the cross-hatching.

4.3 Photoluminescence (PL)

Photoluminescence spectroscopy is a sensitive and non-destructive optical technique that is used to characterise the bandgap and other optical properties of a semiconductor. The light absorbed in a semiconductor is affected by the energy levels of defects or localised states. In order to investigate these effects, the incident laser power and device temperature can be varied to provide further information on the semiconductor sample. Besides, PL can also be used as an indicator for the optical quality of the sample.

4.3.1 Radiative recombination

For the absorption of photons in a semiconductor to occur, the energy of the incident photon must be larger than the bandgap of the material.

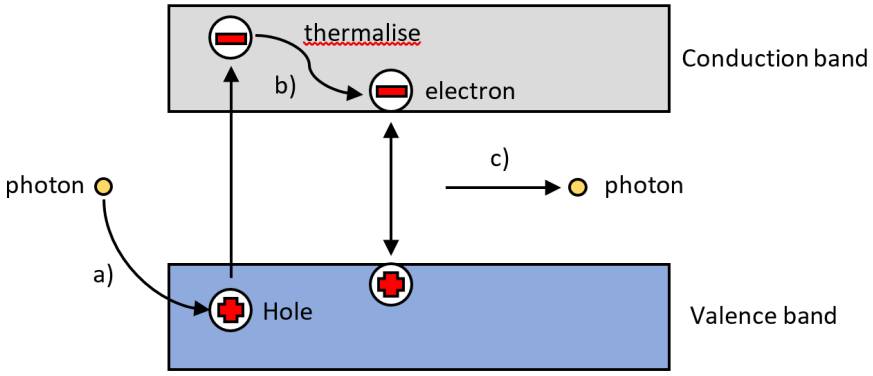

Figure 4.5 The processes involved in PL: a) incoming photon excites an electron from the valence band to the conduction band, leaving a hole in the valence band. b) Electron thermalises to the edge of the conduction band. c) After the recombination process between the electron and the hole, a photon is emitted with the same energy of material's bandgap.

When light shines on a semiconductor, assuming the energy of the light is greater than the energy of the bandgap, the photon will be absorbed which then promotes an electron from the valence band to the conduction band. Within the conduction band, the excess energy of the electron will be thermalised, and the electron will move to the conduction band edge before recombining with a hole from the valence band. A photon with the same energy as the material's bandgap will be emitted. This process usually only occurs in direct bandgap materials since indirect bandgap materials require phonons for recombination. Figure 4.5 shows the schematic diagram of the PL process.

4.3.2 Non-radiative recombination

Other than band to band recombination, non-radiative recombination is another essential form of the recombination process. This mechanism is generally caused by doping-induced defects, impurities and dislocations inside the forbidden energy gap of the semiconductor. A simplified diagram shows the two cases of these mechanisms in figure 4.6 and figure 4.7.

In figure 4.6, the recombination process happens via trap states within the forbidden energy gap of the semiconductor, which is known as Shockley Read-Hall recombination (SRH) [6]. In one case, electrons will move to the 'trap' state and then move into an empty state in the valence band to complete the recombination. The energy is exchanged within these trap states, inducing lattice vibration such as phonons. In another case, both electron and hole meet in the trap.

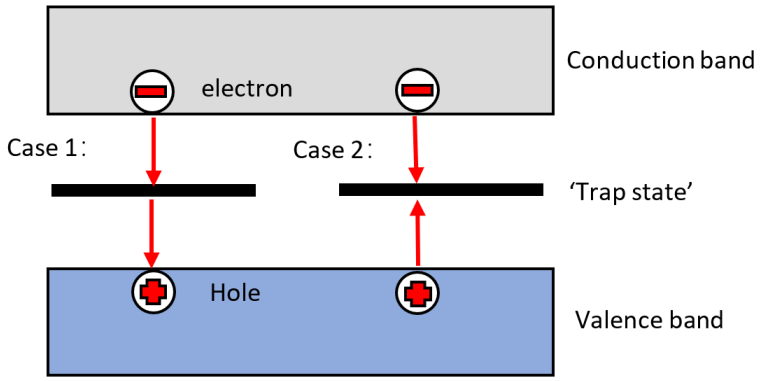

Figure 4.6 Shockley Read-Hall recombination via trap state in the band gap. Case 1: two steps transition of electron from conduction band to valence band. Case 2: Both electron and hole move to the trap state and then recombine.

Auger recombination is another non-radiative recombination. The process is similar to band-to-band recombination, but the energy is transferred to a third carrier instead of the emission of a photon.

Two primary Auger recombination processes are shown in figure 4.7, namely CHCC and CHSH Auger recombination, respectively. CHCC Auger recombination is a process in which an electron in the conduction band recombines with a hole in the heavy hole band where the released energy promotes another electron in the conduction band to a higher energy state. In CHSH Auger recombination, the first process is the same as in CHCC Auger recombination, however, the released energy will excite a hole in the

valence band into the spin-orbit split-off band. Energy and momentum are conserved in both type of Auger recombination process.

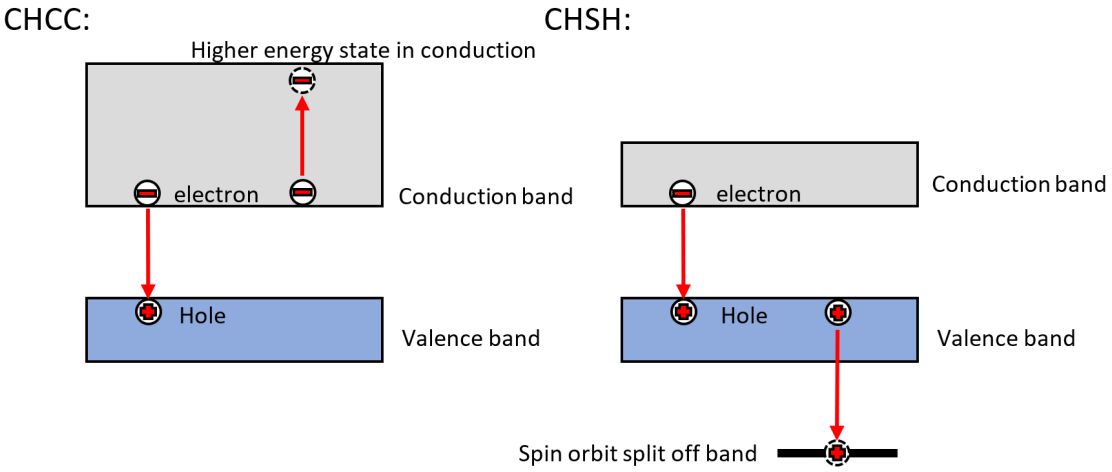

*Figure 4.7 Schematic illustration of a CHCC (**C**onduction band to **H**eavy hole valence band, **C**onduction band to higher energy state of **C**onduction band) and CHSH (**C**onduction band to **H**eavy hole valence band, **S**pin orbit spilt off band to **H**eavy hole valence band) Auger recombination process.*

4.3.3 Experimental setup

The PL setup used in this work consists of a 532nm laser, a chopper, a Jobin-Yvon Triax 550 monochromator, a liquid nitrogen cooled germanium detector and a Stanford Research SR830 lock-in amplifier (LIA).

In order for photon absorption, the energy of the laser beam needs to be larger than the bandgap of the semiconductor sample. As we are using a 532nm laser, the second order effect will happen resulting in an extra peak at the wavelength of 1064nm. Therefore, a long pass filter is used to attenuate background light, which restrain the second order effect. A Cassegrain telescope lens is used to collect and focus the emitted photons through the monochromator slit. A neutral density (ND) filter can be placed in front of the monochromator to attenuate the photon beam, ensuring that the detector will not be saturated. Three diffraction gratings covering a wide range of wavelength are used in the monochromator. In this work, the 900 grooves/mm grating corresponds to blaze wavelengths of 850nm is being used since the wavelength of interest is between 850 and 1400nm for GaAsBi. The germanium detector is used to collect the signal and the signal amplitude is displayed on the LIA. The laser light is chopped at 180 Hz to avoid interference from the ambient environment (The fluorescent light is operating by the mains, at 50 Hz). A schematic diagram of the setup is shown in figure 4.8.

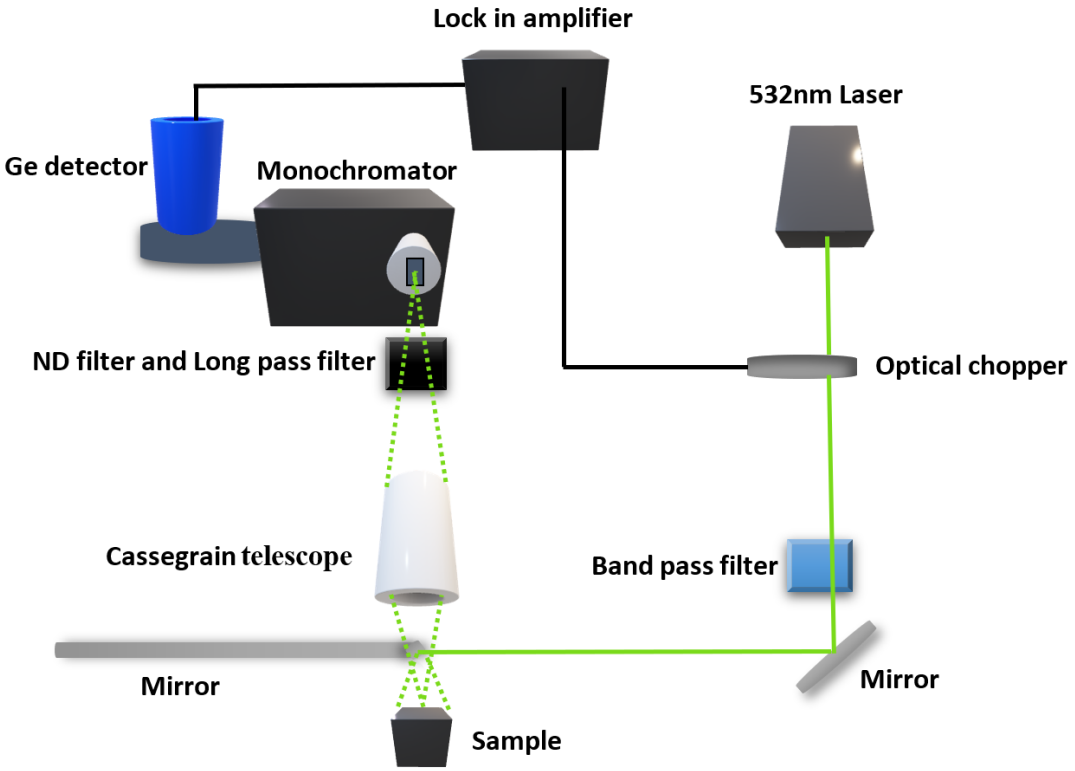

Figure 4.8 The photoluminescence setup used in this work

4.3.4 Monochromator

The model Triax 550 monochromator used in this work, it is a common Czerny–Turner design which consists of two slits, two mirrors and a grating. The principle is illustrated in figure 4.9.

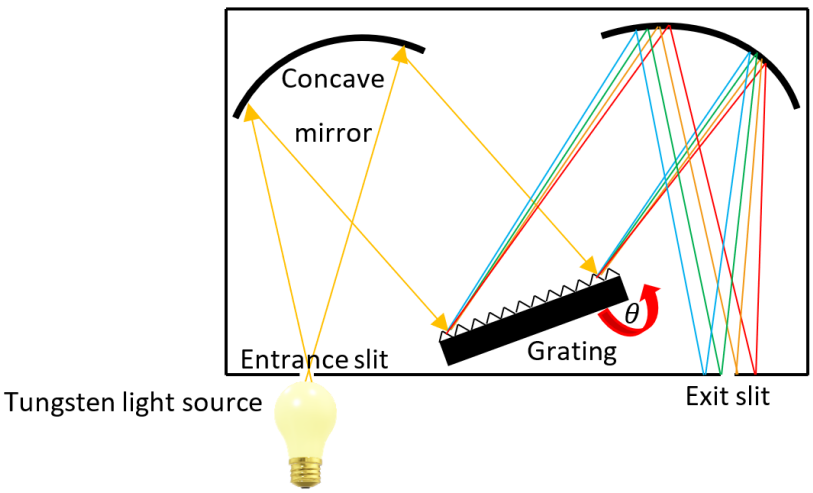

Figure 4.9 Schematic diagram of a Horiba iHR320 monochromator

A tungsten bulb used as the light source, which contains polychromatic light of many colours. The light passes through the entrance slit and hits a concave mirror whose function is to collimate the light and allow it to focus on the grating. The surface of the diffraction grating has a series of finely etched grooves with a periodic distance. The surface is also coated with highly reflective material to increase the reflectivity. Due to the constructive and destructive interference, this polychromatic light that refracted by the grating is no longer parallel, instead of which each wavelength of light is refracted at a different angle. The second concave mirror is used to focus light before it passes out of the exit slit. The angle of the grating θ determines the wavelength of light. Only one selected wavelength can pass through the exit slit, and all other wavelengths will strike the inside wall of the monochromator and be absorbed. Therefore, the internal wall of the monochromator is painted black.

In order to obtain maximum throughput for a selected wavelength range, a proper type of grating needs to be considered. In our setup, three gratings, which classified by its groove per unit of length with specified blaze wavelength, are installed inside the monochromator. For our lab grown GaAsBi material, the cut-off wavelength is around 1300nm. Therefore 600 grooves/mm grating with blaze wavelength at 1000nm was used. The usable wavelength of this grating is based on the $(\frac{2}{3} \times \lambda_{blaze}, \frac{3}{2} \times \lambda_{blaze})$ rules, which is between 667nm and 1500nm.

4.4 Current-voltage (IV) measurement

After the device fabrication, the first measurement is to record the current-voltage characteristic of the device. In order to implement this measurement, a bias is applied across the diode, resulting in current feedback. Most of the time, the I-V measurement can be regarded as a preliminary tool that used to evaluate whether diode fits a reasonable diode characteristic curve.

The schematic diagram of the I-V setup is shown in figure 4.10. In which the device under the test (DUT) is in series connection with either a HP4140B picoammeter or a curve tracer. The curve tracer is used to manually check the connection of the diode and to give a hint to locate the breakdown voltage of the diode. As an alternative, the Keithley 236/237 source-measure unit (SMU) can replace the picoammeter. In general, I-V measurements are performed under dark conditions.

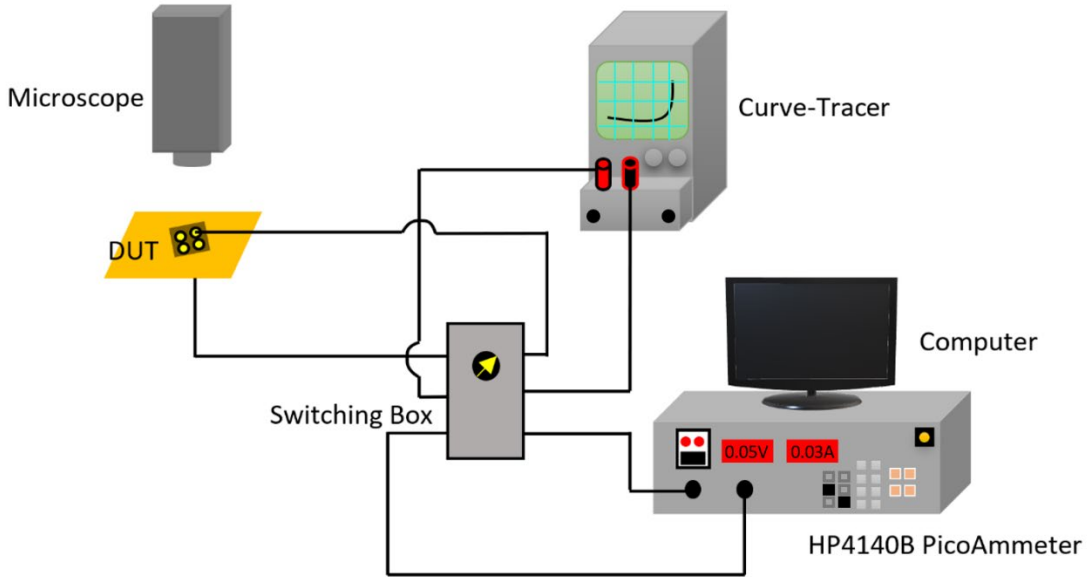

Figure 4.10 Schematic diagram of the I-V measurement setup

Dark current, as its name implies, is the current measured under no incident illumination no matter forward or reverse. A typical photodiode's dark current is determined by material and the size of the active area. Apart from that, the dark current is sensitive to the temperature, which approximately doubles for every 10°C increase. The dark current follows the Shockley diode equation [7], which is given by:

$$J = J_0[\exp(\frac{qV}{n_0 kT}) - 1] \tag{4.2}$$

where J_0 is the saturation current density, q is the electron charge, k is the Boltzmann constant, T is the temperature, n_0 is the ideality factor, representing how closely the diode follows the ideal case, whose value varies between 1 and 2. The value one represents that the current is dominated by diffusion mechanism while value two represents that the current is dominated by generation-recombination mechanism. Under forward bias, the effect of series resistance will need to be considered as the current reach to a high value, therefore, a series resistance parameter R will be added into the equation,

$$J = J_0[\exp(\frac{qV - JR}{n_0 kT}) - 1] \tag{4.3}$$

The contact resistance between metal and semiconductor contributes to the series resistance. The high series resistance will limit the maximum achievable gain in an

APD. Metal contacts with an appropriate work function and annealing is needed to minimise the series resistance.

The reverse bias I-V is one of the most important parameters to evaluate the performance of an APD. There are two reasons for this. Firstly, the avalanche breakdown happens when the reverse bias near the breakdown voltage. Secondly, from the reverse I-V result, we can get the leakage current, which is related to the signal to noise ratio (SNR) of the APD. The total dark current consists of the bulk current, I_{bulk} and the surface current, I_{surf}. Therefore, the contribution of these two components can be determined by measuring the current scaled to the bulk and surface area, A_{bulk} and A_{surf} respectively. This is given as:

$$J_{Total} = \frac{I_{bulk}}{A_{bulk}} + \frac{I_{surf}}{A_{surf}} \tag{4.4}$$

The surface current is an unwanted current that originates from surface defects due to etching. In order to minimise the surface current, passivation is required after the etching process to terminate the surface dangling bonds. In reverse bias, the potential barrier increases in the depletion region and the p-n junction becomes wider. The flow of majority carriers is impeded by the potential barrier and current flow is contributed to by the thermally generated minority carriers. Because the number of minority carrier is much less than the majority carrier, the magnitude of this reverse leakage current will be very low. The Shockley-Read-Hall generation-recombination current is another important mechanism that makes the measured I-V characteristics deviate from the ideal case [8]. Usually, this mechanism takes place due to the recombination-generation centres or trap states inside the forbidden gap and is given by

$$J_{SRH} = \frac{qn_i w}{2\tau_{eff}}[\exp(-\frac{qV}{2k_b T})] \tag{4.5}$$

where q is the electron charge, w is the depletion width and τ_{eff} is the effective carrier generation rate. When the reverse bias is sufficiently high, the width of the depletion region becomes very thin, and the electrons have a probability to tunnel through the potential barrier from the valence band to the conduction band, forming a band-to-band tunnel current. Considering that the work here is by using the wider bandgap material, the tunnelling current is negligibly small. Therefore, the tunnelling current is not discussed further in this work.

4.5 Capacitance-voltage (CV) measurement

A Hewlett-Packard 4275A multi-frequency LCR meter is used for room temperature capacitance-voltage (C-V) measurements. In the circuit diagram, a DC voltage that supplies bias onto the DUT superimposes an AC voltage. The AC signal can be used to provide the impedance and phase angle. The amplitude of the AC signal needs to be small compared with the given DC voltage. Impedance consists of resistance and reactance in the form of a real part and an imaginary part, respectively. The reactance of a capacitance can be expressed as $1/jwC$ which is related to the frequency. For accurate C-V measurements, an appropriate frequency of the AC signal should be chosen depending on the value of capacitance under the measured device. In this work, the value of capacitance is generally in the pico-Farad range, which results in a small AC signal that is difficult to detect. Therefore, in order to obtain a measured signal a high frequency is required to make the reactance part of the AC signal as small as possible. In this CV testing 1MHz is used as the test frequency.

Two models were chosen to measure the impedance in LCR meter, either series or parallel model. Figure 4.11 shows the equivalent circuits of these two models and the guideline of a function as the value of capacitance and test frequency. In the series model, when the reactance is small, a larger AC signal will pass through the circuit. This will make the series model the model of choice. Conversely, if the reactance is large, the parallel model would be better. In this work, the parallel model was adopted because of the low value of capacitance for our device.

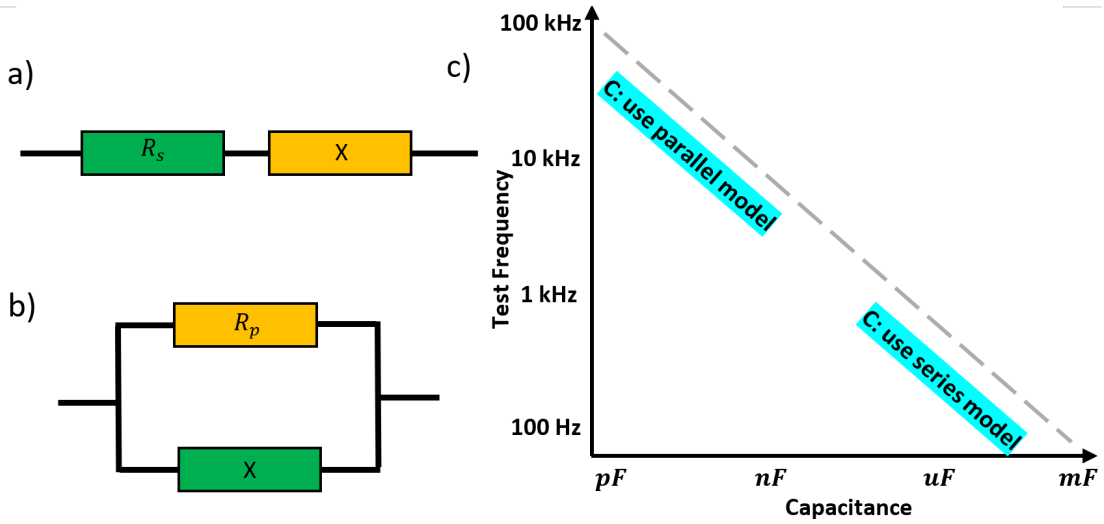

Figure 4.11 a) Equivalent circuit for series model b) Equivalent circuit for parallel model. R_s is the series resistance, R_p is the parallel resistance, and x is the reactance c) Measurement guidelines for capacitance in normal LCR meter.

The quality factor (Q factor) is used to evaluate the performance of a capacitor. It is the ratio between reactance and resistance as shown in below equation:

$$Q = \tan\theta = \frac{|X_C|}{R_C} = \frac{1}{w_o C R_C} \tag{4.6}$$

where θ is the phase angle between current and voltage, X_c is the reactance of the capacitance, and R_c is the series resistance of the capacitance. In an AC system, the Q factor represents a ratio between the energy stored in capacitor and energy dissipated in the form of heat due to the equivalent series resistance. For an ideal capacitor, the Q factor is an infinite value because there is no energy loss in the capacitor. The phase angle is 90°, which is in agreement with phase difference of 90° between current and voltage for a typical capacitor. In this thesis, the CV measurements were taken at room temperature, and the phase angle was recorded in a range between 80° and 90°. As with IV measurements, the bulk properties of the junction capacitance can be verified by measuring whether the properties scale with the device area.

Two common errors in CV measurements are the offset error and the gain error. Figure 4.12 shows an example of these two errors plotted on a log scale. The x-axis represents the actual value of the capacitance, and the y-axis represents the measured value of the capacitance. If in the ideal case, the measurement system is perfect, the results will be the same as a straight line plotted at 45°, which is the black line shown in the graph. In reality, gain and offset errors always need to be taken into account in the measurement

and need to be corrected. Parasitic capacitances in the probe and cable cause the offset error during the measurement. In order to minimise the offset error, the best way is by pressing the open-correction (for small capacitance at 10pF range) or the short-correction (for large capacitance at 10nF range) buttons before probing the device. Gain error changes depend on the amount of capacitance being measured and can be corrected by a load correction**.** In order to achieve the load correction, a known standard load needs to be used to measure and then the ratio between the measured value and actual value is calculated. However, in the load correction, there is one limitation that the selected load needs to have a similar range to the device to be measured.

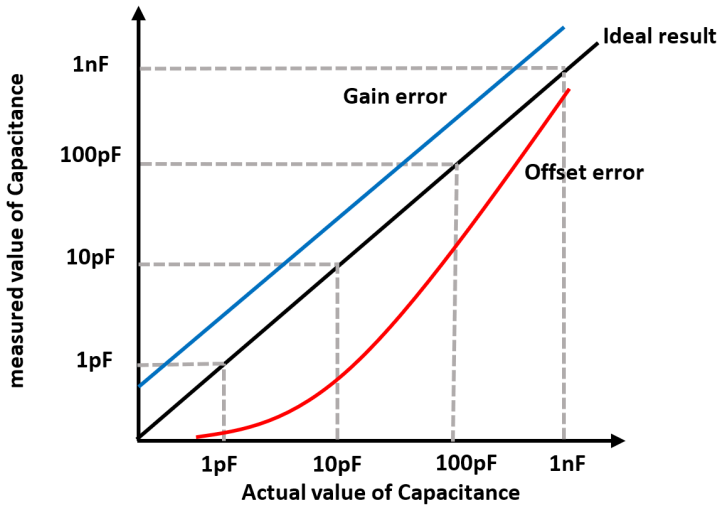

Figure 4.12 Common errors in a capacitance measurement, the ideal result is shown by black line, the offset error is shown by the red line, and the gain error is shown by the blue line. adapted from [9]

C-V measurement is used to show the results of the i-region thickness and doping density for the DUT. In this work, the device structure is p-i-n or n-i-p, i is the intrinsic layer, but in reality, the doping concentration in intrinsic layer can't be zero, and p or n is the highly doped layers. In a typical C-V graph, the capacitance will fall rapidly as the reverse bias increases to a few Volts. As the bias voltage increases, the rate of change of capacitance per unit voltage starts to gradually decrease because the intrinsic region is nearly fully depleted. Eventually, the space charge enters the n or p region, and the rate will hardly change due to the high doping concentration in the n or p region. Therefore, at this point, the depletion width is approximately equal to the i-region thickness of the DUT. The relationship between capacitance and depletion width is shown in Equation 4.7.

$$C = \frac{\varepsilon_o \varepsilon_r A}{W} \tag{4.7}$$

Where ε_o is the vacuum permittivity, ε_r is the material permittivity, A is the area of device and W is the thickness of the depletion region.

For a standard PIN device structure, the P-I region and the N-I region can be regarded as two abrupt junctions because of the vast carrier concentration difference. Therefore, the equation of capacitance also can be given by equation 4.8,

$$C = \frac{\varepsilon_o \varepsilon_r A}{W} = \sqrt{\frac{q\varepsilon_o \varepsilon_r N_b}{2(V_{bi} - V)}} \times A \tag{4.8}$$

Where q is the electron charge, N_b is the doping concentration of the lightly doped material, V is the applied bias voltage and V_{bi} is the built-in voltage of the device.

The built-in voltage can be obtained be rearranging equation 4.8 to form equation 4.9.

$$\frac{1}{C^2} = \frac{2(V_{bi} - V)}{q\varepsilon_o \varepsilon_r N_b A^2} \tag{4.9}$$

From equation 4.8, plotting $1/C^2$ and V can get a straight line whose slope is equal to $2/q\varepsilon_o \varepsilon_r N_b A^2$. The built-in voltage can be obtained by extrapolating the straight line and taking the x-intercept where the $1/C^2$ term is equal to 0.

The doping concentration of the lightly doped region (intrinsic region) is obtained by differentiating equation 4.9 and then rearranging to find equation 4.10 [10].

$$N_b = -\frac{2}{q\varepsilon_o \varepsilon_r A^2} \left(\frac{dV}{d\left[\frac{1}{C^2}\right]} \right) \tag{4.10}$$

In order to get an accurate value of the thickness of the intrinsic region and the doping concentration on the cladding layer, Poisson's equation can be used to fit the experimental data. Further details of the CV modelling will be given in **Appendix I**.

4.6 Photomultiplication

As mentioned in section 2.7, the electron and hole ionisation coefficients of a material can be obtained from gain measurements. The experimental setup of the gain measurements is shown in figure 4.13. In the setup, the laser acts as the light source. A monochromator is not used because the laser light is already monochromatic.

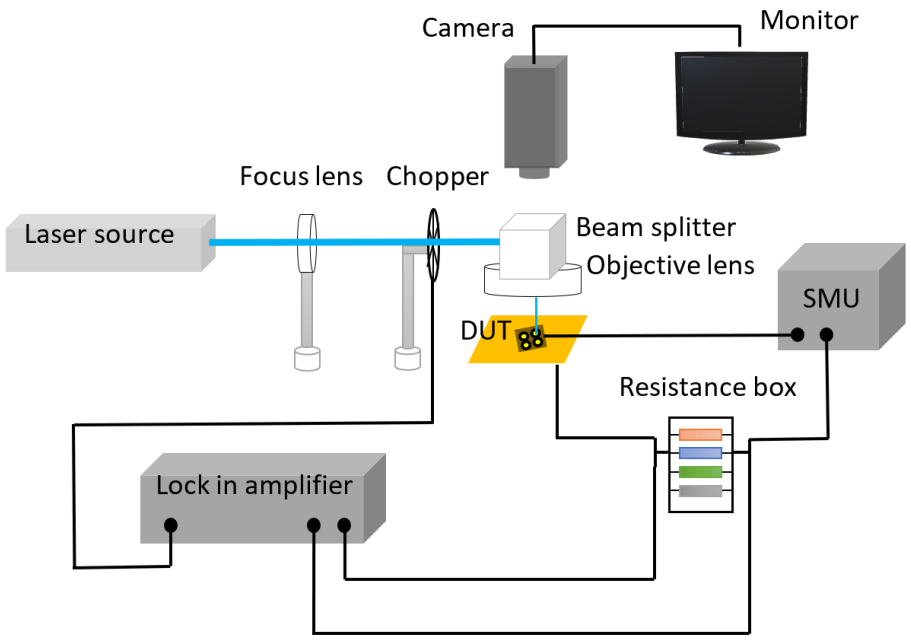

Figure 4.13 Schematic diagram of the multiplication setup used to measure photocurrent versus reverse bias, different wavelength lasers can be used.

After passing through the focus lens, the laser light was focused to a tiny spot on the sample. An optical chopper was used to modulate the signal with the frequency of 180 Hz, and a Keithley 236/237 source-measure unit (SMU) was used to provide the reverse bias voltage. Due to the high leakage current of the device, the photocurrent needs to be recorded by a lock-in amplifier (LIA) that series connects to a resistance box. Further details of LIA will be given in **Appendix II**. The high leakage current of devices significantly affects the multiplication measurement, especially at high voltage biases due to the voltage drop across the resistor. This causes the voltage across the device to be less than the applied bias. In order to minimise this effect, an appropriate resistor value must be chosen to ensure that the voltage drop on the resistance is less than 0.1 volts. The multiplication result is independent of the optical power of the laser. In order to make sure no heating effects are caused by the varying laser power, a variable neutral

density filter can be used to carry out the power-dependent measurements. Besides, the measurement on each size of devices needs to be repeated at least three times to ensure the gain uniformity. In the fabrication, the device etching is not uniform. For the purpose of checking whether this will affect the multiplication results, the measurement was repeated with focusing the laser spot onto different position across the device.

The avalanche gain in multiplication measurements is given in equation 4.11:

$$M(V) = \frac{I_{ph}(V)}{I_{pr}} \tag{4.11}$$

Where $M(V)$ is the avalanche gain as a function of reverse bias, $I_{ph}(V)$ is the total current, which consists of both impact-ionisation-enhanced current and light-produced initiating current. The light-produced initiating current is also named primary current, which is defined as I_{pr}.

It is well known that the photocurrent can increase with reverse bias due to the expansion of the depletion region. Woods et al. [11] proposed a method to approximate the photocurrent before the onset of multiplication by solving the current diffusion equation, the expression for an abrupt *p-n* junction is given by

$$I_{pr} = \frac{qG_0}{\cosh(L / L_{diff})} \tag{4.12}$$

Where G_0 is the generation rate per unit area of hole-electron pairs at the cladding layer, L is the distance between the edge of the depletion region and the sample surface. L_{diff} is the minority carrier diffusion length. The Equation 4.12 is also suitable for the *p-i-n* structure assuming the light is strongly absorbed in a small distance of the cladding layer. If $L_{diff} >> L$ and there is a linear increase of the depletion region entering the cladding layer with reverse bias voltage, then Equation 4.12 can be simplified to

$$I_{pr} = aV_b + b, \tag{4.13}$$

where *a* and *b* are constants. For the devices analysed in this thesis, the variation in the photocurrent prior to avalanche multiplication is small since the light is absorbed by the heavily doped cladding layers. Therefore, the primary current of the devices was fitted with Equation 4.13. The purpose of this is to correct for the increase in collection efficiency of injected carriers with bias. Figure 4.14 (left) gives an example of the

primary photocurrent fit using the equation 4.13 and figure 4.14 (right) is the gain results obtained using equation 4.11.

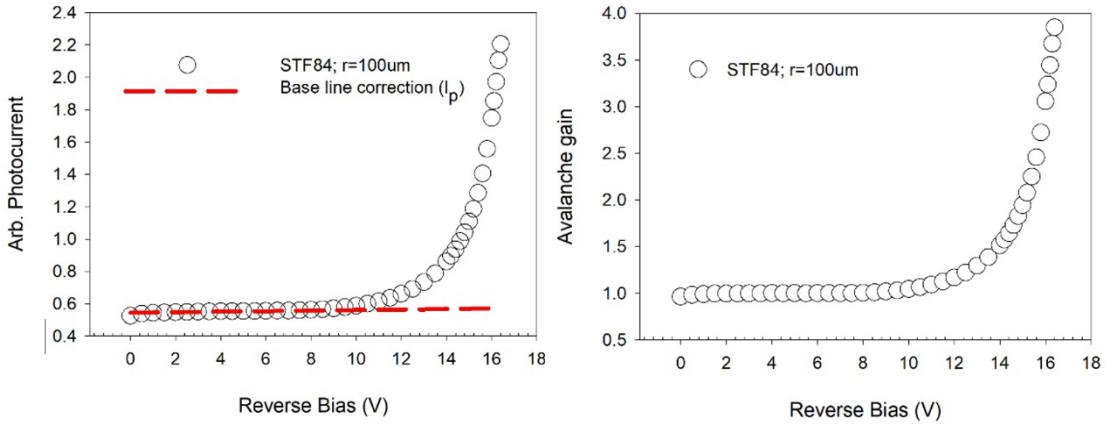

Figure 4.14 An example of base line correction (left) to calculate gain (right) in GaAsBi 400nm p-i-n diode.

In order to determine both M_h and M_e, Stillman and Wolfe proposed several experimental details to follow [12]. Firstly, pure electron and pure hole injection must be measured in the same junction, in this work, a set of p-i-n and n-i-p structures with the same thickness of the intrinsic region and doping concentration will be used. In order to satisfy pure injection conditions, an appropriate laser wavelength was chosen depending on the material and thickness of the cap layer. Pure injection is obtained when over 80% of the incoming light is absorbed in the cap layer. Secondly, the photocurrent before the onset of multiplication must be measured precisely to find an accurate primary photocurrent. Thirdly, the electric field across the intrinsic region must be sufficiently gradual. Therefore, assuming the α and β only related to the electric field in the intrinsic region. This can be achieved by having a high doping concentration in the P and N regions in the structure. Fourthly, the electric field profile of the device must be accurately known. Fitting the C-V data can provide the details of the electric field profile to evaluate if the electric field across the intrinsic region is straight or tapered. Finally, the avalanche gain must be uniform across the device. As mentioned before, this can be verified by testing the multiplication at different positions across the device.

4.7 Reference

[1] D. K. Bowen and B. K. Tanner, *High Resolution X-Ray Diffractometry And Topography*. CRC Press, 1998.

[2] M. Eckert, 'Max von Laue and the discovery of X-ray diffraction in 1912', *Ann. Phys.*, vol. 524, no. 5, pp. A83–A85, May 2012, doi: 10.1002/andp.201200724.

[3] 'The reflection of X-rays by crystals', p. 11.

[4] Gymnos, 'Modern Physics: Mastering Physics: Bremsstrahlung Radiation Conceptual Question', *Modern Physics*, Feb. 13, 2011. http://aeroja.blogspot.com/2011/02/mastering-physics-bremsstrahlung.html (accessed Sep. 30, 2020).

[5] M. Pluta, 'Nomarski's DIC microscopy: a review', Warsaw, Poland, May 1994, pp. 10–25, doi: 10.1117/12.171873.

[6] W. Shockley and W. T. Read, 'Statistics of the Recombinations of Holes and Electrons', *Phys. Rev.*, vol. 87, no. 5, pp. 835–842, Sep. 1952, doi: 10.1103/PhysRev.87.835.

[7] W. Shockley, 'The theory of p-n junctions in semiconductors and p-n junction transistors', *Bell Syst. Tech. J.*, vol. 28, no. 3, pp. 435–489, Jul. 1949, doi: 10.1002/j.1538-7305.1949.tb03645.x.

[8] B. T. Marozas, W. D. Hughes, X. Du, D. E. Sidor, G. R. Savich, and G. W. Wicks, 'Surface dark current mechanisms in III-V infrared photodetectors [Invited]', *Opt. Mater. Express*, vol. 8, no. 6, p. 1419, Jun. 2018, doi: 10.1364/OME.8.001419.

[9] L. Stauffer and K. Instruments, 'C-V Measurement Tips, Tricks, and Traps', p. 14.

[10] S. M. Sze and K. K. Ng, *Physics of Semiconductor Devices*. John Wiley & Sons, 2006.

[11] M. H. Woods, W. C. Johnson, and M. A. Lampert, 'Use of a Schottky barrier to measure impact ionization coefficients in semiconductors', *Solid-State Electron.*, vol. 16, no. 3, pp. 381–394, Mar. 1973, doi: 10.1016/0038-1101(73)90013-0.

[12] W. T. Tsang, *Semiconductors and Semimetals: Lightware Communications Technology v. 22A*. Orlando: Academic Press Inc, 1985.

Chapter 5: The electrical and optical characterisation of GaAsBi bulk samples

5.1 Introduction

In this chapter, detailed studies about the optical and electrical characteristics of bulk GaAsBi diodes will be described. Four sets of p-i-n or n-i-p structures with nominal i-region thicknesses of 0.1, 0.2, 0.4, 0.8 and 1.6 μm were grown using the Omicron STM-MBE system. The composition of these bulk GaAsBi wafers were investigated via optical techniques such as Nomarski microscopy, X-ray diffraction and photoluminescence. The strain and relaxation properties of each wafer will be discussed. After device fabrication, the electrical characteristics of the devices were tested using current-voltage and capacitance-voltage measurements. A dark current model with the diffusion and generation-recombination current is used to fit the measured dark current to investigate the dominant dark current mechanism. The ideality factor of devices will be also discussed and is compared with published results. The doping density and i-region thicknesses are obtained from the CV measurements. In addition, the Bi content calculated from XRD and PL will be compared and discussed, analysing the uncertainty and relationship between these two techniques.

5.2 Wafer growth

Four sets of wafers have been grown and are described in detail in Table 5.1. The first set of samples named STD5 were grown by Danuta F Mendes in 2013. The samples were p-i-n structure with 600 nm n-doped GaAs buffer layer and 1 μm p-doped GaAs cap layer, both of which were grown at around 580 °C using As_2. The intrinsic GaAsBi layer was grown at around 375 °C with a nominal thickness of 400nm using As_4. The growth rate was between 0.45 and 0.55 ML/s, calculated from RHEED oscillation. The sample structure is shown in Figure 5.1. An interrupt technique was used for the growth of the GaAsBi intrinsic layer [1]. This is performed by growing an inverted quantum well structure (GaAsBi/GaAs/GaAsBi) such that a thin layer of GaAs was sandwiched between GaAsBi layers in order to avoid excess Bi segregation on the surface and the formation of Bi droplets.

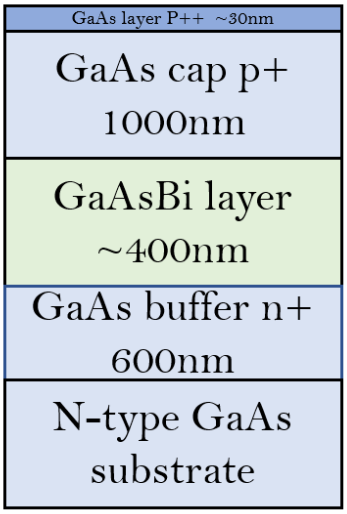

Figure 5.1 Device structure of STD5 p-i-n bulk GaAsBi

The second and third set of samples named STF8, STFA were grown by Thomas Rockett and Zhize Zhou respectively in 2015. Both the STF8 and STFA series have two GaAs control samples in which the i-region thicknesses were 200 and 1600 nm, respectively. The diodes structure and thicknesses of each layer are shown in Figure 5.2. Both p-i-n and n-i-p structures include 350 nm of buffer layer and 450 nm of cap layer, grown at 580°C with As_2. For the GaAs buffer and cap layer growth, the As:Ga atomic flux ratio was 1.5 and 1.45 for p-i-n and n-i-p structure, respectively. The GaAsBi intrinsic layer was grown at 375 °C for all the STF8 samples using As_4 at a growth rate of 0.6 ML/s. In order to facilitate a good Ohmic contact formation, a highly doped thin GaAs buffer (~30nm) was grown on the top of the cap layer. For the STFA series samples, the growth rate was around 0.41 ML/s, and growth temperature was around 360 °C. Despite growing at nominally different temperatures, similar levels of Bi are present in both STF8 and STFA series. The GaAs control samples has the same structure as the p-i-n and n-i-p devices. The only differences being the intrinsic layer is composed of GaAs which was grown at the same temperature as the cap and buffer layer (580 °C). The As:Ga atomic flux ratio used for the GaAs control sample was 1.6.

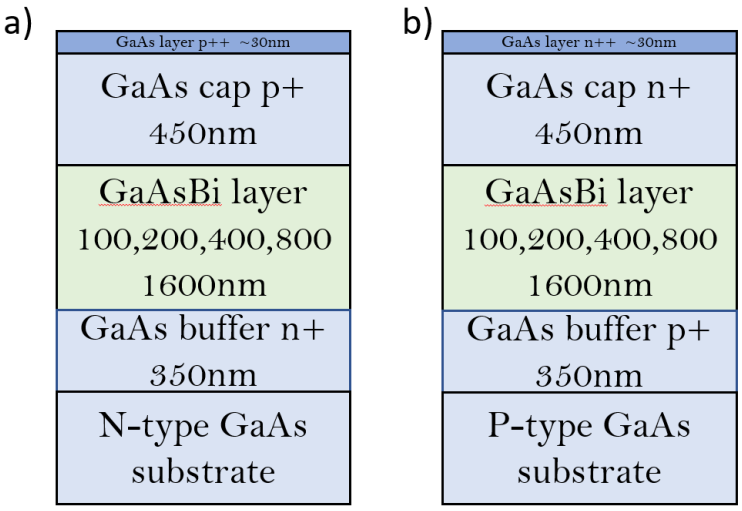

Figure 5.2 Sample structure of STF8, STFA, a) STF8 is p-i-n structure and b) STFA is n-i-p structure.

STJ4 series is the final set of samples, which consists of n-i-p diodes grown by Yuchen Liu and Nick Bailey in July 2019 on GaAs (001) p+ substrates to investigate how the hole ionisation coefficient in GaAsBi varies with the Bi content. The structure, as shown in Figure 5.3, is similar to that of the STFA series. A 400 nm intrinsic region width is chosen to avoid dead space effects when analysing the impact ionisation coefficients. The nominal temperature used for the intrinsic layer growth is 380 °C at a growth rate of 0.297 ML/s. The Bi flux was adjusted to vary the Bi content present in the samples.

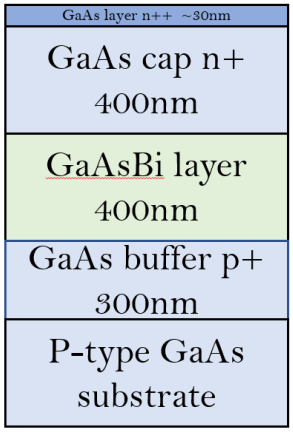

Figure 5.3 Device structure of for STJ4 bulk GaAsBi n-i-p structure diodes

Diode type	Layer No.	Nominal i-region thickness(μm)
p – i – n	STF85	0.1
	STF81	0.2
	STF84	0.4
	STF83	0.8
	STF82	1.6
	STF86(C)	0.2
	STF87(C)	1.6
	STD53	0.4
	STD56	0.4
n – i – p	STFA7	0.1
	STFAD	0.2
	STFAE	0.4
	STFAB	0.8
	STFAC	1.6
	STFAG	0.2
	STFAJ(C)	0.2
	STFAI(C)	1.6
	STJ4A	0.4
	STJ4G	0.4
	STJ4I	0.4

Table 5.1 Brief information of STD5, STF8, STFA and STJ4 series

**(C) means the GaAs control sample*

5.3 Optical Characterisation

5.3.1 Nomarski microscopy image

Nomarski microscopy can be used to observe surface characteristics such as strain relaxation or surface defect. This is eesential as GaAsBi cannot be lattice matched to the GaAs substrate and the sample grows ticker as Bi is being incorporated into the GaAs. Figure 5.4-5.9 shows representative Nomarski images of several samples. The images were taken in the centre of each sample at 50 times magnification.

From Figure 5.4 to 5.7, there is a clear trend where the surface morphology deteriorates with increasing Bi content. Due to low Bi incorporation in STJ4A and STJ4G, there are no obvious orthogonal crosshatch lines in both Figure 5.4 and 5.5. This suggests that there is no strain relaxation on both of samples. As the Bi content increases, clear crosshatch line appears as in Figure 5.6 and 5.7, illustrating the emergence of strain relaxation. It is also observed that 400 nm is sufficient to exceed the critical thickness at a Bi content of 1.7% because the surface starts to show the cross-hatching pattern.

Aside from STJ4A, "oval" defects that may be attributed to Ga-Ga droplets or Bi-Bi droplets are seen on most samples with i-layer thicknesses above 400 nm. The worst surface morphology for 400 nm sample is shown in Figure 5.5, in which the rough pattern covers the whole background surface. It is unlikely that overaggressive cleaning of the substrate causes the roughness of the surface. This is because scratch lines across the surface are not evident. The most likely cause is that the oxide layer of the substrate is not being fully removed.

Figure 5.4 Nomarski image of STJ4A 400nm GaAsBi n-i-p (>0.1% Bi) at 50× magnification

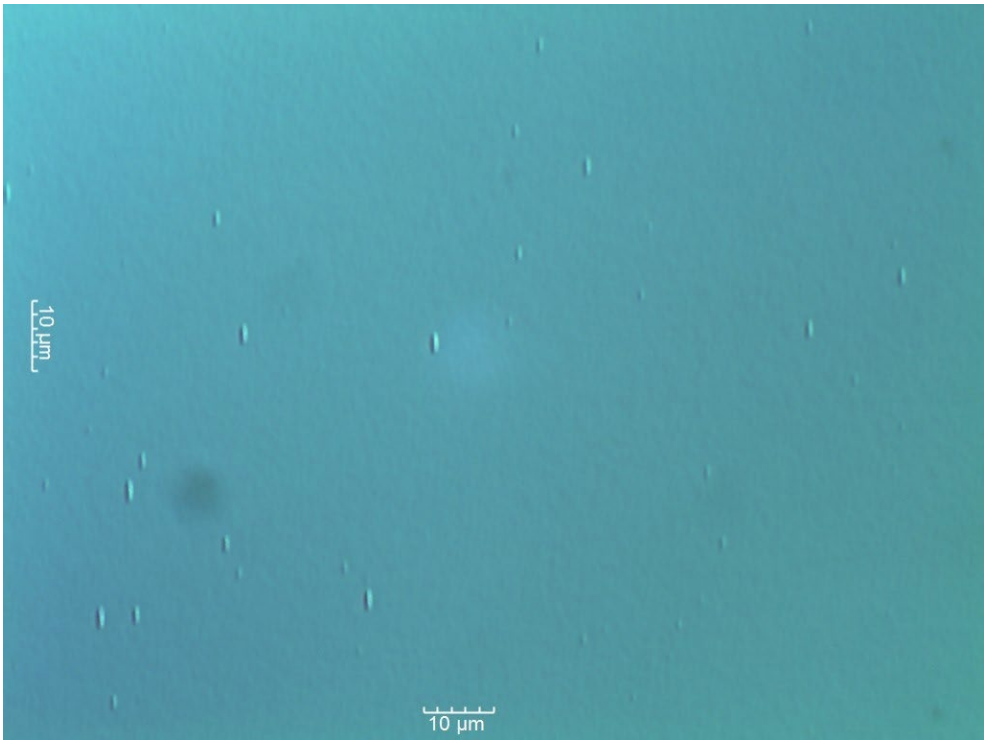

Figure 5.5 Nomarski image of STJ4G 400nm GaAsBi n-i-p (~0.65% Bi) at 50× magnification

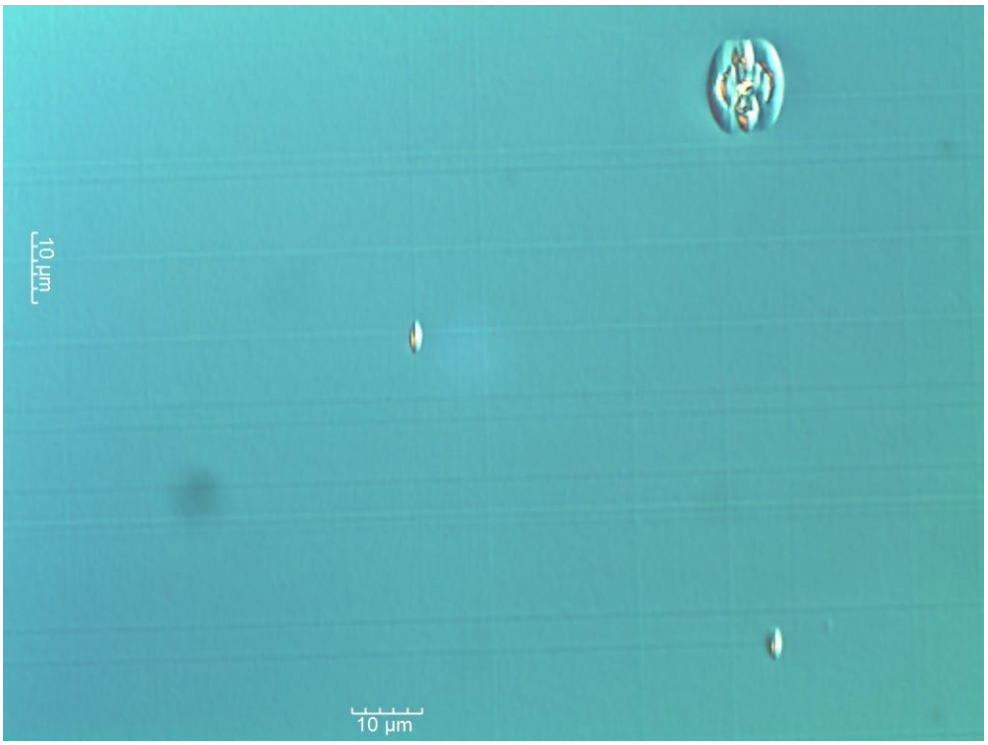

Figure 5.6 Nomarski image of STJ4I 400nm GaAsBi n-i-p (~1.7% Bi) at 50× magnification

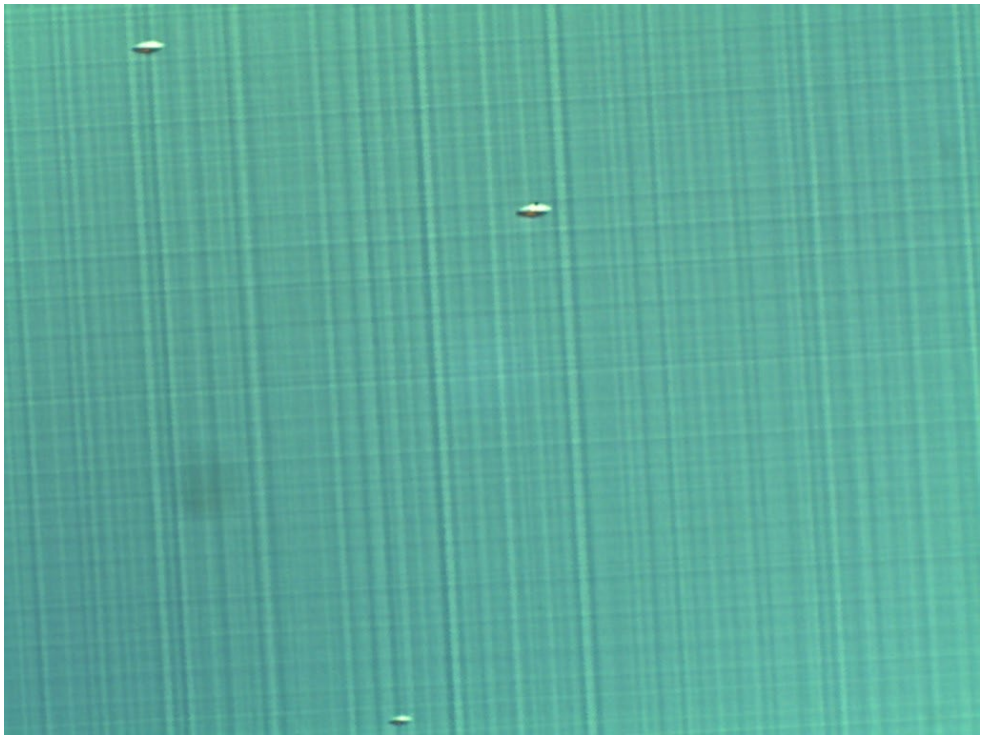

Figure 5.7 Nomarski image of STFAE 400nm GaAsBi n-i-p (~3.5% Bi) at 50× magnification

Figure 5.8 and 5.9 show Nomarski images of 1.6 µm GaAs and GaAsBi (3.7%) n-i-p structure. Even though the 1.6 µm GaAs sample is optically smooth, there are small clumps of Ga-Bi droplet on the surface. The crosshatch pattern arising from stress relaxation is shown in 1.6 µm GaAsBi n-i-p sample. Besides, it also contains a high density of coffee bean shaped defects that may be attributed to the incorrect growth temperature and slow growth rate, which results in Bi segregating on the sample surface during the growth.

Figure 5.8 Nomarski image of STJAI 1.600nm GaAs n-i-p sample at 50× magnification

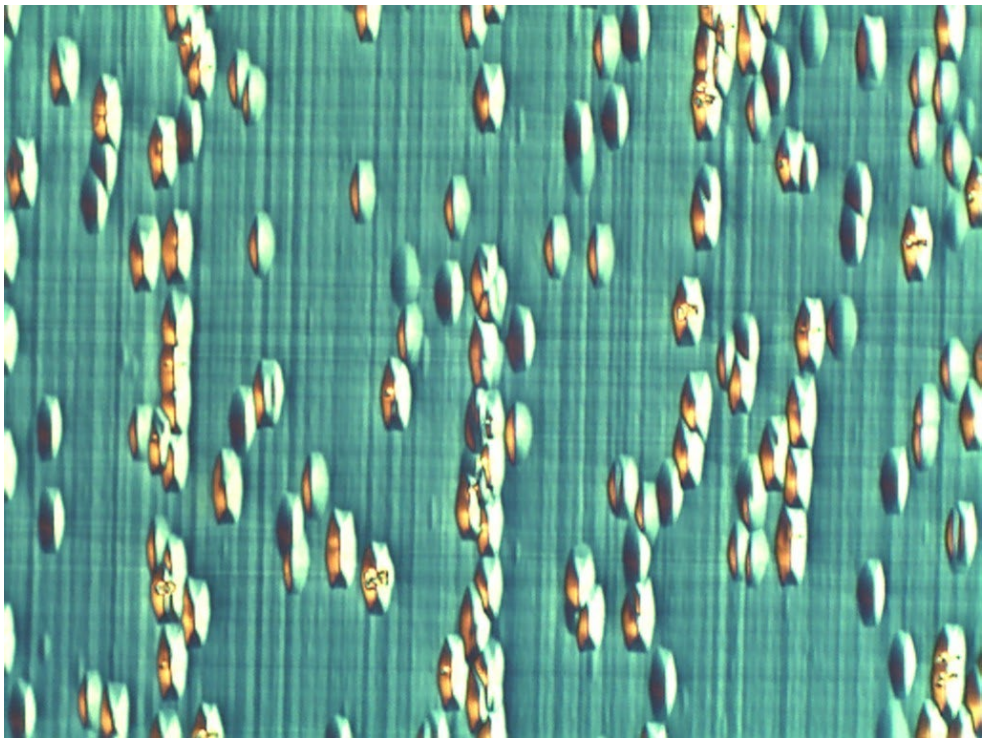

Figure 5.9 Nomarski image of STFAC 1.600nm GaAsBi n-i-p (~3.7% Bi) at 50× magnification

5.3.2 X-ray diffraction results

As a non-destructive technique, XRD can provide an analysis of the layer thickness and composition of samples to identify the structural characteristics of the epitaxial layers and to optimise the growth conditions. The basic principle of XRD has been mentioned in section 3.1. In the last three decades, different research groups investigated the XRD properties of bulk GaAsBi. XRD studies mainly focused on how to grow high-quality samples through constant changes in growth temperature and flux rate as well as attempts to grow on GaAs substrates in different orientations. Annealing effects based on different growth conditions have also been investigated. A few representative XRD results of bulk GaAsBi from literature were shown in figure 5.10.

In 2003, the GaAsBi material was grown using an MBE system for the first time by S. Tixier [2]. Three GaAsBi samples without GaAs capping layer were grown with 270nm, 110nm and 270nm GaAsBi layers with Bi content from XRD measurements was 0.4%, 1.3% and 3.1%, respectively. The Pendellösung fringes were not clear in these samples, which were attributed to a rough interface between the epilayer and the substrate. The XRD results are shown in figure 5.10 (a).

Pacebutas [3] reported that GaAsBi has great potential to be used in THz emitters and detectors. In their works, over 8% Bi content samples have been successfully grown, and the electron lifetime measured in some of the layers was shorter than 1ps. Two angles ($\theta_{Br}+\varphi$) and ($\theta_{Br}-\varphi$) X-ray results based on the crystal plane (004) were shown in figure 5.10 (b), where θ_{Br} is the Bragg angle of the substrate, φ is 3° offset between the substrate and crystallographic (100) planes. From the XRD modelling, the GaAsBi layer was 430nm with 6.7% Bi.

Henini [4] investigated the growth of GaAsBi on different orientations of the GaAs substrate using MBE. Two 1μm thick GaAsBi samples were grown on (001) and (311)B GaAs substrate in their work. From the XRD results, they found that similar patterns were shown in both samples. Although it grew at the same growth rate, the lower intensity of GaAsBi epilayer reflection on (311)B substrate indicates the actual growth rate is reduced for the (311)B direction. Pendellösung fringes were not observed in any of the XRD scans, representing a large degree of structural disorder and Bi inhomogeneous distribution that exists in both the GaAsBi layers.

Puustinen reported that sample annealing affects the variation of lattice constant in GaAsBi, which was determined by growth temperature [5]. The lattice variation had a significantly larger impact on the Bi-containing sample rather than the low-temperature growth GaAs sample. Three 270nm thick GaAsBi samples were grown at 220°C, 270°C and 315°C with Bi content 1.46%, 1.29% and 1.3%, respectively. Figure 5.10 (d) showed the XRD spectra of these three samples at the different annealing temperature. Well-defined Pendellösung fringes were observed in all of three samples for as-grown condition. With increasing annealing temperature, the GaAsBi peak of the samples, grown at 220°C and 270°C shifted towards the GaAs substrate peak while the sample grown at 310°C was virtually unchanged, with only a small degradation of the fringes observed when the annealing temperature reaches 800°C.

Beaudoin investigated the band-edge optical properties of GaAsBi samples [6]. In their work, a series of 230-470nm thick GaAsBi samples were grown using MBE. The Bi content was estimated from the high-resolution XRD scan. The XRD scan spectra are shown in figure 5.10 (e) including clear Pendellösung fringes on each of the samples.

Dybala et al. [7] has reported the optical transitions, including HH, LH and SO transitions, of GaAsBi measured from the electromodulation spectroscopy. Five GaAsBi samples with various Bi content has been grown by MBE. The XRD results were shown in figure 5.10 (g). With increasing Bi content, the GaAsBi peak shifts far away from GaAs substrate peak due to the increase of lattice constant. Clear Pendellösung fringes were obtained in all these samples.

Six representative XRD results of bulk GaAsBi samples within the last 20 years have been reviewed. There is no GaAs capping layer grown in most of the samples. Although some of the samples have a high Bi content, almost all GaAsBi epilayer are fully strained to the substrate due to the thin thickness of the epitaxial layer. In terms of thin samples (epilayer layer thickness<300nm), clear Pendellösung fringes were observed representing high quality of the samples. However, when epilayer thickness is over 400nm with 3% Bi, Pendellösung fringes will disappear, indicating structural disorder and defects, induced by Bi, become more serious. Figure 5.11 provides the summary that the Bi content as the function of GaAsBi layer thickness for these six XRD results. Despite 30 years of continuous innovation and development on growth technique, it is still challenging to obtain thick samples with high bismuth content due to the narrow growth window.

a.

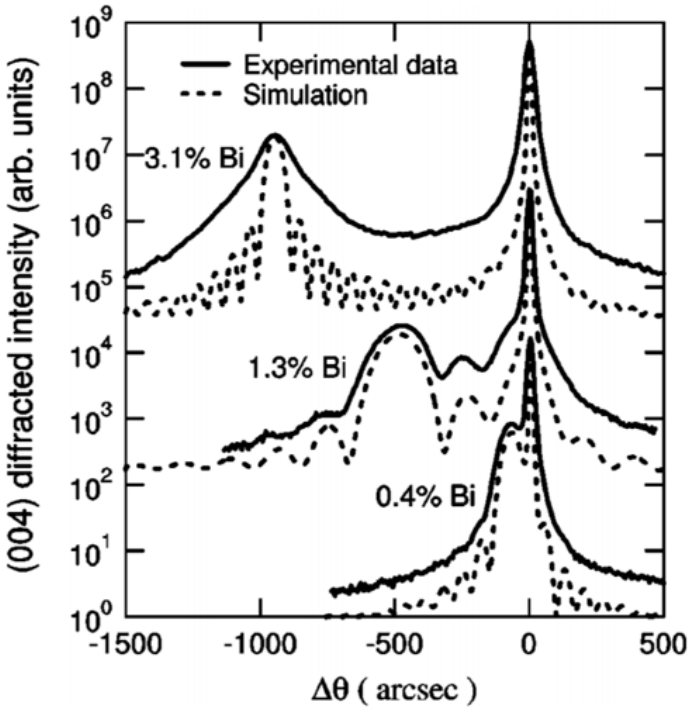
Experimental data
Simulation
3.1% Bi
1.3% Bi
0.4% Bi
(004) diffracted intensity (arb. units)
Δθ (arcsec)

b.

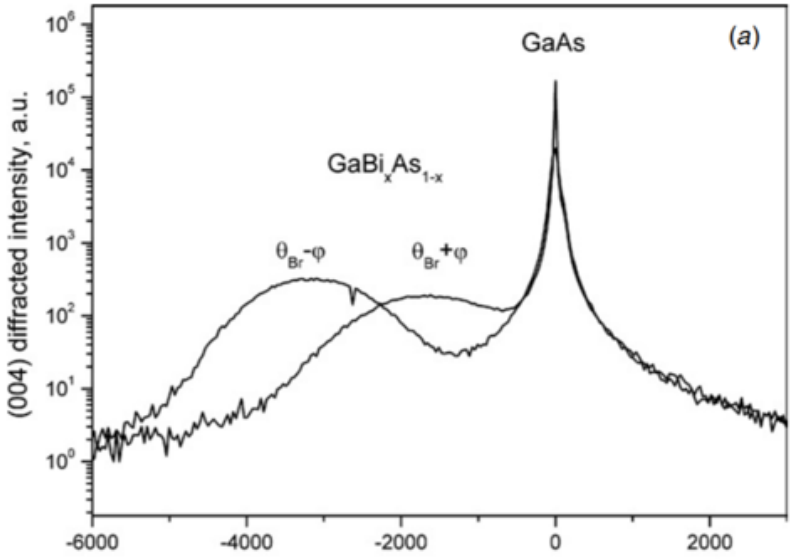
GaAs
(a)
GaBi$_x$As$_{1-x}$
θ_{Br}-φ
θ_{Br}+φ
(004) diffracted intensity, a.u.

c.

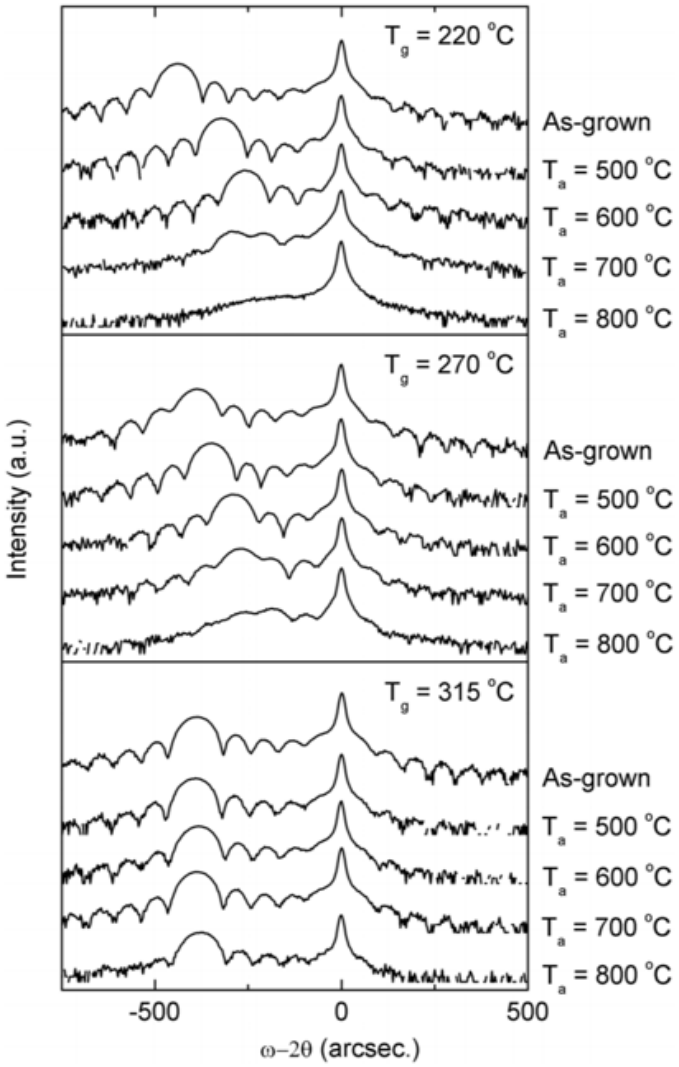
T_g = 220 °C
As-grown
T_a = 500 °C
T_a = 600 °C
T_a = 700 °C
T_a = 800 °C
T_g = 270 °C
As-grown
T_a = 500 °C
T_a = 600 °C
T_a = 700 °C
T_a = 800 °C
T_g = 315 °C
As-grown
T_a = 500 °C
T_a = 600 °C
T_a = 700 °C
T_a = 800 °C
Intensity (a.u.)
-500
0
500
ω–2θ (arcsec.)

d.

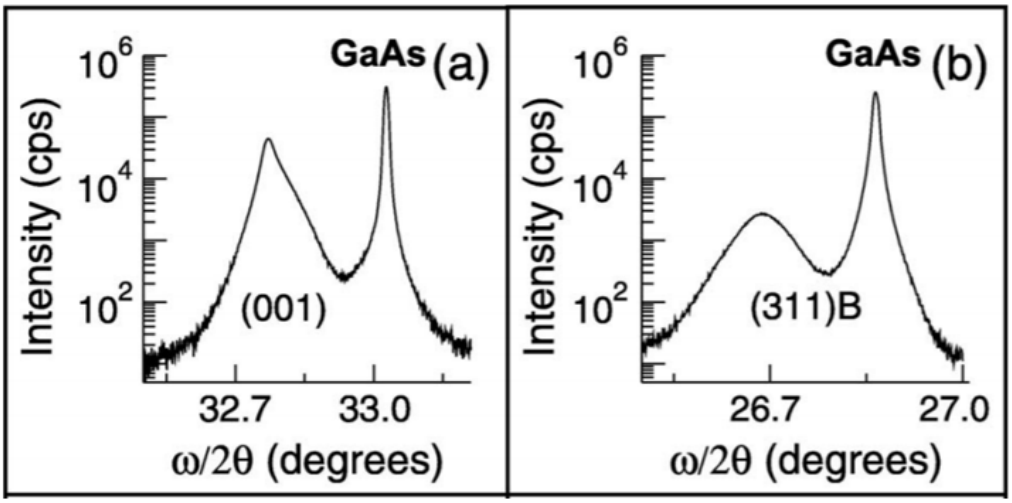
GaAs (a)
10^6
10^4
10^2
Intensity (cps)
(001)
32.7
33.0
ω/2θ (degrees)
GaAs (b)
10^6
10^4
10^2
Intensity (cps)
(311)B
26.7
27.0
ω/2θ (degrees)

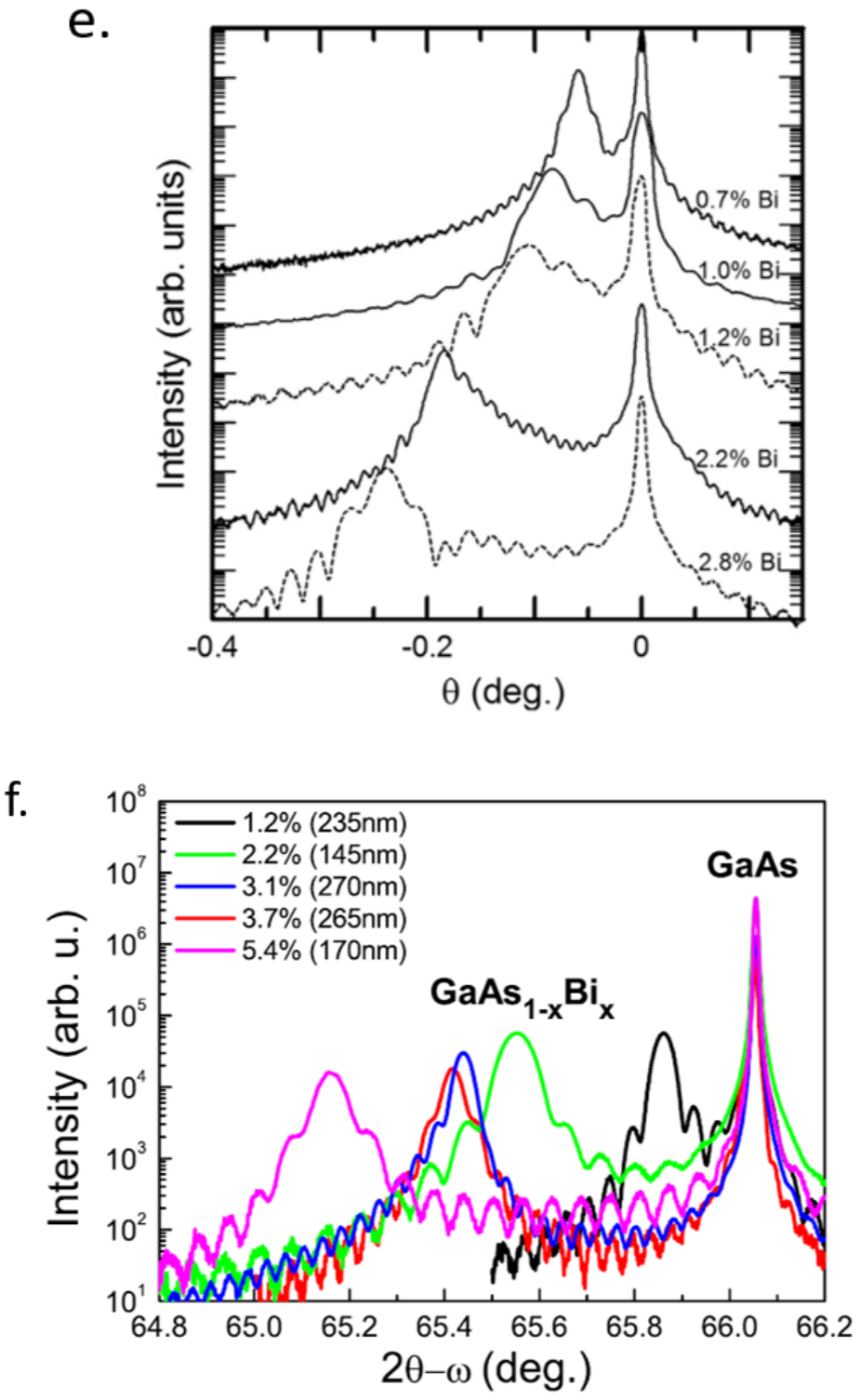

Figure 5.10 Bulk GaAsBi XRD reviews from the literature. a) [2] b) [3] c) [4] d) [5] e) [6] f) [7]

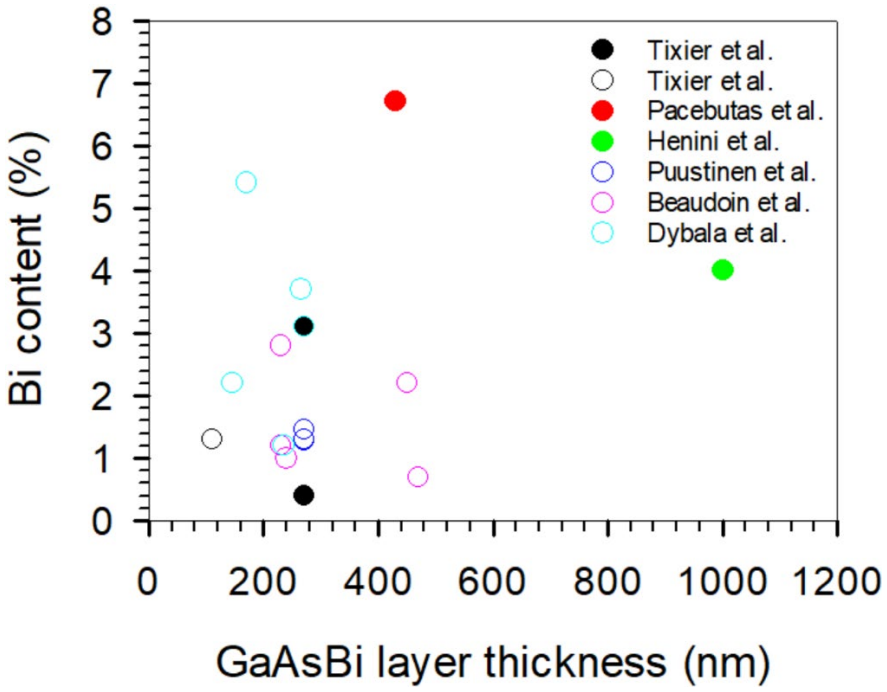

Figure 5.11 Plot of Bi content as the function of GaAsBi layer thickness, indicating whether fringes are present. The open/solid circle represents the XRD spectra with/without fringes.

In this thesis, the XRD characterisation is performed using a Bruker D8 Discover X-ray diffractometer scanning across the ω-2θ mode. The raw data are shown in figures 5.12-5.14 with the modelled data, which are simulated using the RADS Mercury software.

From Figure 5.12 to 5.14, the XRD spectra of STF85 (P100), STF81 (P200), STFA7 (N100) and STJ4G (N400) show clear Pendellösung fringe, which is an indicator of abrupt interfaces between the GaAs and GaAsBi layers. The simulation model shows a good fit with those four devices with clear fringes. However, with increasing sample thickness, the experimental data is harder to fit with the simulation model, possibly due to more severe strain relaxation in thicker samples. In the figures, the shoulder peak on the right side of the substrate peak at 0 arcseconds represents the strain relaxation. Apart from that, the simulation model shows that the GaAsBi peak becomes thinner with increasing sample thickness because the reciprocal space is the inverse of real space. However, the real GaAsBi peak from the experiment is far broader than that from the simulation. The possible reason may be due to the induced dislocation caused by crystal defects, broadening the Bragg peaks [8]. The long tail of the substrate peak is due to the single-reflection collimator used in the X-ray system [8]. As the

incident angle of the X-rays deviates from the Bragg angle of the material, the intensity of the X-ray diffraction spectrum after reflection will reduce dramatically.

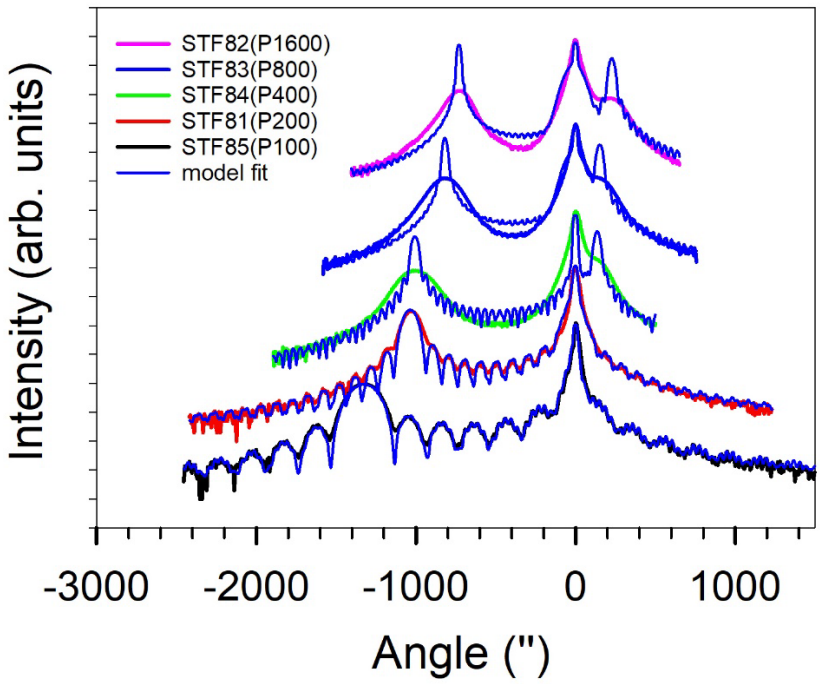

Figure 5.12 X-ray diffraction results for STF8 series p-i-n samples. Scans are normalised and vertically offset for clarity.

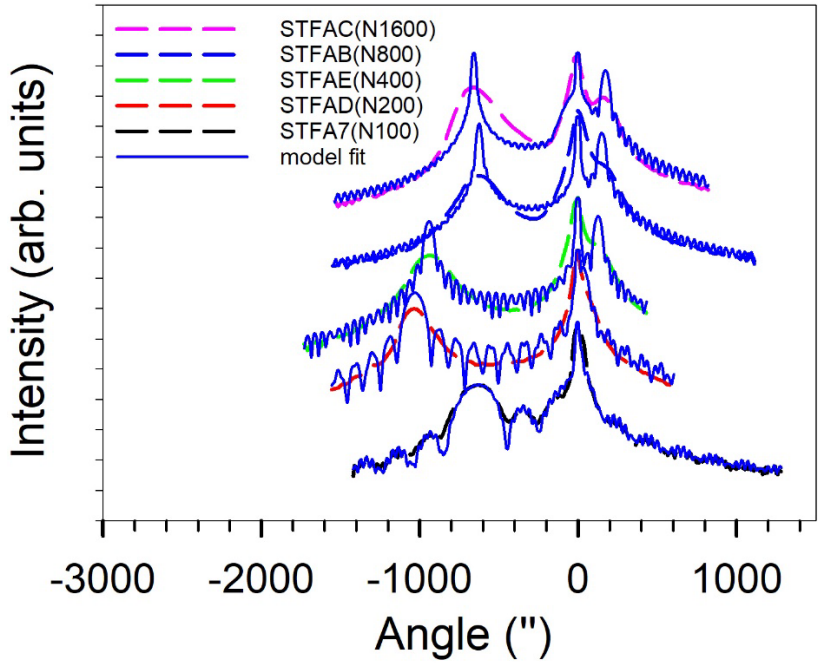

Figure 5.13 X-ray diffraction results for STFA series n-i-p sample. Scans are normalised and vertically offset for clarity.

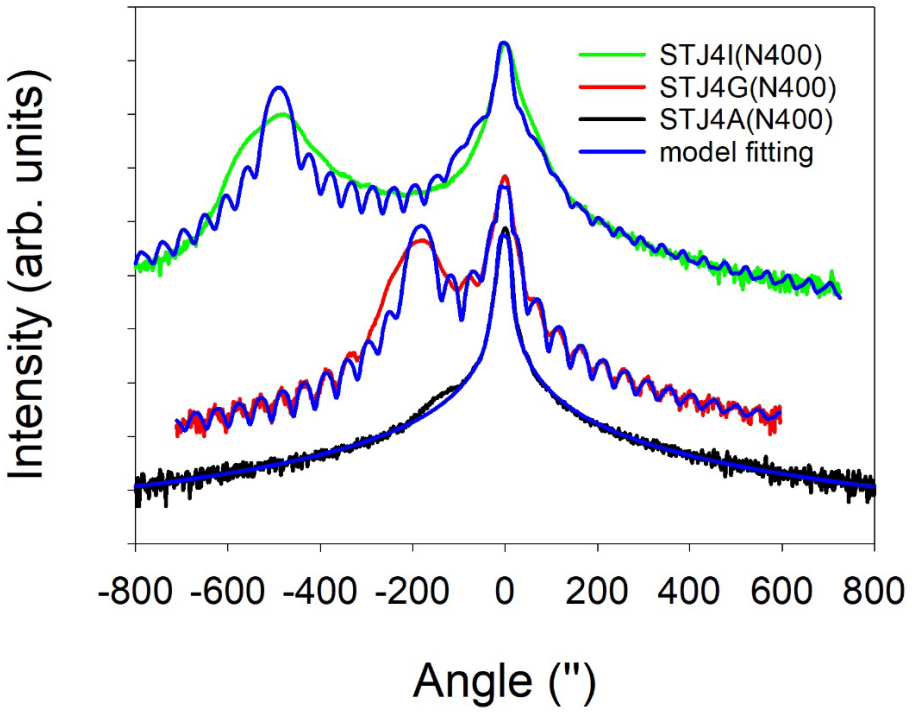

Figure 5.14 X-ray diffraction results for STJ4 series n-i-p sample. Scans are normalised and vertically offset for clarity.

From the XRD spectrum, the layer composition, strain and mismatch are related to the angular separation between the substrate and epitaxial layer. The lattice constant of the epitaxial layer can be calculated from Bragg's law. However, this method is only valid for the pseudomorphic condition because the strain relaxation will affect the lattice constant significantly. In reality, the free-standing lattice constant of GaAsBi is larger than that of GaAs, as shown in Figure 5.15 (a). When grown, the GaAsBi layer will strain compressively to conform to the GaAs layer. In order to release the strain, the out-of-plane lattice constant of the epitaxial layer will elongate. It is a pseudomorphic condition, which is the case for samples STF85, STF81, STFA7 and STJ4G. In this case, the in-plane lattice constant of the top GaAs epilayer, the intrinsic GaAsBi layer and bottom GaAs substrate remain the same, as shown in Figure 5.15(b). However, in the case of other samples with thicker GaAsBi layers, because the strain builds up with increasing thickness of the GaAsBi layer, at a certain point (when the epilayer thickness exceeds the critical thickness), the epitaxial layer will be relaxed by the excessive strain force, generating misfit dislocation at the heterointerface, as shown in Figure 5.15(c). Such behaviour matches the observation from the Nomarski image, where crosshatch patterns on the free surface of the sample manifest. In the meantime, the top GaAs layer will be in tensile strain with respect to the GaAsBi layer below it, the in-plane lattice

constant of the top GaAs layer will be extended. Therefore, the out-of-plane lattice constant of this GaAs layer will be less than that of unstrained ($\alpha'_{GaAs} < \alpha_{GaAs}$).

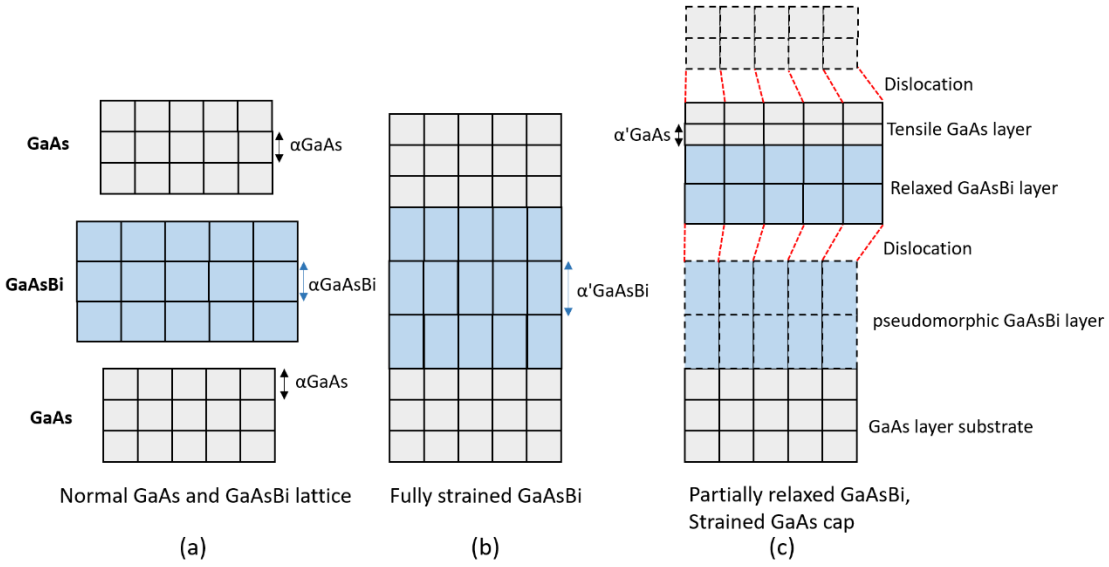

Figure 5.15 Schematic diagram of strained and relaxation of GaAsBi: (a) regular GaAs and GaAsBi lattice structure. (b) Fully strained GaAs/GaAsBi/GaAs heterojunction structure, the thickness of GaAsBi layer is less than the critical thickness. (c)The thickness of GaAsBi layer is over the critical thickness, GaAsBi layer is strain relaxed, the top GaAs layer is tensile strained.

If the sample has no relaxation, the lattice constant of the unstrained GaAsBi layer can be estimated, assuming its Poisson ratio is same as that of GaAs (0.311). Therefore, the composition of the GaAsBi layer can be calculated using Vegard's law from Section 1.2. For a ternary alloy, Vegard's law states that the lattice constant varies linearly with its binary constituents. In our case, it can be described mathematically with the following equation, where x is the Bi composition. In this work, the lattice constant 6.275Å of GaBi taken from [9] was adopted used in the X-ray diffraction simulation model.

$$a_{GaAsBi} = (1-x)a_{GaAs} + xa_{GaBi} \qquad (5.1)$$

From the literature, GaBi is expected to be semi-metallic and has never been successfully synthesised [10], [11]. Over the past decade, many researchers have attempted to estimate the GaBi lattice constant using experimental and theoretical studies. The lattice constant was estimated to be between 6.23Å and 6.33Å from experiment [2], [12], [13] and between 6.186Å and 6.46Å from theory [9]–[11], [14]–[18].

The epilayer thickness, t, can be obtained from the Pendellösung fringe spacing, which is described by the following equation [19], [20]:

$$t = \frac{\lambda_x \sin(\theta_{Br} + \phi)}{\Delta\omega \sin 2\theta_{Br}} \qquad (5.2)$$

where λ_x is the wavelength of the X-rays, θ_{Br} is the Braggs angle, ϕ is the angle between the diffraction plane and the surface plane normal and $\boldsymbol{\Delta}\omega$ is the Pendollösung fringe spacing. Therefore, the samples without Pendellösung fringes cannot give an accurate value of thickness.

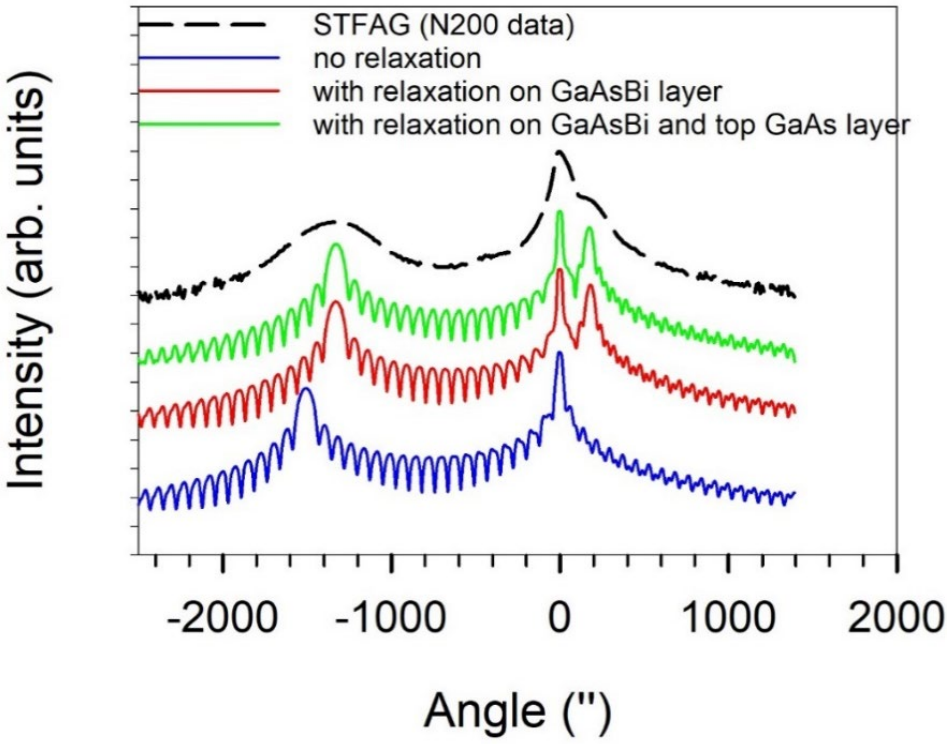

Figure 5.16 XRD results for STFAG(N200) sample, and the simulation with and without relaxation as a comparison.

In order to investigate the strain relaxation effect on the XRD spectrum, simulations were performed on the STFAG(N200) sample, as shown in figure 5.16. The comparison includes the spectra of three simulations with and without relaxation under the condition that the other parameters remain unchanged. When introducing 25% relaxation in the GaAsBi layer, the position of GaAsBi peak will shift to the right side and create a shoulder peak which is near to the substrate, Bi composition from this simulation is 5.3%. However, when introducing 35% relaxation in both GaAsBi and top GaAs cap layer, the Bi composition needs to set 5.8% to fit the experimental data.

Although the value of Bi composition and relaxation sets differently between those two simulations, both green and red simulation get a strikingly similar result. It proves that the final position of shoulder peak depends on not only the varying degree of strain relaxation but also the Bi composition. Therefore, there is a range of composition and relaxation which will provide the same lattice parameter. In this case, the Bi composition from the simulation has a large uncertainty. Other techniques such as photoluminescence and photocurrent can be adopted to confirm the real Bi composition.

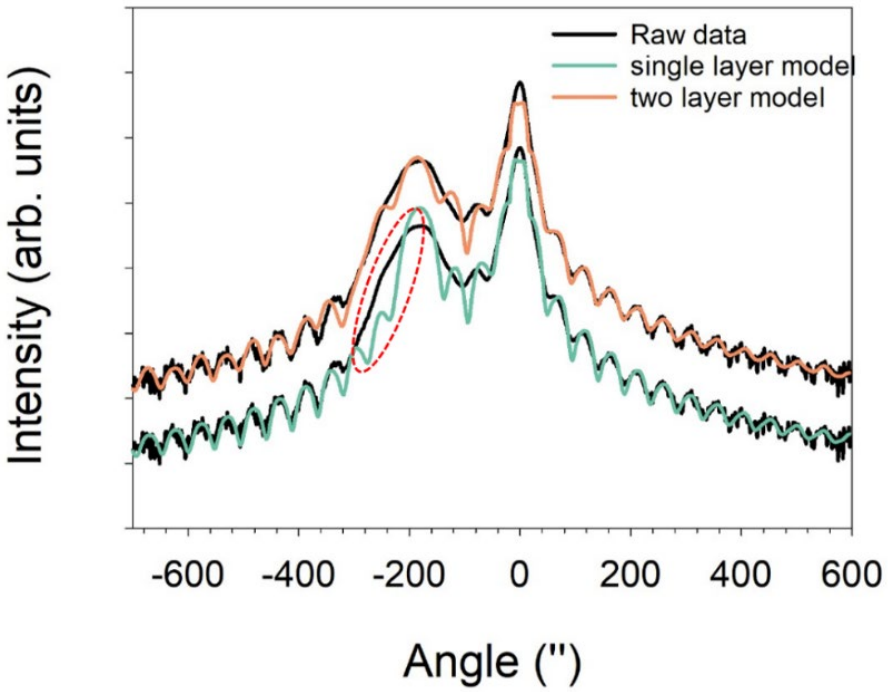

Figure 5.17 XRD results for STJ4G(N400) devices with 0.65% bismuth, using both single-layer and two-layer model to fit the experiment data. The region within red dashed circle shows the spectrum where the single layer model fails to fit the experiment data.

Although the spectra with Pendellösung fringes have a relatively good fit with the experimental data, the real GaAsBi diffraction is broader than the simulation predicts, which may be caused by bismuth content inhomogeneity during the layer growth. In order to investigate this poor agreement between the single layer simulation and the experimental data, a two-layer simulation will be adopted with varying Bi content. Figure 5.17 shows samples STJ4G (Bi content 0.65%) with both single and two-layer XRD simulations. From figure 5.17, the single-layer simulation shows a poor agreement with experimental data at around -300 arc seconds (labelled within a red dashed circle). However, the two-layer model has a much better fitting result. The

fitting parameters calculated from both models with varying layer thickness and Bi content are shown graphically in 5.18.

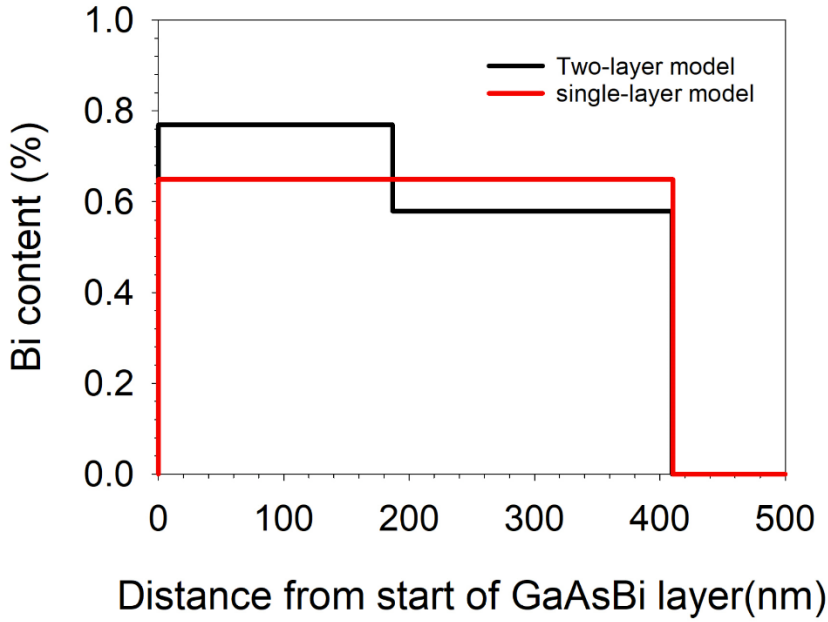

Figure 5.18 Bi content profiles in the GaAsBi layer of STJ4G sample with the single layer (red line) and two-layer (black line) simulations. The growth direction is from left to right (black dashed line).

From figure 5.18, the peak Bi content in the two-layer model is a factor of 1.14 times higher than in the single layer model, it shows that a relatively high Bi content has been incorporated into the initial 180 nm of GaAs layer, similar to the observation from [21], [22]. However, the real Bi incorporation situation is much more complicated than the two-layer simulation. If a more complex model is chosen (three-layer or four-layer simulation), the fitting result might be improved but less believable. This is due to the increased uncertainty associated with introducing more fitting parameters.

The layer thicknesses and Bi content for each sample from the XRD simulation software are shown in table 5.2.

	Device name	Nominal thickness (nm)	Modelled Layer thickness (nm)	Bi content (%)	GaAsBi peak FWHM (’’)	GaAs peak FWHM (’’)	Relaxation (%)
p-i-n	STF85	100	94.6	4.79	180	14.4	0
	STF81	200	191.8	3.7	108	36	0
	STF84	400	412	4.07	194.4	39.6	25
	STF83	800	731.5	4.0	167.4	27	58
	STF82	1600	1418.2	3.95	133.2	36	72
	STD53	400	478.4	0	0	32	0
	STD56	400	440	2.21	175.8	38.9	0
n-i-p	STFA7	100	94.7	2.3	194.4	43.2	0
	STFAD	200	187	3.88	129.6	21.6	8
	STFAE	400	380	3.8	172.8	43.2	25
	STFAB	800	794	2.82	180	54	41
	STFAC	1600	1480	2.95	151.2	43.2	65
	STFAG	200	220	5.4	303	57	25
	STJ4A	400	390	0	0	20.1	0
	STJ4G	400	410	0.65	66	20.3	0
	STJ4I	400	410	1.74	93.6	28.7	0

Table 5.2 Simulation results of layer thickness, Bi content and relaxation for p-i-n and n-i-p sample in this work, assuming single uniform layer of GaAsBi.

The FWHM of the GaAsBi peaks in the layers are relatively broad compared to the GaAs peaks. There is no systematic change in the FWHM with Bi% or with the thickness of the GaAsBi layer. Modelling of the X-ray rocking curves show that the thicker layers of GaAsBi should have a narrow FWHM. It is clear from our Normaski measurements that the larger Bi% and thicker samples have more cross-hatching lines on the surface, indicating the presence of dislocations. However, the broader FWHM that we measure cannot be attributed to the presence of dislocations in our structures. Due to the way that the growth is done, the Bi% can vary slightly across the sample by ± 0.5% as shown by PL studies. The X-ray beam is 0.2mm × 10mm wide, meaning that it will be sampling a range of compositions, and this may be responsible for the broad FWHM that we see.

The Bi content and layer thickness have a greater uncertainty in the samples affected by strain relaxation. The Bi content inhomogeneity across the wafer also contributes to the uncertainty. Therefore, the XRD data will be used as a reference to be compared with the results obtained by photoluminescence measurements, which will be discussed in a later section.

5.3.3 Room temperature photoluminescence results

As a non-contact and non-destructive method for probing semiconductors, PL uses a fixed wavelength of laser light to stimulate the emission of photons from the material.

This technique is fast and provides a convenient analysis for the composition, bandgap and optical quality of the material. In this work, a 532 nm diode-pumped solid-state laser was used to excite carriers in the devices. After passing through a monochromator, the emitted photons from the material are collected by a LN_2-cooled germanium detector. Details of the experiment are discussed in Section 4.2.

Device name (PIN&thickness)	Peak wavelength (nm)	Bandgap (eV)	Bi content (%)	FWHM (meV)	Device name (NIP&thickness)	Peak wavelength (nm)	Bandgap (eV)	Bi content (%)	FWHM (meV)
STF85(P100)	1129	1.099	4.78	83.8	STFA7(N100)	995	1.246	2.35	N/A
STF81(P200)	1070	1.159	3.75	86.7	STFAD(N200)	1074	1.155	3.82	110.9
STF84(P400)	1126	1.101	4.75	**187.9**	STFAE(N400)	1087	1.141	4.05	**97.75**
STF83(P800)	1120	1.107	4.64	109.8	STFAB(N800)	1053	1.178	3.44	97.99
STF82(P1600)	1120	1.107	4.64	103	STFAC(N1600)	1044	1.188	3.27	108.3
STD56(P400)	1003.7	1.235	2.52	**79.6**	STJ4I(N400)	976	1.270	1.99	**77.32**
STF87(P1600) GaAs ref	874	1.420	0	28	STFAG(N200)	1172	1.058	5.52	305.5

Table 5.3 PL results for p-i-n and n-i-p sample in this work, Bi content is calculated from the valence band anti-crossing model. Similar ~400nm thickness of samples was labelled in blue to compare with FWHM.

Figure 5.19 and 5.20 shows room temperature PL spectra of the p-i-n series and n-i-p series samples, which is compared to a 1.6 μm thick GaAs reference sample. The peak wavelength of each of samples plotted as the function of Bi content, extracted from both XRD simulation and VBAC model, was shown in Figure 5.21. Both p-i-n and n-i-p PL peaks shift to longer wavelengths with increasing Bi content as expected. The bandgap change is ~ 67 meV/%Bi for p-i-n and ~ 66 meV/%Bi for n-i-p, which is consistent with the range of Bi induced bandgap reduction from literature (60-90 meV/%Bi) [23]–[31]. From the PL spectra, the curves of STF84 (P400), STF83 (P800) and STF82 (P1600) appear noisy compared with other p-i-n samples. The possible reason might be due to the low As:Ga ratio during the growth. Therefore, the Bi atoms could have a high probability of forming Bi-clusters. Details of the PL results for all p-i-n and n-i-p samples in this work are shown in Table 5.3.

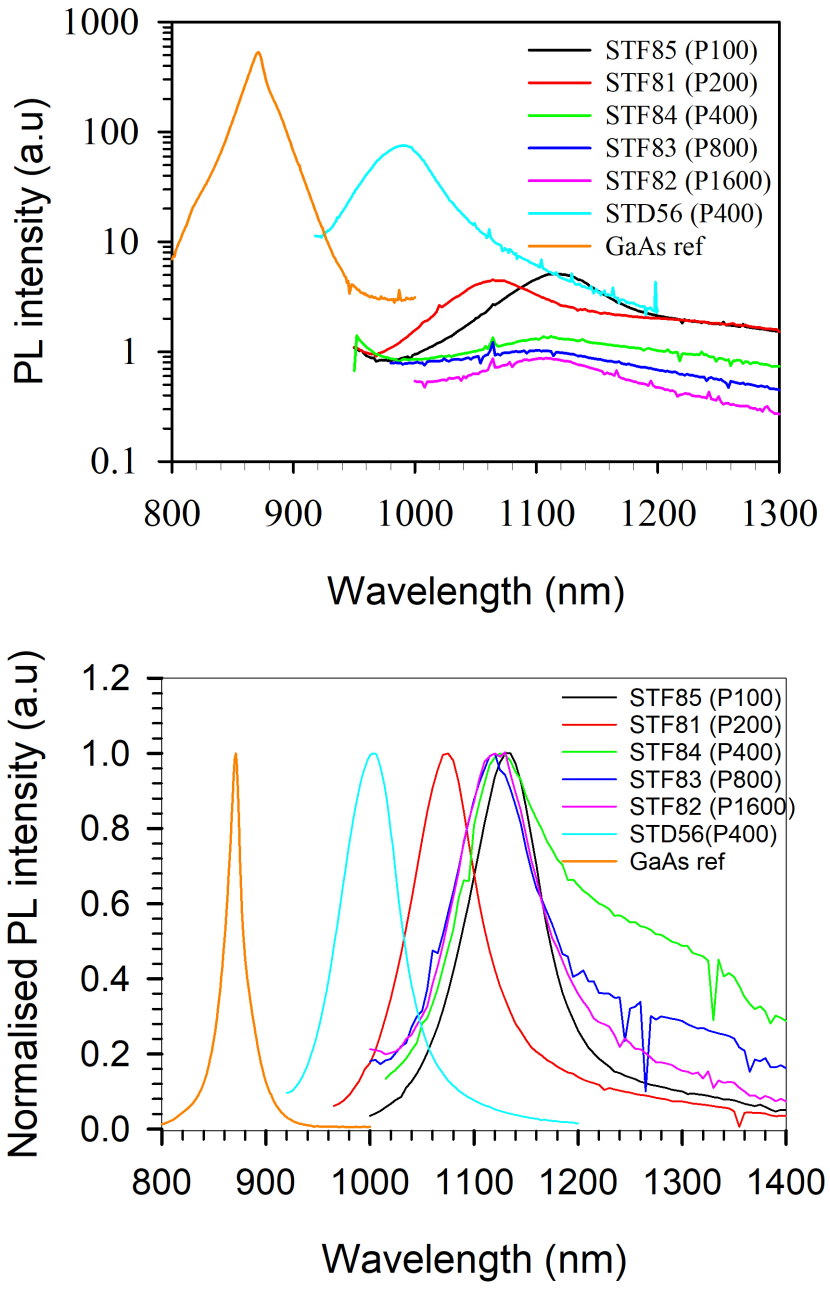

Figure 5.19 Without normalised and normalised room-temperature PL spectra for GaAsBi p-i-n series sample, a 1.6μm thick GaAs sample(STF87) as reference.

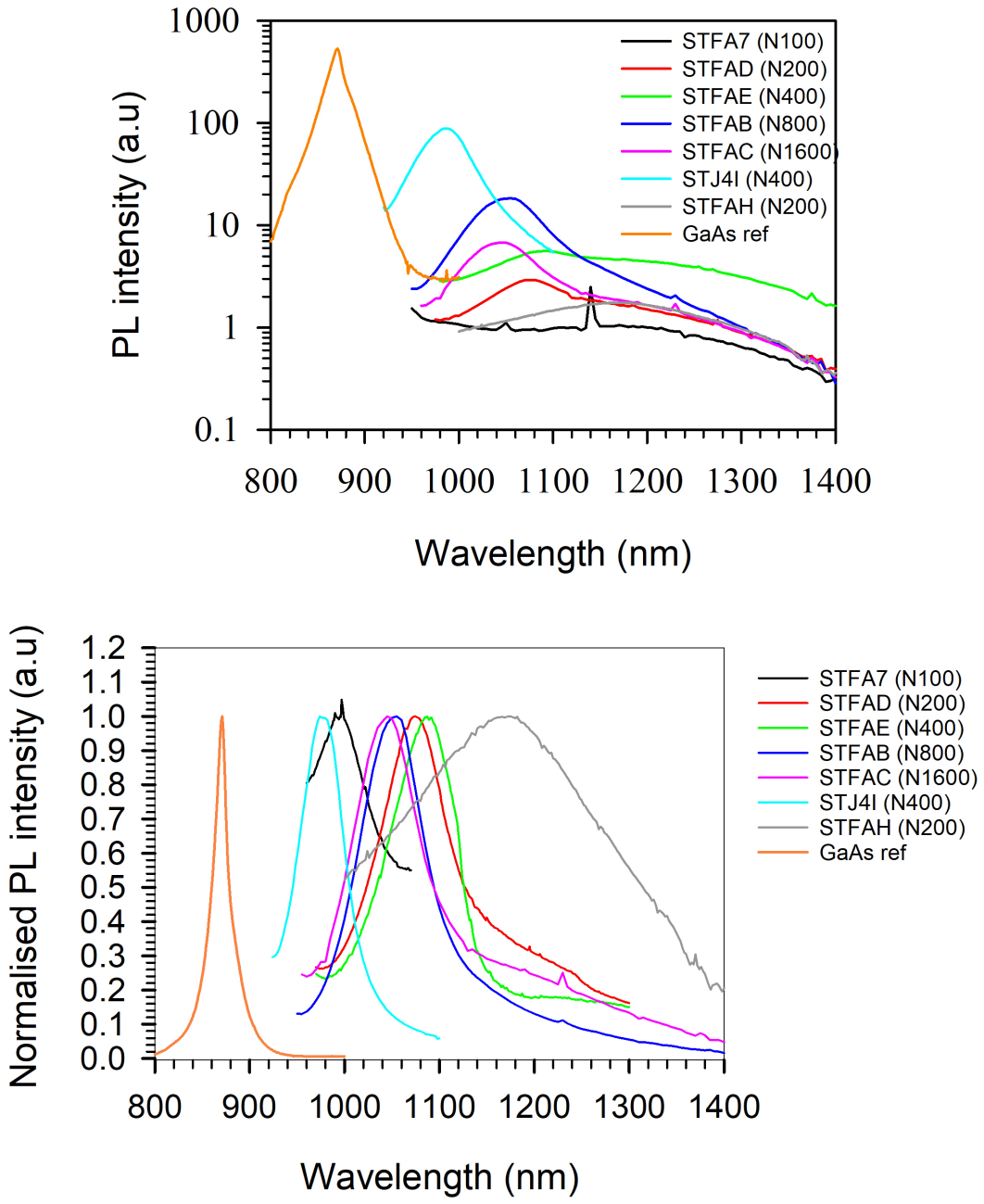

Figure 5.20 Without normalised and normalised room-temperature PL spectra for GaAsBi n-i-p series sample, a 1.6μm thick GaAs sample (STF87) as reference.

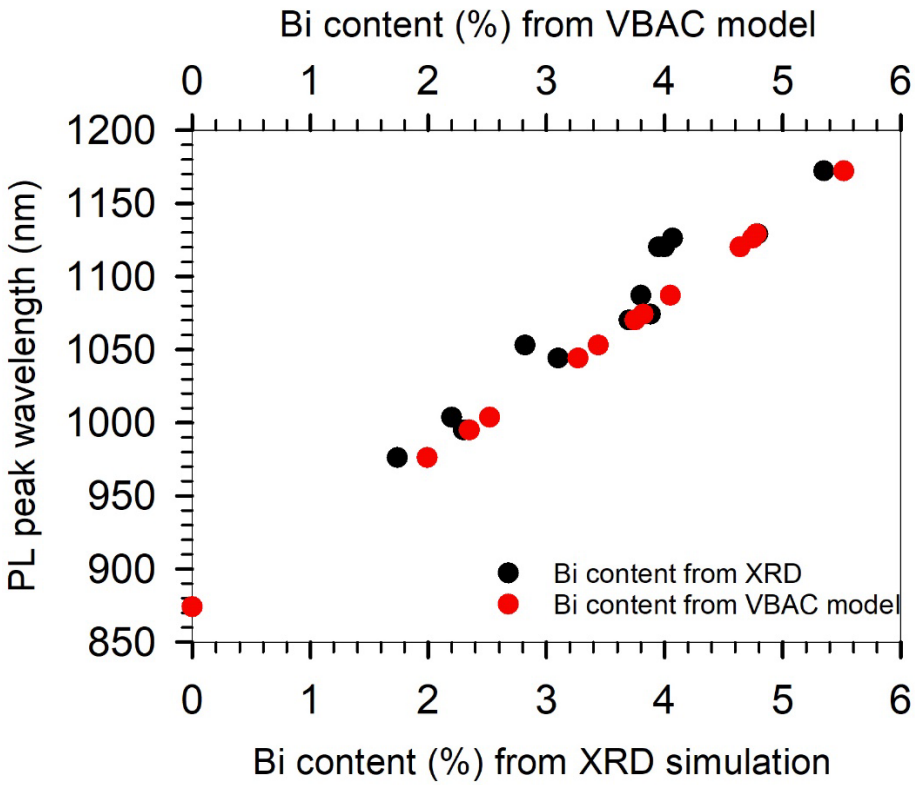

Figure 5.21 PL peak wavelength as the function of Bi content, Bi content of each of samples were extracted from XRD simulation and VBAC model.

Figure 5.22 shows the full width at half maximum (FWHM) as a function of Bi content comparing samples from this work and reports in the literature. It shows that FWHM has a significant increase from 28 meV for GaAs to about 110 meV when adding a small amount of 4.5% Bi into GaAs in this work. There is no clear trend on changing of FWHM value when varying the sample thickness. However, comparing samples with similar thickness, the FWHM increases dramatically with a higher Bi content (labelled as blue in the table), which agrees with the observation from [5]. This phenomenon indicates that the crystal quality is dominated by the amount of Bi in the sample rather than the thickness of the sample. The FWHM of both STF84 (P400) and STFAG (N200) has an abnormally high value, which might be due to substrate emission. The spectra of STFAH seems not a real PL spectrum because the shape is not a normal Gaussian distribution. Apart from these two anomalous samples, most samples grown in Sheffield have a smaller FWHM value at room temperature compared to other works reported in the literature.

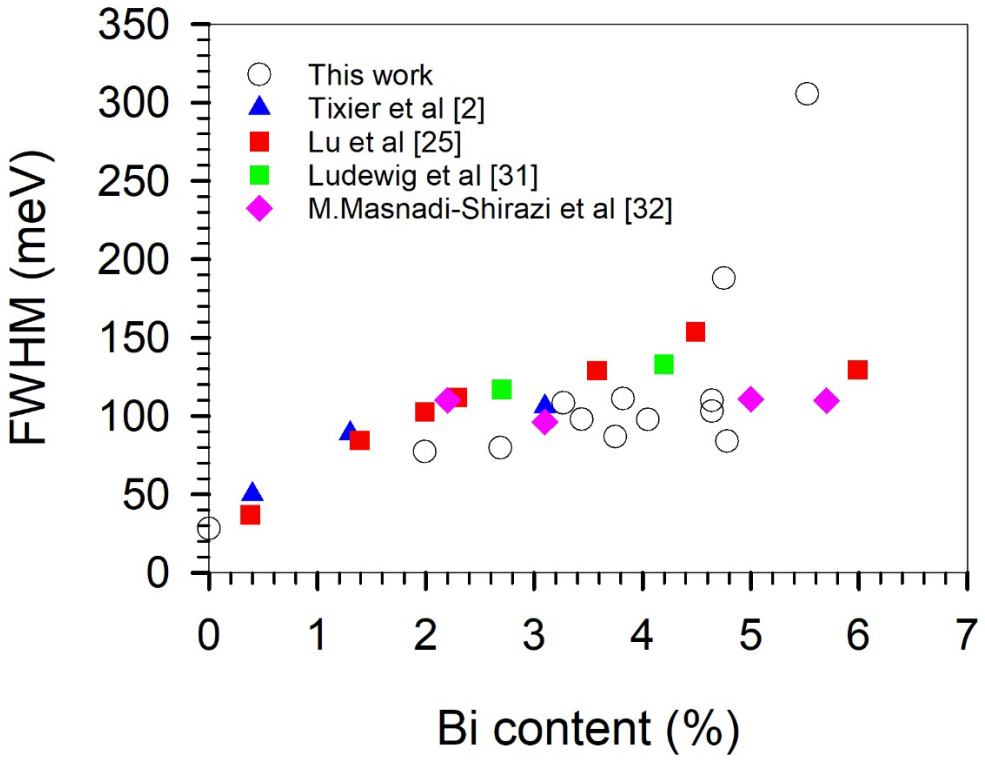

Figure 5.22 FWHM as a function of Bi content of this work compared with reports from other groups [2], [26], [32], [33].

5.3.4 Comparison of Bi content from XRD and PL

The Bi content of each sample, calculated from XRD simulation and VBAC model, are showed in Table 5.4. In general, the Bi content fairly agrees with each other in the thin sample without strain relaxation. As the GaAsBi layer grows thicker, the Bi content doesn't match quite well, possibly due to more severe strain relaxation in thicker samples. The difference of the Bi content taken from those two techniques is ~0.3% for average, and the largest difference is ~0.69% for 1600nm p-i-n sample. There is a uncertainty of Bi content in both measurement methods. As described in the XRD simulation for thick samples, a range of Bi composition and relaxation will provide the same GaAsBi peak position. For Bi content estimated from PL, the inhomogeneity of Bi content at different locations of the sample may lead to a change in PL peak value. In addition, the strain relaxation will reduce the bandgap of the material and thus a larger value Bi content will be overestimated.

Nominal i-region thickness (device name)	Bi content (%) from XRD		Bi content (%) from PL		Difference of Bi (%) between XRD and PL	
	p-i-n	n-i-p	p-i-n	n-i-p	p-i-n	n-i-p
100nm (STF85&STFA7)	**4.79**	**2.3**	**4.78**	**2.35**	0.01	0.05
200nm (STF81&STFAD)	**3.65**	**3.78**	**3.75**	**3.82**	0.1	0.04
400nm (STF84&STFAE)	**4.07**	**3.8**	**4.75**	**4.05**	0.68	0.25
800nm (STF83&STFAB)	**4.0**	**2.82**	**4.64**	**3.44**	0.64	0.62
1600nm (STF82&STFAC)	**3.95**	**2.95**	**4.64**	**3.27**	0.69	0.32
200nm (STFAG)		**5.4**		**5.52**		0.12
400nm (STD56)		**2.2**		**2.52**		0.32
400nm (STJ4I)		**1.74**		**1.99**		0.25

Table 5.4 Bi content is extrapolated from XRD and RT PL measurement.

5.4 Electrical Characterisation

After optical characterisation of the wafers, the wafers were then fabricated into devices via standard cleanroom processing techniques such as metallic contact deposition, photolithography and wet etching. Once the devices have been completed, the first essential electrical test is the dark current-voltage measurement that can give a quick indication of whether the devices have diode rectifying characteristics. Capacitance-voltage measurements are also able to provide some basic parameters of diodes, such as the intrinsic region thickness and doping profile of diodes. In this work, dark current-voltage measurements were performed by using a HP4140B picoammeter and capacitance-voltage measurements were undertaken using a HP4275A LCR meter at a frequency of 1 MHz.

5.4.1 C-V characteristics

The capacitance versus reverse bias results of p-i-n and n-i-p series with mesa diameters of 200 μm are plotted in Figure 5.23. When applying a reverse bias voltage, the diode capacitance decreases rapidly initially followed by a region of constant capacitance. This is because in the first region, the depletion region is expanded rapidly with reverse bias due to the lightly doped i-region. However, with increasing reverse bias voltage, the edge of the depletion region will enter the heavily doped p or n-region, which reduces the rate of expansion of the depletion region. Therefore, it can assume that the intrinsic region has been fully depleted at this point.

Figure 5.24 shows the doping profile as a function of depletion width for p-i-n and n-i-p series. The sharp increase of doping density of each diode is due to the full depletion of the i-region. The GaAs control sample indicates that the doping density of the i-region is roughly 1×10^{15} cm^{-3}, which is similar to our thickest structure n-i-p STFAI 1600nm result. It can, therefore, be assumed that the doping concentration is around 10^{15} cm^{-3} and incorporating Bi into GaAs does not result in a significant change in the i-region doping concentration. In order to further confirm the doping and the thickness of the depletion region, CV modelling was used by solving Poisson's equation. The modelled parameters were given in Table 5.5. The modelled results show a good agreement with the measured data, which is depicted in Figure 5.25. In this work, the dielectric constant of GaAsBi uses the same value as GaAs, 12.95. The built-in voltage is estimated to be ~1.1 V by extrapolating from the $1/C^2$ versus voltage plot as illustrated in Figure 5.26 where STD56 is shown as a representative example.

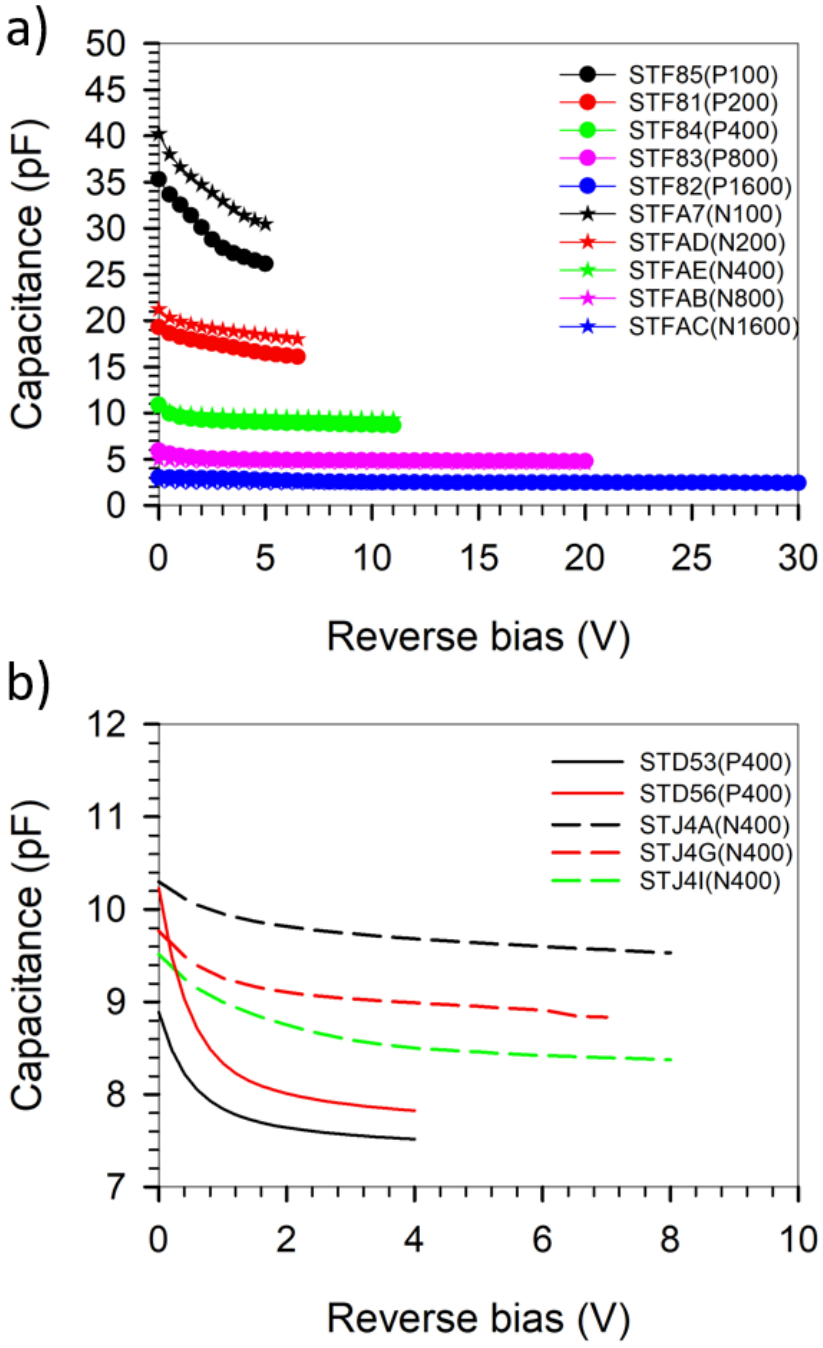

Figure 5.23 a) Capacitance-voltage results for STF8 p-i-n and STFA n-i-p series. b) Capacitance-voltage results for STD5 p-i-n and STJ4 n-i-p series.

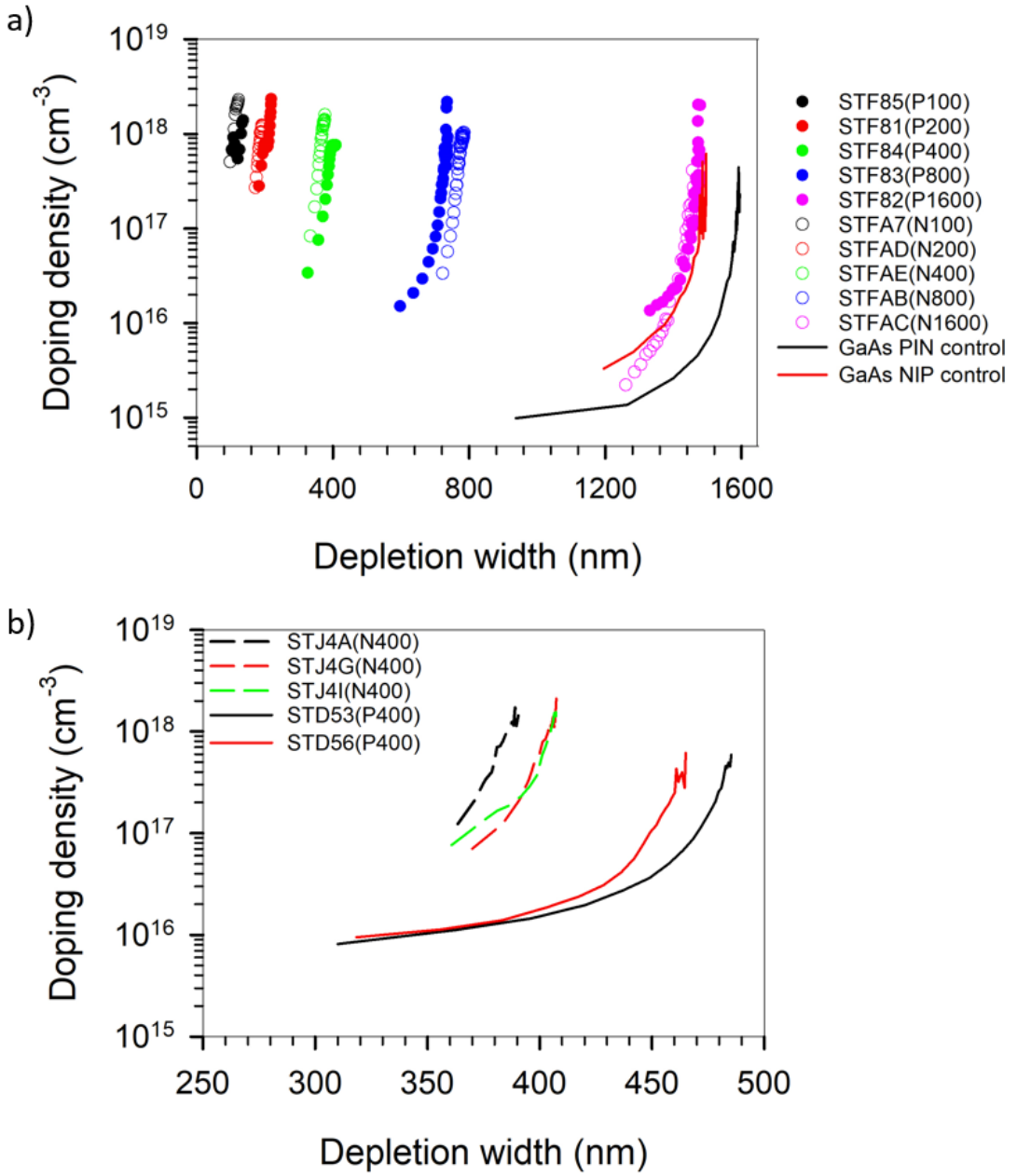

Figure 5.24 a) Doping profile of STF8 p-i-n and STFA n-i-p series with two GaAs 1.6μm p-i-n and n-i-p control sample. b) Doping profile of STD56 and STJ4I series samples.

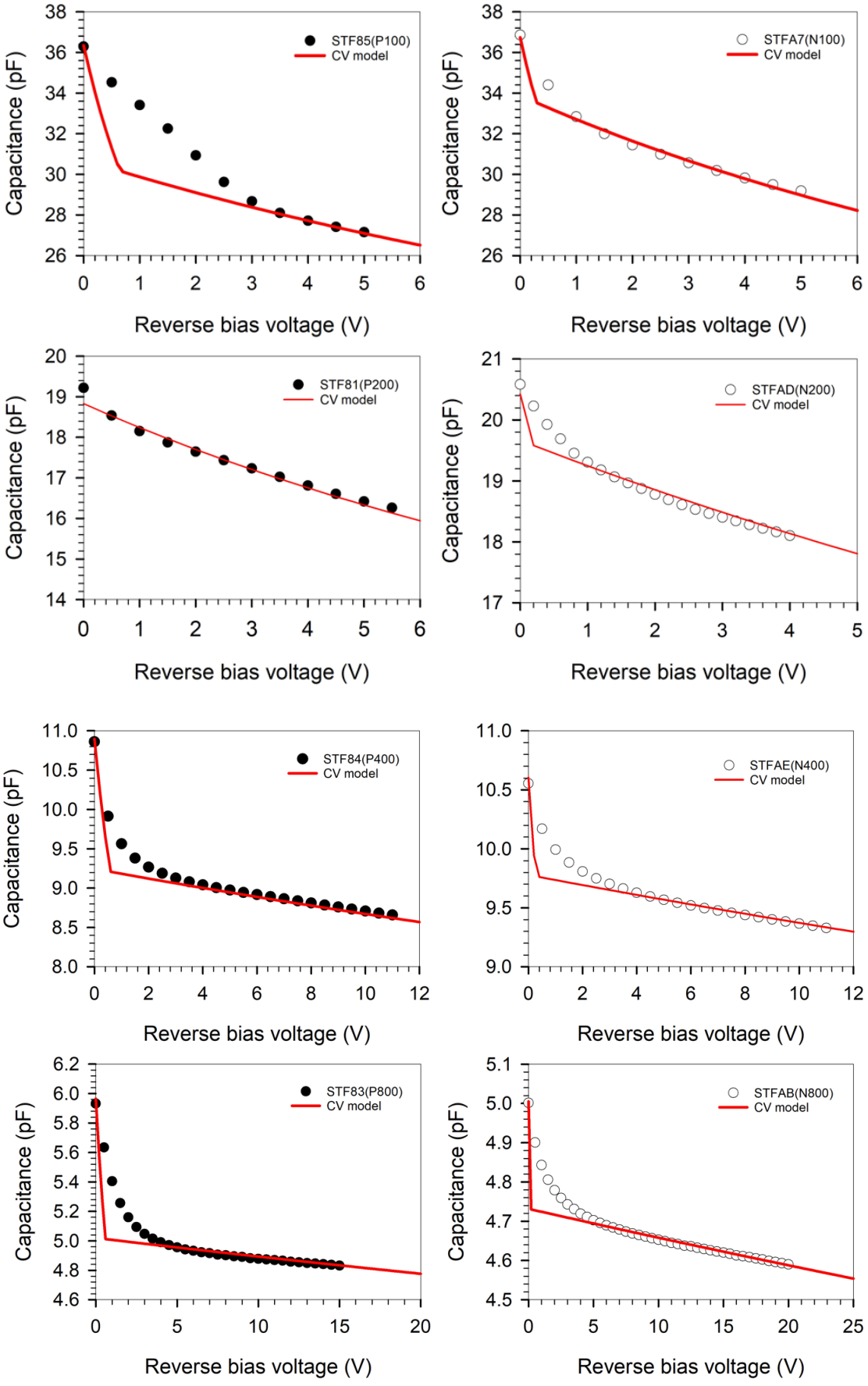
STF85(P100)
CV model
Capacitance (pF)
Reverse bias voltage (V)
STFA7(N100)
CV model
Capacitance (pF)
Reverse bias voltage (V)
STF81(P200)
CV model
Capacitance (pF)
Reverse bias voltage (V)
STFAD(N200)
CV model
Capacitance (pF)
Reverse bias voltage (V)
STF84(P400)
CV model
Capacitance (pF)
Reverse bias voltage (V)
STFAE(N400)
CV model
Reverse bias voltage (V)
STF83(P800)
CV model
Capacitance (pF)
Reverse bias voltage (V)
STFAB(N800)
CV model
Capacitance (pF)
Reverse bias voltage (V)

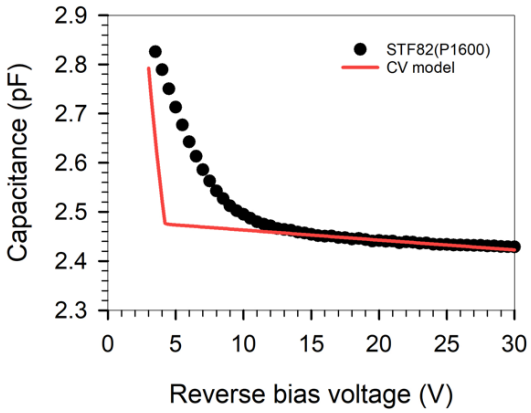
STF82(P1600)
CV model
Capacitance (pF)
Reverse bias voltage (V)

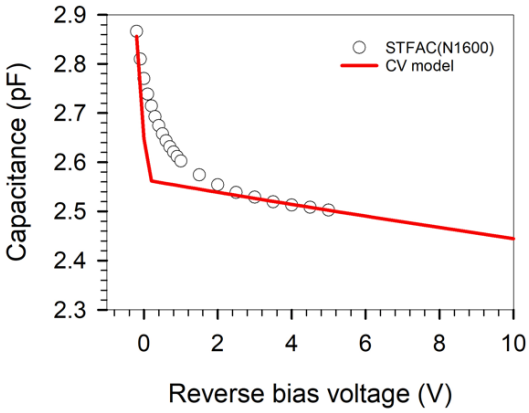
STFAC(N1600)
CV model
Capacitance (pF)
Reverse bias voltage (V)

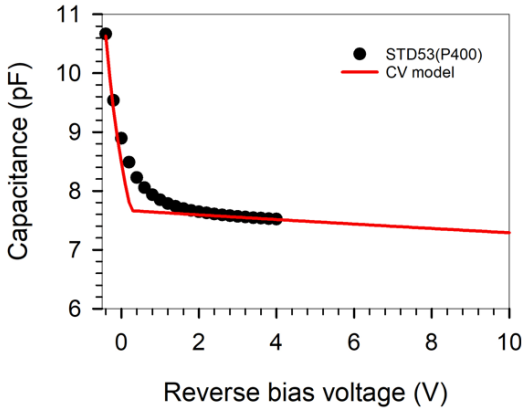
STD53(P400)
CV model
Capacitance (pF)
Reverse bias voltage (V)

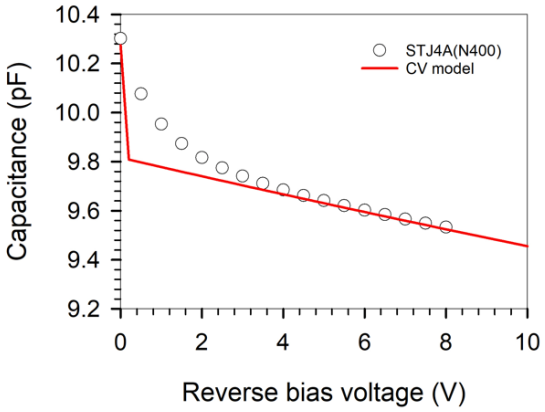
STJ4A(N400)
CV model
Capacitance (pF)
Reverse bias voltage (V)

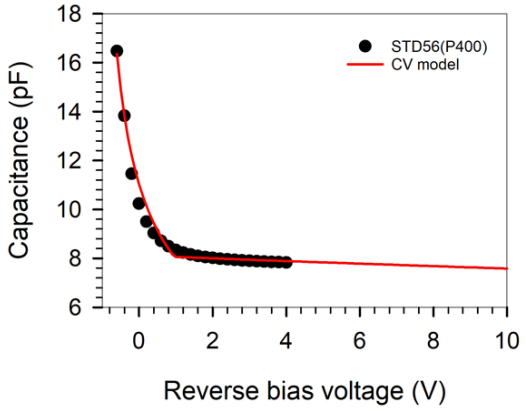
STD56(P400)
CV model
Capacitance (pF)
Reverse bias voltage (V)

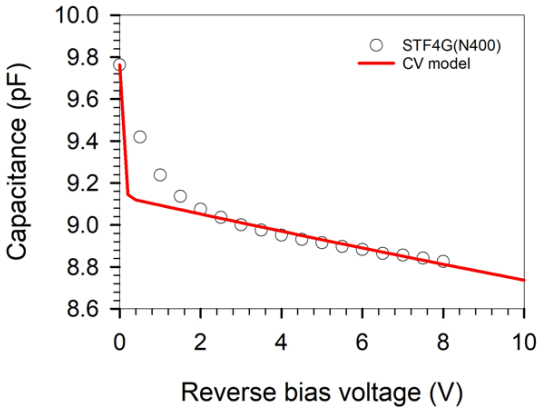
STF4G(N400)
CV model
Capacitance (pF)
Reverse bias voltage (V)

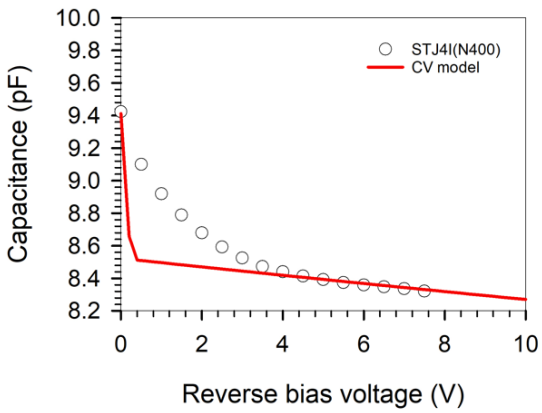
STJ4I(N400)
CV model
Capacitance (pF)
Reverse bias voltage (V)

Figure 5.25 Measured CV characteristics of p-i-n and n-i-p series, circle is the raw data of each sample and solid red line is modelled result from solving Poisson's equation. All CV simulation results were compared with the experimental data in diameter of 200μm devices.

Diode type	Layer No.	Nominal i-region thickness(nm)	CV Modelled results		
			i-region doping ($10^{15}cm^{-3}$)	i-region thickness w(μm)	(%) difference VS nominal thickness
$p-i-n$	STF85	100	216	112	+12
	STF81	200	5.5	185	-7.5
	STF84	400	17.5	397	-2.5
	STF83	800	5.5	730	-10
	STF82	1600	3.85	1442	-9.8
	STD53	400	8.8	477	+19.25
	STD56	400	15	450	+12.5
$n-i-p$	STFA7	100	236	98	-2
	STFAD	200	68	177	-11.5
	STFAE	400	18.2	365	-8.8
	STFAB	800	3.8	772	-3.5
	STFAC	1600	1.12	1380	-13.8
	STJ4A	400	12.9	375	-6.3
	STJ4G	400	11.7	395	-1.3
	STJ4I	400	11.4	410	+2.5

Table 5.5 Measured and modelled parameters of the GaAsBi diodes from CV

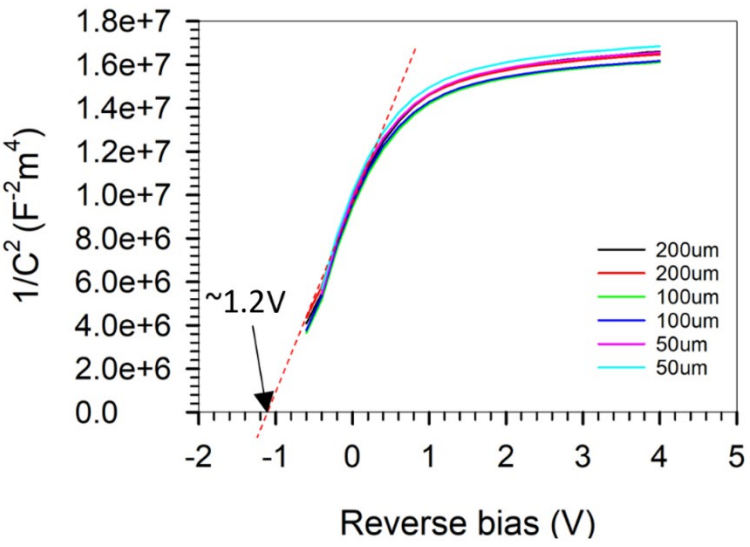

Figure 5.26 An example of $1/C^2$ versus voltage graph for STD56(N400) with different size of devices.

5.4.2 I-V characteristics

- Forward dark (IV) results

Forward I-V measurements were performed on each of the samples. Figure 5.27 shows an example of one p-i-n and n-i-p sample, which were measured with different size of

devices. The current density for both shows good area scaling, indicating the total dark current is determined by bulk mechanisms rather than surface mechanisms. The slope of the dark current as the function of voltage is not a single straight line, which becomes steeper beyond the 0.6 V that is the high injection region. As injecting more and more current, it will saturate the defects of device. Therefore, the ideality factor will improve, which shown in the red circle within the inset figure. This effect is easier to observe on the 25μm radius device because the larger size of the device has a high series resistance that will compensate for this effect.

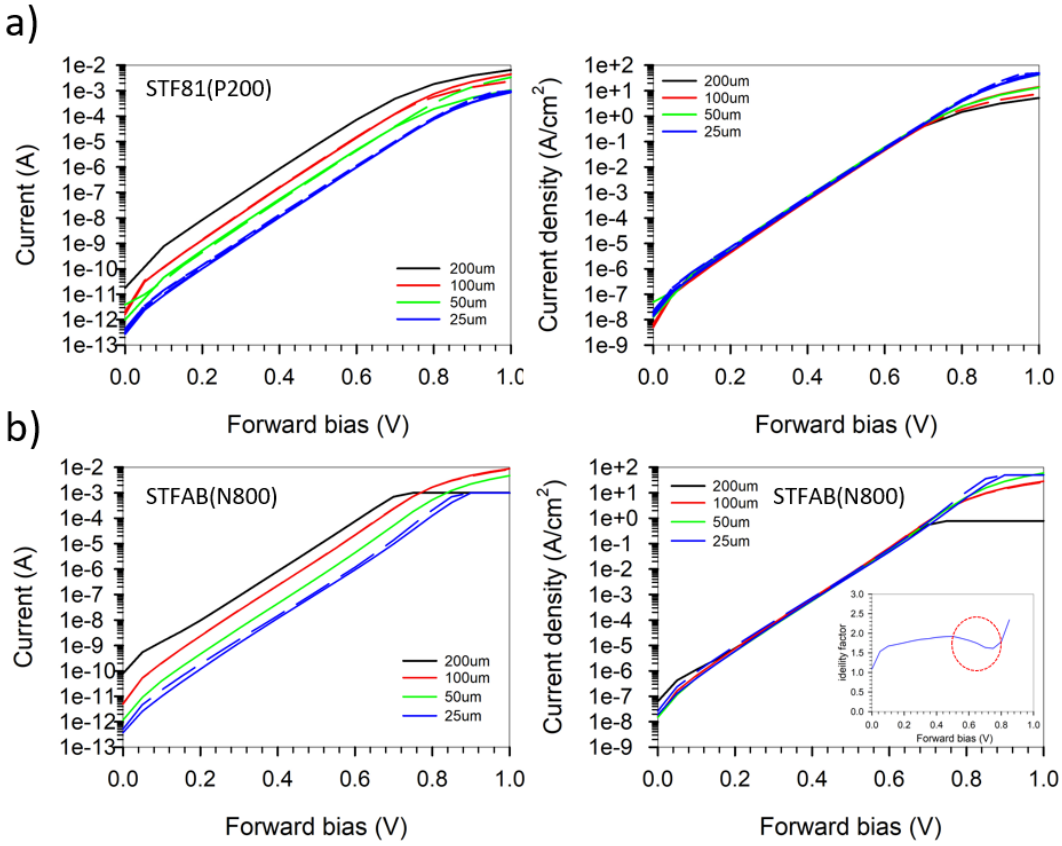

Figure 5.27 Forward IV and JV for a) STF81(P200) and b) STFAB(N200) measured with different size of devices, inset graph shows the ideality factor as a function of forward bias.

Figure 5.28 illustrates the J-V results at room temperature of different Bi content p-i-n and n-i-p samples. As a comparison, two 1.6 μm i-region thickness GaAs control samples and another GaAs solar cell with a low J_0 value reported by Kurtz *et al.* [34] are also shown in the graph. In order to avoid the series resistance effect and make comparison easily, the J-V graph is shown between 0.2 and 0.7 V.

From the graph, one of the dominant factors inducing high dark current is from the Bi content. A 5.5% Bi incorporation into GaAs will lead to a significant increase (over

five orders of magnitude) in dark current. The effect of increasing sample i-region thickness has less significant impact on the dark current when compared to varying Bi content, which can be seen by comparing STF85 and STF83. The dark current only increase less than half order of magnitude despite the increasing i-region thickness of 700nm. The dark current of the GaAs control sample grown by our group shows a two order of magnitude higher than that of the GaAs solar cell grown by Kurtz, suggesting that the sample growth quality can be further improved.

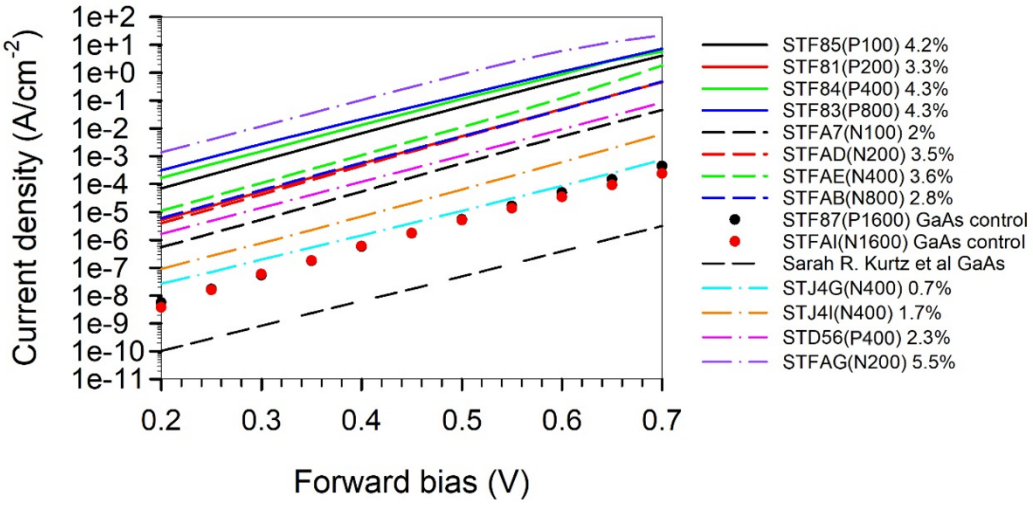

Figure 5.28 The forward IV semi-log plot of GaAsBi with different Bi content, 1.6μm p-i-n and n-i-p GaAs control grown by our group and another better GaAs solar cell result taken from Kurtz et al. [34] as a comparison.

Figure 5.29 shows the forward J-V of this work compared with a result from the literature. Figure a) shows the J-V data for a GaAsBi/GaAs solar cell reported by Muhammetgulyyev et al [35]. The solar cell has a 220nm thick GaAsBi i-region with Bi content (1.7%), which is the same Bi content as STJ4I. Comparing both JV results, the dark current of STJ4I is over two orders of magnitude lower than that of Muhammetgulyyev's solar cell and also has a better ideality factor (n=1.77 for STJ4I compared with n=2.3 for the solar cell). Besides, the solar cell exhibits a high series resistance after 0.6V. It should be noted that both samples have the same Bi content but the i-region thickness of STJ4I is twice as thick as the solar cell. Figure 5.29 b) is the comparison of the forward J-V between this work and GaAsBi photodiodes (PDs) reported by Kakuyama et al [36]. Three samples with same Bi content for our works are used to compare with the GaAsBi PDs. Both J-V and the ideality factor for our work show better results even though our samples have a thicker i-region. The improvement

could be due to the slightly higher growth temperature for our samples (378-410°C for our works rather than 360°C for PDs).

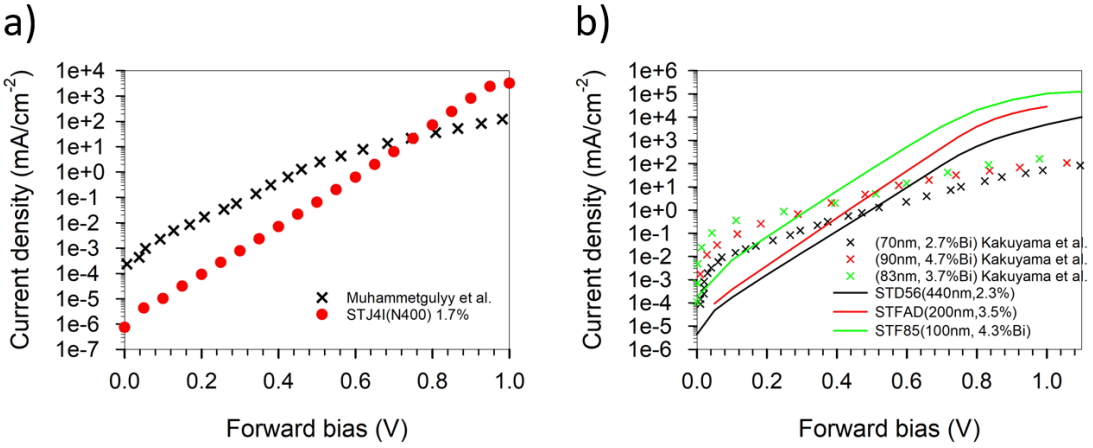

Figure 5.29 Comparison of J-V data between this work and results from the literature. a) J-V data for STJ4I and Muhammetgulyyev et al [35]. b) J-V data for STD56, STFAD, STF85 and Kakuyama et al [36].

The Shockley diode equation was mentioned in Section 4.4. Here we are interested in the J_o term in order to extract parameters for the electrical properties of our material. Table 5.6 lists the saturation current density, *Jo* and ideality factor for all the samples used in this work. The value of J_o can be obtained by extrapolating the intersect point between ln(*J*) and y-axis when V=0.

Diode type	***Layer No.***	***Saturation current density, J_0 (A/cm^2)***	***Ideality factor, n***
$p-i-n$	STF85(P100)	7.31×10^{-7}	1.77
	STF81(P200)	4.13×10^{-8}	1.71
	STF84(P400)	2.04×10^{-6}	1.81
	STF83(P800)	4.04×10^{-6}	1.88
	STF82(P1600)	5.98×10^{-6}	1.96
	STF87(P1600)	7.33×10^{-11}	1.71
	STD56(P400)	1.55×10^{-8}	1.79
$n-i-p$	STFA7(N100)	5.99×10^{-9}	1.70
	STFAD(N200)	3.76×10^{-8}	1.64
	STFAE(N400)	9.7×10^{-8}	1.68
	STFAB(N800)	5.18×10^{-8}	1.73
	STFAC(N1600)	2.43×10^{-7}	1.80
	STFAI(N1600)	5.4×10^{-11}	1.68
	STFAG(N200)	1.84×10^{-5}	1.83
	STJ4G(N400)	3.67×10^{-10}	1.92
	STJ4I(N400)	1.25×10^{-9}	1.77

Table 5.6 Saturation current density and ideality factor for GaAsBi and GaAs control sample.

The J_o from the forward I-V gives an indication of not just the E_g of the semiconductor but also of the quality of the p-i-n and n-i-p diode. The presence of dislocations would result in more mid-band states in the bandgap resulting in a much larger generation-recombination current. Qualitatively, we can see that for samples of similar thicknesses, increasing the Bi% increases the J_o significantly (Fig.5.28), and for samples with similar Bi%, increasing the layer thickness also results in an increase in J_o. Without TEM studies to quantify the dislocation density, we can only qualitatively attribute the increase in J_o to a higher density of dislocations in the structure.

The J_o is dependent on both electron and hole diffusion and generation-recombination mechanisms, which is described in Equation 5.3.

$$J_o \equiv \frac{qD_p n_i^2}{L_p N_D} + \frac{qD_n n_i^2}{L_n N_A} + \frac{qW_D n_i}{2\tau} \qquad (5.3)$$

Where the D_p (D_n) is the carrier diffusion coefficient for holes (electrons), n_i is the intrinsic carrier concentration, L_p(L_n) is the minority carrier diffusion length for holes (electrons) related to the minority carrier lifetime, and N_D and N_A are the donor and acceptor concentrations, respectively. W_D is the i-region thickness *and* τ is the minority carrier lifetime that is temperature-dependent.

Besides, J_o is also related to energy bandgap and temperature by the expression shown in Equation 5.4.

$$n_i^2 \propto \exp(-\frac{E_g}{kT}) \qquad (5.4)$$

By considering both equations, it is clear that J_0 will increase with decreasing energy bandgap. However, changing the energy bandgap is not the main reason causing the high value of J_0. Comparing the J_0 value between STFAG (GaAsBi 5.5%) and STFAI (GaAs) gives an over five orders of magnitude difference. The difference in bandgap values for those two samples should lead to three order of magnitude J_0 increase (assuming the other parameters are constant). Therefore, the possible reason for the further increase in J_0 could be due to the decrease of the carrier diffusion length or the localised trap states within the bandgap of the material when incorporating more Bi.

The total dark current is determined by both diffusion current and generation-recombination current mechanisms. As an indicator, the ideality factor shows which mechanism dominates the dark current density. From Table 5.6, the calculated ideality

factors between 1.6-1.9 for all samples suggests that both mechanisms have an impact on the dark current. The generation-recombination current is the dominating factor in this work since to the value of *n* is closer to 2.

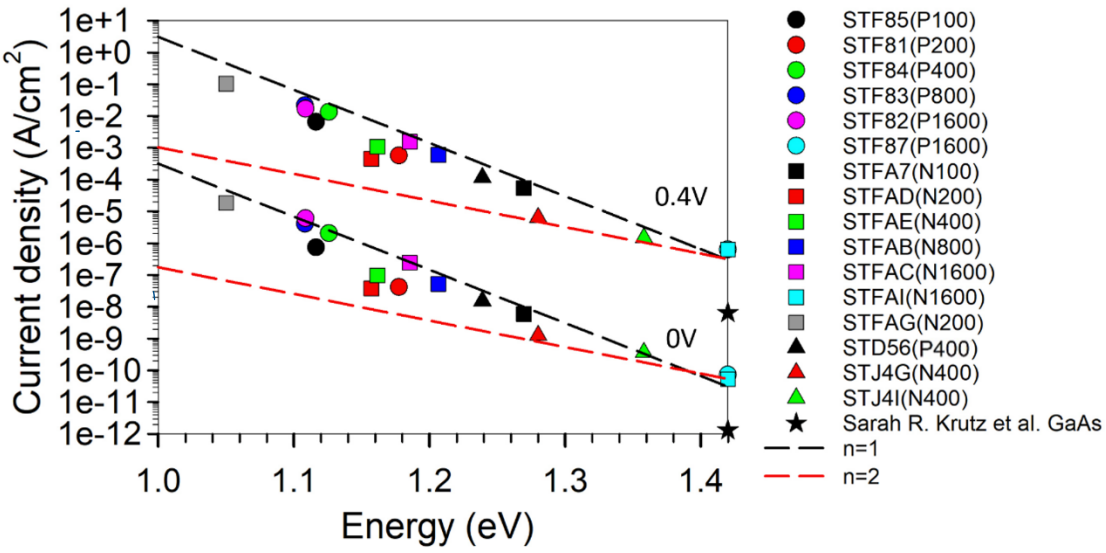

Figure 5.30 Dark current density J_0 at 0V and 0.4V as function of bandgap energy for both GaAsBi p-i-n and n-i-p samples.

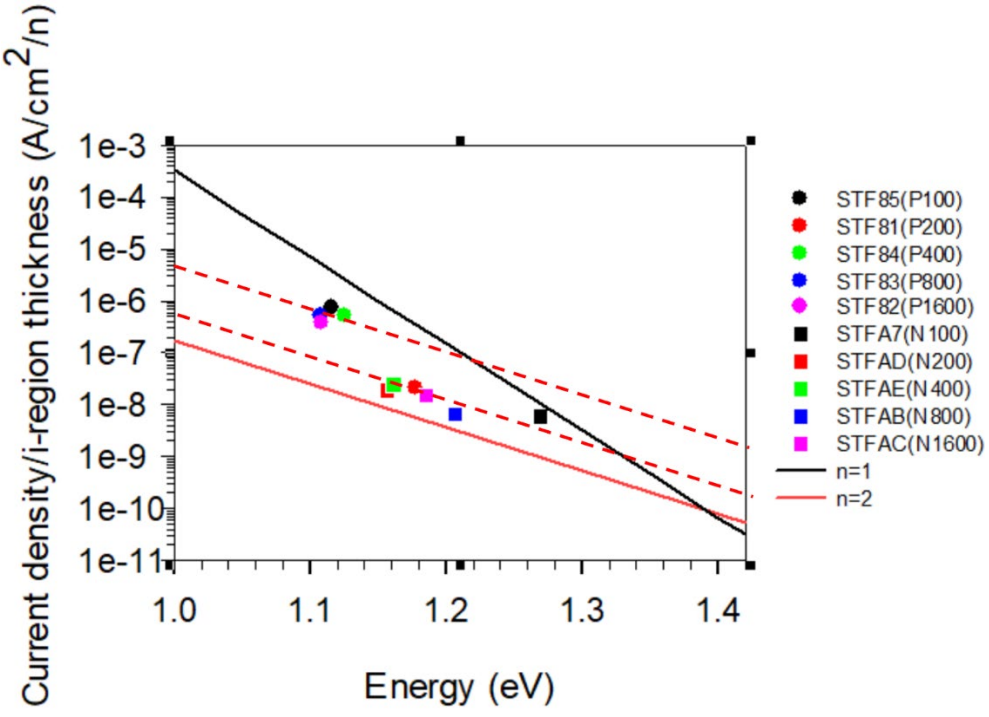

Figure 5.31 Dark current density J_0 for STF8 and STFA series after correcting i-region thickness. Dashed red line is the parallel line for n=2.

Figure 5.30 shows the dark current density J_0 for all samples in this work at 0V and 0.4V as a function of bandgap energy. In order to investigate the impact of Bi content

on the dark currents, Equation 5.5 was used to fit the J_0 data with n=1 and n=2, as shown in the black and red dashed lines in the figure, respectively.

$$J = A\exp(-\frac{E_g}{nkT}) \qquad (5.5)$$

Where A is a fitting constant, E_g is the energy bandgap and n is the ideality factor. From the graph, it shows that the dark current density of most samples lies on the n=1 line at both 0V and 0.4V. There are only two low Bi content samples STJ4G and STJ4I, which follow the n=2 fitting line. The deviation from the ideal case might be attributed to the different i-region thickness and growth temperature of each set of samples. After correcting i-region thickness, figure 5.31 shows J_0 for two sets of p-i-n and n-i-p samples at 0V. Both sets of samples now obey the theoretical generation-recombination n=2 line. The only exception is 200nm PIN sample, the discrepancy is likely due to the less Bi content (~1% difference) in 200nm p-i-n sample compared with other samples in the same set.

- Reverse dark (IV) results

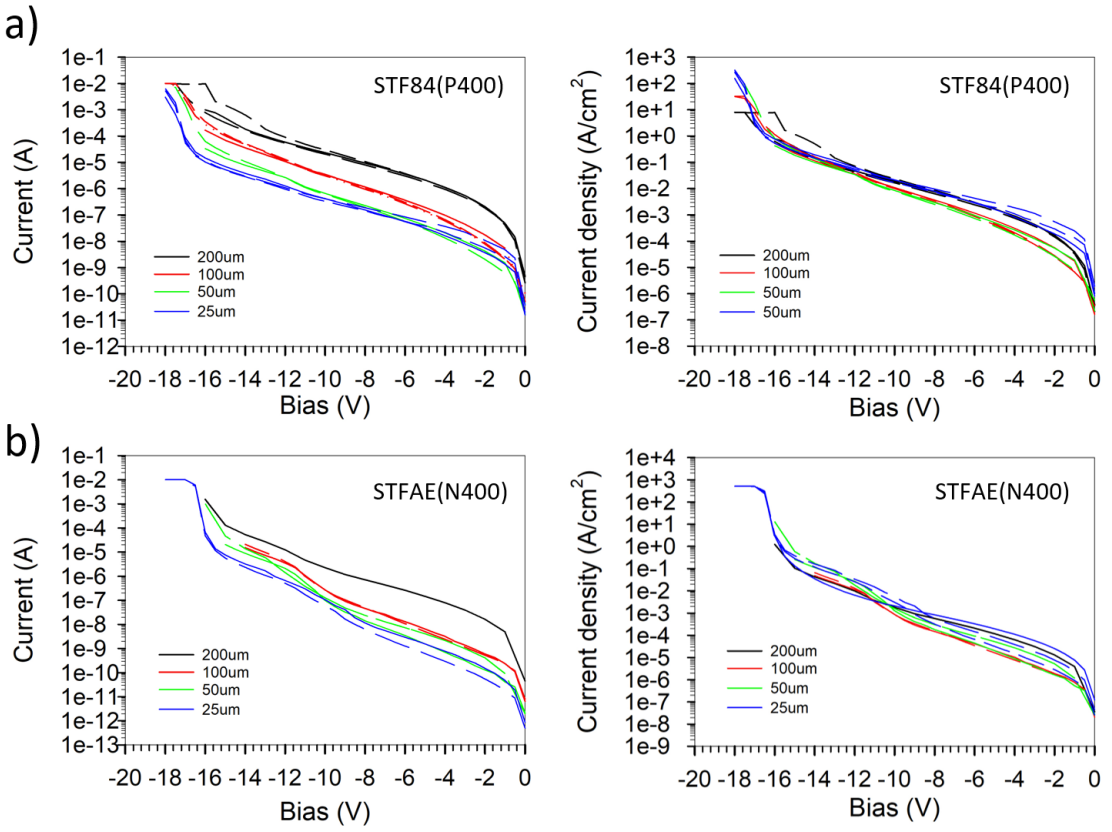

Figure 5.32 RT reverse IV and JV for a) STF84(P400) and b) STFAE(N400) measured with different size of devices.

Reverse bias *I-V* and *J-V* characteristics for STF84 and STFAE are shown in Figure 5.32. Four different sizes of devices were measured. For the same size of devices, the *I-V* results are relatively consistent. However, the *J-V* results show that not all the devices have dark currents that scale with device area. Both devices show one order of magnitude variation, which might be caused by the presence of surface leakage current. The surface conditions can be better controlled by passivating the devices.

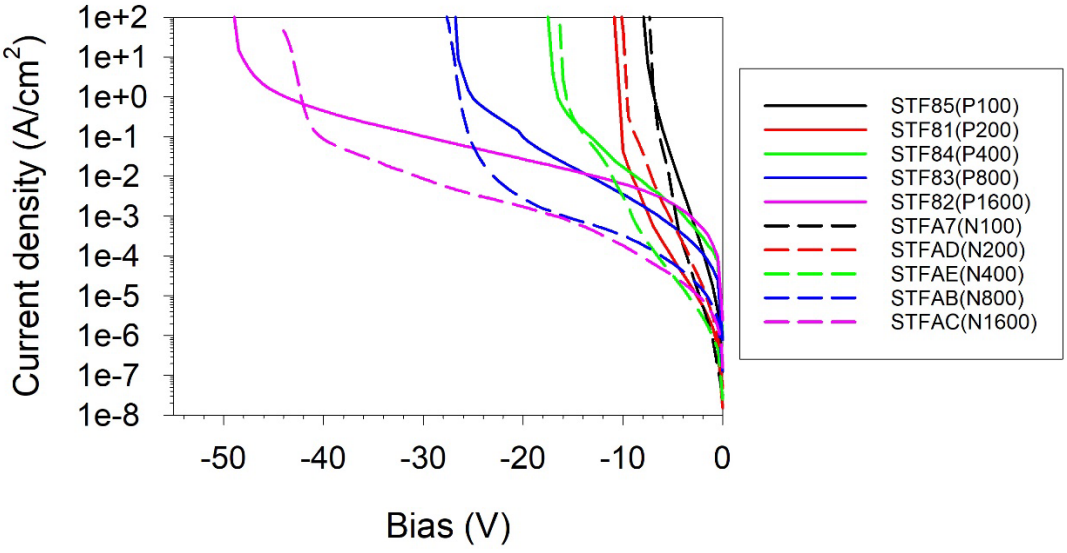

Figure 5.33 The reverse J-V semi-log plot of STF8 (p-i-n) and STFA (n-i-p) series

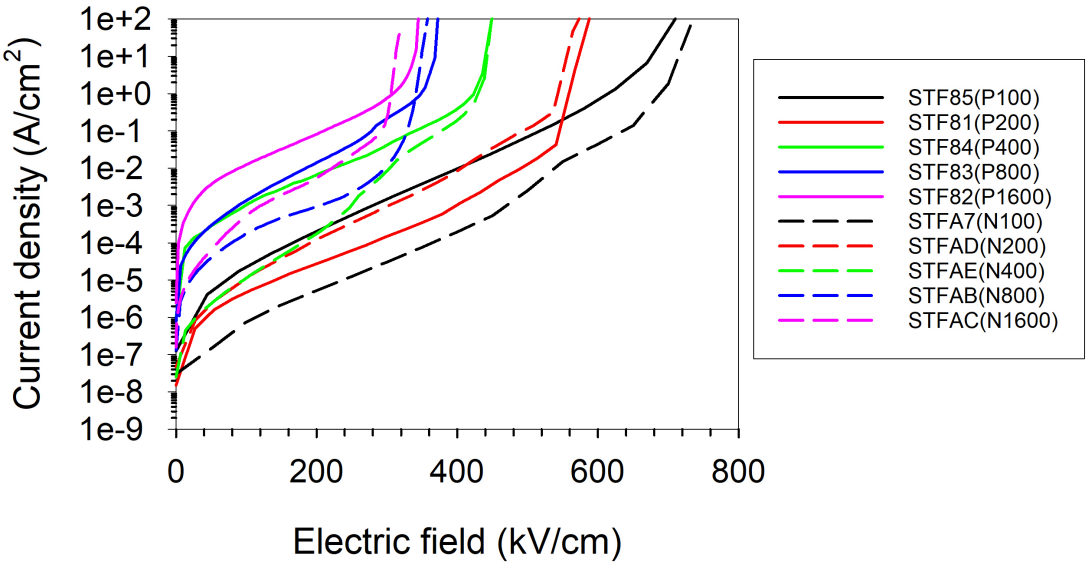

Figure 5.34 The reverse J-V semi-log plot of STF8 (p-i-n) and STFA (n-i-p) series as a function of electric field

The reverse dark current density as the function of reverse bias and electric field for STF8 (p-i-n) and STFA (n-i-p) series is shown in Figure 5.33 and Figure 5.34. The

breakdown voltages of each sample are sharp and well defined. The dark current is much higher compared with other mature materials, which can be explained by several reasons. Firstly, the bismuth is lattice-mismatched on GaAs substrate. When growing thicker layers, the strain relaxation becomes more critical, resulting in an increase of dislocation density in the devices. Secondly, in order to avoid bismuth surface segregation, a low growth temperature is used. The harsh growth condition leads to surface droplets, which will further reduce the performance of devices. From the graph, the dark currents of the n-i-p structures is generally smaller than that of the p-i-n structures with the same i-region thickness because the Bi content in the n-i-p structures is roughly 10% less than the p-i-n structures.

5.5 Summary

In this chapter, four sets of p-i-n and n-i-p diodes with different Bi content and i-region thickness have been studied. Both optical and electrical characteristics of samples have been investigated through various techniques.

Nomarski microscopy images showed that strain relaxation in the epilayer is related to the Bi content and sample thickness. The crosshatch pattern of image is a useful indicator that makes it easy for users to judge the critical thickness of the sample with a certain Bi content.

XRD measurements showed the existence of strain relaxation when layers thicker than 400 nm with 3.5% Bi content, which is consistent with the observations from the Nomarski images. Most of the samples do not show Pendellösung fringes indicating that the interface is not abrupt between the GaAs and GaAsBi layers. Besides, the broader peak of the epilayer indicated Bi content inhomogeneity during the layer growth. The simulation result of the two-layer model provided a better fit than that of the single-layer model.

Room temperature PL measurements showed that incorporating Bi into GaAs significantly reduce the energy bandgap, increasing the wavelength of detection. The bandgap reduction showed ~67meV/Bi for PIN and ~66 meV/%Bi for n-i-p, which is similar to values from the literature. The FWHM of the PL emission was dominated by the Bi content rather than the thickness of the sample. Compared with the work reported from the literature, the FWHM of PL in this work showed a lower value due to the better material quality.

C-V measurements showed that the background doping is on the order of 10^{15} cm^{-3} for the 1.6 μm GaAsBi p-i-n and n-i-p samples. This is similar to the GaAs control sample. C-V fitting was performed to estimate the i-region thickness and doping level by solving Poisson's equation.

I-V measurements were performed on each sample by measuring different sized devices. The results showed dark current characteristics that scaled with device area, indicating the bulk current mechanism is the dominating factor. The forward J-V result showed that the dark current gets higher with increasing Bi content. The high dark currents might be due to the Bi-induced dislocation and low-temperature growth condition. The ideality factor of devices is between 1.6 to 2 in this work. This indicates the generation-recombination mechanism of dark current is via the presence of trap states in the GaAsBi layer. By fitting the dark current density at 0V and 0.4V, the fitting line n=1 deviates from the real case n=2, which was attributed to different i-region thickness and growth temperature of each set of samples.

5.6 Reference

[1] F. Bastiman, A. R. B. Mohmad, J. S. Ng, J. P. R. David, and S. J. Sweeney, 'Non-stoichiometric GaAsBi/GaAs (100) molecular beam epitaxy growth', *J. Cryst. Growth*, vol. 338, no. 1, pp. 57–61, Jan. 2012, doi: 10.1016/j.jcrysgro.2011.07.036.

[2] S. Tixier *et al.*, 'Molecular beam epitaxy growth of GaAs1−xBix', *Appl. Phys. Lett.*, vol. 82, no. 14, pp. 2245–2247, Apr. 2003, doi: 10.1063/1.1565499.

[3] V. Pačebutas *et al.*, 'Characterization of low-temperature molecular-beam-epitaxy grown GaBiAs layers', *Semicond. Sci. Technol.*, vol. 22, no. 7, pp. 819–823, Jul. 2007, doi: 10.1088/0268-1242/22/7/026.

[4] M. Henini *et al.*, 'Molecular beam epitaxy of GaBiAs on (311)B GaAs substrates', *Appl. Phys. Lett.*, vol. 91, no. 25, p. 251909, Dec. 2007, doi: 10.1063/1.2827181.

[5] J. Puustinen *et al.*, 'Variation of lattice constant and cluster formation in GaAsBi', *J. Appl. Phys.*, vol. 114, no. 24, p. 243504, Dec. 2013, doi: 10.1063/1.4851036.

[6] M. Beaudoin *et al.*, 'Bandedge optical properties of MBE grown GaAsBi films measured by photoluminescence and photothermal deflection spectroscopy', *J. Cryst. Growth*, vol. 425, pp. 245–249, Sep. 2015, doi: 10.1016/j.jcrysgro.2015.01.019.

[7] F. Dybała *et al.*, 'Electromodulation spectroscopy of heavy-hole, light-hole, and spin-orbit transitions in GaAsBi layers at hydrostatic pressure', *Appl. Phys. Lett.*, vol. 111, no. 19, p. 192104, Nov. 2017, doi: 10.1063/1.5002622.

[8] C. Ryang Wie, 'High resolution x-ray diffraction characterization of semiconductor structures', *Mater. Sci. Eng. R Rep.*, vol. 13, no. 1, pp. 1–56, Sep. 1994, doi: 10.1016/0927-796X(94)90008-6.

[9] H. Achour, S. Louhibi, B. Amrani, A. Tebboune, and N. Sekkal, 'Structural and electronic properties of GaAsBi', *Superlattices Microstruct.*, vol. 44, no. 2, pp. 223–229, Aug. 2008, doi: 10.1016/j.spmi.2008.05.004.

[10] A. Janotti, S.-H. Wei, and S. B. Zhang, 'Theoretical study of the effects of isovalent coalloying of Bi and N in GaAs', *Phys. Rev. B*, vol. 65, no. 11, p. 115203, Feb. 2002, doi: 10.1103/PhysRevB.65.115203.

[11] D. Madouri, A. Boukra, A. Zaoui, and M. Ferhat, 'Bismuth alloying in GaAs: a first-principles study', *Comput. Mater. Sci.*, vol. 43, no. 4, pp. 818–822, Oct. 2008, doi: 10.1016/j.commatsci.2008.01.059.

[12] Y. Takehara *et al.*, 'Lattice Distortion of GaAsBi Alloy Grown on GaAs by Molecular Beam Epitaxy', *Jpn. J. Appl. Phys.*, vol. 45, no. 1A, pp. 67–69, Jan. 2006, doi: 10.1143/JJAP.45.67.

[13] M. K. Rajpalke *et al.*, 'High Bi content GaSbBi alloys', *J. Appl. Phys.*, vol. 116, no. 4, p. 043511, Jul. 2014, doi: 10.1063/1.4891217.

[14] M. Ferhat and A. Zaoui, 'Structural and electronic properties of III-V bismuth compounds', *Phys. Rev. B*, vol. 73, no. 11, p. 115107, Mar. 2006, doi: 10.1103/PhysRevB.73.115107.

[15] A. Belabbes, A. Zaoui, and M. Ferhat, 'Lattice dynamics study of bismuth III–V compounds', *J. Phys. Condens. Matter*, vol. 20, no. 41, p. 415221, Oct. 2008, doi: 10.1088/0953-8984/20/41/415221.

[16] A. Abdiche, H. Abid, R. Riane, and A. Bouaza, 'Structural and electronic properties of zinc blend GaAs1−xBix solid solutions', *Phys. B Condens. Matter*, vol. 405, no. 9, pp. 2311–2316, May 2010, doi: 10.1016/j.physb.2010.02.034.

[17] M. Mbarki and A. Rebey, 'First-principles calculation of the physical properties of GaAs $_{1-x}$ Bi $_{x}$ alloys', *Semicond. Sci. Technol.*, vol. 26, no. 10, p. 105020, Oct. 2011, doi: 10.1088/0268-1242/26/10/105020.

[18] M. Usman, C. A. Broderick, A. Lindsay, and E. P. O'Reilly, 'Tight-binding analysis of the electronic structure of dilute bismide alloys of GaP and GaAs', *Phys. Rev. B*, vol. 84, no. 24, p. 245202, Dec. 2011, doi: 10.1103/PhysRevB.84.245202.
[19] W. T. Stacy and M. M. Janssen, 'X-ray Pendellösung in garnet epitaxial layers', *J. Cryst. Growth*, vol. 27, pp. 282–286, Dec. 1974, doi: 10.1016/0022-0248(74)90444-8.
[20] P. F. Fewster, 'X-ray diffraction from low-dimensional structures', *Semicond. Sci. Technol.*, vol. 8, no. 11, pp. 1915–1934, Nov. 1993, doi: 10.1088/0268-1242/8/11/001.
[21] D. F. Reyes *et al.*, 'Bismuth incorporation and the role of ordering in GaAsBi/GaAs structures', *Nanoscale Res. Lett.*, vol. 9, no. 1, p. 23, Dec. 2014, doi: 10.1186/1556-276X-9-23.
[22] T. B. O. Rockett *et al.*, 'Influence of growth conditions on the structural and opto-electronic quality of GaAsBi', *J. Cryst. Growth*, vol. 477, pp. 139–143, Nov. 2017, doi: 10.1016/j.jcrysgro.2017.02.004.
[23] S. Francoeur, M.-J. Seong, A. Mascarenhas, S. Tixier, M. Adamcyk, and T. Tiedje, 'Band gap of GaAs1−xBix, 0<x<3.6%', *Appl. Phys. Lett.*, vol. 82, no. 22, pp. 3874–3876, Jun. 2003, doi: 10.1063/1.1581983.
[24] S. Mazzucato *et al.*, 'Low-temperature photoluminescence study of exciton recombination in bulk GaAsBi', *Nanoscale Res. Lett.*, vol. 9, no. 1, p. 19, Dec. 2014, doi: 10.1186/1556-276X-9-19.
[25] M. Yoshimoto, W. Huang, G. Feng, and K. Oe, 'New semiconductor alloy GaNAsBi with temperature-insensitive bandgap', *Phys. Status Solidi B*, vol. 243, no. 7, pp. 1421–1425, Jun. 2006, doi: 10.1002/pssb.200565270.
[26] X. Lu, D. A. Beaton, R. B. Lewis, T. Tiedje, and Y. Zhang, 'Composition dependence of photoluminescence of GaAs1−xBix alloys', *Appl. Phys. Lett.*, vol. 95, no. 4, p. 041903, Jul. 2009, doi: 10.1063/1.3191675.
[27] Z. Batool, K. Hild, T. J. C. Hosea, X. Lu, T. Tiedje, and S. J. Sweeney, 'The electronic band structure of GaBiAs/GaAs layers: Influence of strain and band anti-crossing', *J. Appl. Phys.*, vol. 111, no. 11, p. 113108, Jun. 2012, doi: 10.1063/1.4728028.
[28] J. Yoshida, T. Kita, O. Wada, and K. Oe, 'Temperature Dependence of GaAs $_{1-x}$ Bi $_{x}$ Band Gap Studied by Photoreflectance Spectroscopy', *Jpn. J. Appl. Phys.*, vol. 42, no. Part 1, No. 2A, pp. 371–374, Feb. 2003, doi: 10.1143/JJAP.42.371.
[29] K. Alberi, O. D. Dubon, W. Walukiewicz, K. M. Yu, K. Bertulis, and A. Krotkus, 'Valence band anticrossing in GaBixAs1−x', *Appl. Phys. Lett.*, vol. 91, no. 5, p. 051909, Jul. 2007, doi: 10.1063/1.2768312.
[30] V. Pačebutas, K. Bertulis, G. Aleksejenko, and A. Krotkus, 'Molecular-beam-epitaxy grown GaBiAs for terahertz optoelectronic applications', *J. Mater. Sci. Mater. Electron.*, vol. 20, pp. 363–366, 2009.
[31] B. Fluegel, S. Francoeur, A. Mascarenhas, S. Tixier, E. C. Young, and T. Tiedje, 'Giant Spin-Orbit Bowing in GaAs 1 − x Bi x', *Phys. Rev. Lett.*, vol. 97, no. 6, p. 067205, Aug. 2006, doi: 10.1103/PhysRevLett.97.067205.
[32] M. Masnadi-Shirazi, R. B. Lewis, V. Bahrami-Yekta, T. Tiedje, M. Chicoine, and P. Servati, 'Bandgap and optical absorption edge of GaAs $_{1-x}$ Bi $_{x}$ alloys with 0 < x < 17.8%', *J. Appl. Phys.*, vol. 116, no. 22, p. 223506, Dec. 2014, doi: 10.1063/1.4904081.
[33] P. Ludewig, N. Knaub, W. Stolz, and K. Volz, 'MOVPE growth of Ga(AsBi)/GaAs multi quantum well structures', *J. Cryst. Growth*, vol. 370, pp. 186–190, May 2013, doi: 10.1016/j.jcrysgro.2012.07.002.

[34] S. R. Kurtz, J. M. Olson, and A. Kibbler, ‘High efficiency GaAs solar cells using GaInP/sub 2/ window layers’, in *IEEE Conference on Photovoltaic Specialists*, May 1990, pp. 138–140 vol.1, doi: 10.1109/PVSC.1990.111605.
[35] A. Muhammetgulyyev, O. G. Erbas, B. Kinaci, O. Donmez, Y. G. Celebi, and A. Erol, ‘Characterization of a GaAs/GaAsBi *pin* solar cell’, *Semicond. Sci. Technol.*, vol. 34, no. 8, p. 085001, Aug. 2019, doi: 10.1088/1361-6641/ab23ab.
[36] K. Kakuyama, S. Hasegawa, H. Nishinaka, and M. Yoshimoto, ‘Impact of a small change in growth temperature on the tail states of GaAsBi’, *J. Appl. Phys.*, vol. 126, no. 4, p. 045702, Jul. 2019, doi: 10.1063/1.5109362.

Chapter 6. Room Temperature Avalanche Multiplication and Ionisation Coefficients of $GaAs_{1-x}Bi_x$ ($0 < x < 5.5\%$) Diodes

6.1 Introduction

With the continuous development of optical communication and optical fibre technology, the demand for high performance photodetectors increases. For both long haul and local area networks transmission, the 1.3 μm and 1.55 μm wavelength bands are widely concerned due to its low attenuation loss rate.

As internal photoelectric devices, PIN PDs and APDs have always been a popular choice to facilitate fibre optic networks, with a broad spectral coverage from UV to IR wavelengths. Owing to the requirement of low resistance ohmic contacts, a typical PDs structure consists of two highly doped p and n regions and a sandwiched intrinsic region. The advantages of PDs are low operating bias voltage, good temperature stability and a simple design. However, due to the lack of any internal signal amplification, it requires the assistance of an external amplifier. Unfortunately, the extra external amplification inevitably introduces noise (thus limiting the overall sensitivity), especially when a high bandwidth is required. An alternative to improve the signal to noise ratio is by employing an APD because of the internal gain mechanism obtained via carrier multiplication through the impact ionisation process. The SNR of the optical receiver (an APD incorporated with a preamplifier) can be expressed as

$$SNR = \frac{P_s}{FN_{sn} + N_{preamp} / M^2} \qquad (6.1)$$

Where P_s is the electrical signal power at unity gain, M and F are the multiplication gain and excess noise factors of the APD respectively. N_{sn} is the unity gain shot noise power of the APD and N_{preamp} is the noise power of the preamplifier. From the equation, when $N_{preamp} >> N_{sn}$ the SNR of the receiver is limited by term of N_{preamp}/M^2 at M=1. Therefore, operating a high gain APD will improve SNR significantly. Figure 6.1shows the case of $P_s > N_{preamp}$ and $P_s < N_{preamp}$ respectively. The SNR of the receiver is dominated by the excess noise of the APD. In order to obtain the maximum of SNR the APD noise should equal to the preamplifier noise, as shown in figure 6.1.

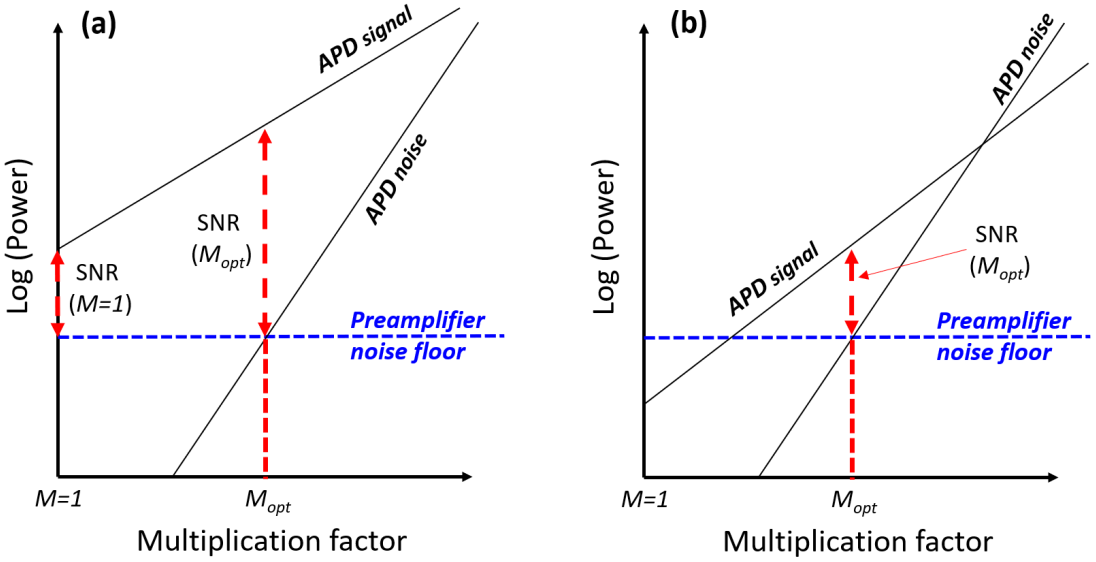

Figure 6.1 Schematic diagram illustrating the advantage of an APD over a p-i-n photodiode (M=1) in an optical receiver system. a) when the electrical signal power at unity gain is bigger than the preamplifier noise floor. b) when the electrical signal power at unity gain is smaller than the preamplifier noise floor. To optimise the SNR, the APD noise should equal to the preamplifier noise floor.

The internal gain, M, allows APDs to detect weak signals but also results in an avalanche excess noise, arising from the stochastic nature of the impact ionisation, limiting the maximum sensitivity of APDs. As mentioned in chapter 2, the excess noise is determined by the mean gain and the ionisation coefficient ratio, based on the work by McIntyre [1]. In order to achieve the lowest excess noise to make better performance APDs, one of the key solutions is to find a material with large disparate value of α and β. In the ideal case of β=0, there is only one carrier type involved during the impact ionisation process, so it will result in a small fluctuation in the ionisation events. Consequently, such small fluctuation will cause small changes in the mean gain and hence a lower excess noise.

A large number of efforts have been made to try to find the best way to reduce excess noise in APDs. The three main approaches will be described in the following sections.

- **Low excess noise APD with large disparate value of ionisation coefficient**

It is reported that silicon has made up over 25% of the total mass of the earth's crust [2]. Due to its large ratio of ionisation coefficient and low raw material cost, silicon has always been the best choice for high speed and low noise APDs. Figure 6.2 shows the

silicon ionisation coefficient for electron and hole, taken from [3], [4]. A high α/β ratio over 50 has been reported in the range of electric fields.

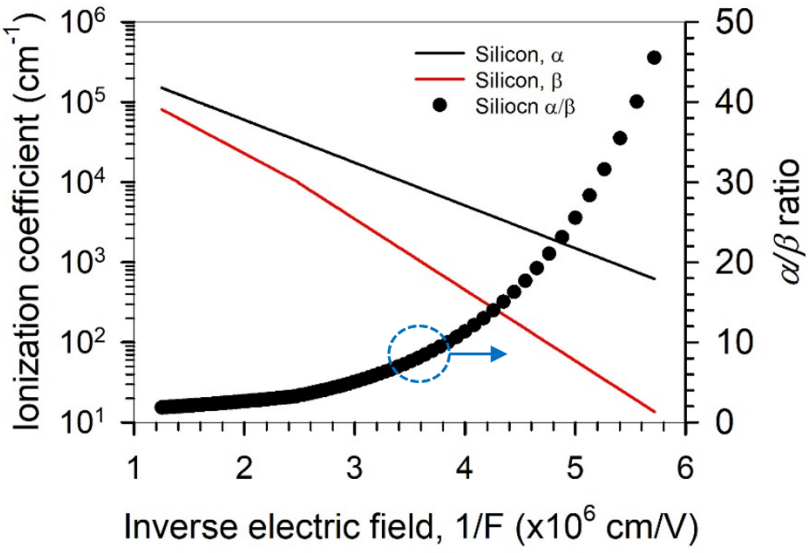

Figure 6.2 electron and hole ionisation coefficient of Silicon as a function inverse electric field, taken from [3], [4]. The dot line represents its α/β ratio.

Although silicon has an excellent ionisation coefficient ratio and extremely low excess noise, its cut-off wavelength limits the work performance to longer wavelengths near 1.3μm and 1.55μm.

Recently, two alloys, $Al_xIn_{1-x}AsSb$ [5], [6] and $AlAs_{0.56}Sb_{0.44}$ [7], [8] (lattice matched to GaSb and InP respectively) with bandgap energies of 1.5-1.3 eV have demonstrated large α/β ratios of between 10-100 and high avalanche gains with low excess noise. The large α/β ratio in $Al_xIn_{1-x}AsSb$ has been attributed to the digital alloy growth creating mini-bands in the valence band structure which impede holes from gaining the ionisation threshold energy from the electric field [9]. Although a digital alloy technique was also used to grow the $AlAs_{0.56}Sb_{0.44}$, its periodicity was much smaller and the reason for the large suppression of β was not clear.

- **Dead space effect improves the excess noise**

The multiplication and excess noise theory described in chapter 2 employed the local model that highly simplifies the impact ionisation process. In the local model, it assumes the carrier distribution is constant within the local electric field, neglecting the distance of a carrier that can acquire sufficient energy before initiating impact ionisation. This distance is called the dead-space distance. Early experimental works were mainly focused on thick bulk-like structures. Therefore, ignoring dead-space distance would

not change the experimental results because the distance of the dead space is much smaller relative to the whole avalanche region. A thick bulk-like structure limits the transmission speed and transit time of APDs. In these thin structures, it is found that the local model overestimates the multiplication gain and excess noise of the devices since the dead space distance is comparable to the multiplication region. Hu [10] and Li [11] have reported the excess noise characteristics of thin GaAs layers (W<1μm). They demonstrated that the excess noise decreases with decreasing avalanche width, even as the α/β ratio approaches unity, which is in contrary to McIntyre's noise theory [1]. Although these results proved that the dead-space effect is beneficial to lower the excess noise of APDs, the high tunnelling current incurred in these thin structures degrade the device performance. Therefore, it will be a trade-off between signal transmission speed and sensitivity.

- **Advanced APD structures**

In 2016, Ren *et al.* [12] demonstrated a 1-step AlInAsSb/GaSb APD based on the proposed staircase structure by Capasso *et al.* in 1982 [13]. A wide bandgap AlInAsSb layer is used to inject photogenerated carriers followed by a narrow bandgap AlInAsSb where impact ionisation will occur. This combination of materials is able to provide a conduction band discontinuity of 0.6 eV. The Monte Carlo simulations suggest a nearly excess-noise-free gain of ~2 and the measured noise is better than the control AlInAsSb photodiode. Recently, Chen *et al.* [14] showed low dark currents in InAs quantum dots grown on Si substrate operating at 1.31 μm. These complex structures increase the complexity of growth. In addition to that, under the high electric field, the carrier-initiated impact ionisation process occurs in the higher-lying bands rather than the minima of the conduction and valence band [15], [16]. Therefore, finding an effective way to enhance the α/β ratio of this higher-lying band will be a new challenge.

In this chapter, electron and hole multiplication characteristics have been obtained on the $GaAs_{1-x}Bi_x$ p-i-n and n-i-p structure with nominal i-region thicknesses of 100, 200, 400, 800 and 1600 nm. The electron and hole ionisation coefficients of this material have been, for the first time, determined using conventional local model analysis over an electric field range between 200 to 555 kV/cm. To verify the effect of varying Bi percentage on the ionisation coefficients, other sets of ~400nm thick p-i-n and n-i-p with varying Bi content have also been investigated. The optical and electrical

characteristics of the samples discussed in this chapter have been described in the previously.

6.2 Photomultiplication characterisation

The photomultiplication measurements on GaAsBi diodes were carried out using three different wavelength lasers, 405nm for pure injection; 633nm and 980nm for mixed injection. The laser spot needs to less than 20 μm shining on top optical windows of the diodes. As the reverse bias increases, the dark current of device increases quickly and so a lock-in-amplifier was used to extract the generated photocurrents. In order to evaluate the onset of multiplication, a baseline correction for primary photocurrent was proposed by Woods *et al.* [17] as mentioned in section 4.6. The repeatability of results can be evaluated by taking measurements on devices of different sizes and with different laser powers. The 405nm multiplication results for STF8 and STFA are shown in **Appendix III**. Details on the photomultiplication measurements can be found in section 4.6.

The thickness of top GaAs cap layer is 450nm for STF8 series p-i-n and STFA series n-i-p GaAsBi diodes. Based on the absorption coefficient of GaAs, the most striking difference is that the GaAs cap will absorb different proportions of light when a different wavelength laser, 99.9% for 405nm laser and 0.0001% for 980nm laser is used. Therefore, the 405nm light can be regarded as pure injection multiplication for both the p-i-n and n-i-p structure. In this case, minority carriers, either electrons or holes (depends on the device structure), generated in the cap layer will diffuse to the high electric field multiplication region. During this process, it is only one type of carrier that initiates the impact ionisation process.

When the 980nm laser is used, only 0.0001% of the light will be absorbed in the cap layer. In this situation, a mixed injection carrier profile will be present in the multiplication region. As the light will be absorbed in the multiplication region, within which electrons and holes will be generated, both of which will undergo impact ionisation. To support results obtained from the 405nm and 980nm wavelengths, measurements are also performed at 633nm wavelength. By using a 633nm laser, roughly 83.5% of photons will be absorbed in the 450nm GaAs cap. Therefore, the 633nm will generate an injection profile that is between 405nm and 980nm.

Table 6.1 lists the cap layer thicknesses of all samples used in this work. Besides, the proportion of light absorbed by the cap layer for each sample, information on the carrier injection profile at each measured wavelengths is also given.

Device name (i-region thickness)	Cap layer thickness (nm)	405nm laser		633nm laser		980nm laser	
		Test(√) or not(×)	Proportion of photon absorbed by cap layer(%)	Test(√) or not(×)	Proportion of photon absorbed by cap layer(%)	Test(√) or not(×)	Proportion of photon absorbed by cap layer(%)
STF85(P100)	450	√	~100 (Pure injection)	√	~83.5	√	~0 (mixed injection)
STF81(P200)		√		√		√	
STF84(P400)		√		√		√	
STF83(P800)		√		√		√	
STF82(P1600)		√		√		√	
STFA7(N100)		√		√		√	
STFAD(N200)		√		√		√	
STFAE(N400)		√		√		√	
STFAB(N800)		√		√		√	
STJ4A(N400*)	400	√	~100 (Pure injection)	√	~79.6	×	~0
STJ4G(N400*)		√		√		×	
STJ4I(N400*)		√		√		×	
STD53(P400*)	1000	√	~100 (Pure injection)	√	~98.1	×	~0
STD56(P400*)		√		√		×	

Table 6.1 Device testing information is this work

Figure 6.3 depicts the raw photocurrent data obtained from both p-i-n and n-i-p structures with nominal i-region thickness 100, 200, 400, 800 and 1600nm under 405nm, 633nm and 980nm light illumination. Due to the high dark current and bad surface morphology, it lacks data on n-i-p 1600nm structure. The magnitude of photocurrent depends on laser power, device size, measured resistance and absorption coefficient of the different wavelength. Therefore, the photocurrent in y-axis plotted in log scale are shown in arbitrary units to highlight the relative intensities. The photocurrent results are hard to see obvious difference in figure a) and b) due to the thin i-region. From figure c) and d), as devices goes thicker, a significant photocurrent increase (marked within dashed circle) is observed in the n-i-p structure initially, while this change is hardly find in the p-i-n structure within the same region. The rapid photocurrent change is affected by the wavelength of light, depending on absorption. Similar behaviour was also shown in thick 1600nm p-i-n structure in figure 6.3(e).

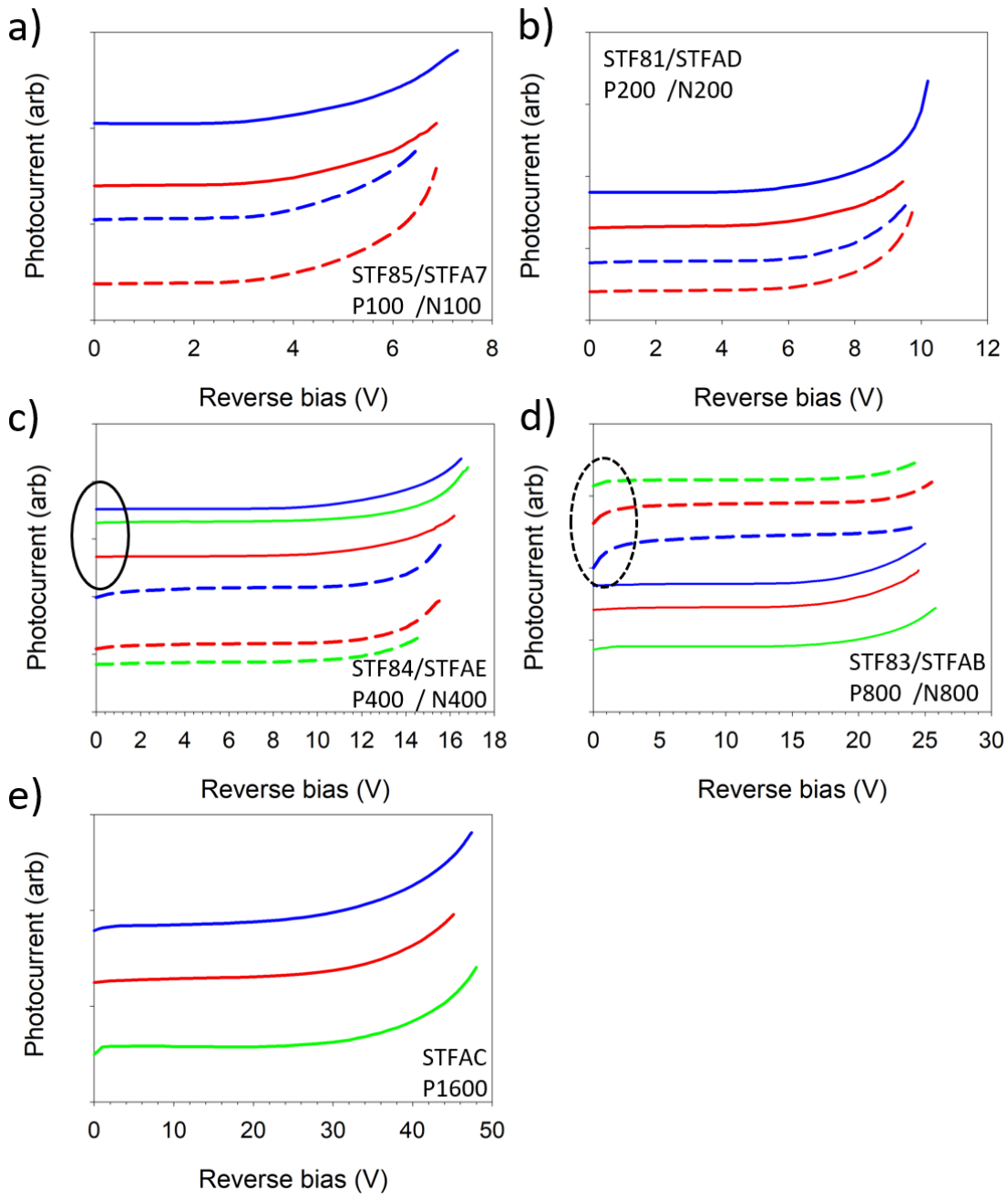

Figure 6.3 a)-e) The photocurrent measurement of 100nm-1600nm thick GaAsBi device illuminated with 405nm (blue), 633nm(red) and 980nm(green) laser light. The solid line represents the p-i-n structure and dashed line represents the n-i-p structure. In order to analysis the effect of wavelength-dependent multiplication on each of devices, the raw photocurrent data plotted in log scale are vertically offset for clarity.

Such behaviour can be explained as in Figure 6.4. The intrinsic region is unintentionally n-type doped so the p-n junction forms at p-i interface and i-p interface in p-i-n and n-i-p strucutre respectively. The incident light shines on either p^+ or n^+ layer for the p-i-n and n-i-p structure. The generated electron-hole pair diffuses into the intrinsic region,

as shown in Figure 6.3 a) and b). Based on the absorption coefficients of cap materials, the distribution of light absorption across the diode varies with the wavelength. As the reverse bias increases, the depletion edge moves towards to the bottom n^+ layer in the p-i-n structure and vice verse in the n-i-p structure. Therefore, regardless of any different wavelength laser, there is no significant change of the photocurrent at the iniatial few bias voltage in the p-i-n strucuture. In contrast, in the n-i-p structure, a certain diffusion distance restricts the carrier collection efficiency, especially at short wavelength.

For the thin structure with 100nm and 200nm i-region, the intrinsic region is fully depleted at zero volts. Therefore, at the initial few volts the photocurrent does not show any obviously changed for the thin layer structure.

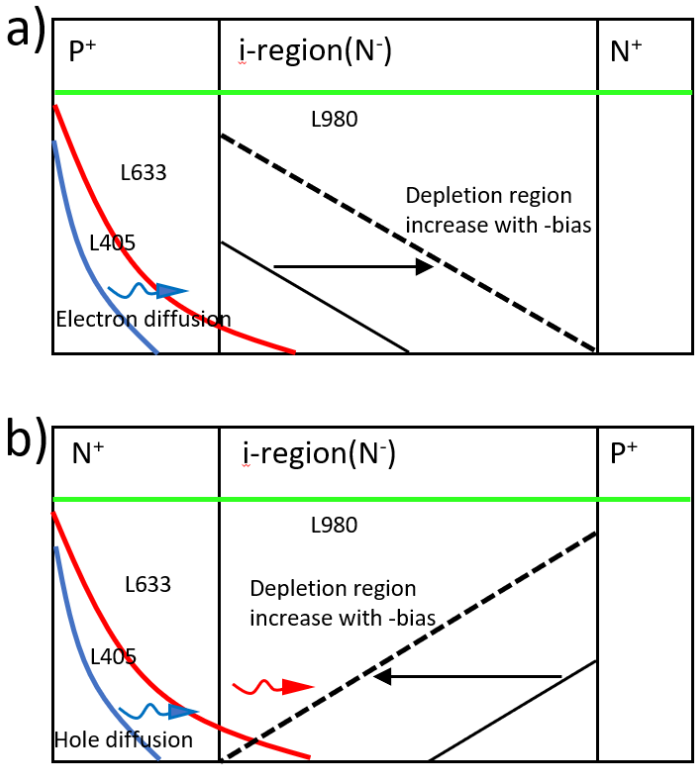

Figure 6.4 Illustration of the mechanism for the initial photocurrent on a) p-i-n and b) n-i-p structure under 405nm (blue), 633nm(red) and 980nm(green) laser light.

In order to obtain the actual primary photocurrent with increasing bias and the onset of multiplication, a baseline correction in the form of $I_{pr}=aV_b+b$ needs to be applied (full details of baseline correction are described in the section 4.6). Examples of baseline correction for the P400 and N800 samples, under the different carrier injection conditions, are shown in Figure 6.5. The red dashed line is the primary photocurrent of

the devices. The multiplication of each device is the ratio between the total photocurrent and primary photocurrent at each bias. It is clear that the onset of multiplication occurs earlier for the pure injection(405nm) rather than the mixed injection (633nm and 980nm) in the p-i-n structure and is opposite in the n-i-p structure.

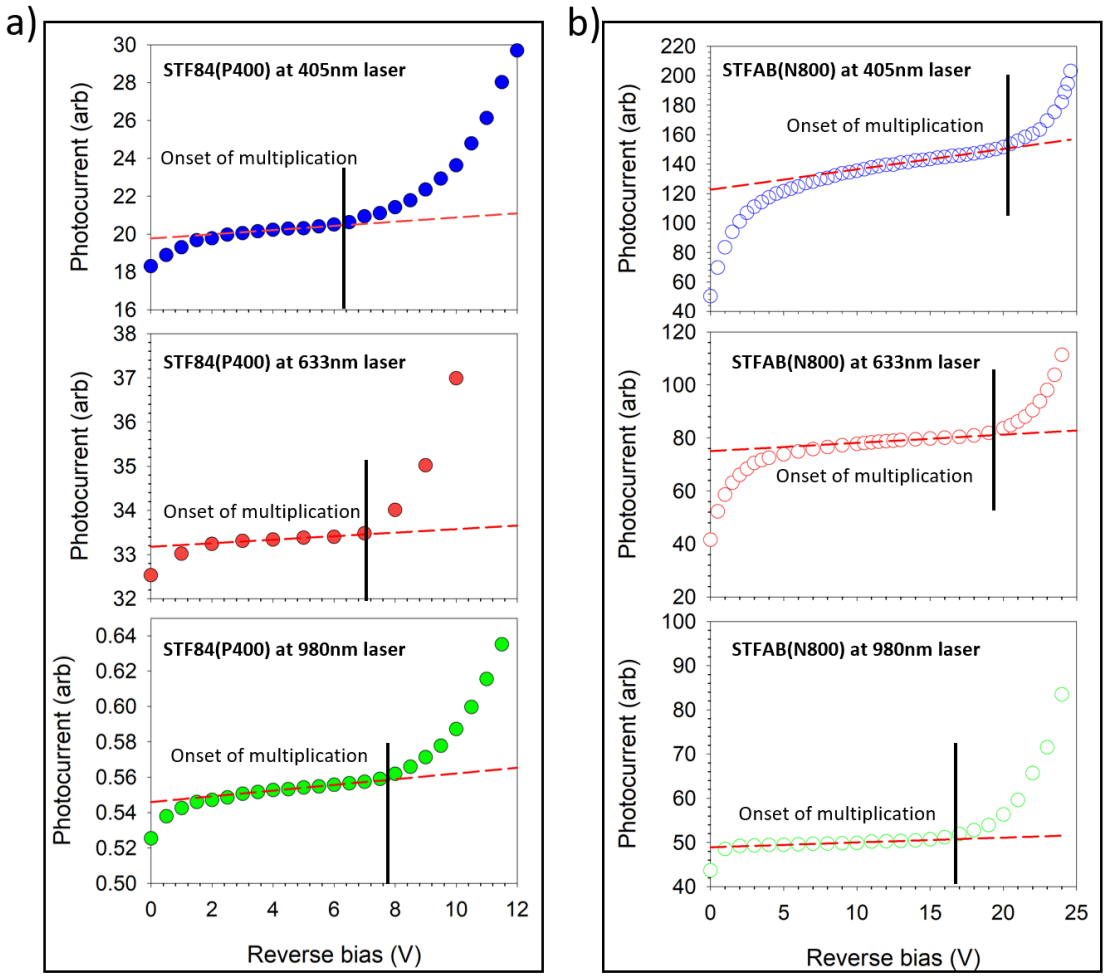

Figure 6.5 a) Baseline correction of STF84 p-i-n 400nm GaAsBi structure and b) STFAB n-i-p 800nm GaAsBi under the 405nm (Blue), 633nm (Red) and 980nm (Green) light, the dash red line represents the primary photocurrent based on the woods' correction.

The examples of multiplication characteristics with nominal i-region thickness 400, 800 and 1600nm p-i-n and n-i-p structure are shown in Figure 6.6. After the normalisation, identical multiplication results were obtained by taking measurements on different devices, of different sizes and with different laser powers to ensure the repeatability of results. From Figure 6.6(a), (c) and (e), it can be seen that the pure electron injection multiplication, using 405nm laser, are consistently higher than those measured under the mixed injection condition, using 633nm and 980nm laser, in the p-i-n structure. The opposite, is shown in Figure 6.6(b) and (d) for the n-i-p structure, where the mixed

injection multiplication is higher than pure hole injection multiplication. Such behaviours give the indicator of $\alpha > \beta$ in this material. For the 800nm n-i-p structure, it is noticeable that multiplication due to pure hole injection is extremely low, even at near breakdown voltages. It is a strong indication that hole impact ionisation is suppressed in this electric field range.

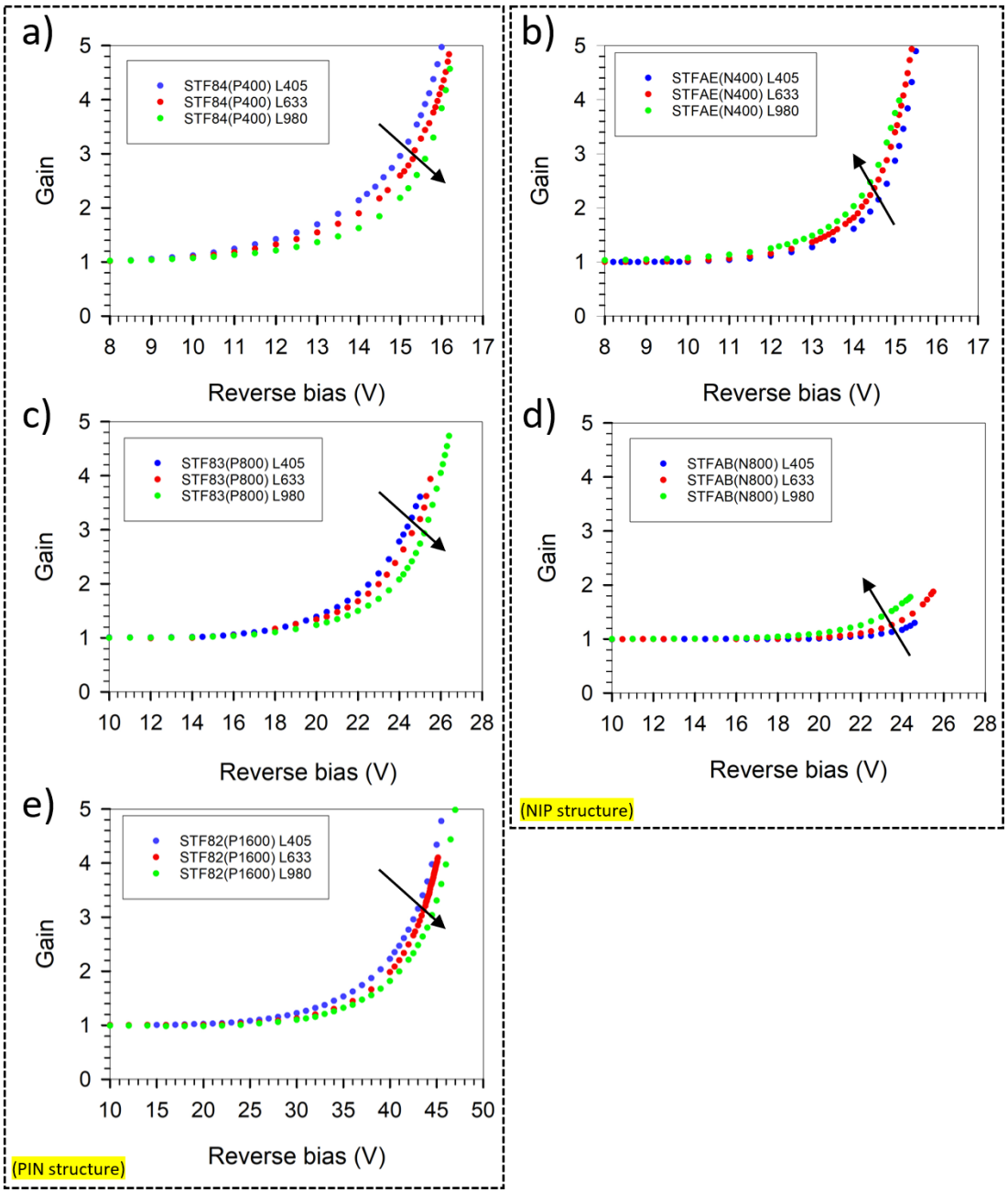

Figure 6.6 a)-e)Wavelength-dependent photomultiplication results on STF84(400nm)p-i-n, STFAE(400nm)n-i-p, STF82(800nm)p-i-n, STFAB(800nm)n-i-p and STF82(1600nm)p-i-n are illuminated under the 405nm(blue), 633nm(red) and 980nm(green) laser light, respectively.

The wavelength dependence of multiplication results for four thin structure with nominal i-region thickness 100nm and 200nm are plotted in *M-1* to distinguish the difference in the low gain region, as shown in Figure 6.7(a)-(d). The wavelength of 980nm laser was too long for reliable multiplication to be obtained in the thin structure. Therefore, only 405nm and 633nm results are given here. The thin structure in comparison with thick structure showed similar wavelength dependence of multiplication. It is found that the pure injection multiplication using 405nm light is marginally higher than the mixed injection multiplication extracted by using 633nm in the p-i-n structure and vice versa in the n-i-p structure. The small difference between 405nm and 633nm results can be explained by three factors. First, based on the absorption measurement for penetrating 450nm cap layer, 405nm light is fully absorbed while 633nm light is roughly 83.5% absorbed. Consequently, M_{mix} does not differ as significantly as M_e or M_h. Second, the ionisation coefficients of electron and hole are approaching unity at the high electric field range. Besides, the thin structure is also strongly affected by the dead space effect, which further complicates the analysis.

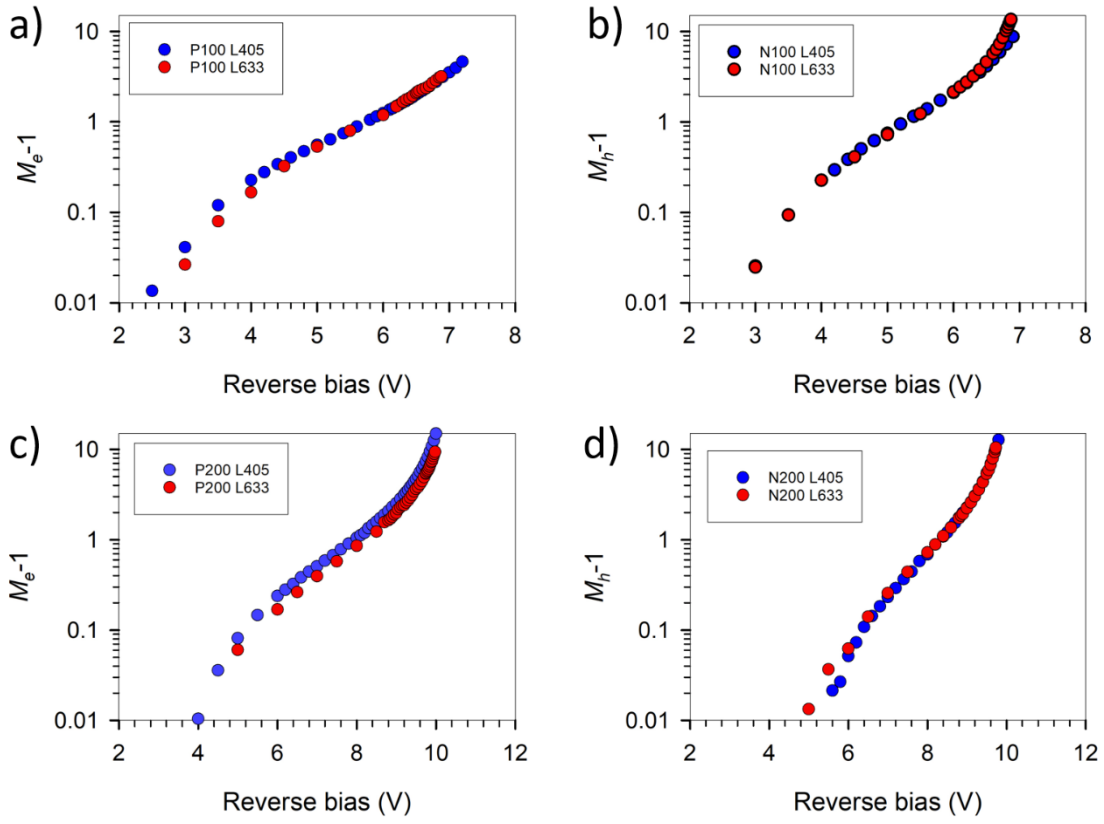

Figure 6.7 a)-d) photomultiplication results on thin 100nm and 200nm GaAsBi p-i-n and n-i-p structure are illuminated under the 405nm(blue) pure and 633nm(red) light.

The multiplication characteristics of varying Bi content samples will be discussed in the following section. To investigate the relationship among the onset multiplication, Bi content and i-region thickness, Figure 6.8 shows the four different cases in the p-i-n and n-i-p structure. In here, we consider only the pure injection multiplication.

The electron and hole-initiated multiplication characteristics with increasing Bi% are shown in Figure 6.8(a) and (b) respectively. Figure 6.8(c) and (d) shows the electron and hole-initiated multiplication of varying thick intrinsic region samples with similar Bi content. These graphs were shown by the plot of *M-1* on a logarithmic scale to highlight the onset of impact ionisation (defined here as when M=1.01) in the p-i-n and n-i-p structure.

From these results, the Bi% is clearly the more dominant factor in controlling the onset of impact ionisation than the thickness of the intrinsic region. In Figure 6.8(c), although these three samples have similar Bi content with different thickness, the threshold electric field is unchanged. Similar results are observed in Figure 6.8(d), the threshold electric field for the onset of ionisation is very close for the 400nm thick sample (STFAE) with 3.6% Bi and 200nm thick sample (STFAD) with 3.5% Bi. In contrary, for samples with a similar thickness but with different Bi%, the onset of ionisation of the p-i-n sample has much less effect compared with that of the n-i-p sample, as shown

in Figure 6.8(a) and (b). The hole ionisation is affected more by Bi% than electron ionisation.

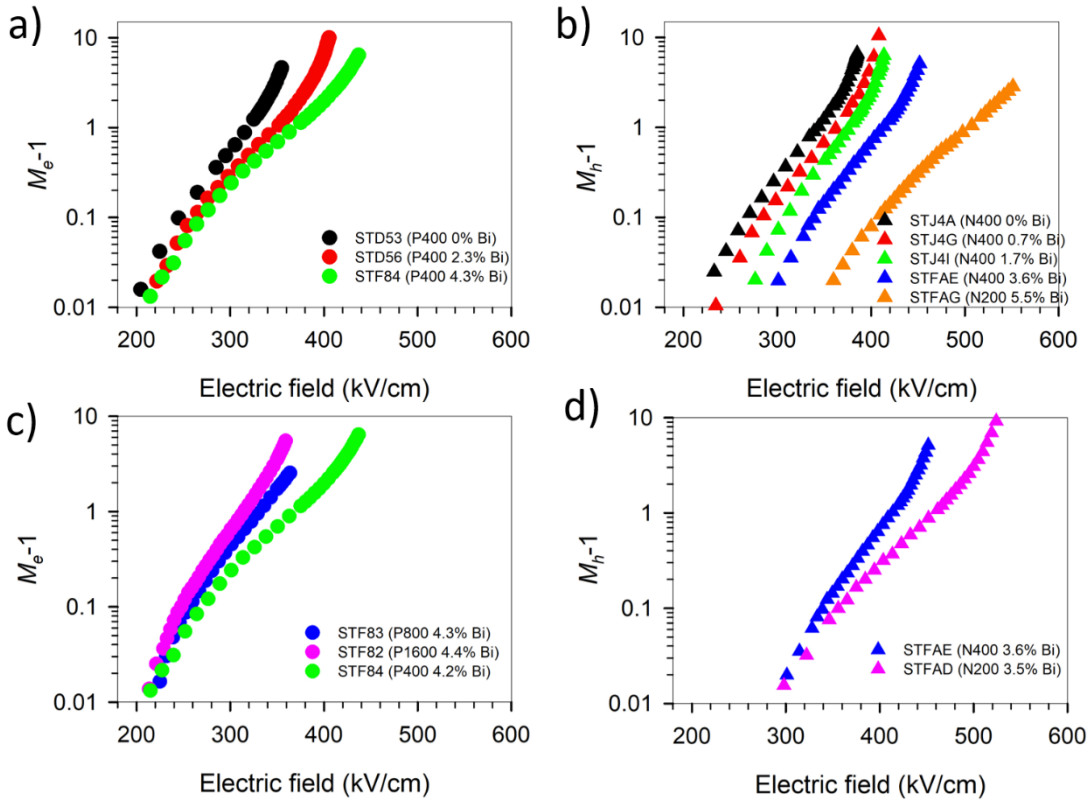

Figure 6.8 Me-1 (Mh-1) vs electric field for the 400 nm thick p-i-n (n-i-p) diodes of varying Bi content at 405nm light. The simulated results are also plotted in Figure as blue solid line for purposes of comparison. c), d) Me-1(Mh-1) vs electric field for different i-region thick p-i-n diodes with similar Bi content.

During the photomultiplication measurements, a series of problems related to the sample itself and the external influence will affect the accuracy and correctness of the experimental data, so to understand these problems and try to avoid it will benefit the experiment. The challenges in photomultiplication measurements can be summarised in four points.

- The low growth temperature used will degrade both the electrical and optical properties. The dark currents for most of the samples are in the μA levels.
- Due to the high dark current, it is hard to do the measurement on the biggest size of diodes (200μm radius) to obtain desirable result. However, a lower photocurrent will be obtained from the smaller devices due to the smaller optical window. Therefore, in order to obtain a measurable photocurrent and a precise primary photocurrent, either a higher resistance or a higher laser power should

be used. The higher resistance might result in a strong series resistance effect in the measurements. Besides, at the low electric field, the high resistance we used will introduce a voltage drop on the multiplication results, causing the actual voltage applied on the devices to be lower than the voltage we set. Although the high laser power can provide strong photocurrent, the overall dimension of the laser spots will increase. If the size of the laser spot is larger than that of the DUT, the light will fall on the sidewall of the mesa structure. In such a case, the injection profile will become mixed and affect the multiplication measurement.

- The Franz-Keldysh effect is also a big issue during the measurement. Due to the Bi content varying with the sample, the bandgap of each sample is different. Therefore, to avoid within Franz-Keldysh region, choosing a proper wavelength of the laser is important.
- The uniformity testing of devices is crucial for pure injection multiplication in both the p-i-n and n-i-p structure, the method is to move the laser spot on the different positions of the device and then compare the photocurrent that is recorded. For example, the photomultiplication results of the three n-i-p structure devices that measured by using laser on the different position are shown in Figure 6.9(a)-(c). Figure 6.9(d) depicts the laser spot position on the devices in this work. Whatever the location of laser spot in the measurement, the n-i-p 100nm sample shows an excellent uniformity of devices. However, the uniformity of the n-i-p 400nm and n-i-p 800nm devices are not as good as we expected. When the laser spot shines on the top and right position, it is observed that the onset of multiplication starts at a lower reverse bias, which is quite similar to mix injected multiplication. This might be due to the non-uniformity of etching. Therefore, the laser spot must be kept away from these two positions during the pure carrier injection measurement.

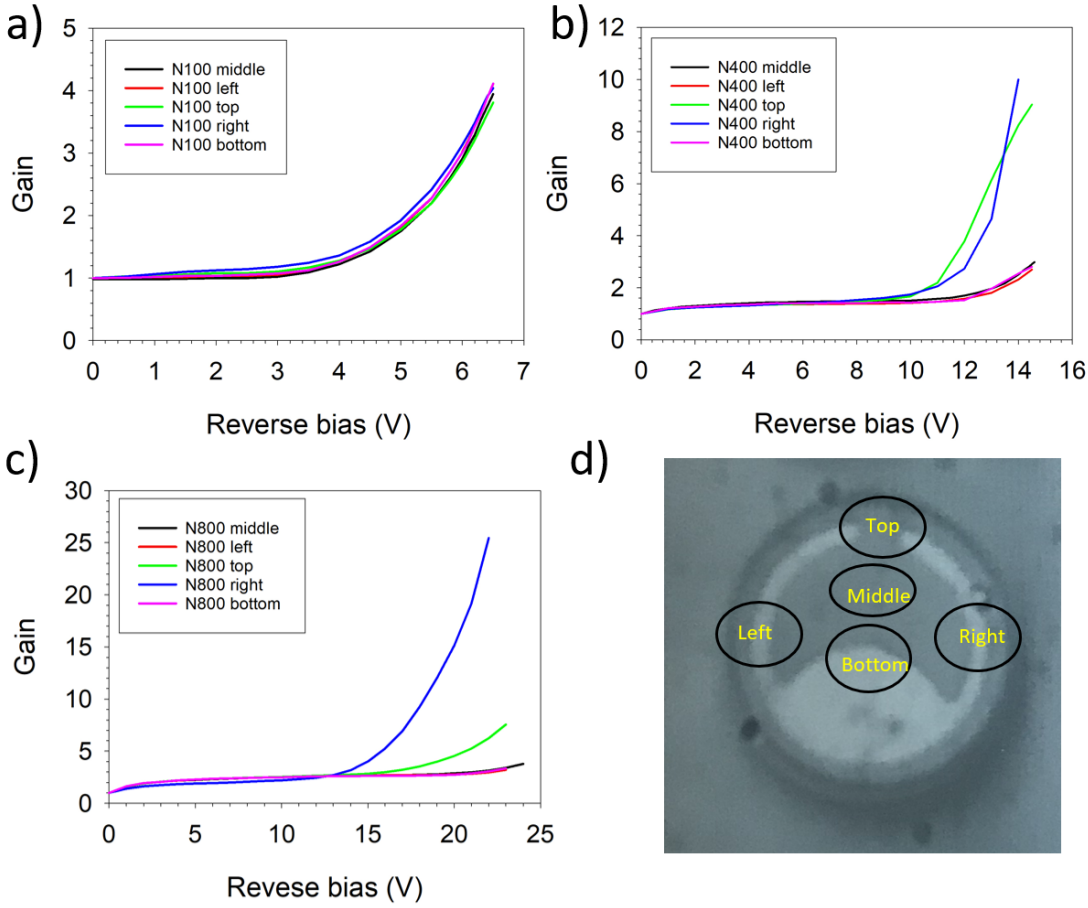

Figure 6.9 a)-c) Multiplication gain on different position of n-i-p 100nm, n-i-p 400nm and n-i-p 800nm sample b) Position of laser spot on the 100μm radius device under test.

6.3 Discussion

6.3.1 Impact ionisation coefficient

The thickness and doping density of intrinsic layer for each diode can be extrapolated from CV measurements, the unintentional doping density of the thickest sample is similar to the GaAs control sample, in which the doping density is $1e^{15}cm^{-3}$. Therefore, the local model is adapted in this case, assuming a uniform electric field applied in the intrinsic region.

With the assistance of the 405nm laser, the pure carrier injected multiplication, M_e and M_h of the p-i-n and n-i-p diodes as a function of reverse bias voltage are obtained. From M_e, the multiplication taken from the p-i-n structure with the similar Bi content and the different intrinsic thickness, it will obtain two alpha lines assuming that two extreme cases $\alpha = \beta$ or $\beta = 0$. These two α lines diverge at the high electric field and combine at the low electric filed, and such trend can give an initial accurate indication of α at the low electric field. The approximate location of the α line for a certain Bi content can

be extracted by using the simulation based on the empirical expression to fit the α at the low electric field. In order to extract the β line for a certain Bi content, the M_e and M_h for the same thickness p-i-n and n-i-p diodes need to be obtained. Due to the lack of pairs of sample with similar Bi content between the p-i-n and n-i-p diodes, the α and β of some Bi content samples were extrapolated by the simulated M_e and measured M_h. The true α and β was verified by an iterative technique until a good fit of M_e-1 and M_h-1 was found between the experimental and simulation data by adjusting the thickness of the intrinsic region slightly.

Both experimental data and the simulated results for all samples in this work are plotted in *M-1* on a logarithmic scale as the function of reverse bias, as shown in Figure 6.10. The simulated results use the parameterised ionisation coefficients taken from Table 6.2. An excellent fitting is obtained even at low gains around 1.01.

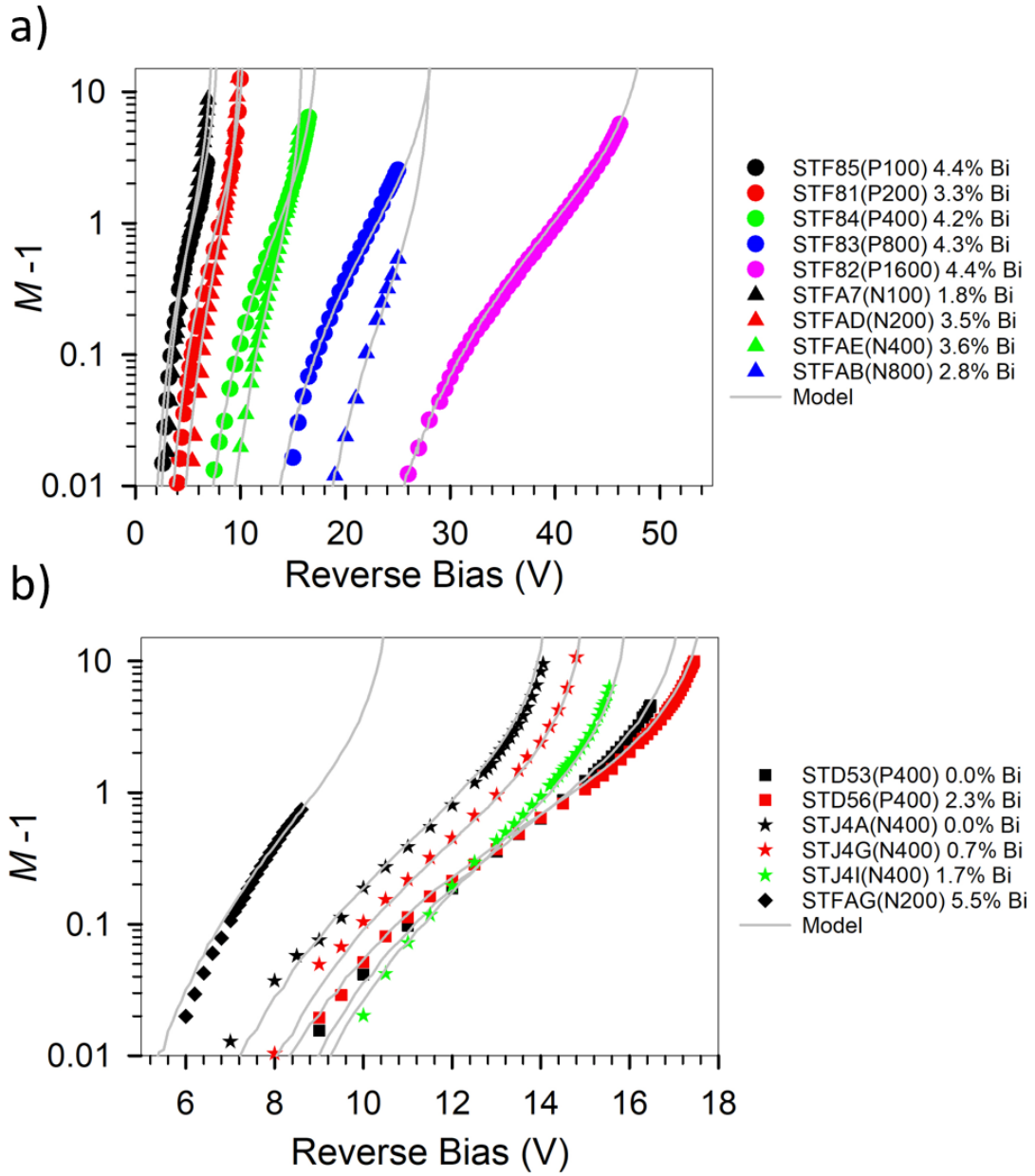

Figure 6.10 a) Experimentally obtained M-1and modelled(lines) for STF8 series(●symbol) and STFA series(▲symbol) samples. b) a) Experimentally obtained M-1 and modelled (lines) for STD5 series (■ symbol), STJ4 series (★ symbol) and STFAG sample(♦symbol).

Figure 6.11 and 6.12 depict the ionisation coefficients, α and β, for different Bi content from 0% to 5.5%. It can be seen from Figure 6.11 that α value only decreases slightly from GaAs to 5.5% GaAsBi sample. However, a dramatic decrease was observed in β, especially at the lower electric fields. The unique changes that ionisation coefficient of β has a significant drop while ionisation coefficient of α virtually unchanged was the first time observed in III-V alloy system.

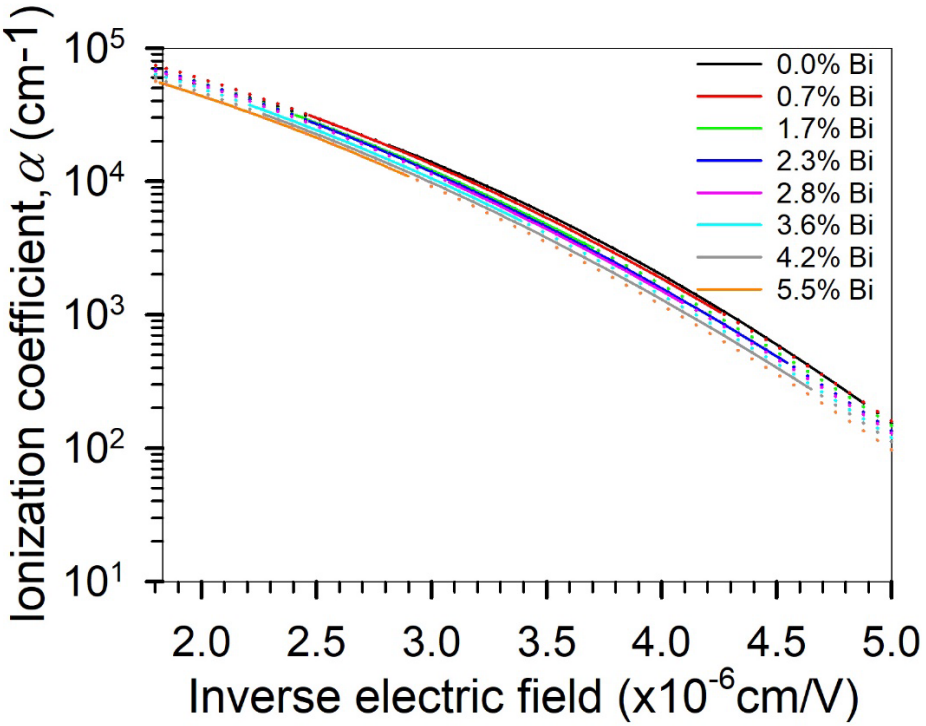

Figure 6.11 Alpha of GaAs1-xBix as a function of inverse electric field at a range of Bi contents. Dashed lines are the simulation and solid lines represents the experimental data.

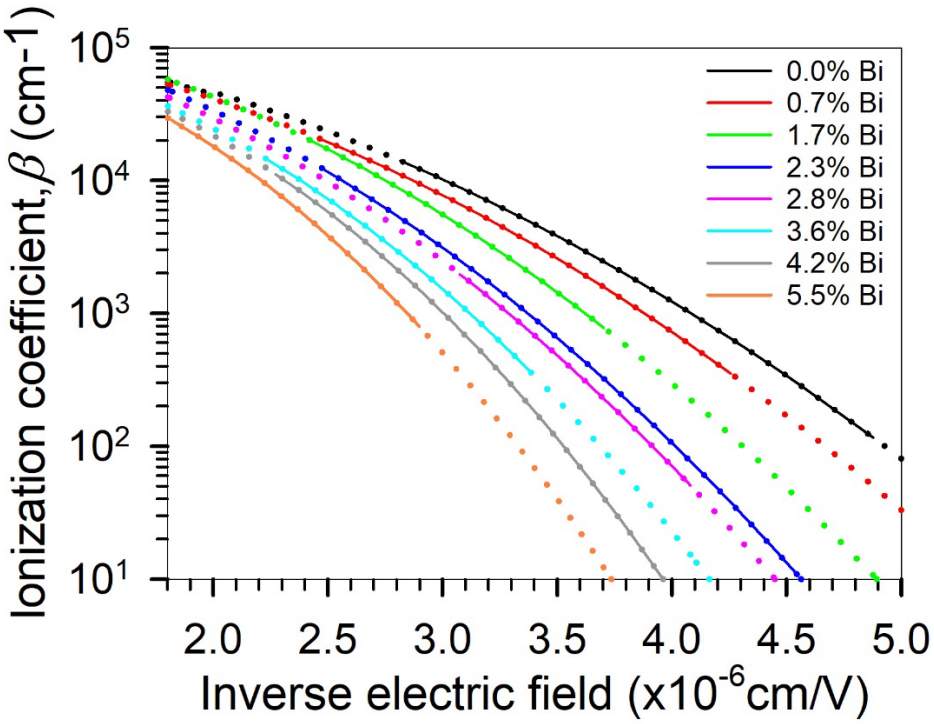

Figure 6.12 Beta of GaAs1-xBix as a function of inverse electric field at a range of Bi contents. Dashed lines are the simulation and solid lines represents the experimental data.

Table 6.2 lists the parameterised ionisation coefficients for GaAsBi of various Bi content between 0.65 and 5.5%. The parameters A, B and C were obtained by using the experimental data to fit the expression α (or β) = A exp [-(B/F) ^{C}], where F is the electric field. The ionisation coefficients as a function of Bi content for electric fields of 250, 300 and 350 kV/cm are plotted in Figure 6.13. The rate of change of 10% reduction in α per Bi% is much smaller than that for β. Both the α and β shows a good linear relationship for the different electric fields, which further illustrates the rationality of α and β line for the certain Bi content.

Bismuth content, *x*		***A*** **(×10^5 cm^{-1})**	***B*** **(×10^5 cm^{-1})**	***C***
0.65	α	2.15	5.75	1.87
	β	1.48	5.65	2.05
1.7-1.8	α	2.2	6	1.81
	β	1.98	6.15	2.08
2.2	α	2.23	6.05	1.81
	β	2.1	6.72	2.05
2.7	α	2.2	6.1	1.8
	β	1.9	6.75	2.08
3.5-3.6	α	2.15	6.2	1.78
	B	1.62	6.65	2.23
4.3-4.4	A	2	6.2	1.78
	β	1.45	6.55	2.37
5.5	α	1.9	6.2	1.79
	β	1.7	7.05	2.35

Table 6.2 Parametrised ionisation coefficient in $GaAs_{1-x}Bi_x$ express as $a(\beta) = A\exp\left[-(B/F)^c\right]$ *, where F is electric filed strength in V/cm.*

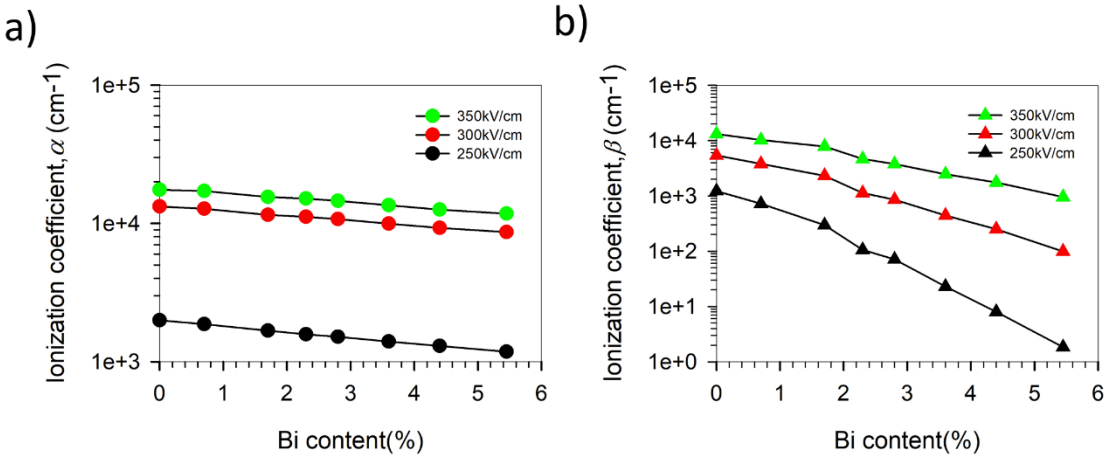

Figure 6.13 a(b) Ionisation coefficient of α(β) plotted against Bi content at electric field of 250, 300 and 350 kV/cm.

Figure 6.14 shows the variation of α/β ratio as a function of electric field with different Bi content. With 5.5 Bi%, large α/β ratios up to 10000 can be obtained at electric fields of 200kV/cm. While such a large ratio is impressive, APDs mainly operate at higher electric fields. To account for common APD operation, also included in the graph are the α/β ratios to obtain M values between 1.01 to 15 by simulating a 400nm GaAsBi structure. In general, the α/β ratio at high electric fields is not as striking as at low electric fields. However, for a GaAsBi sample with 4.2% Bi, the α/β ratio is sat least twice of that of GaAs at electric fields >400 kV/cm. The mechanism responsible for the large α/β ratio in this material may be due to the split-orbit splitting energy(Δso) increase with Bi, more details will be described in section 6.3.3. Apart from Bi, the other large group V atoms like antimony (Sb) has seen the same effect. Large α/β ratios between 10-100 with high avalanche gains have been demonstrated in $Al_xIn_{1-x}AsSb$ [5], [6] and $AlAs_{0.56}Sb_{0.44}$ [7], [8] recently.

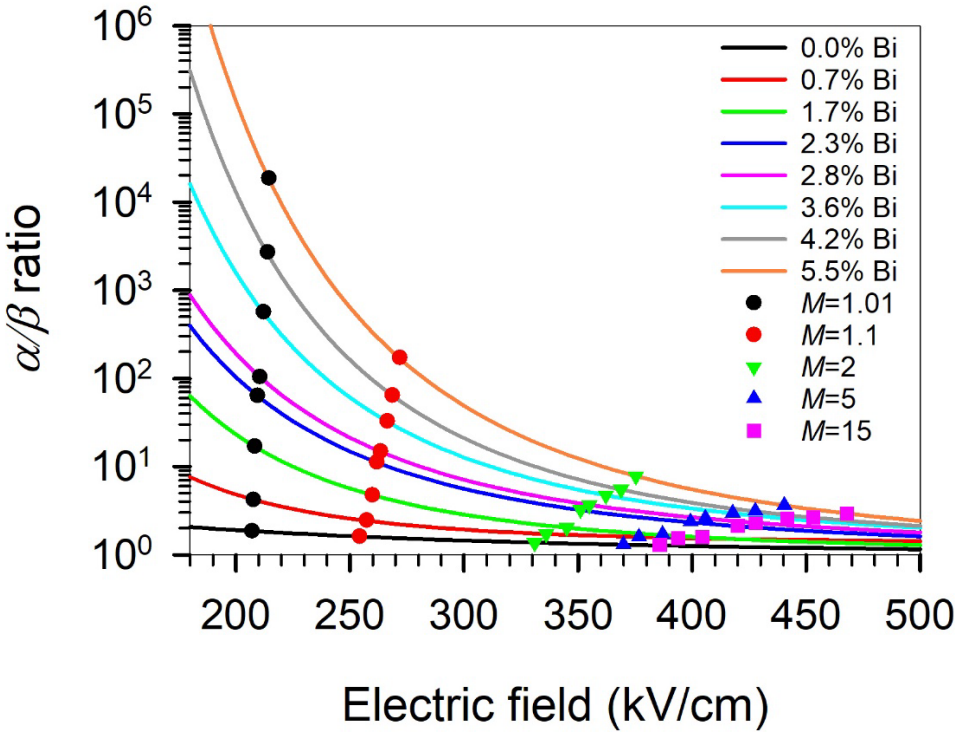

Figure 6.14 The electric-field dependence of the α/β ratio for different Bi%. The symbols show the calculated α/β ratio at Me values of 1.01, 1.1, 2, 5 and 15 in 400 nm GaAsBi p-i-n diodes.

6.3.2 Breakdown voltage (V_{bd})

The breakdown voltage, V_{bd} of the STF8 and the STFA series diodes obtained from reverse dark current and multiplication measurement are shown in the Figure 6.15(a) and (b). From the reverse dark current measurements, the breakdown of device is

obtained by gradually increasing the reverse bias voltages until a sharp breakdown happened (defined as the dark currents reaching 1 mA). To confirm the accuracy of the breakdown voltage, another method is to extrapolate the reciprocal of multiplication (*1/M*) and taking the *x*-intercept. From Figure 6.15(a) and (b), the breakdown voltage deduced from the dark current characteristics shows good agreement with the 1/*M* results, which also can confirm the breakdown showed in the reverse dark current characteristics is due to the avalanching process.

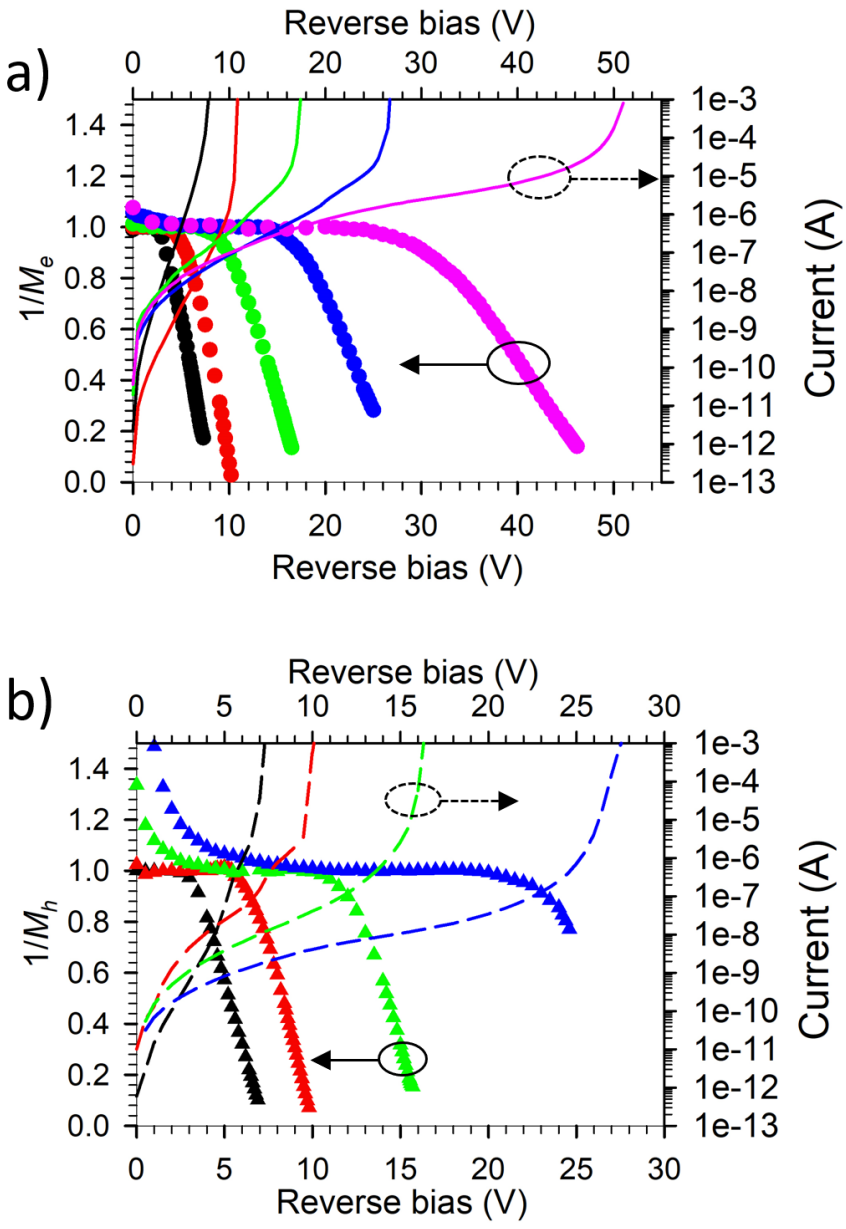

Figure 6.15 a), b) Breakdown voltage extracted from 1/Me (1/Mh) for the STF8 p-i-n (STFA n-i-p) diodes, the solid(dashed) line represents dark reverse current. The sample thickness follows the colour: 100nm (Black), 200nm (Red), 400nm (Green), 800nm (Blue) and 1600nm (Pink).

The strain relaxation becomes serious when incorporating more Bi into GaAs, which has been confirmed by Nomarski and XRD results from section 5.3.1 and 5.3.2. It is well known that the strain relaxation will change the lattice constant of the material. Allam *et al.* investigated the strain dependent breakdown characteristics in GaAs by measuring the breakdown voltage as a function of hydrostatic pressure [18]. From their results, it showed that breakdown voltage of GaAs decreases with increasing pressure. The rate of change for breakdown voltage is only a 4% reduction from 0 up to 14 kbar hydrostatic pressure. These results indirectly indicated that breakdown voltage of a material decreases with increasing strain.

Due to lack of same thickness sample with the different Bi content, Figure 6.16(a) shows the simulated electron multiplication characteristic of 400nm thick devices with different Bi by using the parametrised ionisation coefficient from Table 6.2 and equation 2.17. The breakdown voltage of each sample is taken from when M=100. From Figure 6.16(b), it shows that breakdown voltage increases with increasing the Bi content for 400nm thick sample. The simulated results are opposite to [18], suggesting that the inclusion of Bi is the dominant factor affecting the material's breakdown property rather than strain relaxation.

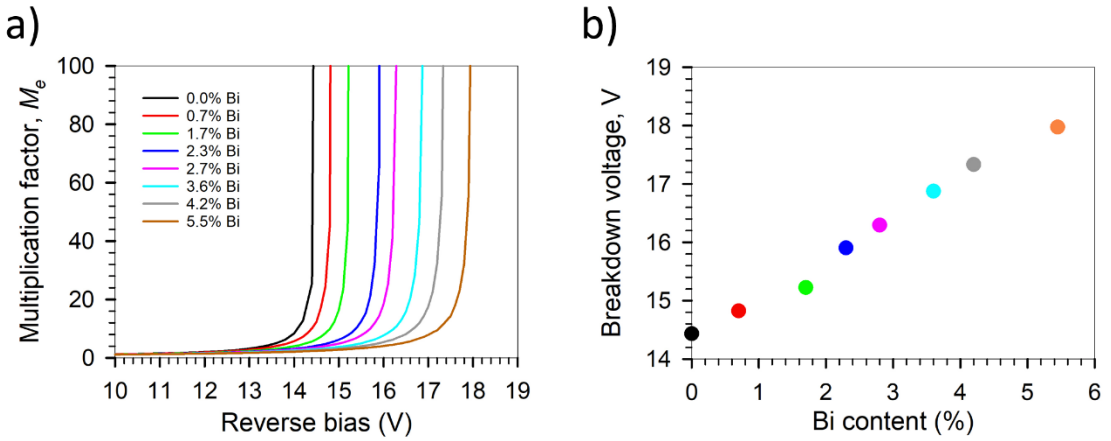

Figure 6.16 a) Simulated multiplication with different Bi content for 400nm thick i-region structure b) Breakdown voltage (taken from multiplication gain at 100 from a)) as a function of Bi content % for 400nm thick i-region structure

In 1996, Allam J. [19] had proposed a theory on universal avalanche breakdown voltage that is related to the Brillouin-zone-average indirect energy gap rather than the typical bandgap (conduction band minima to valence band maxima) for wide bandgap materials. In his results, a perfect linear relationship between the breakdown voltage

and the average indirect energy gap has been found for several wide-gap materials. The zinc-blende structure is one of common crystal structure in III-V semiconductor, whose conduction band has one Γ-valley, three X-valleys and four L-valleys. Therefore, the Brillouin-zone average indirect energy gap based on can be expressed with the approximation as follows [20].

$$\langle E_{ind} \rangle = \frac{1}{8} \times \left(E_{\Gamma} + 3E_X + 4E_L \right) \quad (6.2)$$

where E_{Γ}, E_X and E_L are the energy of Γ-valley, X-valleys and L-valleys, respectively. For Si, the k-p model overestimates the average effect related to the energy of Γ-valley. Therefore, the expression of modified average energy for Si is given by

$$\langle E \rangle_{kp-Si} = \frac{1}{7} \left[3E_X + 4E_L \right] \quad (6.3)$$

A simple linear expression has been found after contrasting the relationship between breakdown voltage and average indirect energy gap for several wide bandgap semiconductors, which is the black dashed line in figure 6.17. This can be described by

$$V_b = 45.8 \left(\langle E_{ind.} \rangle - 1.01 \right) \quad (6.4)$$

In order to investigate whether GaAsBi (4%) fits Allen's breakdown relation, two parameters, breakdown voltage for 1μm GaAsBi and average indirect energy gap need to be found. The multiplication as a function of voltage for a 1μm perfect p-i-n structure GaAsBi (4%) was obtained by using the local model and previously obtained parameterised ionisation coefficients. The breakdown voltage was estimated from the intersect point between 1/*M* and x-axis, which is roughly 36.2V. It was found that incorporating Bi into GaAs will induce a small increase on the L and X valley with rates of 18 meV%Bi and 25 meV%/Bi, respectively, as reported in [21]. As GaAsBi is a direct bandgap material, the energy of the Γ valley can be extracted from equation 2.5. As a result, the average indirect energy gap is 1.79 eV for GaAsBi (4%) by assuming conduction band energies at the Γ, X, L valleys as 1.126, 2.005 and 1.7856 eV, respectively. Plotting GaAsBi (4%) in figure 6.17, it shows Allen's universal breakdown relation still valid for this material.

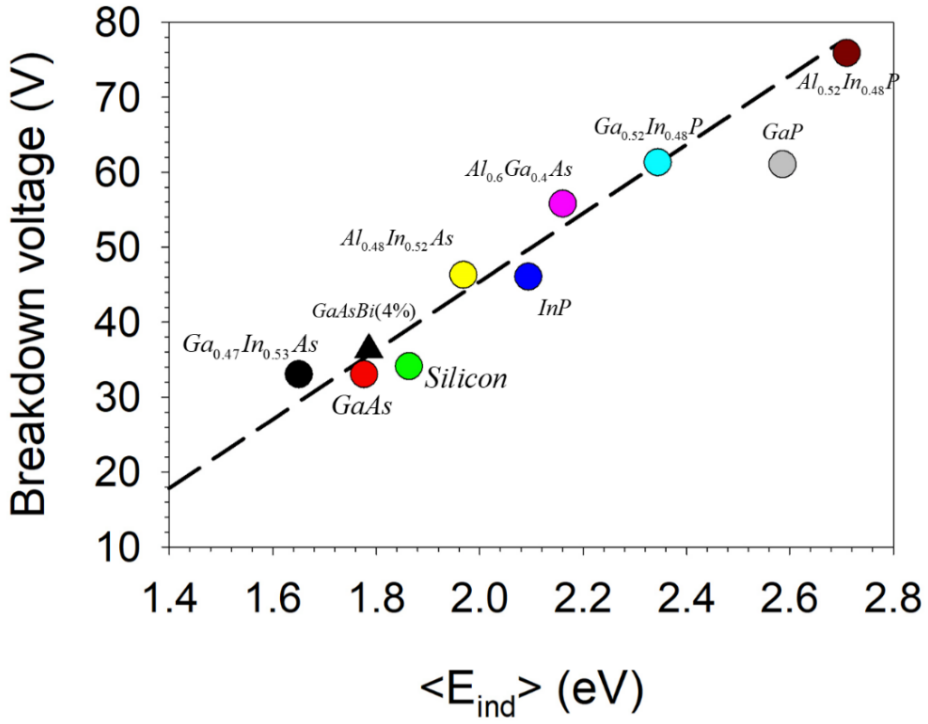

Figure 6.17 Measured breakdown voltage for 1μm several wide-gap materials as the function of <E_{ind}> Black dashed line is plotted using equation 6.3. The black triangle shows GaAsBi (~4%) in this work.

6.3.3 Explanation of large α/β ratio in the GaAsBi

Figure 6.18 shows the relationship between the impact of the Bi on the minimum electric field for the onset of the impact ionisation (defined as when $M_{e,h} = 1.01$ from Figure 6.8(a) and (b)) and spin-orbit splitting energy. The threshold electric field for electron ionisation is hardly changed from 205 kV/cm for 0% Bi (GaAs) to 212 kV/cm for 4.2% Bi structure. Whereas, the impact of Bi% has a strong effect on the threshold electric field for hole ionisation, which sees a significant increase from 217 kV/cm for 0% Bi (GaAs) to 333 kV/cm for 5.5% Bi structure. The significant rate of change in hole threshold electric field correlates with increasing Δso energy. Research has been shown that the vast majority of hole initiated impact ionisation events in GaAs is dominated by the spin-off band than the heavy- and light-hole band calculated from the Monte Carlo calculation [16], which can be explained due to the ionisation transition rate in these two bands is much lower than the competing phonon scattering rate. Therefore, ionisation events only have a low chance to occur for holes to transfer to heavy- and light-hole band. The band structure of GaAsBi is similar to that of GaAs, so it can be assumed that the vast majority of hole ionisation events also depend primarily on the spin-off band on GaAsBi. Adding Bi into the GaAs will lead to an

increase of spin-off band (shown as the green line in the Figure 6.18), making hole transitions to the spin-off band more difficult and improbable, resulting in a reduction of hole impact ionisation rate.

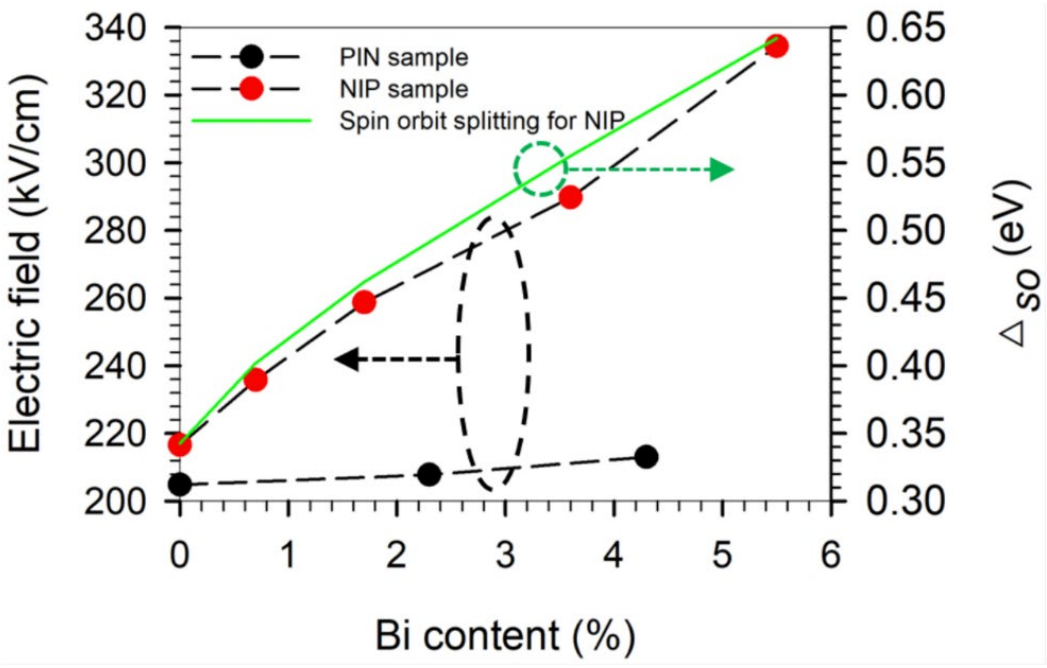

Figure 6.18 The minimum electric field required to cause electrons and holes to ionise (defined as when Me,h=1.01) in nominally 400 nm GaAsBi p-i-ns and n-i-ps. The Δso energy vs Bi% is also shown.

6.4 Conclusion

The avalanche multiplication characteristics of $GaAs_{1-x}Bi_x$ ($0<x<5.5\%$) with a nominal thickness from 100 to 1600 nm were investigated using 405, 633 and 980 nm wavelength lasers. The pure and mixed carrier injection multiplication of the p-i-n and n-i-p structure proved that $\alpha>\beta$ in this material. The appreciable difference between pure and mixed injection results in the thick n-i-p sample strongly supports that the hole ionisation coefficient is suppressed in this material, indicating $\alpha>>\beta$ in the low electric field regime. Further analysis showed that adding Bi into GaAs significantly reduces the hole ionisation coefficient while the electron ionisation coefficient is barely unchanged. It concluded that this novel find is related to the changes in the spin-orbit splitting energy.

The multiplication results were fitted with the local model of impact ionisation. An excellent agreement between model and experimental results is achieved even at M=1.01. The ionisation coefficients of electron and hole for different Bi content are

extrapolated from the p-i-n and n-i-p multiplication results. An impressive α/β ratio over 1000 was showed at the electric fields of 250 kV/cm for 5.5% Bi.

By modelling, the breakdown voltage increases with Bi content, which is contrary to the results from [18], suggesting that strain relaxation has less of an effect on the ionisation coefficients than the inclusion of Bi.

6.5 Reference

[1] R. J. McIntyre, 'Multiplication noise in uniform avalanche diodes', *IEEE Trans. Electron Devices*, vol. ED-13, no. 1, pp. 164–168, Jan. 1966, doi: 10.1109/T-ED.1966.15651.

[2] P. Woditsch and W. Koch, 'Solar grade silicon feedstock supply for PV industry', *Sol. Energy Mater. Sol. Cells*, vol. 72, no. 1, pp. 11–26, Apr. 2002, doi: 10.1016/S0927-0248(01)00146-5.

[3] R. Van Overstraeten and H. De Man, 'Measurement of the ionization rates in diffused silicon p-n junctions', *Solid-State Electron.*, vol. 13, no. 5, pp. 583–608, May 1970, doi: 10.1016/0038-1101(70)90139-5.

[4] J. S. Cheong, M. M. Hayat, X. Zhou, and J. P. R. David, 'Relating the Experimental Ionization Coefficients in Semiconductors to the Nonlocal Ionization Coefficients', *IEEE Trans. Electron Devices*, vol. 62, no. 6, pp. 1946–1952, Jun. 2015, doi: 10.1109/TED.2015.2422789.

[5] S. R. Bank *et al.*, 'Avalanche Photodiodes Based on the AlInAsSb Materials System', *IEEE J. Sel. Top. Quantum Electron.*, vol. 24, no. 2, pp. 1–7, Mar. 2018, doi: 10.1109/JSTQE.2017.2737880.

[6] A. H. Jones, S. D. March, S. R. Bank, and J. C. Campbell, 'Low-noise high-temperature AlInAsSb/GaSb avalanche photodiodes for 2-μm applications', *Nat. Photonics*, vol. 14, no. 9, pp. 559–563, Sep. 2020, doi: 10.1038/s41566-020-0637-6.

[7] X. Yi *et al.*, 'Demonstration of large ionization coefficient ratio in AlAs 0.56 Sb 0.44 lattice matched to InP', *Sci. Rep.*, vol. 8, no. 1, Art. no. 1, Jun. 2018, doi: 10.1038/s41598-018-27507-w.

[8] X. Yi *et al.*, 'Extremely low excess noise and high sensitivity AlAs 0.56 Sb 0.44 avalanche photodiodes', *Nat. Photonics*, vol. 13, no. 10, Art. no. 10, Oct. 2019, doi: 10.1038/s41566-019-0477-4.

[9] J. Zheng *et al.*, 'Full band Monte Carlo simulation of AlInAsSb digital alloys', *InfoMat*, vol. 2, no. 6, pp. 1236–1240, 2020, doi: https://doi.org/10.1002/inf2.12112.

[10] C. Hu, K. A. Anselm, B. G. Streetman, and J. C. Campbell, 'Noise characteristics of thin multiplication region GaAs avalanche photodiodes', *Appl. Phys. Lett.*, vol. 69, no. 24, pp. 3734–3736, Dec. 1996, doi: 10.1063/1.117205.

[11] K. F. Li *et al.*, 'Avalanche multiplication noise characteristics in thin GaAs p/sup +/-i-n/sup +/ diodes', *IEEE Trans. Electron Devices*, vol. 45, no. 10, pp. 2102–2107, Oct. 1998, doi: 10.1109/16.725242.

[12] M. Ren, S. Maddox, Y. Chen, M. Woodson, J. C. Campbell, and S. Bank, 'AlInAsSb/GaSb staircase avalanche photodiode', *Appl. Phys. Lett.*, vol. 108, no. 8, p. 081101, Feb. 2016, doi: 10.1063/1.4942370.

[13] F. Capasso, Won-Tien Tsang, and G. F. Williams, 'Staircase solid-state photomultipliers and avalanche photodiodes with enhanced ionization rates ratio', *IEEE Trans. Electron Devices*, vol. 30, no. 4, pp. 381–390, Apr. 1983, doi: 10.1109/T-ED.1983.21132.

[14] B. Chen *et al.*, 'Low Dark Current High Gain InAs Quantum Dot Avalanche Photodiodes Monolithically Grown on Si', *ACS Photonics*, vol. 7, no. 2, pp. 528–533, Feb. 2020, doi: 10.1021/acsphotonics.9b01709.

[15] J. Kolník, Y. Wang, I. H. Oğuzman, and K. F. Brennan, 'Theoretical investigation of wave-vector-dependent analytical and numerical formulations of the interband impact-ionization transition rate for electrons in bulk silicon and

GaAs', *J. Appl. Phys.*, vol. 76, no. 6, pp. 3542–3551, Sep. 1994, doi: 10.1063/1.357412.
[16] İ. H. Oğuzman, Y. Wang, J. Kolník, and K. F. Brennan, 'Theoretical study of hole initiated impact ionization in bulk silicon and GaAs using a wave-vector-dependent numerical transition rate formulation within an ensemble Monte Carlo calculation', *J. Appl. Phys.*, vol. 77, no. 1, pp. 225–232, Jan. 1995, doi: 10.1063/1.359374.
[17] M. H. Woods, W. C. Johnson, and M. A. Lampert, 'Use of a Schottky barrier to measure impact ionization coefficients in semiconductors', *Solid-State Electron.*, vol. 16, no. 3, pp. 381–394, Mar. 1973, doi: 10.1016/0038-1101(73)90013-0.
[18] J. Allam, A. R. Adams, M. A. Pate, and J. S. Roberts, 'Impact ionization in GaAs: Distribution of final electron states determined from hydrostatic pressure measurements', *Appl. Phys. Lett.*, vol. 67, no. 22, pp. 3304–3306, Nov. 1995, doi: 10.1063/1.115228.
[19] J. A. J. Allam, '"Universal" Dependence of Avalanche Breakdown on Bandstructure: Choosing Materials for High-Power Devices', *Jpn. J. Appl. Phys.*, vol. 36, no. 3S, p. 1529, Mar. 1997, doi: 10.1143/JJAP.36.1529.
[20] D. J. Chadi and K. J. Chang, 'Theory of the Atomic and Electronic Structure of DX Centers in GaAs and Al x Ga 1 − x As Alloys', *Phys. Rev. Lett.*, vol. 61, no. 7, pp. 873–876, Aug. 1988, doi: 10.1103/PhysRevLett.61.873.
[21] V. Pačebutas *et al.*, 'Terahertz excitation spectra of GaAsBi alloys', *J. Phys. Appl. Phys.*, vol. 51, no. 47, p. 474001, Nov. 2018, doi: 10.1088/1361-6463/aadb11.

Chapter 7: Summary, conclusions, and future work

7.1 Summary

A series of 400 nm thick intrinsic region bulk GaAsBi n-i-p diodes with various Bi content were grown by MBE. Together with two other GaAsBi p-i-n and n-i-p series grown previously by other PhD students, optical characterisation techniques such as Nomarski microscopy, XRD and PL are used to investigate the structural and optical properties of these samples. Electrical characterisation of devices was performed by I-V and C-V. Fundamental electrical properties of devices such as dark current, breakdown voltage and doping profile were understood through measurements. The ionisation coefficient of GaAsBi with various Bi content was extracted and characterised by photomultiplication measurement for the first time.

7.2 Conclusions

Three sets of p-i-n and n-i-p GaAsBi samples with various i-region thicknesses and Bi contents have been grown by MBE. Nomarski images showed the presence of strain relaxation on the sample surface in the form of cross-hatching pattern. This was determined by critical thickness at certain Bi content. The XRD results of this work were comparable to that from the literature. Besides that, it also was the first time to show XRD results of over 400nm thick GaAsBi samples with the capping layer. Clear shoulder peak on the right side of the substrate peak is indicative of strain relaxation, which is consistent with Nomarski results.

The RT PL results showed adding the Bi into GaAs significantly reduce the bandgap, and the sample with 5.5% Bi can extend the detectable wavelength up to 1.2 μm. The FWHM values of most of the samples were between 77 and 110 nm. The I-V characteristics of the samples showed rectifying diode behaviour. Forward I-V results showed that the dark current goes up with increasing Bi content. A five orders of magnitude difference is seen in samples with 5.5% Bi when compared with a GaAs control sample. The increase is attributed to Bi-induced defects and dislocation or non-optimal vacuum condition for our MBE machine.

Nevertheless, compared with I-V results with same Bi content from literature, our devices still showed better results despite the fact that our device has a thicker structure. The ideality factors were 1.68-1.92 in this work, indicating the generation-

recombination mechanism dominates the forward current. In the reverse dark currents region, sharp breakdown voltages were observed in all devices.

The avalanche multiplication characteristics of GaAsBi diodes with dilute Bi content varying from 0.6-5.5% have been studied in detail using p-i-n and n-i-p with i-region thicknesses ranging from 0.1 μm to 1.6 μm. Pure and mixed carrier injection (using 405 and 980 nm wavelengths respectively) multiplication was measured. Noticeable difference between pure and mixed multiplication of n-i-p samples were observed as compared to that of p-i-n samples, especially in the thicker structures.

Such phenomenon indicated that $\alpha>\beta$ in this material and also supported that $\alpha \gg \beta$ at the low electric field for the thick structures. With increasing Bi content, the α of GaAsBi decreases very slightly compared to GaAs. However, there is a significant decrease of β, especially at the low electric field region. It is worth noting that this is the first ever alloy system where such a dramatic change in only one type of carrier ionisation profile is observed. This is due to the change of spin-orbit splitting energy in the band structure by increasing the Bi content. This finding might become a new route to enhance the α/β ratio in other III-V alloy systems, making the dilute Bi alloy a potential candidate for low-noise APDs.

In addition to that, effective values of α and β of GaAsBi with various Bi content deduced from the pure carrier multiplication over a large electric field range were parameterised. The local model was adopted to fit the experimental data without considering the dead-space effect. A good agreement with experimental data was achieved even at low multiplication of 1.01. Furthermore, the breakdown voltage of ~4% Bi samples is in line with the universal breakdown voltage rule for typical wide bandgap material.

7.3 Future work

1. The present work can be extended to study the temperature-dependent of the avalanche characteristics of GaAsBi. From these characteristics, it will give us a better understanding of the device properties under the high temperature conditions.
2. Adding N into GaAsBi can strain balance the lattice mismatch. Therefore, a thick structure of GaAsBiN could be obtained, which is lattice-matched to the GaAs substrate. Currently, the alloy of GaAsBiN has been considered as the

potential third layer used in the multi-junction solar cell. The growth study, such as how to find correct growth parameter for high-quality materials, will be a prerequisite for understanding the properties of the material. The addition of nitrogen will also induce additional band interactions in the conduction band, which is similar to bismuth acting on band anti-crossing in the valence band.

3. Another exciting project might be incorporating Bismuth (Bi) atoms into other III-V semiconductors such as InAs and InGaAs. Due to the large bandgap reduction properties of Bi, the new alloy InAsBi and InGaAsBi will achieve a wide range of detectable wavelengths by tuning the Bi composition. Such new materials will lead to a new range of infrared detectors. This will have a significant impact on applications such as night vision imaging, medical diagnostic sensors, environmental monitors and accurate temperature measurements in manufacturing processes. From current work, we understand that the Bi has an enormous impact on the valence band. The effect on the conduction band is rarely changed. Therefore, incorporating Bi into InAs will alter the valence band, and consequently only electrons will gain significant energy from the electric field. In the meanwhile, the holes will be suppressed. Using this idea, it will support us to design very high gain APD across a wide range of electric field while concomitantly suppressing the noise associated with impact ionisation.
4. The work of Chia *et al*. [1], [2] investigated the effect of the band edge discontinuities on impact ionisation for $Al_xGa_{1-x}As$/GaAs heterostructures. In early studies, artificial semiconductors use band edge discontinuities in multiple quantum well and superlattice as a method to alter the bulk impact ionisation coefficients. The heterojunction was thought as an alternative way to enhance the electron ionisation coefficient because hot electrons would gain kinetic energy from the conduction band edge discontinuity when travelling from the barrier to the well. Currently, there is no study to investigate the band edge discontinuities for GaAsBi/GaAs heterostructures. The band diagram of GaAsBi/GaAs p-i-n and n-i-p heterostructure is designed in figure 7.1.

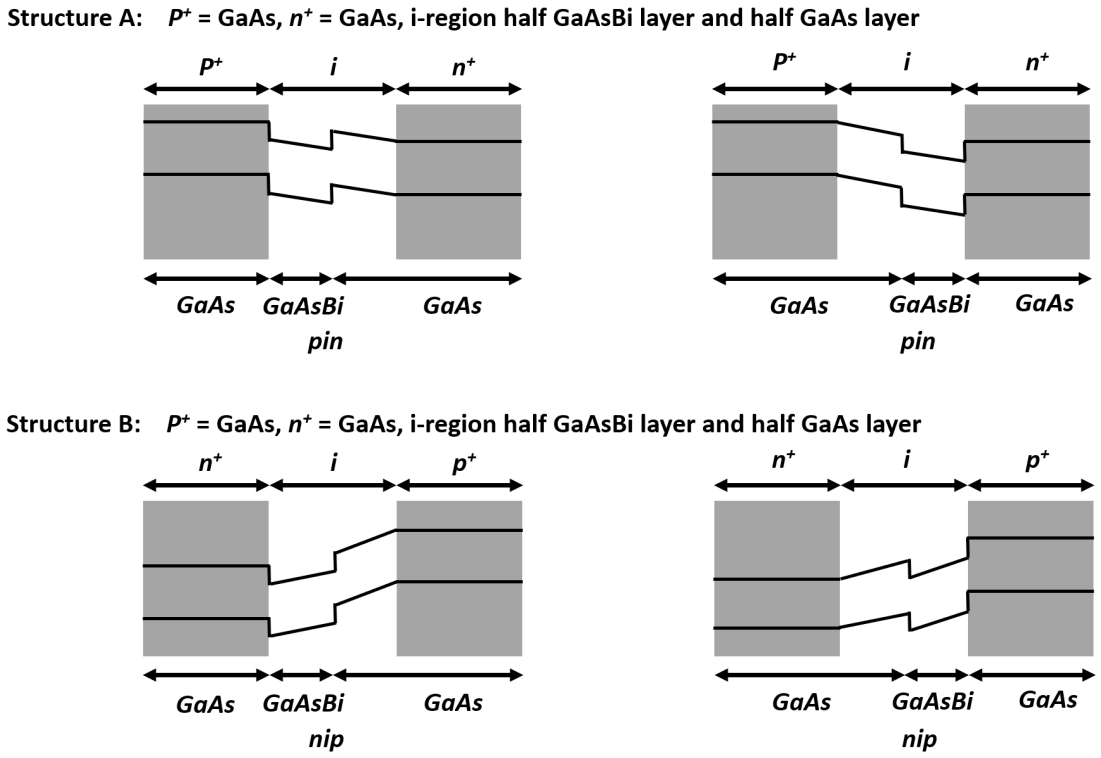

Figure 7.1 Designed band diagram of multilayer structure

7.4 Reference

[1] Chia *et al.*, 'Electron multiplication in AlxGa1-xAs/GaAs heterostructures', *Appl. Phys. Lett.*, vol. 71, no. 26, pp. 3877–3879, Dec. 1997, doi: 10.1063/1.120531.

[2] Chia *et al.*, 'Impact ionization in AlxGa1-xAs.GaAs single heterostrucutre', *J. Appl. Phys.*, vol. 84, no. 8, pp. 4363–4369, Oct. 1998, doi: 10.1063/1.368656.

Appendix I

C-V modelling

This section is to explain the C-V modelling using a p-i-n structure as an example. A p-i-n structure with the i-region thickness of w is shown in figure A-I.1. The doping concentration on each layer is N_p, N_i and N_n for p^+, i and n^+ layer respectively. The *i*-region is slightly *n*-type doped in this diagram. Based on the Poisson's equation, the electric field in each region is described by

$$\text{p}^+\text{-region} \qquad G_p = \left.\frac{dE}{dx}\right|_p = \frac{qN_p}{\varepsilon} \tag{A-I.1}$$

$$\text{i-region} \qquad G_i = \left.\frac{dE}{dx}\right|_i = \frac{qN_i}{\varepsilon} \tag{A-I.2}$$

$$\text{n}^+\text{-region} \qquad G_n = \left.\frac{dE}{dx}\right|_n = \frac{qN_n}{\varepsilon} \tag{A-I.3}$$

where E is the electric field, q is the electron charge and ε is the permittivity of the semiconductor.

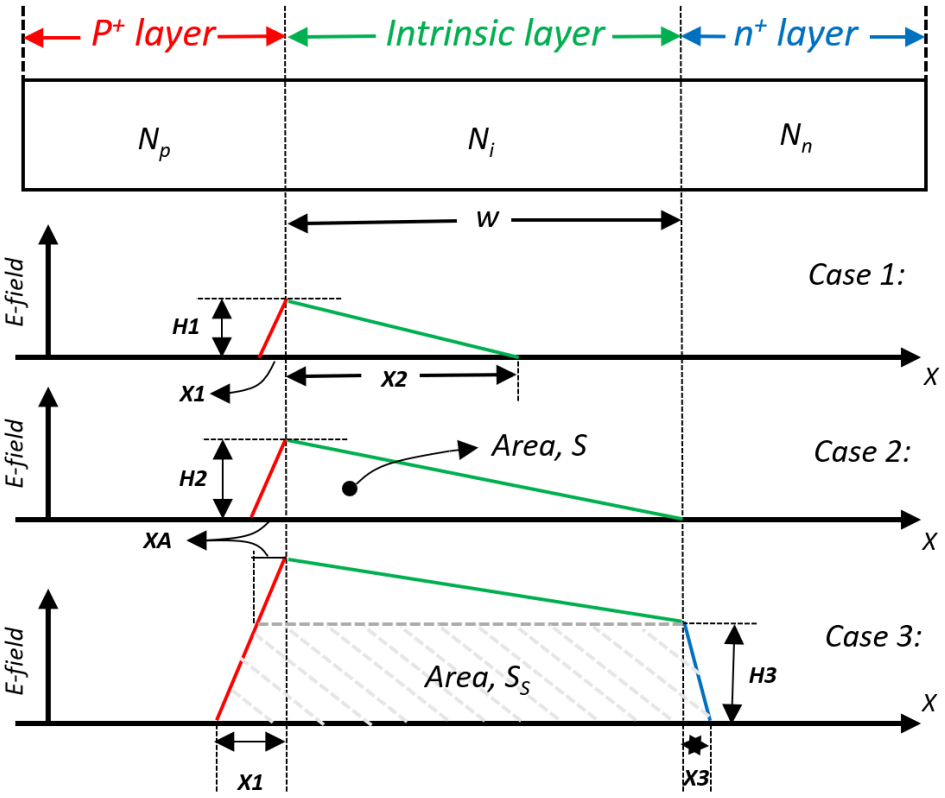

Figure A-I.1 Schematic diagram of p-i-n structure under the reverse bias voltage and the electric profile in three cases. Case 1: the i-region is partially depleted. Case 2: the i-region is just depleted. Case 3: the i-region is fully depleted, and some depletion width is in the n^+ region.

The three depleted cases in the i-region is depicted in figure A-I.1. In the case 2, the area, *S*, under the electric field profile is the area of the triangle, which can be given by $S = \frac{1}{2} \times H2 \times (w + xA)$ where $H2 = w \left. \frac{dE}{dx} \right|_i = wG_i$ and $xA = \frac{H2}{G_p}$. Therefore, the area, S, and *xA* can also be expressed as

$$S = \frac{1}{2} \times H2 \times (w + xA) = \frac{1}{2} \times wG_i \times (w\frac{G_i}{G_p} + w) = \frac{1}{2} w^2 G_i (\frac{G_i}{G_p} + 1) \tag{A-I.4}$$

$$xA = \frac{H2}{G_p} = \frac{wG_i}{G_p} \tag{A-I.5}$$

The total reverse bias voltage V_t, across the depletion region is the sum of the applied reverse bias voltage V_r and the build-in voltage V_{bi}, which is given by

$$V_t = V_r + V_{bi} \tag{A-I.6}$$

The area under the electric field is the total reverse bias voltage applied, therefore two cases, $V_t \le S$ and $V_t > S$, will be described in the below section.

If $V_t \le S$, in this case the i-region is in either the partially depleted or just depleted, the total depletion width is described by

$$W_t = x_1 + x_2 \tag{A-I.7}$$

In this case, $H1 = x1G_p = x2G_i$ and $V_t = \frac{1}{2} \times H1 \times (x1 + x2)$, rearranging these equations with A-I.7, the *x1* and *x2* is given by

$$x1 = \sqrt{\frac{2V_t}{G_p(1 + \frac{G_p}{G_i})}} \tag{A-I.8}$$

$$x2 = \frac{x1G_p}{G_i} \tag{A-I.9}$$

If $V_t > S$, in which the shadow area S_s, as shown in Figure A-I.1(case 2), is given by

$$S_s = V_t - S = \frac{1}{2} \times H3 \times \big((xA + w) + (x1 + w + x3)\big) = \frac{1}{2} \times H3 \times (2w + xA + x1 + x3) \tag{A-I.10}$$

Where $x1 = \frac{H3}{G_p} + xA$ and $x3 = \frac{H3}{G_n}$. Putting *x1* and *x3* into the equation (A-I.10) yields

$$\frac{1}{2}\times(\frac{1}{G_p}+\frac{1}{G_n})\times H3^2+(w+xA)\times H3+(V_t-S)=0 \qquad \text{(A-I.11)}$$

To solve the quadratic equation ($y=ax^2+bx+c$) can use the formula $x=\frac{-b\pm\sqrt{b^2-4ac}}{2a}$, since the *H3 is* always the positive value, the solution of *H3* is given by

$$H3=\frac{-(w+xA)+\sqrt{(w+xA)^2+2(\frac{1}{G_p}+\frac{1}{G_n})(V_t-S)}}{(\frac{1}{G_p}+\frac{1}{G_n})} \qquad \text{(A-I.12)}$$

In this case, the total depletion width is

$$W_t=x1+w+x3=xA+w+H3(\frac{1}{G_p}+\frac{1}{G_n}) \qquad \text{(A-I.13)}$$

The capacitance of p-i-n structure within these three cases can be calculated by

$$C=\frac{\varepsilon A}{W_t} \qquad \text{(A-I.14)}$$

where A is the area of the measured diode.

Appendix II

Lock in amplifier (LIA)

A LIA is used to measure signals that are buried under noise by phase sensitive detection which requires a reference signal at a fixed frequency. In this case, an optical chopper generates a reference of the square wave. Figure A-II.1 illustrates the basic principle of the lock-in amplifier.

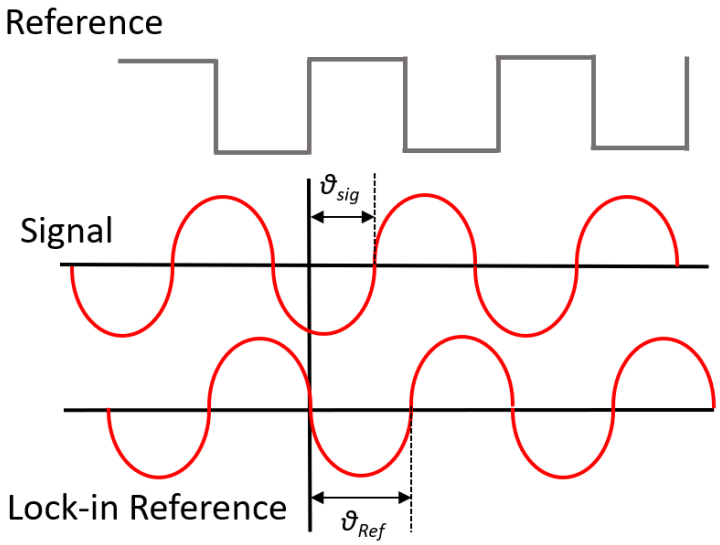

Figure A-II.1 Diagram of phase-sensitive detection technique.

The input signal is a sine wave which is detected by the DUT, and the lock-in generates its own reference signal with same frequency as chopper reference. The expression of both waveforms is given below.

$$V_{sig} = A_{sig}\sin(w_{sig}t + \theta_{sig}) \tag{A-II.1}$$

$$V_{ref} = A_{ref}\sin(w_{ref}t + \theta_{ref}) \tag{A-II.2}$$

Where V_{sig} and V_{ref} are the amplitudes of the sine wave of the signal and lock-in reference, respectively. θ_{sig} and θ_{ref} are the phase angles of the signal and reference signal for lock-in, respectively. Based on the transformation of trigonometric formulae, the output signal is the product of both sine wave and yields

$$V_{out} = V_{sig} \times V_{ref} = A_{ref}A_{sig}\sin(w_{sig}t + \theta_{sig})\sin(w_{ref}t + \theta_{ref}) \tag{A-II.3}$$

$$= \frac{1}{2}A_{sig}A_{ref}\cos[(w_{sig} - w_{ref})t + \theta_{sig} - \theta_{ref}] - \frac{1}{2}A_{sig}A_{ref}\cos[(w_{sig} + w_{ref})t + \theta_{sig} + \theta_{ref}]$$

(A-II.4)

Two AC signals at difference frequency $w_{sig} + w_{ref}$ and $w_{sig} - w_{ref}$ are produced. Assume $w_{sig} = w_{ref}$, Equation A-II.4 simplifier to

$$V_{out} = \frac{1}{2} A_{sig} A_{ref} \cos(\theta_{sig} - \theta_{ref}) - \frac{1}{2} A_{sig} A_{ref} \cos(2w_{ref} t + \theta_{sig} + \theta_{ref}) \quad \text{(A-II.5)}$$

Now, the output signal is made of one time-independent DC signal component and another time-dependent AC signal component. After passing through a low-pass filter, any frequencies that are higher than the reference frequency will be eliminated. Therefore, the AC component in Equation A-II.5 is removed. The output signal becomes

$$V_{out} = \frac{1}{2} A_{sig} A_{ref} \cos(\theta_{sig} - \theta_{ref}) \quad \text{(A-II.6)}$$

From Equation A-II.6, V_{out} is proportional to the $A_{sig} \cos(\theta_{sig} - \theta_{ref})$. Therefore, to get the maximum output signal, the phase difference between the signal and the lock-in reference needs to be close to zero to make $\cos(0) = 1$. In practice, a phase difference of $\pm 5°$ is acceptable.

In this case, the external reference is a square waveform function which can be considered as the sum of many harmonic sinusoid waves based on a Fourier transform. The equation is given by

$$V_{square} = \frac{2A_{sig}}{\pi} [\sin(2\pi ft) + \sin(6\pi ft) + \sin(10\pi ft) + \cdots] \quad \text{(A-II.7)}$$

The value displayed on the LIA in its RMS value (0.7 times peak value) will only take into account the first term of this sinusoid wave, therefore, the final output value is yielded

$$V_{out} = \frac{2A_{sig}}{\pi} \times 0.7 \approx 0.45 A_{sig}$$

Appendix III

Photo-multiplication results of STF8 p-i-n and STFA n-i-p samples

During the photomultiplication measurement, the power of the lasers was set between 1 mW and 5mW and was attenuated to around ten times less by mirrors and beam splitter when the beams arrived at the optical window of devices. The repeatability of results can be evaluated by taking measurements on devices of different sizes and with different laser powers. Figures A-III.1 to A-III.9 show the multiplication gain results as a function of reverse bias voltage for STF8 p-i-n and STFA n-i-p samples under 405nm light. The gain results taken on the different size of devices under different laser powers show almost the same, representing the excellent repeatability on each sample.

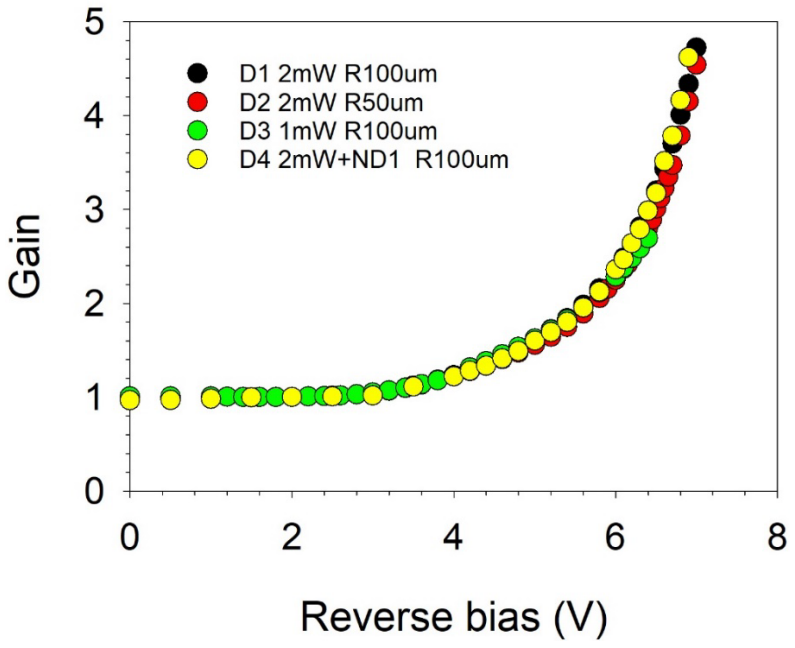

Figure A-III.1 Multiplication results for STF85(P100) using 405nm laser in different size devices and laser power.

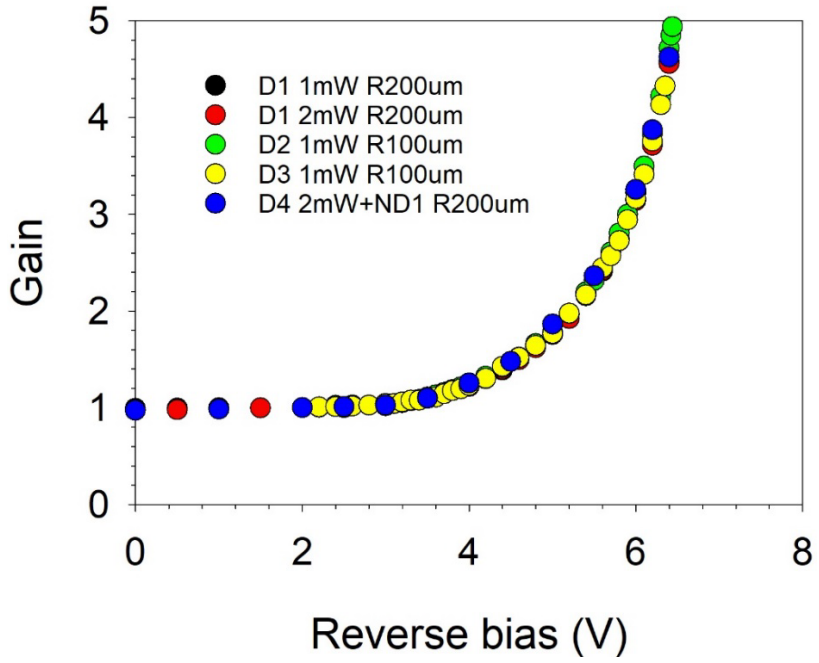

Figure A-III.2 Multiplication results for STFA7(N100) using 405nm laser in different size devices and laser power.

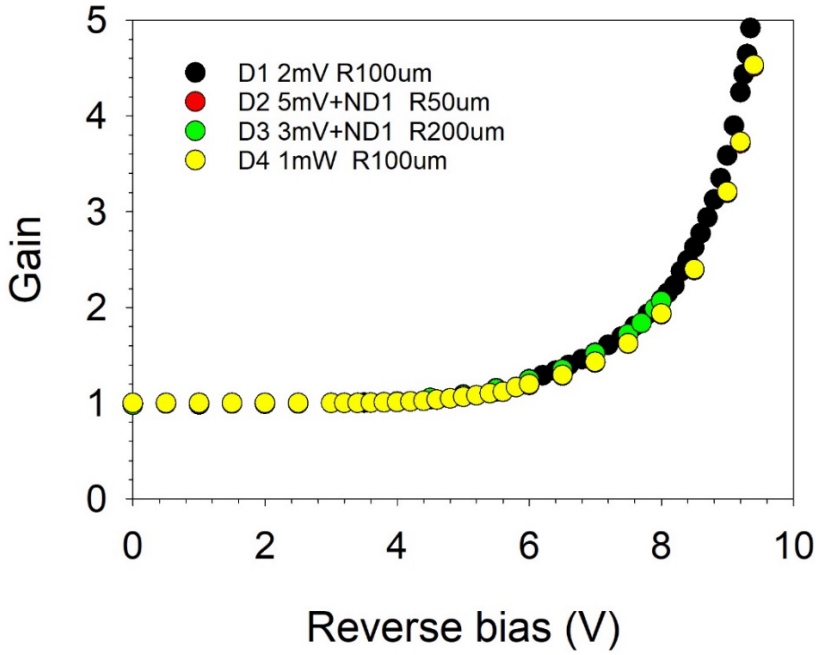

Figure A-III.3 Multiplication results for STF81(P200) using 405nm laser in different size devices and laser power.

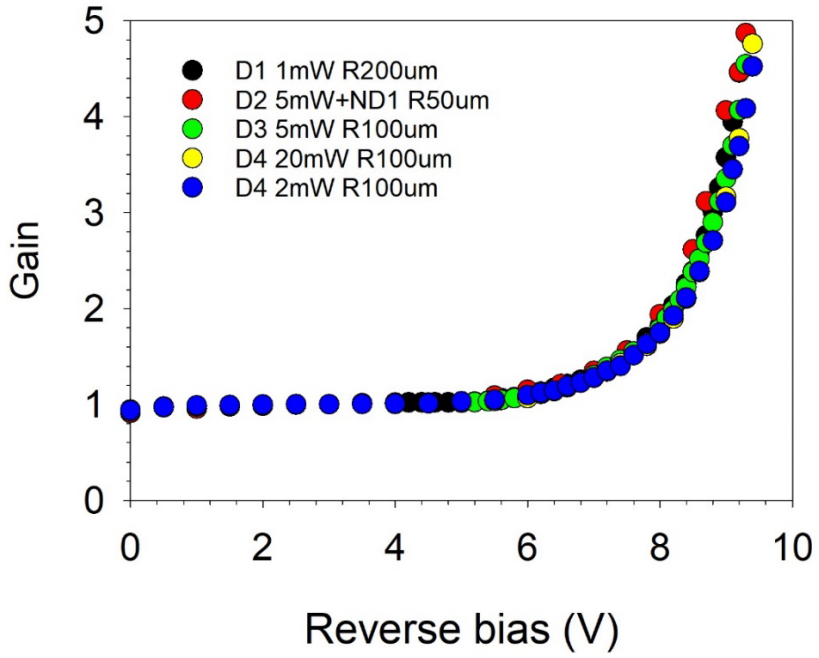

Figure A-III.4 Multiplication results for STFAD(N200) using 405nm laser in different size devices and laser power.

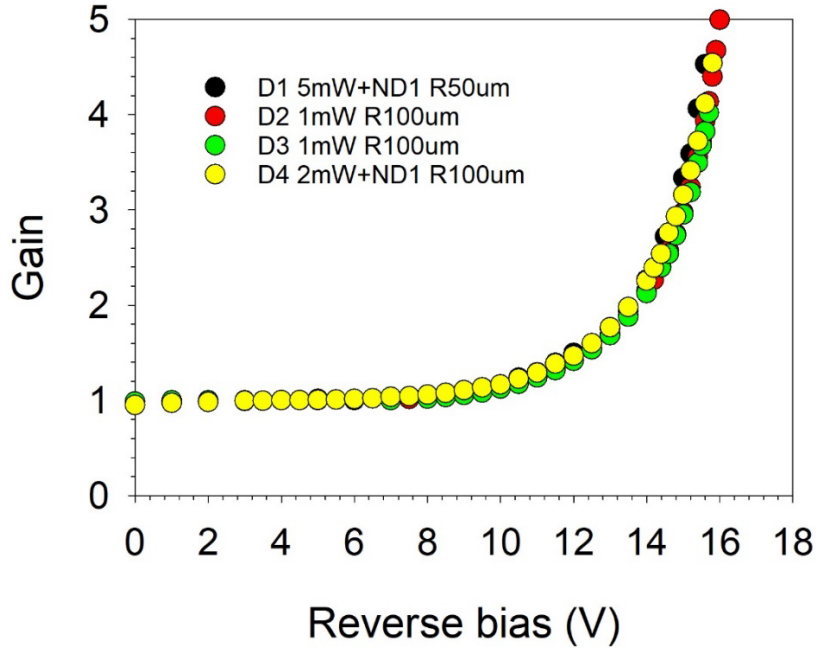

Figure A-III.5 Multiplication results for STF84(P400) using 405nm laser in different size devices and laser power.

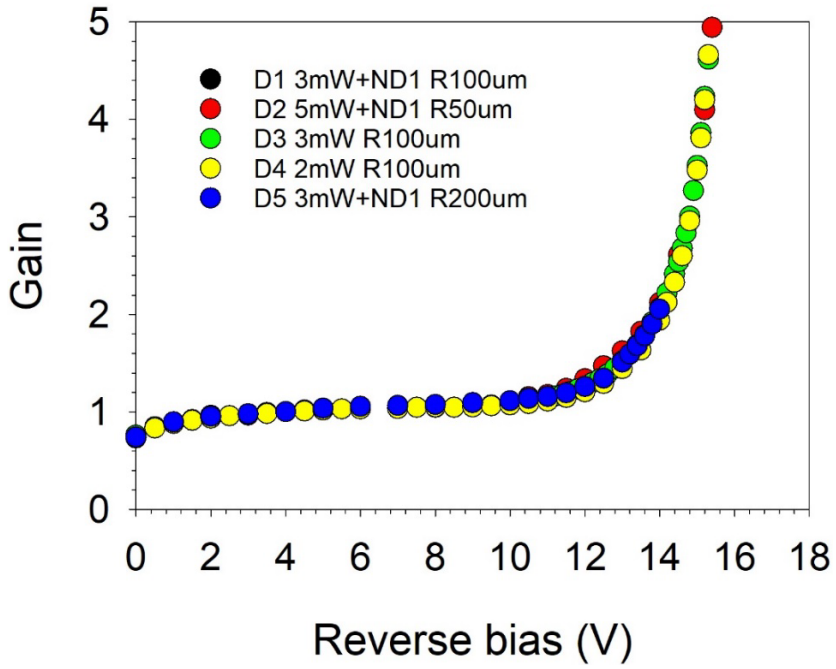

Figure A-III.6 Multiplication results for STFAE(N400) using 405nm laser in different size devices and laser power.

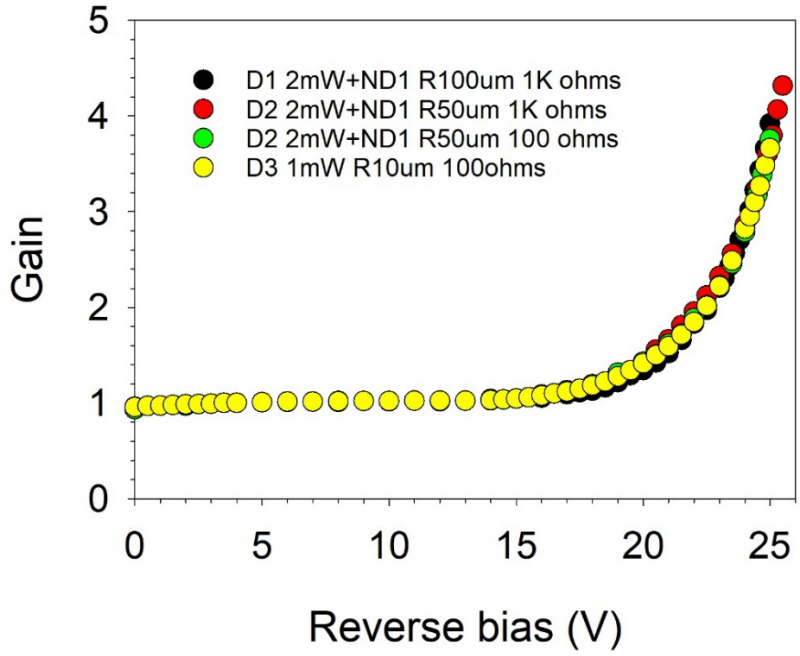

Figure A-III.7 Multiplication results for STF83(P800) using 405nm laser in different size devices and laser power.

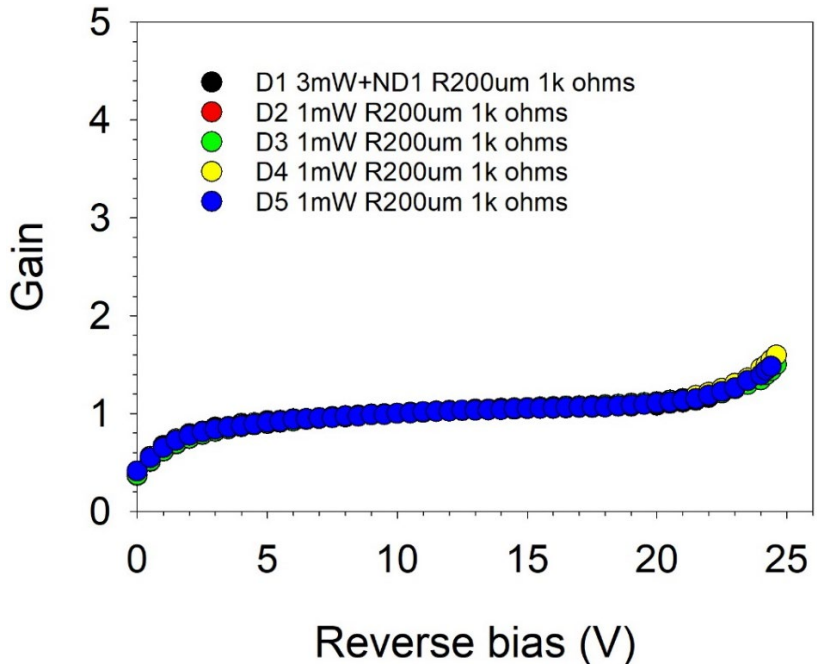

Figure A-III.8 Multiplication results for STFAB(N800) using 405nm laser in different size devices and laser power.

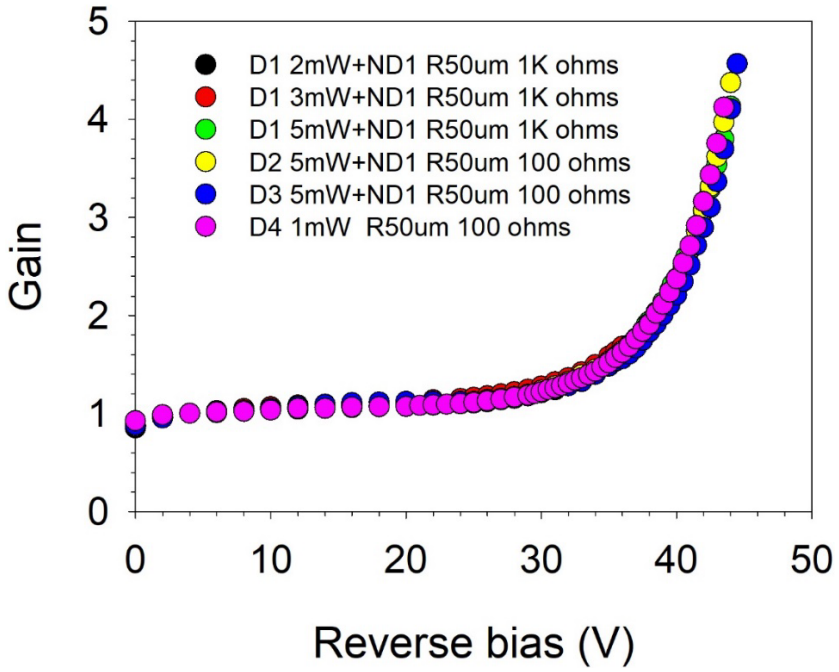

Figure A-III.9 Multiplication results for STF82(P1600) using 405nm laser in different size devices and laser power.